Hydrodynamics of Cyclogenesis from Numerical Simulations

Veeraraghavan Kannan

Department of Engineering
University of Cambridge

This dissertation is submitted for the degree of
Doctor of Philosophy

Robinson College October 2022

Declaration

This thesis is the result of my own work and includes nothing which is the outcome of work done in collaboration except as declared in the Preface and specified in the text. I further state that no substantial part of my thesis has already been submitted, or, is being concurrently submitted for any such degree, diploma or other qualification at the University of Cambridge or any other University or similar institution except as declared in the Preface and specified in the text. It does not exceed the prescribed word limit for the Engineering Degree Committee. This thesis contains approximately 35000 words, 60 figures and 6 tables.

Veeraraghavan Kannan
October 2022

Hydrodynamics of Cyclogenesis from Numerical Simulations

Veeraraghavan Kannan

Cyclogenesis is referred to as a transition of low-pressure disturbances on the tropical ocean into a more symmetric warm-core cyclone. This has been studied in detail for the past 100 years. However, no laboratory analogue for tropical cyclones has been discovered to date. Thus, the fundamental understanding of cyclogenesis remains challenging and limited as one has to rely on satellite imagery, which has disadvantages. This calls for further research to develop a simple model that can be replicated in the laboratory to better understand cyclogenesis. The main advantage of using a simple model is that the birth of a tropical cyclone from a quiescent environment can be continuously tracked, and the various hydrodynamic processes involved in its genesis can be better understood in a confined domain. This understanding can help in developing better forecasting models.

The rotating Rayleigh-Benard convection (RRBC) model has been very effective and widely used in numerical simulations and by experimentalists to understand complex geophysical flows. Therefore in this work, the same RRBC model is used to carry out 3D numerical experiments in a shallow cylindrical domain filled with Boussinesq fluid. In atmospheric flows, the large eddies are responsible for turbulent transport since they contain most of the turbulent kinetic energy. Thus, the Large Eddy Simulation (LES) technique that explicitly resolves the larger eddies and models the effects of smaller eddies is appropriate for atmospheric flows and is used in this work to simulate a tropical cyclone-like vortex. This thesis attempts to tackle the problem of cyclogenesis purely based on hydrodynamics, neglecting the effects of stratification, thermodynamics and external wind shear. Therefore, the resulting large-scale vortex simulated is referred to as a tropical cyclone-like vortex.

This thesis explores the capability of the RRBC model in simulating tropical cyclone-like vortex and understanding cyclogenesis in detail. The first part of the thesis focuses on fixing suitable boundary conditions and finding the parameter space

necessary for forming a tropical cyclone-like vortex. This is because a tropical cyclone-like vortex has not been observed in a 3D RRBC model. This is a continuation of the previous studies, which focussed on simulating tropical cyclone-like vortex with axisymmetric approximation. The numerical experiments are then performed for a wide parameter range spanning several orders of magnitude. The simulated vortex is compared quantitatively with an actual tropical cyclone. It was found that the distinct structure of the vortex, namely the eye, eyewall and spiral bands, as well as the force balance of the simulated tropical cyclone-like vortex, is in good agreement with an actual tropical cyclone.

In the second part of the thesis, the data obtained from the simulation are analysed to understand the cyclogenesis in the simple model. The timescale for the cyclogenesis phase is proposed by taking advantage of simulating the vortex from a quiescent initial state. The cyclogenesis phase is the time difference between the start of the spinup of the cyclonic vortex and the vortex is fully evolved in the flow. The time for the start of the spinup of the cyclonic vortex is directly proportional to $\Omega^{-1}\sqrt{Re_t}$, where Ω is the background rotation rate and Re_t is the turbulent Reynolds number. The vortex fully evolves at Ekman spinup time, proportional to $\Omega^{-1}/\sqrt{E_t}$, where E_t is the turbulent Ekman number. During this period, unique spatial features appear in the large-scale vortex, namely, the eye, eyewall and spiral bands, and the vortex simultaneously becomes more intense. The proposed cyclogenesis timescale in the simple model agrees well with the real tropical cyclone track data from the United States Military's Joint Typhoon Warning Centre (JTWC) database. In addition, the simulated data are used to understand the energy exchange between the large-scale symmetric vortex and the asymmetric spiral bands in a tropical cyclone-like vortex by looking at the energy budget. Finally, the reason behind the formation and sustenance of tropical cyclone-like vortex in the RRBC setup is studied. The spontaneous onset of barotropic instability during the start of the spinup of the cyclonic vortex is seen as a plausible reason for the formation of a tropical cyclone-like vortex in the computational model used for this work.

Acknowledgements

I should first express my gratitude to my supervisor, Prof. N. Swaminathan, for taking me as his PhD student, providing me with an opportunity to work on a challenging problem for the past four years, and teaching me much despite myself. He has been a constant source of interesting problems (though I did not work on as many as I should have), and his infectious energy and enthusiasm have often served as great inspiration. I have learnt much from him on addressing a scientific problem, and I am sure I have much to learn.

I would like to thank my advisor, Prof. P. A. Davidson, for his constant support in clearing my doubts and reviewing results throughout my PhD. His critical insights have been immensely useful and have opened me up to new ideas and thoughts. It helped fine-tune my understanding of the problem and also helped me to prepare a better thesis.

I would like to thank Prof. Anurag Agarwal and Prof. Jan-Bert Flŏr for examining this thesis and for providing valuable comments to imporve the final form of this thesis. I am grateful to few people I have been fortunate enough to meet during my studies at Cambridge. I would like to especially mention Dr. James Massey and Dr. Zhi Chen for helping me during the initial phase of my PhD in setting up my workstation and settling down in Cambridge. I also want to thank James for clearing doubts outside my research, reading my thesis, and providing non-technical comments to improve my thesis. I am very thankful to Peter Benie for his constant help with computational resources throughout my PhD. Useful discussion with Dr. Jack Atkinson regarding my PhD problem during the first year is also acknowledged. The newcomers of Prof. Swaminathan's group during the final leg of my PhD also have my thanks for an eventful and engaging time.

I am thankful to the Cambridge Trust and Science and Engineering Research Board, India, for providing me with funding to undertake my doctoral research. This work has been performed using computational resources provided by the Cambridge Tier-2 system operated by the University of Cambridge Research Computing Service (www.hpc.cam.ac.uk) funded by EPSRC Tier-2 capital grant EP/T022159/1. I am also thankful to Robinson College, and my college tutor Dr. Geraint Jones for the help provided throughout my PhD.

I could not have made it anywhere without my family. My parents have encouraged and supported me selflessly for the past twenty six years, and of everything good I have done, I owe them a significant part. I am incredibly grateful to my grandmother, brother, sister-in-law, and everyone else in my family who have cared for me and remain pillars of support. Also, I am forever indebted to my mentor, Dr. P. R. Naren, for instilling interest in computational research during my undergraduate studies, which inspired me to take up this doctoral journey.

Finally, I would like to thank almighty for giving me such a fantastic opportunity to study at the University of Cambridge and for fostering grit and tenacity to tide over this adventurous journey.

To all my family, still present or not, for all they taught me.

Table of contents

List of figures

List of tables

Nomenclature

Acronyms

Symbol	Description
ABL	Atmospheric Boundary Layer
DNS	Direct Numerical Simulation
FFT	Fast Fourier Transform
GPI	Genesis Potential Index
JTWC	Joint Typhoon Warning Center
LES	Large Eddy Simulation
LSV	Large Scale Vortex
NASA	National Aeronautics and Space Administration
RANS	Reynolds-Averaged Navier-Stokes
RBC	Rayleigh Benard Convection
RRBC	Rotating Rayleigh Benard Convection
SGS	Sub-Grid Scale
TC	Tropical Cyclone

Dimensionless Numbers

Symbol	Description	Definition
Γ	Aspect Ratio	$\frac{H}{R}$

E	Ekman number	$\frac{\nu}{\Omega H^2}$
Pr	Prandtl number	$\frac{\nu}{\kappa}$
Re	Reynolds number	$\frac{VH}{\nu}$
Re_G	Reynolds number based on geostrophic velocity	$\frac{G}{\sqrt{\Omega\nu}}$
Ro	Rossby number	$\frac{V}{\Omega H}$

Greek Symbols

Symbol	**Description**	**Dimensions**	**Units**
α	thermal expansion coefficient	Θ^{-1}	K^{-1}
β	temperature lapse rate	$L^{-1}\Theta$	Km^{-1}
δ_{BL}	Ekman boundary layer thickness	L	m
δ_{ew}	thickness of eyewall	L	m
η	mixing length	L	m
Γ	Aspect Ratio	-	-
γ_{u_φ}	axisymmetricity of tangential velocity	-	-
κ	thermal diffusivity	L^2T^{-1}	m^2s^{-1}
κ_t	turbulent diffusivity	L^2T^{-1}	m^2s^{-1}
ν	kinematic viscosity	L^2T^{-1}	m^2s^{-1}
ν_t	turbulent eddy viscosity	L^2T^{-1}	m^2s^{-1}
Ω	Background rotation rate	T^{-1}	s^{-1}
ω_i	Vorticity in i-direction	T^{-1}	s^{-1}
ρ	density	ML^{-3}	kgm^{-3}

σ	von Karman constant	-	-
θ	temperature perturbation	Θ	K

Miscellaneous

Symbol	**Description**	**Definition**
$\ddot{X}$	depth average of quantity X	$\frac{1}{H}\int_0^H X\,dz$
$\langle X\rangle$	azimuthal average of quantity X	$\frac{1}{2\pi}\int_0^{2\pi} X\,d\varphi$
$\langle X\rangle_v$	volume average of quantity X	$\frac{1}{\pi R^2 H}\int_0^{2\pi}\int_0^R\int_0^H X\,rdzdrd\varphi$
$\overline{\overline{X}}$	surface average of quantity X	$\frac{1}{L_x\times L_y}\int_0^{L_y}\int_0^{L_x} X\,dxdy$
$\tilde{X}$	time Average of quantity X	$\frac{1}{t_2-t_1}\int_{t_1}^{t_2} X\,dt$
X^*	non-dimensionalised value of quantity X	$-$
X'	azimuthal asymmetry of quantity X	$X-\langle X\rangle$

Roman Symbols

Symbol	**Description**	**Dimensions**	**Units**
ℓ	turbulent length scale	L	m
A	potential energy per unit mass	L^2T^{-2}	m^2s^{-2}

C_s	Smagorinsky constant	-	-
G	Geostrophic velocity	LT^{-1}	ms^{-1}
g	acceleration due to gravity	LT^{-2}	ms^{-2}
H	height of the domain	L	m
K	kinetic energy per unit mass	L^2T^{-2}	m^2s^{-2}
P	reduced pressure	$ML^{-1}T^{-2}$	Pa
R	radius of the domain	L	m
T	temperature	Θ	K
t	time	T	s
u_*	friction velocity	LT^{-1}	ms^{-1}
u_i	velocity in i-direction	LT^{-1}	ms^{-1}
V	buoyancy velocity	LT^{-1}	ms^{-1}
V_ℓ	buoyancy velocity for case 1 in Table 5.1	LT^{-1}	ms^{-1}

Chapter 1

Introduction

1.1 Motivation

A tropical cyclone is a collective term used by meteorologists to describe a rotating, organized system of clouds and thunderstorms originating over tropical or subtropical waters with closed low-level circulation (Emanuel, 2018). Low-level circulation is a weak cyclonic circulation that develops around a low-pressure region. This system is classified as a hurricane, typhoon, or cyclone, depending on the geographical origin of the storm. A typical tropical cyclone is shown in Fig. 1.1 and its anatomy is shown in Fig. 1.2 schematically. Tropical cyclones develop by drawing energy from the ocean surface. They can only form when the sea surface temperature is above 26°C, and their intensity is sensitive to the temperature at the sea surface (Riehl, 1950). The higher the temperature, the larger its intensity.

Tropical cyclones (TCs) cause widespread damage in specific regions due to high winds and flooding. Studies have shown that in the aftermath of severe storms, there is a 25% increase in the onset of mental depression for the survivors after the storm event (Neria & Shultz, 2012). Apart from the health effect, there is also a significant economic impact. A study by the International Monetary Fund (IMF) showed that the destruction caused by the storms cost countries around the world about 100 billion US dollars per year from 2000 to 2010 (Sebastian et al., 2017). In addition to the socio-economic impacts of a tropical cyclone, there are also environmental impacts. A tropical cyclone is always accompanied by strong winds and flooding, which can uproot trees and plants and over-saturate the soil, thereby affecting the local natural ecosystem (Ibanez et al., 2019).

Tropical cyclones usually help maintain the global heat balance by moving warm tropical air from the equator towards the poles. However, due to rapid climate change

Fig. 1.1 Hurricane Hector was captured from the International Space Station nearly 250 miles above the Pacific Ocean just south of the Hawaiian island chain (Expedition 56 Crew NASA, 2018).

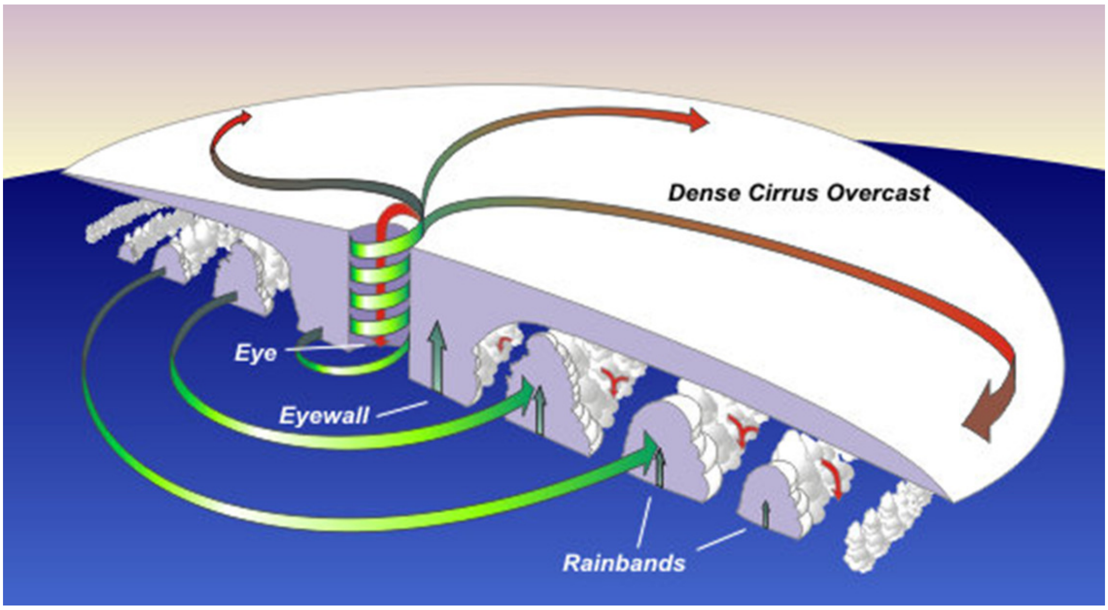

Fig. 1.2 Anatomy of a typical tropical cyclone (National Weather Service, 2019).

occurring around the world, there is an increase in the sea level, which can influence the behaviour of tropical cyclones (Knutson et al., 2010, 2019, 2020). A summary of modelled TC projections for a 2°C anthropogenic global warming is shown in Fig. 1.3. It is expected that the tropical cyclone's frequency and intensity will increase due to global warming. Therefore, improving the cyclone forecasting model is required to minimise its impact on the economy and living beings.

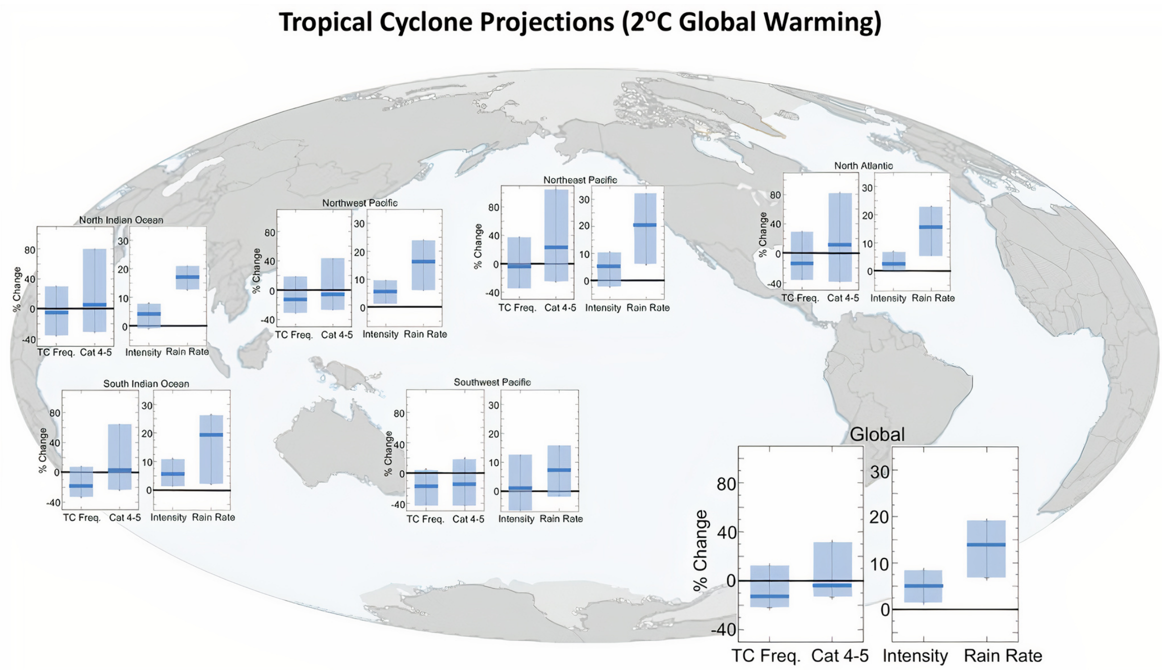

Fig. 1.3 Summary of TC projections for a 2°C global anthropogenic warming (Knutson et al., 2020).

Tropical cyclones are usually forecasted using metrological data with the help of numerical models. They are of three types, namely, dynamic, statistical, and combined statistical-dynamical models. The dynamic model is a global model that solves the governing equations for the atmospheric flow on the global scale (Holland, 1993). Some widely used global dynamic models are the United Kingdom Met Office Model (UKMET), Weather Research and Forecasting (WRF) model, Geophysical Fluid Dynamics Laboratory model (GFDL), and European Center for Medium-Range Weather Forecasting (ECMWF) (Holland, 1993). Dynamical models utilise powerful supercomputers and metrological data to calculate the subsequent development of tropical cyclones. The statistical model predicts the cyclone behaviour by extrapolating the previously available datasets; since this model does not solve the mathematical equations at a global scale, they are faster than the dynamic model (Holland, 1993).

There are also hybrid statistical/dynamical models that combine dynamic and statistical model functions and features. The three models specified here are mainly used to forecast storm tracks, the storm's intensity, coastal flood, and rainfall (Roy & Kovordányi, 2012). These forecasting models require various inputs such as topography, bottom friction, tidal level characteristics, and meteorological data.

There are two significant issues in forecasting tropical cyclones: predicting the storm track and its intensity. Storm track forecasts have significantly improved in the past 25 years, but progress is comparatively less for intensity forecasting (Montgomery & Smith, 2017). The improvement is because track forecasting depends on large-scale atmospheric flows, included predominantly in almost all global forecasting models. On the other hand, intensity forecasting depends on internal variability (within tropical cyclones) and air-sea interaction. The intensity appears to depend on processes of wide-ranging scales spanning many orders of magnitude. Improving the cyclone prediction model involves a better understanding of cyclogenesis and the complex processes involved in sustaining a mature cyclone.

Understanding and predicting the genesis of a tropical cyclone is a challenging task. There are several intermediary stages involved in the formation of tropical cyclones. These stages are, as summarised in many textbooks for example, see Anthes (2016),

1. **Tropical Disturbance**
   The formation of clouds and precipitation combined with surface winds is called a tropical disturbance. These disturbances create an area of low-pressure circulation without any presence of a closed isobar. The disturbance is usually formed over a large area of warm water, which facilitates the formation of clouds and precipitation through organized convection. In addition, the radial temperature difference between warm ocean and cold surrounding set up surface wind. In some cases, the reminiscence of tropical cyclones that travelled through the region for a few days can also contribute to the tropical disturbance. This disturbance in the atmosphere above the ocean must be sustained for more than 24 hours, leading to the formation of low-pressure circulation. Typhoon Bopha, which has a basic round shape in Fig. 1.4, is a tropical disturbance yet to develop into a depression system. Typically, the tropical disturbance has a size of about 100 to 200 km.

2. **Tropical Depression**
   The tropical disturbance upgrades to a tropical depression when the sustained wind speed is between 20 to 35 knots (10 to 18 m/s). In this stage, there is a

closed circulation where at least one closed isobar is seen, accompanied by a drop in pressure in the centre of the storm. The pressure drop will help create subsidence in the storm, referred to as the "eye", see Fig. 1.2. Once formed, the eye will play a vital role in increasing the intensity of the storm at a later stage. A thunderstorm also accompanies the low-pressure storm. In Fig. 1.4, typhoon Maria is on the verge of forming a spiral structure and central eye. Therefore, it can be inferred that the tropical disturbance has sustained to form a tropical depression and is on the verge of developing into a tropical cyclone with its unique spatial features. These depressions have a typical size of about 500 km.

3. **Tropical Storm**
   In this stage, the maximum sustained winds ranging from 35 to 64 knots (18 to 33 m/s), and the pressure will drop even further at the storm's centre, aiding in the eye formation. The convection begins to concentrate in the vicinity of the eye in the form of an annular ring. The rainfall resulting from the thunderstorm begins to organize itself into distinct rain bands (see typhoon Saomai Fig. 1.4) in the outer region of the storm due to intensified circulation.

4. **Tropical Cyclone**
   A tropical storm becomes a tropical cyclone when the sustained wind speed exceeds 64 knots (33 m/s). In this stage, the pressure drops, and the rotation becomes intense. The rain bands start to rotate around the eye of the Storm. The region of strongest winds near the eye is referred to as the "eyewall", which is the most destructive part of the tropical cyclone. In Fig. 1.4, typhoon Saomai is seen to have developed into a tropical cyclone with an organized convection pattern of about 1000 km in size.

The fundamental understanding of cyclogenesis is limited and further research is still required to understand this better. Developing an improved theory for cyclogenesis, which can predict this process using large-scale flow parameters, can help to improve intensity forecasting. Since the large-scale parameters are inherently present in the global forecasting models. The improved prediction model can help to minimise damages and loss of life caused by the destructive forces of tropical cyclones.

1.2 Background on Cyclogenesis

As discussed in the previous section, cyclogenesis involves several intermediatory stages, and developing a good understanding of it is challenging. There is no widespread

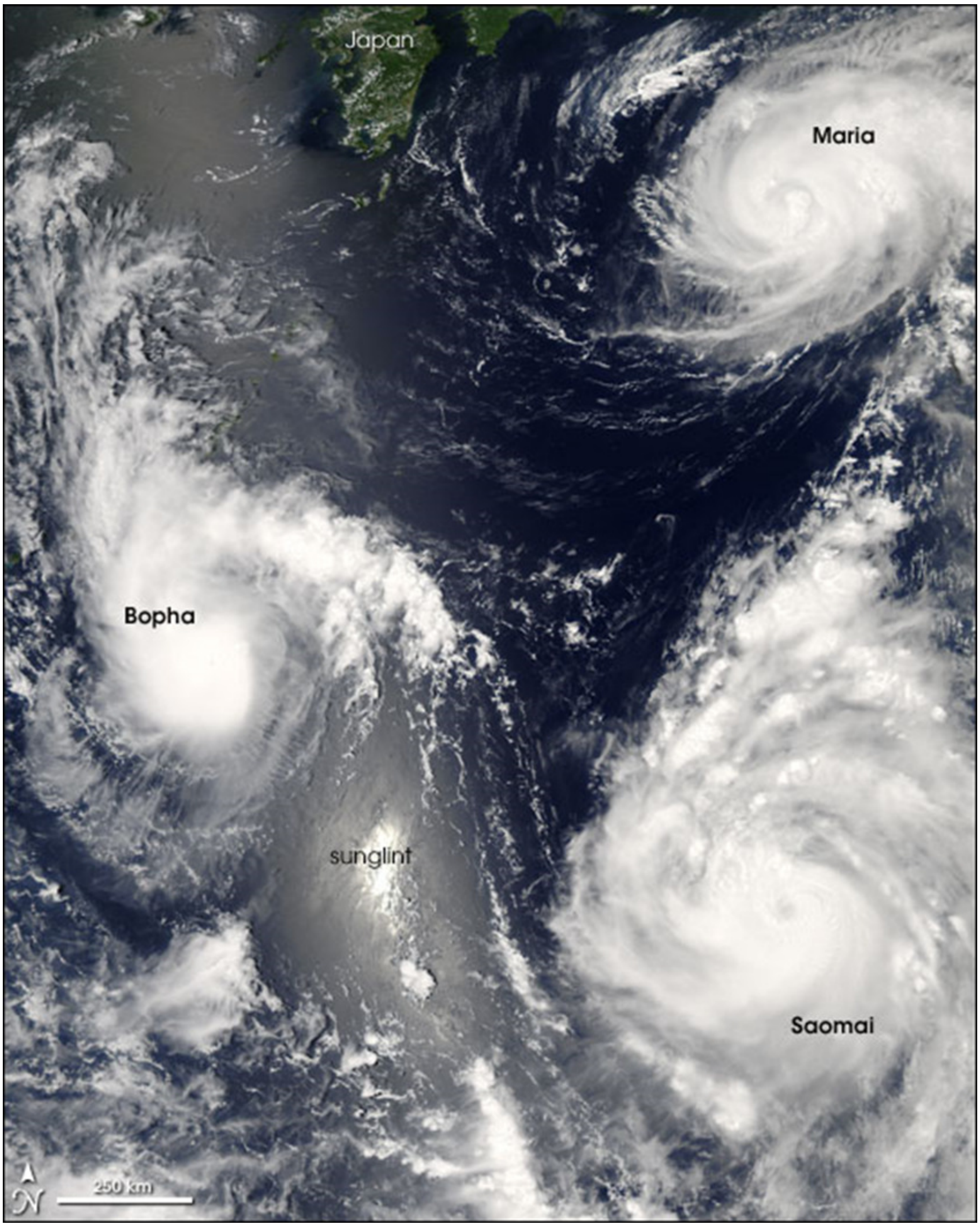

Fig. 1.4 Stages of development of tropical cyclone (NASA, 2006).

consensus on the definition of this term in the literature, though very broadly, it is referred to as a transition of the system from a disturbance often observed in the tropics to a more symmetric warm-core cyclone with a low-pressure centre. One thing that is accepted from the earliest studies of cyclogenesis is that tropical cyclones originate only in the presence of some disturbance (Riehl, 1948). Bergeron (1954) attempts to explain why a finite-amplitude disturbance is required for the formation of the cyclone. It is highlighted that groups of convective storms in the ocean are always accompanied by cool, anticyclonic outflow near the surface. It stabilizes the atmosphere and prevents the formation of the cyclone. Bergeron (1954) postulates that if the convective storms occur over a sufficiently warm ocean (acts as disturbance), then the cooled outflow is reheated on coming in contact with the warm ocean. This, in turn, initiates the convection process and results in the formation of a tropical cyclone. When numerical models are initialized using environments where the moist convection is statistically equilibrated, a finite amplitude disturbance is required to initiate intensification by wind-surface flux feedback, and the too weak disturbances decay (Rotunno & Emanuel, 1987, Emanuel, 1989, Dengler & Reeder, 1997). It is consistent with the observation that an external disturbance must trigger the genesis.

Another necessary condition agreed upon in the literature for genesis is that the potential intensity, a measure of the maximum wind in the system, must be sufficiently large (Emanuel, 2018). This maximum wind speed strongly correlates with the ocean surface temperature (Riehl, 1950). Palmen (1948) established that tropical cyclones form only when the ocean surface temperature is larger than about 26° C, which supports the conclusion of Riehl (1950). Gray (1968) showed that genesis occurs only in environments characterized by small vertical shear of the horizontal wind and also favours regions of relatively large, low-level cyclonic vorticity. Gray (1979) later established a set of conditions that are necessary (but not sufficient) for the genesis. Further to the two factors noted above, Gray (1979) identifies higher values of the Coriolis parameter, relative humidity of the middle troposphere, ocean thermal energy, and the difference between the equivalent potential temperatures at the surface and 500 hPa height favour the genesis process.

The early studies, such as that of Riehl (1948) and Bergeron (1954), argued whether tropical cyclones arise from pre-existing disturbances near the surface, such as fronts, or from disturbances in the upper troposphere. Later observations showed that there are many routes to the genesis, including nearly classic baroclinic development (Bosart & Bartlo, 1991), the interaction of easterly waves or other low-level disturbances with upper troposphere tropical disturbance (Ramage, 1959, Sadler, 1976, Montgomery & Farrell, 1993), and possibly, accumulation of energy from the wave into large-scale diverging flows (Shapiro, 1977, Sobel & Bretherton, 1999).

Another theory for cyclogenesis is developed using the idea that patches of high vorticity associated with individual convective systems can, under certain circumstances, merge to form a more powerful emerging cyclone (simply called vortex merging).

Fujiwhara (1921) proposed the idea that genesis involves the fusion of several small vortices. This theory has been revived by conducting a series of numerical experiments using idealized quasi-geostrophic, asymmetric balance, and shallow water primitive equation model (Ritchie & Holland, 1993, Simpson et al., 1997, Montgomery & Enagonio, 1998, Möller & Montgomery, 1999, 2000, Montgomery et al., 2006), where it has been shown that small-scale patches of vorticity (also known as hot towers) introduced into the flow field with a larger-scale vortex have quickly become axisymmetric. The small-scale vorticity patches feed their energy into the vortex scale flow. This suggests that mesoscale convective systems that develop outside the eyewall may help intensify the vortex.

The primary problem in the genesis is the transformation of an existing disturbance in the environment into a system operating on the feedback between surface enthalpy fluxes and surface wind. Any theory for the cyclogenesis must consider that such transformations are relatively unusual and, in any event, only occur under the conditions reviewed by Gray (1968). Gray (1968) identified six environmental properties upon which genesis depends: the Coriolis parameter, low-level relative vorticity, shear of the horizontal wind through the depth of the troposphere, relative humidity of the middle troposphere, ocean thermal energy, and the difference between the temperatures at the surface and at 500 hPa height. Bergeron (1954) concluded that, under normal circumstances, convective downdrafts extinguish the tendency for the boundary layer entropy to increase. This study also suggested that if the surface cyclone could be made strong enough, by some means, the inward Ekman drift would overcome the anticyclonic outflow, leading to positive feedback between surface enthalpy flux and wind and transformation into a warm-core system. But it has become apparent from a series of numerical experiments (Emanuel, 1989, 1995) and a field experiment (Emanuel, 1994, Bister & Emanuel, 1997) that a necessary condition for the genesis is the establishment of the order of a 100-km-wide column of nearly saturated air in the system core. Any environmental influence that disrupts the formation of such a saturated column will prevent the genesis and weaken any existing system. This has been pointed out clearly by Simpson & Riehl (1958), the ventilation of low entropy air in the middle troposphere through a nascent system will have this effect, which explains why sometimes vertical shear tends to obstruct the genesis. In axisymmetric models, establishing the order of 100-km-wide saturated column also appears to be sufficient for genesis (Emanuel, 1995).

An important remaining question is how such a column is established and what conditions are required to sustain it. Bister & Emanuel (1997) tried to address this question in an axisymmetric model with moisture and with an additional assumption of an artificial “showerhead” (rain) in the middle troposphere. The evaporation of the rain cooled and moistened the column spinning up a mesocyclone near the altitude of the assumed showerhead. When the wind-induced by heat exchange on the sea surface reaches sufficient strength, it forms a warm core cyclone in the pre-moistened column. The observations by Davidson (1995a,b) of evolving cloud clusters and Hurricane Guillermo observed in the eastern North Pacific in 1991 by Bister & Emanuel (1997) suggest in these developments. The saturation was achieved by evaporation of rain falling from clouds associated with the cumulus convection. The vital ingredient in the genesis process is the downward advection of angular momentum in the evaporatively driven downdraft. However, it is still unclear whether such a mechanism works in the genesis. This suggests the need for more field and numerical experiments dedicated to the problem of understanding the processes involved in cyclogenesis. Therefore, a lot of dedicated research is required.

1.3 Aims and Objectives

In the previous section, it can be seen that the cyclogenesis problem is studied with the help of field experiments, numerical models with complete moist physics, or approximated dry convective models (like axisymmetric approximation, shallow water equation, quasi-geostrophic approximation, etc.,). Even in numerical experiments, most of the problems focussed on studying the transition of disturbance to the tropical cyclone with a pre-defined disturbance (100 km wide column of saturated air in the system). More focus was given to the effect of thermodynamics on cyclogenesis. In this thesis, we try to to understand the hydrodnamics of cyclogenesis by considering a simple rotating 3D Rayleigh-Benard convection (RRBC) setup with Boussinesq approximation (Boussinesq, 1903). The RRBC setup has high relevance to geophysical and astrophysical flows. It has been used in the past to study the mechanism behind eye formation in a tropical cyclone-like vortex (Oruba et al., 2017) by conducting laminar axisymmetric simulations. The upsweep of the bottom boundary layer by strong poloidal flow was shown to form an eye and eyewall in axisymmetric RRBC of Boussinesq fluid (Oruba et al., 2017, 2018) which was also suggested by Atkinson et al. (2019).

The main aim of this thesis is to explore the capability of the RRBC model to simulate a 3D tropical cyclone-like vortex starting from a quiescent initial state and to better understand the hydrodynamics involved in the cyclogenesis using the simple model. In this work, Large Eddy Simulation (LES) paradigm will be used to model the turbulence. The next chapter will present a detailed explanation of the LES framework and why it is used for this study. Since we don't consider moisture physics in the model, we call the resulting large-scale vortex a *tropical cyclone-like vortex*.

An attempt is made to answer the following questions forming the objective of this work.

1. How different is the tropical cyclone-like vortex dynamics in a 3D model compared to the earlier axisymmetric counterpart studied? Is there any significant effect of adding an extra degree of freedom to the fluid on the evolution of the vortex?

2. What is the role of the sidewall thermal boundary condition on the evolution of tropical cyclone-like vortex? The effect of thermal boundary conditions is assessed using adiabatic and isothermal boundary conditions along the sidewall. This question is addressed because there isn't a sidewall in reality, but that is not the case in an experiment/numerical model. Therefore, it is essential to understand the role of the sidewall boundary condition, precisely the thermal boundary condition, in the model.

3. When does a tropical cyclone-like vortex emerge in a RRBC model? Can a condition be deduced for cyclogenesis using the control parameters of the problem? If it can be deduced, this condition helps to improve the forecast of tropical cyclones because large-scale atmospheric flow parameters are inherently present in the global weather forecasting models.

4. Are the features of a simulated tropical cyclone-like vortex similar to that seen in an actual tropical cyclone using field measurements (see Fig. 1.2)?

5. Characterize the energetics of symmetric vortex scale and asymmetries during the evolution of the tropical cyclone-like vortex.

6. How is the large-scale tropical cyclone-like vortex formed from a quiescent initial state? What is/are the probable reason(s) for the formation of these large-scale structures?

Addressing these objectives will help us understand the cyclogenesis conditions in controlled numerical experiments, which will probably also help to design controlled physical experiments. The experiments can be used to unravel the intricate hydrodynamic complexities in cyclogenesis further.

1.4 Thesis Structure

The structure of the rest of this thesis is as follows. Chapter 2 describes the governing equations, control parameters and the methodology used to simulate the tropical cyclone-like vortex in a RRBC setup using LES. The sub-grid closure model used in this work is also discussed.

The capabilities of the *OpenFOAM* software to simulate atmospheric flows are tested and validated in chapter 3. In particular, the classical problem of the turbulent Ekman layer is simulated using the LES framework. The mean velocity, second-order statistics, and eddy viscosity are computed in LES using the dynamic Smagorinsky sub-grid closure model at different Reynolds numbers discussed in detail to show the capabilities of the LES framework. The results obtained are validated with the DNS (Coleman et al., 1990, Coleman, 1999) and experimental results (Caldwell et al., 1972). The thesis will subsequently use the same LES model for the turbulent tropical cyclone-like vortex simulations.

Further validations of the code with rotational effects and the temperature equation implemented are performed by conducting laminar axisymmetric tropical cyclone-like vortex investigated by Oruba et al. (2017, 2018) and Atkinson et al. (2019). The effects of 3D and sidewall thermal boundary conditions in laminar flows are discussed, along with the validation results in Chapter 4. This chapter address the first two objectives.

The third objective is addressed in chapter 5. A condition for cyclogenesis is deduced through an order of magnitude analysis of the azimuthal vorticity equation. The LES calculations are performed for a wide range of flow parameters to test and validate the condition, and the results are discussed in this chapter. The timescale for cyclogenesis is also proposed through data analysis.

The symmetric and asymmetric features of tropical cyclone-like vortex deduced from the simulation are compared with field measurements of actual tropical cyclones in chapters 5 and 6 to address the fourth objective. The different energy exchange mechanisms at play between the azimuthally symmetric and asymmetric energy during the cyclogenesis are discussed to address the fifth objective. The possible reasons for the formation of a large-scale vortex from a quiescent state, the sixth objective, is investigated in chapter 7. In particular, the role of barotropic instability in the formation and sustenance of tropical cyclone-like vortex is studied in detail. The main findings of this thesis work are summarized in chapter 8, along with directions for future work.

Chapter 2

Research Methodology

Fluid flow driven by buoyancy is prevalent in nature. In these flows, thermal convection driven by density difference plays an important role. In some cases, rotation, in addition to buoyancy, affects these fluid flows. Large-scale motion in the Earth's atmosphere and ocean are driven by buoyancy induced by sufficiently strong temperature gradients and have large length scales such that rotation of the Earth plays a significant role in its development. Rotating Rayleigh-Benard convection may be a simple model, but it is very effective and helpful for understanding complex geophysical flows. Furthermore, the rotating convection model is a very intriguing flow configuration of fundamental interest. Insights gathered from rotating convection problems can be used to model geophysical flows. Since tropical cyclones are large-scale, organized, rotating convective vortices, numerical experiments of rotating convection are conducted in a low aspect ratio (vertical scale $\ll$ horizontal scale) domain deduced from an actual tropical cyclone for this work.

In this chapter, the governing equations used are introduced. The Earth's rotation is incorporated into the model by adding Coriolis and centrifugal forces into the momentum equation. The tropical cyclone circulation is relatively limited on the horizontal scale, so the rotation rate is assumed to be independent of latitude. This is referred to as f-plane approximation, where f denotes the Coriolis parameter defined by $f = 2\Omega \sin\phi$, with Ω as the Earth's rotation rate and ϕ as the latitude (Montgomery & Smith, 2017). The governing equations presented later are simplified using Boussinesq approximation (Boussinesq, 1903), which is acceptable for dry convective flows typically used to model tropical cyclones. Much of the information provided in this chapter can be found in the textbooks by Davidson (2013), Pope (2000) and Chandrasekhar (1961).

2.1 Equations of Motion

This section introduces the fluid flow equations for a tropical cyclone-like vortex. The fluid is considered to be incompressible. In an incompressible flow, the volume of fluid is conserved. Apart from the volume of the fluid, the mass of the fluid is also conserved. The mass and volume conservation is the same in incompressible flow. The mass conservation equation for an incompressible flow is given as (Davidson, 2013, Pope, 2000, Chandrasekhar, 1961),

$$\frac{\partial u_i}{\partial x_i} = 0 \tag{2.1}$$

where, u_i is the fluid velocity in the spatial direction x_i.

The momentum balance in rotating frame of reference is (Davidson, 2013, Chandrasekhar, 1961),

$$\rho\left[\frac{\partial u_i}{\partial t} + u_j\frac{\partial u_i}{\partial x_j}\right] = -\frac{\partial P}{\partial x_i} + \mu\frac{\partial^2 u_i}{\partial x_j \partial x_j} - 2\rho\Omega u_j \varepsilon_{ij3} + F_b \tag{2.2}$$

The temperature equation is given by (Davidson, 2013, Chandrasekhar, 1961)

$$\frac{\partial T}{\partial t} + u_j\frac{\partial T}{\partial x_j} = \kappa\frac{\partial^2 T}{\partial x_j \partial x_j} + \dot{Q}_s \tag{2.3}$$

The body forces, F_b, that are relevant for the atmospheric flow system include buoyancy force due to gravitational effect. Therefore, $F_b = -\rho g \delta_{i3}$. μ is the molecular viscosity, κ is the thermal diffusivity, T is the temperature, P is the pressure, the term $2\rho\Omega U_j \varepsilon_{ij3}$ is the Coriolis force; a fictitious body force that manifests as a result of moving in a non-inertial frame, δ_{i3} is the Kronecker delta which is one if i =3 and otherwise it is zero, ε_{ij3} is Levi-Civita symbol which is zero if $i = j$, 1 if $(i,j) =$ (1,2) and -1 if $(i,j) =$ (2,1), Q_s is the source term in the temperature equation which usually includes the evaporation, condensation term given by $\dot{Q}_s = L_e\dot{q}_e + L_c\dot{q}_c$, where L_e is the latent heat of evaporation, L_c is the latent heat of condensation, $\dot{q}_e$ is the rate of evaporation and $\dot{q}_c$ is the rate of condensation. Since the equation for fluid is solved in a dry state, the source term $\dot{Q}_s$ is neglected while solving for temperature equation. Since the density difference created by thermal gradients drives the flow, the Boussinesq approximation (Boussinesq, 1903) can be invoked for the body force F_b. According to this approximation, the density variation can be expressed as $\rho = \rho_o + \rho'$, where ρ is the density, ρ_o is the background density distribution, and ρ' is the density perturbation.

In the same way, as for density, it is often helpful to separate the temperature field into two parts; a background temperature T_o and a perturbation θ such that $T = T_o + \theta$. One can link the density and temperature variations through a thermal expansion coefficient $\alpha = -(\partial\rho/\partial T)_p/\rho_o$ as follows (Chandrasekhar, 1961),

$$\rho' = -\rho_o \alpha \theta \tag{2.4}$$

Therefore after including the body forces with Boussinesq approximation, the momentum and temperature perturbation equations are given by (Chandrasekhar, 1961, Davidson, 2013):

$$\frac{\partial u_i}{\partial t} + u_j \frac{\partial u_i}{\partial x_j} = -\frac{1}{\rho_o}\frac{\partial P}{\partial x_i} + \nu \frac{\partial^2 u_i}{\partial x_j \partial x_j} - 2\Omega u_j \varepsilon_{ij3} - \alpha(T - T_o) g \delta_{i3} \tag{2.5}$$

$$\frac{\partial T}{\partial t} + u_j \frac{\partial T}{\partial x_j} = \kappa \frac{\partial^2 T}{\partial x_j \partial x_j} \tag{2.6}$$

where $P = p + p_o(z) - (\rho_o(\mathbf{\Omega} \times \mathbf{x})/2)$ is the reduced pressure term which includes hydrostatic pressure due to ρ_o and centrifugal force contribution, the kinematic viscosity is $\nu = \mu/\rho_o$.

2.1.1 Dimensionless Numbers

The governing equations, Eqs. (2.5) and (2.6), can be non-dimensionalised by introducing H, V, and ΔT as the reference length, convective velocity and temperature scales respectively, where $V = \sqrt{g\alpha\Delta T H}$ is the maximum buoyancy-generated velocity (Prandtl, 1932). The non-dimensionalised equations are then given as:

$$\frac{\partial {u_i}^*}{\partial t^*} + {u_j}^* \frac{\partial {u_i}^*}{\partial {x_j}^*} = -\frac{\partial P^*}{\partial {x_i}^*} + \frac{1}{\mathrm{Re}} \frac{\partial^2 {u_i}^*}{\partial {x_j}^* \partial {x_j}^*} - \frac{2}{\mathrm{Ro}} {u_j}^* \varepsilon_{ij3} - T^* \delta_{i3} \tag{2.7}$$

$$\frac{\partial T^*}{\partial t^*} + {u_j}^* \frac{\partial T^*}{\partial {x_j}^*} = \frac{1}{\mathrm{RePr}} \frac{\partial^2 T^*}{\partial {x_j}^* \partial {x_j}^*} \tag{2.8}$$

where, dimensionless distance is ${x_i}^* = x_i/H$, velocity is ${u_i}^* = u_i/V$, time is $t^* = tV/H$, temperature $T^* = T/\Delta T$, pressure $P^* = P/V^2$. The dimensionless numbers are Reynolds number $Re = VH/\nu$, which is the ratio of convective to viscous force, Prandtl number $Pr = \nu/\kappa$, Ekman number $E = \nu/\Omega H^2$ is the ratio of viscous to rotational force and Rossby Number $Ro = V/\Omega H = ReE$. It is also useful to define a geometrical parameter called aspect ratio $\Gamma = H/R$ for a convective flow inside a bounded domain, which can influence the flow dynamics. The equations discussed in this section are to be supplemented with appropriate initial and boundary conditions before solving them.

2.2 Simulation Methods

High Reynolds number time-evolving three-dimensional turbulent motion consists of a wide range of scales of chaotic motion. Numerical integration of the governing equations without any approximation to explicitly calculate all the relevant scales of turbulent motion is known as Direct Numerical Simulation (DNS). The drawback of this method is that it can be used only for low-moderate Reynolds number flow due to its computational demand. The relevant scales range from the energy-containing large scale to the dissipative Kolmogorov scale. The Kolmogorov scales are defined as (Kolmogorov, 1941, Tennekes & Lumley, 1972):

- Length scale
$$\ell = \left(\frac{\nu^3}{\epsilon}\right)^{1/4}$$
- Timescale
$$\tau = \left(\frac{\nu}{\epsilon}\right)^{1/2}$$
- Velocity scale
$$v = \frac{\ell}{\tau} = (\nu\epsilon)^{1/4}$$

where ν is the kinematic viscosity, and ϵ is the kinetic energy dissipation rate. These scales define the ratio of the largest to the smallest scale of motion. The largest length, time and velocity scale be denoted as l_o, t_o and U_o respectively. Therefore, the energy dissipation at a large scale is approximated as $\epsilon \sim {U_o}^3/l_o$ (Tennekes & Lumley, 1972). This expression for ϵ when substituted into the length scale gives the ratio of largest to smallest length scale and is given as,

$$\frac{l_o}{\ell} \sim \mathrm{Re}^{3/4} \tag{2.9}$$

where the Reynolds number, $Re = (U_o l_o)/\nu$. A similar ratio can be obtained for velocity and timescale ratios.

The number of grid points required for the DNS is based on Eq. (2.9). The total number of grid points accurately required for the DNS study of 3D turbulence is given by (Geurts, 2003):

$$N = (n\mathrm{Re}^{3/4})^3 = n^3\mathrm{Re}^{9/4} \tag{2.10}$$

where n is a constant with a value ranging from 3 to 5 is typically used (Geurts, 2003). Equation (2.10) shows that as the Reynolds number increases, more grid points are required for DNS to resolve all the relevant scales of motion. The Reynolds number is $\mathrm{Re} \sim 10^9$ (Stull, 2012) for a typical atmospheric boundary layer flow. The number of grid points required to fully resolve the flow is $N = 64 \times (10^9)^{9/4} \sim 1.14 \times 10^{22}$ for $n = 4$ in Eq. (2.10). It is not possible to conduct simulations with this huge number of grid points; the current capabilities of the modern computer allow for simulating grid sizes with $\mathcal{O}(10^{11})$ points. Thus, DNS is unsuitable for atmospheric flows, although it is an excellent tool to investigate at moderate Re.

The turbulent fluctuating velocity in the Navier-Stokes equation can be statistically described using a model instead of fully resolving the turbulence as in DNS; this approach is known as Reynolds-Averaged Navier-Stokes (RANS) calculation. This method can be used for studying flows with realistic complexity but cannot be used for studying dynamic influences and consequences for all the scales involved.

There is another turbulence modelling approach known as Large Eddy Simulation (LES), wherein the large-scale motions are resolved, and the small scales that are insensitive to the specifics of the flow are modelled (Pope, 2000). Thus, the model can be simple and universal. The LES framework compromises between DNS (fluctuations are resolved) and RANS (fluctuations are modelled).

The schematic of the turbulent kinetic energy spectrum in wavenumber space is shown in Fig. 2.1. The schematic of the energy spectrum plot summarises the extent of turbulent length scales modelled/computed for the different turbulence modelling approaches. The typical numerical resolution requirements and complexity that different turbulence modelling approaches can handle are detailed in Fig. 2.1. DNS is usually preferred for simple problems, requiring a higher resolution of the numerical grid to compute the relevant scales of turbulence. The numerical grid resolution requirement decreases for LES and even more for RANS modelling approaches compared to DNS. Hence, problems with a higher complexity are usually solved using LES and RANS approaches.

In atmospheric flows, the largest turbulent eddies are of the order of kilometres and the smallest scale is in the order of a millimetre. The entire range of scales covers six orders of magnitude. Integrating the governing equations to resolve this entire range of scales using the currently available massively parallel exascale machines is unfavourable. Given this limitation, the LES approach is ideal, since the important

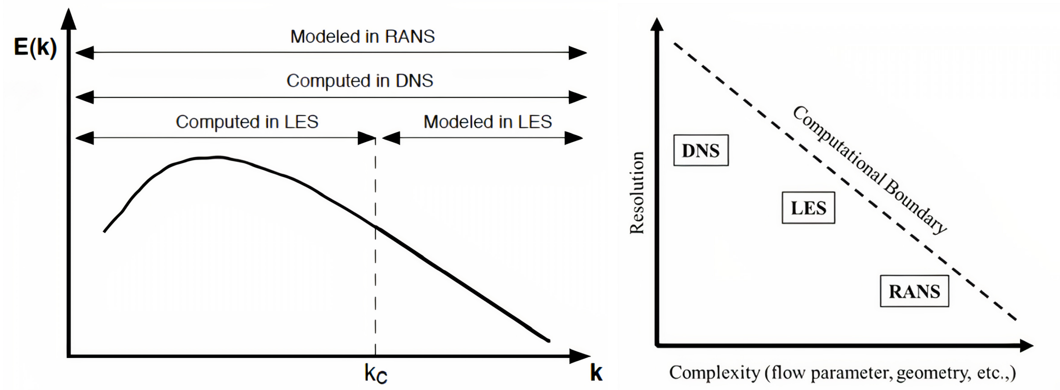

Fig. 2.1 Schematic showing the capabilities of different turbulent approaches (adapted from Geurts (2003)).

energy-containing large scales can be resolved, and other scales of physical relevance can be modelled. In atmospheric flows, the large eddies are responsible for turbulent transport since they contain most of the turbulent kinetic energy (Wyngaard, 2010). Thus, the LES technique that explicitly resolves the larger eddies and models the effects of smaller eddies is appropriate for atmospheric flows and is used in this work to simulate a tropical cyclone-like vortex.

2.3 Large Eddy Simulation

In LES technique the governing equations, Eq. (2.5) and Eq. (2.6), are spatially filtered and the filtered equations are obtained by decomposing the dependant variables into filtered and subgrid parts. For example, velocity (u_i) in the momentum equation is decomposed as $u_i = \overline{u}_i - {u_i}'$ where $\overline{u}_i$ is the filtered or resolved component and ${u_i}'$ is the subgrid scale component. The resolved scale component is defined as (Pope, 2000)

$$\overline{u}_i(x_i) = \iiint_V u_i(x_i')G(x_i - x_i')\, dx_i' \tag{2.11}$$

Equation (2.11) is written for one-dimension for the sake of simplicity, and it can be easily extended to three dimensions as demonstrated in (Pope, 2000). The homogeneous filter function G whose shape is chosen such that it approaches zero when $x_i - x_i'$ exceeds filter size Δ. In addition, the filter function must also satisfy the normalisation condition $\int G(x_i')dx_i' = 1$ (Pope, 2000). A few important points should be noted with regard to the filtering operation for LES:

1. The rules for filtering in LES are $\overline{\overline{u}}_i \neq \overline{u}_i$ and $\overline{u'}_i \neq 0$, where $u'_i = u_i - \overline{u}_i$ is the residual or sub-grid part of u_i.

2. The operation of filtering and differentiation with respect to time do commute i.e.,
$$\overline{\left(\frac{\partial u_i}{\partial t}\right)} = \frac{\partial \overline{u}_i}{\partial t}$$

3. The operation of filtering and differentiation with respect to position do not commute in general i.e.,
$$\overline{\left(\frac{\partial u_i}{\partial x_j}\right)} \neq \frac{\partial \overline{u}_i}{\partial x_j}$$
It is to be noted that the above operation of filtering for spatial derivative do commute when homogeneous filter is used (Pope, 2000) and hence
$$\overline{\left(\frac{\partial u_i}{\partial x_j}\right)} = \frac{\partial \overline{u}_i}{\partial x_j}$$

The filter should be chosen with care since it determines the accuracy of LES. Filtering is a weighted spatial average, where the shape of the filter determines its weight distribution, and its magnitude is determined by filter width. The most commonly used LES filters are Box (or top-hat) filter, Gaussian filter, and Spectral (or sharp-cut off) filter.

Applying the filtering procedure, term by term to Eq. (2.5) and Eq. (2.6) leads to the equations that govern resolved eddies (North et al., 2014, Pope, 2000):

$$\frac{\partial \overline{u_i}}{\partial t} + \frac{\partial \overline{u_i u_j}}{\partial x_j} = -\frac{1}{\rho_o}\frac{\partial \overline{P}}{\partial x_i} - \frac{\partial \tau_{ij}}{\partial x_j} + \nu \frac{\partial^2 \overline{u_i}}{\partial x_j \partial x_j} - 2\Omega \overline{u_j} \varepsilon_{ij3} - \alpha(\overline{T} - T_o) g \delta_{i3} \tag{2.12}$$

$$\frac{\partial \overline{T}}{\partial t} + \frac{\partial \overline{u_j} \overline{T}}{\partial x_j} = \kappa \frac{\partial^2 \overline{T}}{\partial x_j \partial x_j} - \frac{\partial \tau_j^T}{\partial x_j} \tag{2.13}$$

where the subgrid-scale (SGS) stress per unit mass is defined as $\tau_{ij} = \overline{u_i u_j} - \overline{u}_i \overline{u}_j$ and SGS heat flux is given by $\tau_j^T = \overline{T u_j} - \overline{T}\,\overline{u}_j$ which are used to model the residual Reynolds stress and heat flux, respectively. In order to solve the filtered equations, SGS models (closure equation) are required for the SGS stresses and heat fluxes. The choice of these models depends on the flow problem, and the models used in this work are detailed next.

2.3.1 Sub-grid Scale Closure

This study aims at simulating a large-scale phenomena. Hence, a simple SGS model that dissipates energy properly is preferred (also adequate) to represent the net effect of small-scale eddies. Therefore, the dynamic Smagorinsky model of Lilly (1992) is implemented into the *OpenFOAM* solver for this work. Other types of LES models are described in chapter 13 of Pope (2000) book. In this work, only the dynamic Smagorinsky model of Lilly (1992) is used; hence that approach is described in detail.

Dynamic Smagorinsky Model

The SGS stress per unit mass, τ_{ij} in the Eq. (2.12) can be written as the sum of its trace and an anisotropic part (Pope, 2000):

$$\tau_{ij} = \frac{\delta_{\mathrm{ij}}}{3} \overline{\tau}_{\mathrm{ij}}{}^{\mathrm{R}} + \tau_{\mathrm{ij}}{}^{\mathrm{r}} \tag{2.14}$$

The trace is added to the pressure term in Eq. (2.12) and computed implicitly in a pressure-corrector algorithm. The anisotropic residual term, $\tau_{\mathrm{ij}}{}^{\mathrm{r}}$, is modelled in this work using the dynamic Smagorinsky model of (Lilly, 1992) which is an extension of the Smagorinsky model (Smagorinsky, 1963), where the model constant is computed dynamically from the flow variables as described by Lilly (1992). This model is based on the assumption that the anisotropic residual tensor is aligned to the filtered strain. It can be expressed as

$$\tau_{\mathrm{ij}}{}^{\mathrm{r}} = -2\nu_t \overline{S}_{ij} = -\nu_t \left(\partial \overline{u}_i / \partial x_j + \partial \overline{u}_j / \partial x_i \right) \tag{2.15}$$

Similarly the SGS heat flux, τ_j^T, in Eq. (2.13) is related to local gradient of filtered temperature field as,

$$\tau_j^T = -\kappa_t \frac{\partial \overline{T}}{\partial x_i} \tag{2.16}$$

where $\overline{S}_{ij}$ is the filtered strain, ν_t is the subgrid scale turbulent eddy viscosity and κ_t is the subgrid-scale turbulent thermal diffusivity.

The subgrid-scale eddy viscosity and thermal diffusivity are expressed by

$$\nu_t = C_s (\Delta_f)^2 (2 \overline{S}_{ij} \overline{S}_{ij})^{0.5} \tag{2.17}$$

$$\kappa_t = \frac{\nu_t}{Pr_t} \tag{2.18}$$

where filtered length scale Δ_f is proportional to the grid size through $\Delta_f = (\mathrm{V_{cell}})^{1/3}$ and V $_{\mathrm{cell}}$ is the numerical cell volume, Pr_t is the turbulent Prandtl number.

The dynamic Smagorinsky model assumes scale invariance and exploits the resolved scales to compute the model coefficients C_s and Pr_t. The original dynamic model by Germano et al. (1991) computes one global averaged value for the whole flow field and assumes that the model constant is filter-invariant. In this work, the localised mixed formulation by Lilly (1992) is used, which computes the model constants, namely Smagorinsky constant C_s and turbulent Prandtl number Pr_t locally and also does not rely on the assumption of filter-invariance. The C_s computed based on Lilly (1992) approach is the square of actual C_s defined by Smagorinsky (1963).

Some advantages of using dynamic approach of Lilly (1992) compared to constant Smagorinsky model (Smagorinsky, 1963) are,

1. It is self-contained, and no need to specify any parameters as the model constants are computed dynamically.

2. No need for near-wall correction as the stresses are calculated from the flow variables as it evolves.

3. Inexpensive as it does not solve any additional transport equation for sub-grid scale variable.

4. Applied successfully to many flows (Free shear flows, rotating flows, atmospheric boundary layer, etc.,)

The specific boundary conditions used in this work are detailed in the following chapters.

2.4 Summary

The governing equations, both instantaneous and filtered, for an RRBC model are presented and described. The non-dimensional parameters governing this problem are identified and discussed. They are deduced by non-dimensionalising the equation. The need for LES to model turbulence in atmospheric flows is discussed, and the sub-grid scale model used in this study is described and justified. The LES model implemented in *OpenFOAM* will be validated in the next chapter by simulating the turbulent Ekman layer, as the first case for rotating flow, and comparing the results with DNS and experimental results.

Chapter 3

Turbulent Ekman Layer Simulation

In this chapter, the dynamic Smagorinsky model implemented in *OpenFOAM* is validated for a rotating flow as a first step. The classical problem of a turbulent flow generated near the ocean surface by steady wind stress in the presence of Earth's rotation is considered. Interest in this flow goes back to the early 1900. The first set of works was published by Ekman (1905). Ekman assumed a balance between the Coriolis force, viscous friction and the pressure gradient, adopted the approximation of constant vertical eddy viscosity ν_t, and derived a solution now known as the "Ekman spiral". In the case of a steady wind in the x-direction, the steady-state Ekman velocity profile in the open ocean is (for the northern hemisphere) (Ekman, 1905),

$$u_x = V_o \cos\left(\frac{\pi}{4} + \frac{\pi}{D}z\right)\exp\left(-\frac{\pi}{D}z\right),\ u_y = -V_o \sin\left(\frac{\pi}{4} + \frac{\pi}{D}z\right)\exp\left(-\frac{\pi}{D}z\right) \quad (3.1)$$

where u_x and u_y are the components of mean horizontal velocity, z is the downward directed vertical distance, $V_o = \sqrt{2}\pi\tau_o/(Df\rho)$ is the amplitude of the surface velocity, $D = \pi\left(2\nu_t/f\right)^{1/2}$ is the Ekman depth, τ_o is the surface shear stress and $f = 2\Omega\sin\phi$ is the Coriolis parameter, with Ω and ϕ denoting the Earth's rotation and latitude, respectively. According to the above solution, the mean horizontal velocities spiral clockwise and decay exponentially with depth. At the surface, the velocity is directed at 45° to the right (northern hemisphere) or the left (southern hemisphere) of the wind direction.

The Ekman model is, however, simple, elegant, and clearly supported by laminar laboratory experiments, rather dissimilar to the actual turbulent flow near an ocean or a lake surface. A persistent well-developed Ekman spiral has probably, never been observed in field measurements, (see Price & Sundermeyer (1999); for a detailed review). The reason is that the over-simplified character of the model leads to significant inconsistencies between the predicted and actual flows.

The basic assumptions of the Ekman model of a steady-state wind and the absence of any geostrophic currents are never observed in the open ocean. The effect of transient winds is significant. Attempts have been made to reconcile the Ekman layer theory and the measured data (Price et al., 1987, Chereskin & Roemmich, 1991, Gnanadesikan & Weller, 1995). Some important observations are made; in particular, the angle between the surface current and the wind was typically smaller than the 45° predicted by the Ekman model. However, a high degree of uncertainty remains associated with field observations of the phenomenon.

The assumption of a constant turbulent viscosity ν_t is a crude approximation. This is because, in real flows, the intensity of turbulent momentum transport expressed by ν_t is expected to vary with depth and time. This problem was recognized soon after the study by Ekman (1905). Rossby & Montgomery (1935) used the mixing length theory to derive a realistic distribution of turbulent viscosity $\nu_t(z)$. The mixing length η was assumed to decrease with depth in the bulk flow but to increase linearly in a thin boundary layer near the surface. This adjustment resulted in a modification of the Ekman velocity profile. The angle between the wind and surface current depends on the wind speed and latitude and, in most cases, is slightly smaller than 45°.

The classical Ekman model is based on the 'f -plane' approximation and, thus, neglects the possible influence of the horizontal (tangential to the Earth surface) component of the Earth's rotation vector and, thus, the possible dependence of the flow on latitude and wind direction. Evidence that this simplification is not always justified was found in the systematic linear stability analysis of the Ekman profile by Leibovich & Lele (1985). Both for the atmospheric and oceanic Ekman layers, the properties of unstable modes (growth rates and bands of unstable wavelengths) were found to be strongly affected by the horizontal component of the Earth's rotation vector. Further indications of the possible impact of the latitude and the wind direction on flow properties were obtained in a DNS study of the turbulent atmospheric Ekman layer by Coleman et al. (1990). It was found that variations as significant as 20% in the surface friction velocity and as large as 70% in the angle between the free-stream velocity and the wall shear stress were found. In this work, the turbulent Ekman layer is simulated in an 'f-plane' approximation because the objective of the current study, as stated at the end of chapter 2, is to validate the LES model using available results without adding much complexity arising from the horizontal component of the rotation vector.

The Reynolds number is very high in the meteorological context and the Atmospheric Boundary Layer (ABL) can be idealized as an Ekman layer in the fully turbulent regime (see chapter 5 of Holton 2004). The correct scaling of characteristic quantities of the ABL is of prime importance in numerical modelling, where it is required to relate unknown surface fluxes to known model variables. In addition to the Coriolis force due to Earth rotation, the structure of the ABL is strongly influenced by buoyancy owing to surface cooling or heating. Although the influence of buoyancy is an essential part of the ABL analysis, the present study refers to the neutral case of a homogeneous fluid. This neutral case may be approached in the atmosphere for windy conditions under a heavy cloud cover. The neutral ABL is described as two overlapping layers (see chapter 5 of Holton 2004). In the outer layer, generally called the Ekman layer, the Coriolis force strongly influences the flow structure and the velocity direction change with height by as much as 25°. In the inner layer, also called the wall or surface layer, shear stress is assumed to be constant, leading to the usual logarithmic profile for the mean velocity.

As stated at the beginning of this chapter, this task of simulating the turbulent Ekman layer is carried out to validate the LES model implemented in *OpenFOAM* and to test the capabilities of the *OpenFOAM* solver in simulating atmospheric flows. The particular problem of the Ekman layer is taken up in this study because even in the RRBC model, the boundary layer plays a crucial role in the formation of the eye in the TCLV, as seen from the previous studies (Oruba et al., 2017, 2018, Atkinson et al., 2019). It was observed that the sweeping up of the bottom boundary layer results in the formation of the eye in the cyclonic vortices. Therefore, checking whether the LES model can simulate the turbulent Ekman layer is crucial. The results obtained from LES are compared with the DNS of Coleman et al. (1990), Coleman (1999) and the experimental study of the Ekman layer by Caldwell et al. (1972).

3.1 Numerical Procedure

Governing equations and sub-grid scale model

The equations considered in the present study for conducting numerical simulations are grid-filtered continuity and Navier-Stokes equation with added Coriolis term (in f -plane approximation).

$$\frac{\partial \overline{u}_i}{\partial x_i} = 0 \tag{3.2}$$

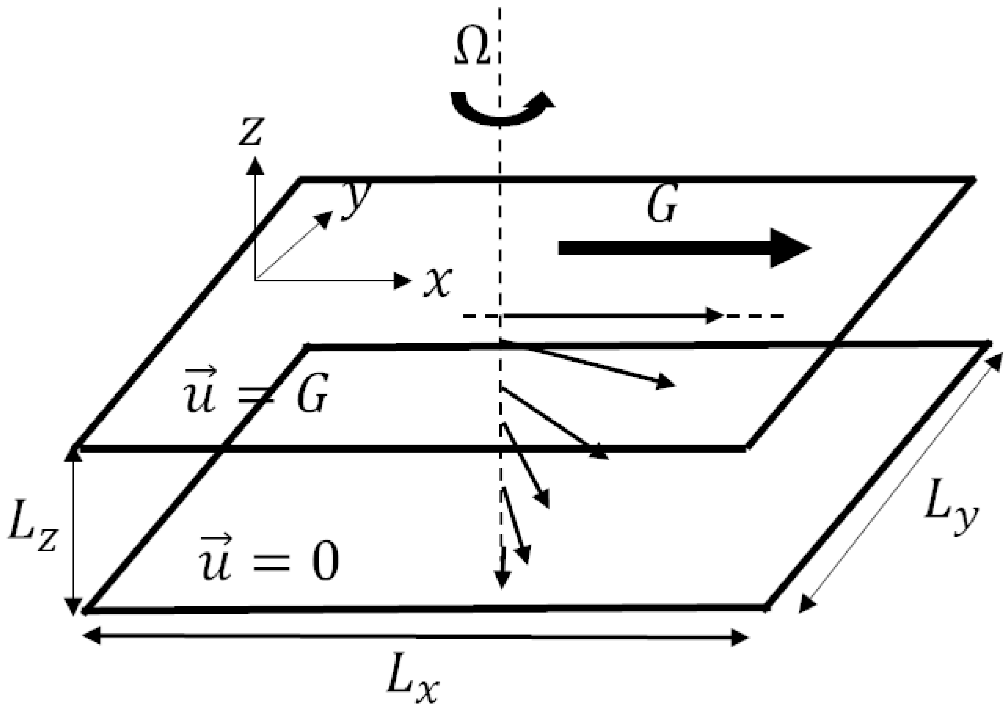

Fig. 3.1 Computational domain with periodic sidewalls.

$$\frac{\partial \overline{u}_i}{\partial t} + \frac{\partial \overline{u}_i \overline{u}_j}{\partial x_j} = -\frac{1}{\rho_o}\frac{\partial \overline{P}}{\partial x_i} - \frac{\partial \tau_{ij}}{\partial x_j} + \nu \frac{\partial^2 \overline{u}_i}{\partial x_j \partial x_j} - 2\Omega \overline{u}_j \epsilon_{ij3} \tag{3.3}$$

The above equation is the same as the filtered equation Eq. (2.12) discussed in the last chapter but without the buoyancy term. In the above equations, the overbar on the variable indicates the grid filtered quantity, $\overline{u}_i$ (where $i = 1, 2, 3$) are the velocity components in the direction (x_1, x_2, x_3) respectively, where $x_1 = x$ and $x_2 = y$ are the horizontal coordinates and $x_3 = z$ is the coordinate in the vertical direction pointing upwards, Ω is the background rotation rate of the system pointing in the vertical direction, $\overline{P}$ is the reduced pressure term containing the contribution from centrifugal acceleration and symmetric part of stress, ν is the kinematic viscosity of the fluid and τ_{ij} is the turbulent stress.

The turbulent stress in the filtered equation is given by,

$$\tau_{ij} = \overline{u_i u_j} - \overline{u}_i \overline{u}_j \tag{3.4}$$

A closure model for subgrid-scale stress relates to the sub-grid scale stress with resolved scale variables which enables the above-filtered equations to be integrated. This study aims at simulating a large-scale phenomenon. Hence, the dynamic Smagorinsky model described in section 2.3 is used for the present turbulent Ekman layer simulation.

The velocity and length scales which define the Reynolds number are geostrophic velocity G and viscous depth $D = \sqrt{\nu/\Omega}$. The Reynolds number within the Ekman layer based on G is given by,

$$Re_G = \frac{GD}{\nu} = \frac{G}{\sqrt{\nu\Omega}} \tag{3.5}$$

The validation for the case "A90" and "New" in the DNS paper by Coleman et al. (1990), Coleman (1999) for $Re_G = 400$ and 1000 are carried out in the current study using *OpenFOAM* to check for its capability in simulating turbulent Ekman layer.

Numerical Methods

Equations (3.2) and (3.3) are solved numerically in a rectangular computational domain of dimensions $L_x \times L_y \times L_z$ using appropriate subgrid-scale model, boundary, and initial conditions, see Fig. 3.1. The value of L_z is taken to be 20 times the viscous depth D, that is, $L_z = 20D$ and for the case considered in this chapter for validation, $L_x = L_y = 40D$. Since the flow is assumed to be homogeneous in the horizontal plane, periodic boundary conditions are applied in the x and y directions. The flow can evolve freely without any bias in the computational domain. At the bottom of the computational domain, a no-slip condition is imposed. At the top of the domain, velocity $\mathbf{u}$ takes the value of geostrophic velocity $\mathbf{G}$. The typical computational domain and the boundary conditions are shown in Fig.3.1.

The simulation is initiated from a quiescent state. Second-order central difference spatial discretisation schemes and first-order Euler time integration schemes are used in the numerical simulation. The CFL number of 0.3 is used for the simulations. The simulations are carried out in a numerical grid with 1 million mesh cells ($100 \times 100 \times 100$) for $Re_G = 400$ and 2 million mesh cells ($100 \times 100 \times 200$) for $Re_G = 1000$. In the present calculations, the grid sizes are $\Delta_x = \Delta_y$, and the ratio Δ_z/Δ_x varies between approximately 0.4 next to the surface and 1.9 near the top. Therefore, no anisotropy corrections were included in the dynamic procedure. The mesh sensitivity is tested by analysing the subgrid-scale ratio of residual kinetic energy to the total kinetic energy (Pope, 2000). The mean and the mode for the distribution of this ratio are observed to be less than 10% when 1, 2 or 4M cells are used for $Re_G = 400$. Hence, the above criterion is used to select the numerical grid for other Re_G, and 2M cells are used for $Re_G = 1000$.

3.2 Results & Discussion

3.2.1 Mean Velocity Profiles

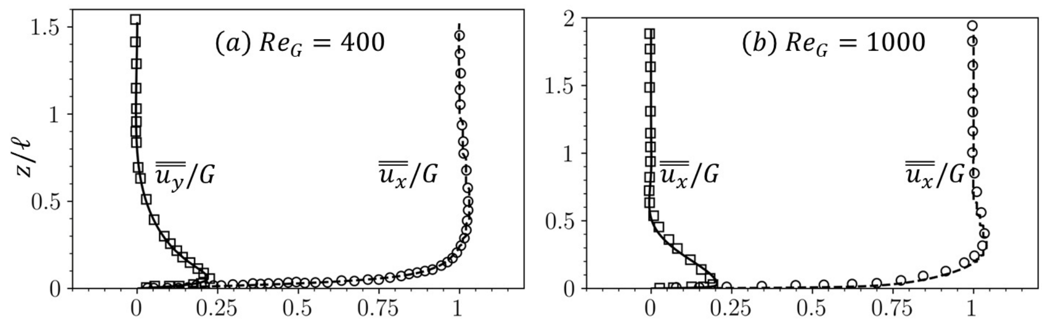

Fig. 3.2 Mean velocity profiles computed from LES (lines) are compared with DNS data of Coleman et al. (1990) (symbols).

The vertical profiles of mean velocities for $Re_G = 400$ and $Re_G = 1000$ normalised with G are shown in Fig. 3.2 from the simulations with the corresponding values reported in DNS studies of (Coleman et al., 1990, Coleman, 1999). The following symbol, "$\overline{\overline{\cdots}}$" is used to denote surface averaging over a horizontal plane throughout this chapter. The vertical coordinate is normalised with turbulent length scale $\ell = u_*/f$, where u_* is the frictional velocity and $f = 2\Omega$ is the Coriolis parameter. The friction velocity is computed by taking the square root of shear stress at the lower boundary in the domain. The results from LES agree well with the DNS results. The profile indicates that the Ekman-layer height, defined as the minimum height where $\overline{\overline{u_x}}$ and G are parallel, and it is about 0.7ℓ for $Re_G = 400$ and 0.5ℓ for $Re_G = 1000$. As Re_G is increased, the Ekman-layer height decreases. The SGS parametrization used in LES and the numerical schemes used in the present simulation could capture the velocity profiles without significant deviation from the DNS results. It is well known that the mean velocity follows the logarithmic region in the near wall region, expressed as (Holton, 2004),

$$Q^+ = \frac{1}{\sigma} \log z^+ + C \tag{3.6}$$

where σ is the von Karman constant, $Q^+ = \sqrt{\overline{\overline{u_x}}^2 + \overline{\overline{u_x}}^2}/u_*$ is the absolute mean velocity normalised with u_* and z^+ is the vertical coordinate normalised with u_*/ν. The von Karman constant σ can be obtained using Eq. (3.6) as

$$\frac{1}{\sigma} = z^+ \frac{\partial Q^+}{\partial z^+} \tag{3.7}$$

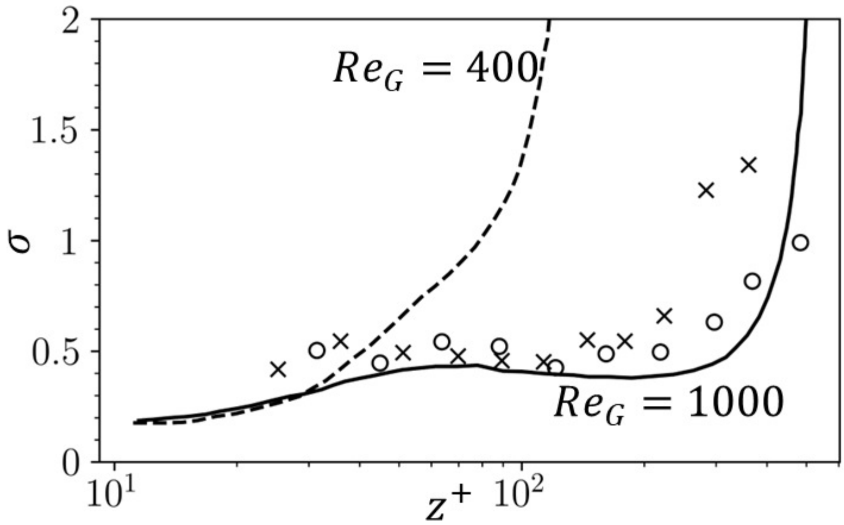

Fig. 3.3 von Karman constant σ computed from LES (lines) are compared with experimental data of Caldwell et al. (1972) ($\circ \rightarrow Re_G = 1159$, $\times \rightarrow Re_G = 1234$).

The common value of σ for non-rotating turbulent boundary layers varies from 0.4 to 0.42 (Holton, 2004). Figure 3.3 shows the values of σ obtained in this study for $Re_G = 400$ and 1000. In the case of $Re_G = 400$, the von Karman constant does not exhibit any constant region but increases monotonically. However, in the case of a higher Reynolds number $Re_G = 1000$, σ exhibits a local maximum and stays nearly at a constant value in a wider region. Thus, if the mean velocity is expressed in terms of Q^+, the logarithmic nature of the mean velocity is very robust, despite the three-dimensionality of the velocity field. The result of σ for higher Reynolds numbers shows a similar trend compared to the experimental results of Caldwell et al. (1972).

The hodographs of the mean velocities for $Re_G = 400$ and 1000 are shown in Fig. 3.4. The analytical solution in the laminar Ekman boundary layer is also shown. The spiral shrinks as the Reynolds number increases. This suggests that the mean flow direction becomes closer to the geostrophic wind. The angle ϕ_{u0} between the shear direction at the bottom wall and the geostrophic wind is shown in Table 3.1. The analytical solution of the laminar Ekman boundary layer gives $\phi_{u0} = 45°$. However, the angle ϕ_{u0} obtained from the simulation of the turbulent Ekman layer decreases to a smaller value of $\phi_{u0} = 28.2°$ and 19.8° for $Re_G = 400$ and 1000 respectively. The experiments by Caldwell et al. (1972) and the DNS studies of Coleman et al. (1990), Coleman (1999) also obtained smaller angle of ϕ_{u0} ranging between 19° to 28°. The angle ϕ_{u0} decreases with an increase in the Reynolds number. This is attributed to the enhancement of momentum transfer in the vertical direction with an increase in the

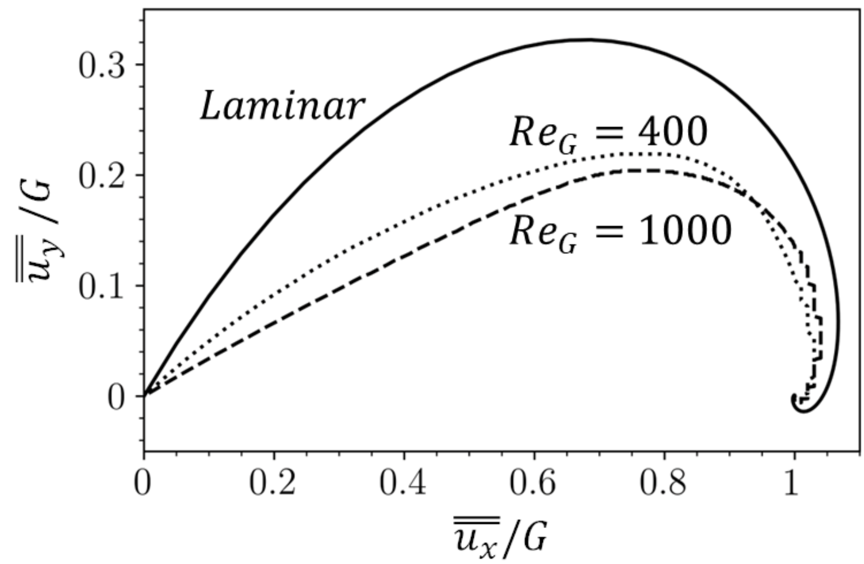

Fig. 3.4 Hodographs of mean velocities.

Reynolds number. Thus, the momentum of the geostrophic wind penetrates more into the near-wall region for a higher Reynolds number.

Table 3.1 Mean shear direction at the wall.

S.no	Re_G	ϕ_{u0}
1	400	28.2
2	1000	19.8

3.2.2 Turbulence Intensity & Reynolds Stress

Root mean square fluctuations of the individual velocity components for $Re_G = 400$ and 1000 are shown in Fig. 3.5 using both inner z^+ and outer z/ℓ scaling. In the case of $Re_G = 400$, the magnitude of the vertical velocity components is smaller than its streamwise and spanwise counterparts in the boundary layer. The trend is reversed near the top of the simulation domain. The small velocity fluctuations near the top of the domain are due to the slowly decaying velocity field (see Fig. 12a of Coleman et al. 1990). The streamwise velocity fluctuations are larger near the wall region than the spanwise velocity component, which is due to the three-dimensionality of the flow. While moving away from the boundary layer region, both components behave similarly. This behaviour of the velocity components remains the same for $Re_G = 1000$ except that the fluctuations have a higher magnitude since the Reynolds number is increased more than two folds. The trend observed for the individual velocity components in Fig. 3.5 are in line with that observed in the DNS calculations of Coleman et al. (1990), Coleman (1999) for $Re_G = 400$ and 1000.

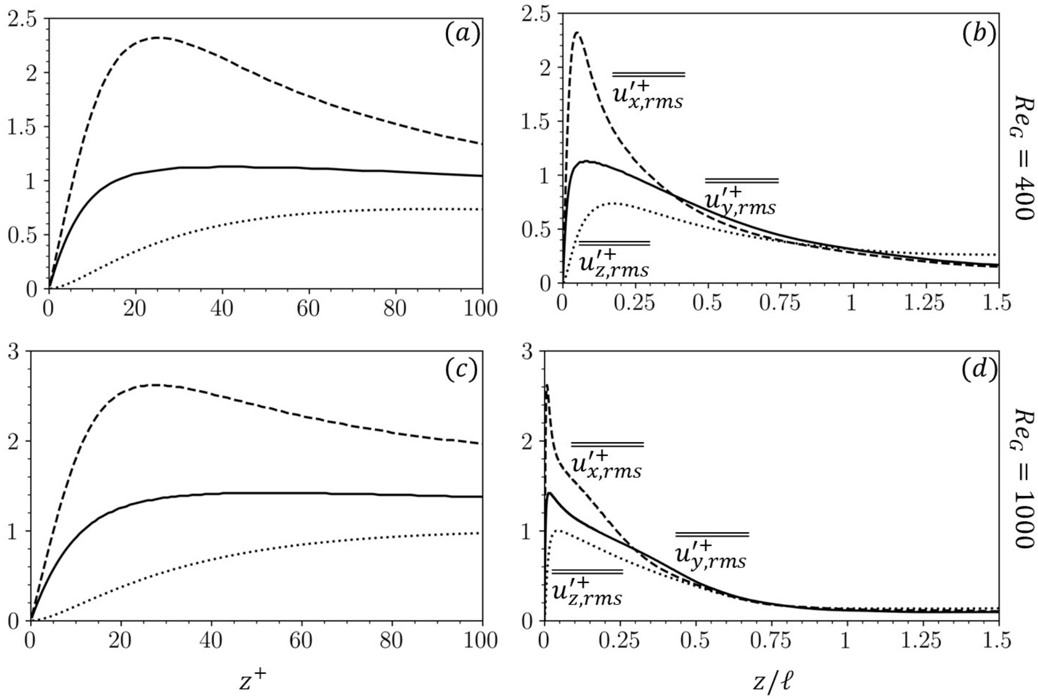

Fig. 3.5 Turbulent intensities as a function of $z^+ = zu_*/\nu$ is shown in figures (a) and (c). The figures (b) and (d) show the variation with z/ℓ.

The vertical profiles of Reynolds stress curves normalized with the square of friction velocity u_* are shown in Fig. 3.6 for $Re_G = 400$ and 1000. The present results from the LES (line) agree well with the DNS (symbols) results in the previous studies by Coleman et al. (1990), Coleman (1999) for all the stress components of the flow for both the lower and higher Reynolds number. This indicates that the LES model used in the study can capture the second-order statistics very well over the range of Reynolds numbers.

3.2.3 Eddy Viscosity Model

Many theoretical approaches to the turbulent Ekman problem have employed some empirical specifications for the eddy-viscosity. The mixing length model proposed by Blackadar (1962) is compared with the present LES data. The results are also compared with those from the experiments from Caldwell et al. (1972). In mixing

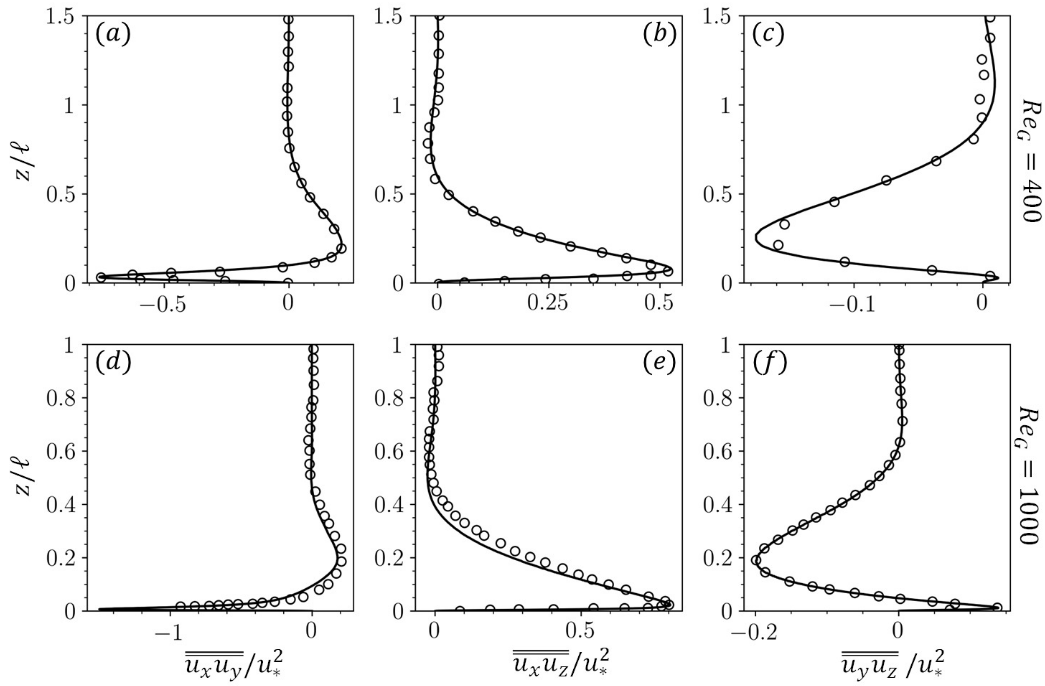

Fig. 3.6 Vertical profiles of Reynolds stress computed from LES (line) and DNS of Coleman et al. (1990) (symbols).

length representations, the eddy-viscosity is expressed as

$$\nu_t = \eta^2 S \tag{3.8}$$

where η is the mixing length and S is the magnitude of wind shear given by,

$$S = \left[\left(\frac{\partial u_x}{\partial z} \right)^2 + \left(\frac{\partial u_y}{\partial z} \right)^2 \right]^{\frac{1}{2}} \tag{3.9}$$

The mixing length in Eq. (3.8) is assumed to have a form (Blackadar, 1962)

$$\frac{1}{\eta} = \frac{1}{\sigma z} + \frac{1}{\lambda} \tag{3.10}$$

Here, λ is an empirical parameter which specifies a maximum value of η as z approaches infinity. Blackadar (1962) used the following empirical relation for λ:

$$\lambda = u_* \frac{\delta_{\mathrm{BL}}}{G} \tag{3.11}$$

where δ_{BL} is the boundary layer thickness, and u_* is the friction velocity. The u_* and H are computed from the LES data. Here, H is the height at which the wind direction becomes first parallel to the geostrophic wind.

Figure 3.7 shows the eddy-viscosity profiles. The dashed lines show the results computed from the Blackadar (1962) model. The solid line shows the viscosity profiles obtained from LES. The eddy viscosity is calculated in LES based on Eq. (2.17). The Blackadar (1962) model does not agree well with the LES data for both $Re_G = 400$ and 1000. In the near-wall region, the results of the Blackadar (1962) model are larger than the present results. This is because the effect of viscosity is not considered in Eq. (3.10). In the remaining part, the eddy-viscosity obtained from Blackadar (1962) model is smaller. The eddy-viscosity from LES data is in line with the values observed from the experiments by Caldwell et al. (1972) for all the Reynolds numbers considered in the study.

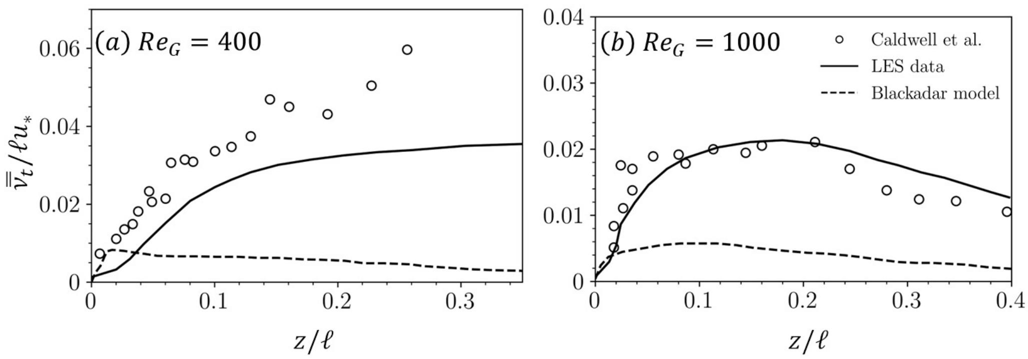

Fig. 3.7 Eddy-viscosity variation with height (z/ℓ).

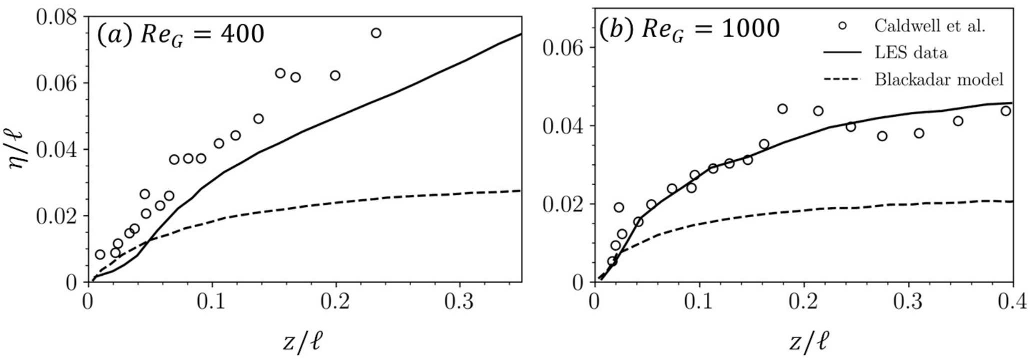

Fig. 3.8 Mixing length variation with height (z/ℓ).

The mixing length profiles are shown in Fig. 3.8 and compared with experiments of Caldwell et al. The mixing length can be computed by applying the following definition:

$$\eta(z) = \sqrt{\overline{\overline{\nu_t / S}}} \tag{3.12}$$

The mixing lengths computed from LES calculations agree well with the experiments. The deviation increases with an increase in height, and this is because the mean velocity gradients become smaller at larger heights. Thus, the derivation of η becomes less accurate in the experiment. The mixing length calculated from the Blackadar (1962) model does not agree with the LES or experimental data. This behaviour can be attributed to the lack of inclusion of viscous effects in the model.

3.3 Summary

Large eddy simulation of turbulent Ekman layer is undertaken using the *OpenFOAM* code with the implemented dynamic Smagorinsky closure model proposed by Lilly (1992). The simulations are carried out for $Re_G = 400$ and 1000, and the results are compared with the DNS results of Coleman et al. (1990), Coleman (1999) and the experimental results of Caldwell et al. (1972). In addition, the results are also compared with the well-known eddy-viscosity model for the turbulent Ekman problem. The conclusions are as follows:

1. The velocity profiles obtained for both $Re_G = 400$ and 1000 agree well with the DNS results of Coleman et al. (1990), Coleman (1999) At a higher Reynolds number, the von Karman constant σ exhibits and local maximum and nearly stays constant in a wider region.

2. The Ekman spiral shrinks on increasing $Re_G = 400$ to 1000 as the vertical momentum transfer is enhanced with an increase in Re_G. Also, the spiral angle (mean shear angle at the bottom surface) ϕ_{u0} obtained from simulation agrees well with Caldwell et al. (1972) experiments and DNS results of Coleman et al. (1990) and Coleman (1999).

3. The second-order statistics obtained from LES calculations agree well with the DNS results of Coleman et al. (1990), Coleman (1999) for both $Re_G = 400$ and 1000.

4. The trends of eddy viscosity and mixing length obtained from LES data agree well with the results from Caldwell et al. (1972) experiments. However, the present results do not show good agreement with the Blackadar (1962) model. This

discrepancy can be attributed to neglecting the viscous effect in the presumed model.

The LES model in the *OpenFOAM* code can simulate the turbulent Ekman layer and show good agreement with the previously published results in the literature. Therefore, the same LES model is used in the thesis to simulate a tropical cyclone-like vortex in a RRBC paradigm. The results obtained from the simulation of a tropical cyclone-like vortex in a RRBC paradigm are discussed in the following chapters.

Chapter 4

Tropical Cyclone-like Vortex: 3D & Boundary Condition Effects

In this chapter, Tropical Cyclone-like Vortex obtained in the past laminar axisymmetric studies (Oruba et al., 2017, 2018, Atkinson et al., 2019) within the Rotating Rayleigh Benard Convection (RRBC) setup is simulated in a 3D shallow cylindrical domain without any constraints on the flow evolution. The cyclonic vortex formed is referred to as a tropical cyclone-like vortex because of the very low aspect ratio (radius $\gg$ height) of the vortex with features such as eye and eyewall similar to that seen in a tropical cyclone. The streamlines of a typical tropical cyclone-like vortex, along with the iso-surface of the eye and eyewall, are shown in Fig. 4.1. The poloidal flow fills the domain with subsidence near the centre for the tropical cyclone-like vortex and spiralling outwards and inwards fluid motion near the top and bottom boundary, respectively. This chapter addresses the first two questions posed in section 1.3 of Chapter 1.

Moeng et al. (2004) found that in a rotating convection system, the convective entrainment within a planetary boundary layer in a 3D model is less compared to the 2D model with axisymmetric approximations. This is because the flow evolution is more organised/constrained in the 2D model than its 3D counterpart due to the restricted degree of freedom. Therefore, this suggests that the axisymmetric convections occurring in concentric rings may be likewise overly efficient in generating buoyancy fluxes compared to 3D convection leading to excessive heating and extremely rapid spin-up in the tropical cyclone context. Following Moeng et al. (2004), other studies also pointed out that some of the results published using axisymmetric models may have to be re-evaluated using three-dimensional simulations (Bryan & Rotunno, 2009). Persing et al. (2013) found that observations of Moeng et al. (2004) hold well for numerical simulation of tropical cyclones as well by comparing the results from 3D and axisymmetric simulations. It was found that the 3D model predicted significantly reduced intensity (15-50%) compared to their axisymmetric counterpart (Persing et al., 2013). In addition, 3D simulations are required to improve our understanding of cyclogenesis and subsequent intensification process, which are highly asymmetric (Nguyen et al., 2011). It was noted that only the most intense storms exhibit a substantial degree of axial symmetry, and even then, only in their inner-core region (Nguyen et al., 2011). Therefore, it is essential to carry out 3D simulations of a tropical cyclone-like vortex and compare the results with their axisymmetric counterpart to gain clear fundamental perspectives.

Besides the dimensionality of the computational domain, another challenge is to devise suitable boundary conditions, specifically for the sidewall of the 3D computational domain, to observe tropical cyclone-like vortex. This is because there is no sidewall boundary for a real cyclone, but it is required for the computational or experimental model. Therefore, it is important to understand the effect of this artificial boundary and, specifically, its thermal boundary condition on the formation of a tropical cyclone-like vortex. The effect of these thermal, either isothermal or insulated, boundary conditions has been studied extensively in the past for non-rotating Rayleigh Benard Convection (RBC). Buell & Catton (1983) and Hébert et al. (2010) observed that the convection onset was delayed for isothermal condition compared to the insulated condition. This also affected the flow stability. The stability curve was observed to be more complex for the isothermal sidewall than its insulated counterpart due to enhanced thermal activity near the wall (Puigjaner et al., 2004, 2008). The sidewall thermal condition also influences the formation of flow pattern, specifically when the RBC system is close to the onset of convection (Cross & Hohenberg, 1993) even in a very shallow domain with $\Gamma = 0.024$ and 0.023 as observed in the experiments of Hu et al. (1993). Direct Numerical Simulation (DNS) studies showed that the heat transport and flow structures are influenced significantly by the thermal conductance along the sidewall and its thermal boundary condition (Verzicco, 2002, Stevens et al., 2014, Wan et al., 2019). These studies used a large aspect ratio of $\Gamma = 4$. In the low Ra regime ($Ra \leq 10^8$), the heat transport is higher for the isothermal sidewall than for the insulated counterpart. In contrast, the difference in the heat transport decreases for the higher Ra regime since the convection in bulk dominates (Verzicco, 2002, Stevens et al., 2014, Wan et al., 2019). Many past DNS studies investigated the effects of rotation on the heat transport (Zhong et al., 2009, King & Aurnou, 2013) and energy balance (Horn & Shishkina, 2015) using RRBC and RBC systems with insulated sidewall. All of these studies focused on the regime of convection onset. The effects of this boundary condition on the formation of tropical cyclone-like vortex in a 3D domain have not been investigated hitherto. Therefore, in this chapter, further to understand the 3D effects in the simulation of a tropical cyclone-like vortex, the influence of sidewall thermal BC on the flow evolution and the formation of the tropical cyclone-like vortex are studied using the RRBC paradigm. The 3D simulations are performed within the flow parameter regime wherein a tropical cyclone-like vortex is observed previously using axisymmetric calculation (Oruba et al., 2017, 2018, Atkinson et al., 2019).

The remainder of the chapter is structured as follows. First, the numerical procedure employed is discussed in section 4.1, detailing the equation solved, the boundary conditions used, the computational domain, the mesh information, and the flow parameter values used for the simulations. Also, the code *OpenFOAM* (Weller et al., 1998) used to perform the simulations is tested by comparing the current results for 2D- axisymmetric simulations with the previously published works (Oruba et al., 2017, 2018, Atkinson et al., 2019). It is worth noting that the previous chapter discussed the validation of this code for rotating flows without buoyancy. In section 4.2.1, the instantaneous flow fields are studied for the 3D simulations with insulated and isothermal sidewall boundary conditions. The momentum budget analysis compares the results of 3D simulations with the axisymmetric counterpart in section 4.2.2. The flow behaviour near the isothermal and insulated sidewall is compared and analysed in section 4.2.3. The chapter is concluded with a summary.

4.1 Numerical Procedure

4.1.1 Governing Equations

A cylindrical domain having a radius R and height H, giving an aspect ratio of $\Gamma = H/R$, considered for this is shown in Fig. 4.1. This domain rotates at a rate of Ω and has a background temperature variation of $T_o(z) = T_{\text{ref}} - \beta z$ to maintain static equilibrium, where T_{ref} is a reference temperature taken to be $T(z = 0)$. The flow is initiated by imposing a uniform vertical heat flux, proportional to β in the domain. This flow is computed by solving an equation for temperature perturbation, $\theta = T - T_o(z)$ along with the continuity and Navier-Stokes equations. These equations

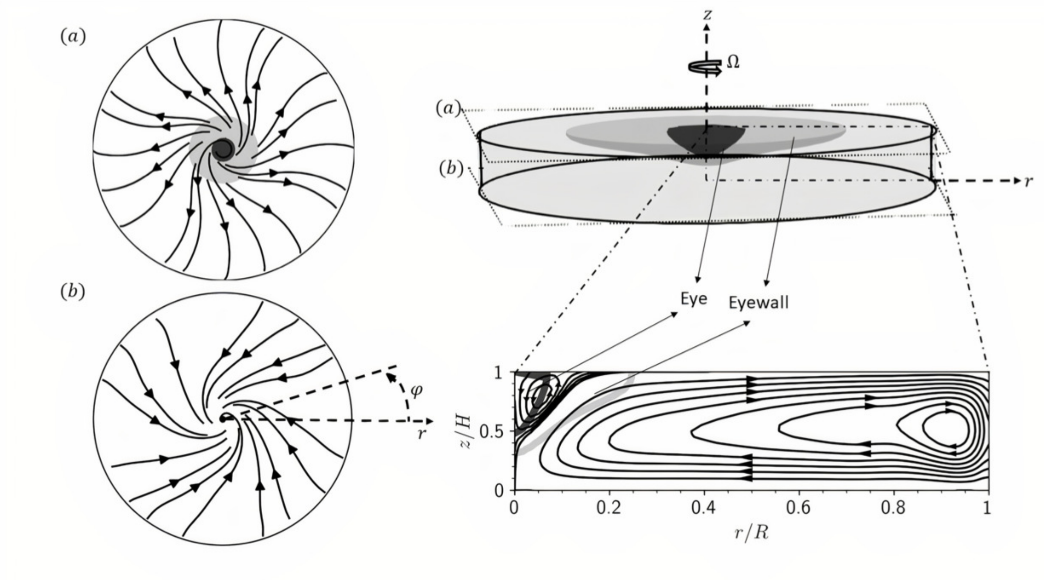

Fig. 4.1 Streamlines in a typical tropical cyclone-like vortex along with the eyewall denoted using $\omega_\varphi = 0$ iso-surface coloured gray and eye marked using the black iso-surface for $u_z = 0$ (drawn not to scale).

written in rotating frame of reference are

$$\frac{\partial \boldsymbol{u}}{\partial t} + \boldsymbol{u} \cdot \nabla \boldsymbol{u} = -\frac{1}{\rho_o} \nabla P + \nu \nabla^2 \boldsymbol{u} - 2\boldsymbol{\Omega} \times \boldsymbol{u} - \alpha\theta\boldsymbol{g}, \tag{4.1}$$

$$\frac{\partial \theta}{\partial t} + \boldsymbol{u} \cdot \nabla \theta = \kappa \nabla^2 \theta + \beta u_z, \tag{4.2}$$

with Boussinesq approximation and the continuity equation is $\nabla \cdot \boldsymbol{u} = 0$. The velocity vector is $\boldsymbol{u}$ and the reduced pressure is $P = p - \rho_o \boldsymbol{g} \cdot \boldsymbol{x} - \rho_o(\boldsymbol{\Omega} \times \boldsymbol{x})^2/2$, where ρ_o is the fluid density at T_o and $\boldsymbol{g}$ is the acceleration due to gravity pointing in vertically downward direction. The symbol ν is the fluid kinematic viscosity, α is the thermal expansion coefficient, κ is the thermal diffusivity, and t is the time.

The objective of this chapter is to conduct 3D simulations to investigate the three-dimensional effects on the formation of the tropical cyclone-like vortex. Hence, conditions of Oruba et al. (2018) yielding tropical cyclone-like vortex in their axisymmetric calculations are chosen. The aspect ratio of the computational domain, $\Gamma = 0.1$, and the boundary conditions used by them are kept for this study. The bottom and sidewalls are specified as no-slip, while the top boundary at $z = H$ has the free-slip condition. These bottom and top boundaries are specified to have $\partial\theta/\partial z = 0$ so that a uniform and constant heat flux of $\lambda\beta$ is maintained in the vertical direction within the domain, where λ is the thermal conductivity of the fluid. The sidewall is treated to be insulated with $\partial\theta/\partial r = 0$ as in Oruba et al. (2018). The effects of sidewall thermal boundary conditions are also investigated in this study by using $\theta = 0$. The simulations are run as an initial value problem starting from quiescence until a steady-state is reached.

If one uses H as a reference length, the buoyancy velocity $V = \sqrt{\alpha\beta g H^2}$ as the reference velocity, and Ω^{-1} as a reference timescale to non-dimensionalise the governing equations then the dimensionless flow parameters involved are,

$$\Gamma = \frac{H}{R}, Pr = \frac{\nu}{\kappa}, E = \frac{\nu}{\Omega H^2}, Ra = \frac{\alpha g \beta H^4}{\nu\kappa}, Re = \frac{VH}{\nu}, Ro = ReE \tag{4.3}$$

where Pr is the Prandtl number of the fluid. The Rayleigh number Ra is related to Reynolds number Re through $Ra = Re^2 Pr$ and the Rossby number $Ro = ReE$ is related to Re and Ekman number E. The values of these parameters explored in this study are listed in Table 4.1 which are taken from previous axisymmetric simulations showing tropical cyclone-like vortex for $\Gamma = 0.1$ (Oruba et al., 2017, 2018, Atkinson et al., 2019).

4.1.2 Numerical Method

The governing equations written in Cartesian systems are solved using a finite volume solver, *OpenFOAM* (Jasak et al., 2007), employing a second-order central difference scheme with implicit Euler time-stepping. The pressure and velocity fields are coupled through PISO algorithm (Issa, 1986) available in *OpenFOAM*. The discretised governing equation are advanced in time using a variable time-stepping which kept the CFL number, defined as $\Delta t \times max(|\boldsymbol{u}|/\delta_c)$, to be below 0.3, where δ_c is the computational cell size, $|\boldsymbol{u}|$ is the velocity magnitude, and time step is given by Δt. The Coriolis and buoyancy term in the momentum equation and the transport equation for θ are implemented in *OpenFOAM* and validated first.

The cylindrical computational domain has about 2.1M numerical cells, which are distributed as $N_x = 200$, $N_y = 200$ and $N_z = 54$ after extensive tests with 1M cells as reference grid. The various characteristics such as the thickness of bottom boundary layer ($\delta^*_{\mathrm{BL}} = \delta_{\mathrm{BL}}/H$), width of eyewall ($\delta^*_{\mathrm{ew}} = \delta_{\mathrm{ew}}/H$) and the radius of tropical cyclone-like vortex ($r^*_{\mathrm{tc}} = r_{\mathrm{tc}}/R$) compared are observed not to change beyond 2.1 M grid when the tropical cyclone-like vortex is fully evolved as shown in Table 4.2 and hence 2.1 M grid is used for all the results explored in this study. δ^*_{BL} evaluated at mid-radius $r/R = 0.5$ is the vertical extent of negative azimuthal vorticity (Oruba et al., 2018). The width of the eyewall δ^*_{ew} is the horizontal extent of the negative

Table 4.1 Summary of the parameter values considered for this study with $\Gamma = Pr = 0.1$.

Case	E	Ra	Re	Ro	$Ro^{max}_{\varphi,axi}$	$Ro^{max}_{\varphi,3D}$	TC-like vortex?		
							Axisymmetric	3D-ins	3D-iso
1	0.05	9000	300	15	4.75	4.24	✓	✘	✓
2	0.05	15000	387.3	19.36	23.03	22.32	✓	✘	✓
3	0.05	20000	447.21	22.36	26.73	24.81	✓	✘	✓
4	0.075	4000	200	15	12.28	11.68	✓	✘	✓
5	0.075	9000	300	22.5	21.82	20.45	✓	✘	✓
6	0.075	12000	346.41	25.98	25.2	22.82	✓	✘	✓
7	0.075	18000	424.26	31.82	29.14	5.28	✓	✘	✘
8	0.1	1500	122.47	12.25	6.15	6.1	✘	✘	✘
9	0.1	2000	141.42	14.14	9.52	8.87	✓	✘	✓
10	0.1	3000	173.21	17.32	12.85	11.51	✓	✘	✓
11	0.1	4000	200	20	16.28	13.47	✓	✘	✓
12	0.1	5000	223.61	22.36	18.1	15.33	✓	✘	✓
13	0.1	6000	244.95	24.5	19.6	16.18	✓	✘	✓
14	0.1	7500	273.86	27.38	22.16	17.27	✓	✘	✓
15	0.1	9000	300	30	24.35	13.47	✓	✘	✘
16	0.1	23040	480	48	34.94	5.62	✓	✘	✘
17	0.1	30000	547.72	54.77	37.63	4.67	✓	✘	✘
18	0.15	1800	134.16	20.12	13.29	7.59	✓	✘	✓
19	0.15	3000	173.21	25.98	17.81	6.21	✓	✘	✓
20	0.15	4000	200	30	19.62	5.44	✓	✘	✘
21	0.15	8000	282.84	42.43	25.82	4.94	✓	✘	✘
22	0.15	12000	346.41	51.96	29.95	4.71	✓	✘	✘
23	0.15	16000	400	60	32.27	4.75	✓	✘	✘
24	0.15	20000	447.21	67.08	34.08	4.65	✓	✘	✘
25	0.15	24000	489.9	73.48	35.63	4.9	✓	✘	✘
26	0.15	28000	529.15	79.37	37.05	4.77	✓	✘	✘
27	0.15	32000	565.69	84.85	37.7	4.2	✓	✘	✘

azimuthal vorticity at the height of the eye centre z_{eye} (Oruba et al., 2018). The radius of tropical cyclone-like vortex, r^*_{tc} is defined as the radial extent from the domain centre at which the radial gradient of depth averaged pressure first changes sign.

Table 4.2 Results from Grid sensitivity analysis for Case 3 in Table 4.1.

Grid (in M) ($N_x \times N_y \times N_z$)	δ^*_{BL}	δ^*_{ew}	r^*_{tc}
0.6 (150 × 150 × 27)	0.274	1.48	0.83
1 (200 × 200 × 27)	0.259	1.36	0.81
2.1 (200 × 200 × 54)	0.255	1.32	0.8
3.6 (300 × 300 × 40)	0.255	1.3	0.8
4.9 (300 × 300 × 54)	0.254	1.3	0.8

The simulations are started from the quiescence with $\theta = 0$ in the computational domain and are run until the flow has evolved to a steady state which is monitored using volume-averaged kinetic energy per unit mass $\langle K \rangle_v = \langle \boldsymbol{u} \cdot \boldsymbol{u} \rangle_v / 2$. The simulations are stopped when there isn't a significant change in the $\langle K \rangle_v$ for many tens of rotation time. Before embarking on 3D simulations, axisymmetric calculations are performed to validate the implementation of the Coriolis and buoyancy terms, and this is discussed next. In total, 81 cases listed in Table 4.1 are simulated for this study, including 27 2D axisymmetric cases with the same boundary conditions used by Oruba et al. (2017, 2018) and Atkinson et al. (2019) i.e., no-slip at the bottom and sidewall and free-slip at the top for velocity and uniform heat flux thermal boundary conditions at the top and bottom bottom boundary and insulated condition at the sidewall. The remaining cases are the corresponding 3D cases with insulated and isothermal sidewalls.

4.1.3 Code Validation

The axisymmetric simulations employ 1000 radial $\times$ 100 axial numerical grid cells following the past work of (Atkinson et al., 2019). These calculations yield a tropical cyclone-like vortex for the combinations of Re and E chosen except for one condition, which is listed as Case 8 in Table 4.1. Figure 4.2 compares the radial variation of time and depth-averaged total angular velocity $(r\Omega + u_\varphi)$ computed here to the results of Atkinson et al. (2019), see their figure 5. The angular velocity is normalised using $r\Omega$, and the agreement is excellent. As one would expect for a cyclonic flow, the depth-averaged angular velocity is maximum near the eyewall region and reduces to the background rotation velocity as one moves away from this region. The spatial variation of the azimuthal vorticity, streamlines and the angular momentum shown in Fig. 4.2 are the same as shown by Atkinson et al. (2019) in figure 4d. These variations suggest that ω_φ is swept up from the bottom boundary layer, and the eye is formed as a consequence of this upsweep as observed in the previous studies (Oruba et al., 2017, 2018). The conservation of angular momentum suggests that the streamlines and the angular momentum contours should follow each other in regions with weak diffusion (Oruba et al., 2017), which is also observed in Fig. 4.2. Specifically, this is seen in the region above the Ekman layer and outside the eyewall region. These steady-state results are in accord with the previous works (Oruba et al., 2017, 2018, Atkinson et al., 2019).

The modified *OpenFOAM* code is also tested to verify its capability to capture unsteady behaviours reported in Atkinson et al. (2019). When the heat flux at the bottom boundary is increased for a given value of E, the eye, identified from the

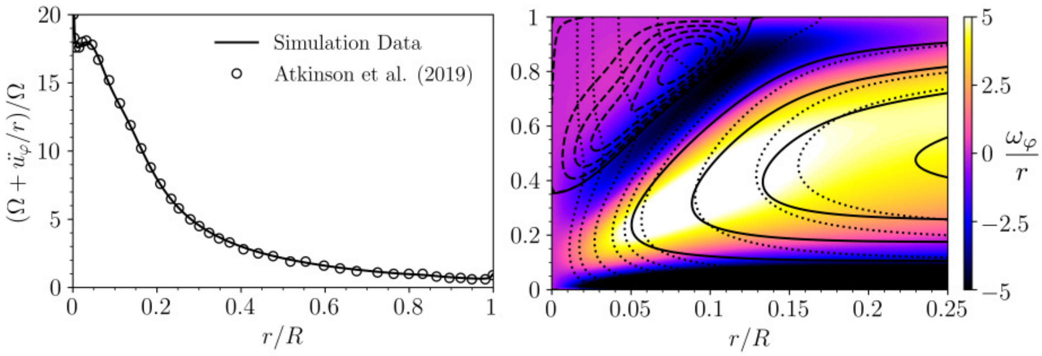

Fig. 4.2 The computed radial variation of depth averaged total angular velocity is compared to the results of Atkinson et al. (2019) in the left frame. The pseudo colour-map of ω_φ/r along with streamlines (solid lines, dashed lines denoted negative streamlines) and the angular momentum contour (dotted) is shown in the right frame. The results are for $Re = 300$ and $Pr = E = \Gamma = 0.1$, Case 15 in Table 4.1.

negative streamlines, pinches off from the axis and moves into the annulus. Then, this pinched-off eye moves towards the axis as the downward flow strength increases leading to some oscillatory behaviour of the eye. This unsteady behaviour was suggested to emerge from inertial waves trapped within the eye (Atkinson et al., 2019) and the modified *OpenFOAM* code is also able to capture this unsteady behaviour as demonstrated in Fig. 4.3. The snapshot of ω_φ/r contours along with the streamlines are shown for six instant within one oscillation period, τ_o from Fig. 4.3a to 4.3f. Figure 4.3g compares the radial variation of depth-averaged total angular velocity, which is also time-averaged over an oscillation period, compared here to that of Atkinson et al. (2019), see their figure 12. The modified code captures the unsteady behaviour well. It is clear that this code captures the behaviours of tropical cyclone-like vortex in axisymmetric cases reported in past studies (Oruba et al., 2017, 2018, Atkinson et al., 2019) is used to conduct corresponding 3D simulations. This will help us to address the objectives listed in the introduction of this chapter. In total, 81 simulations listed in Table 4.1 are considered for this study, and typical behaviours discussed in the following sections are presented using Case 12 as an example since similar behaviours are observed in other cases.

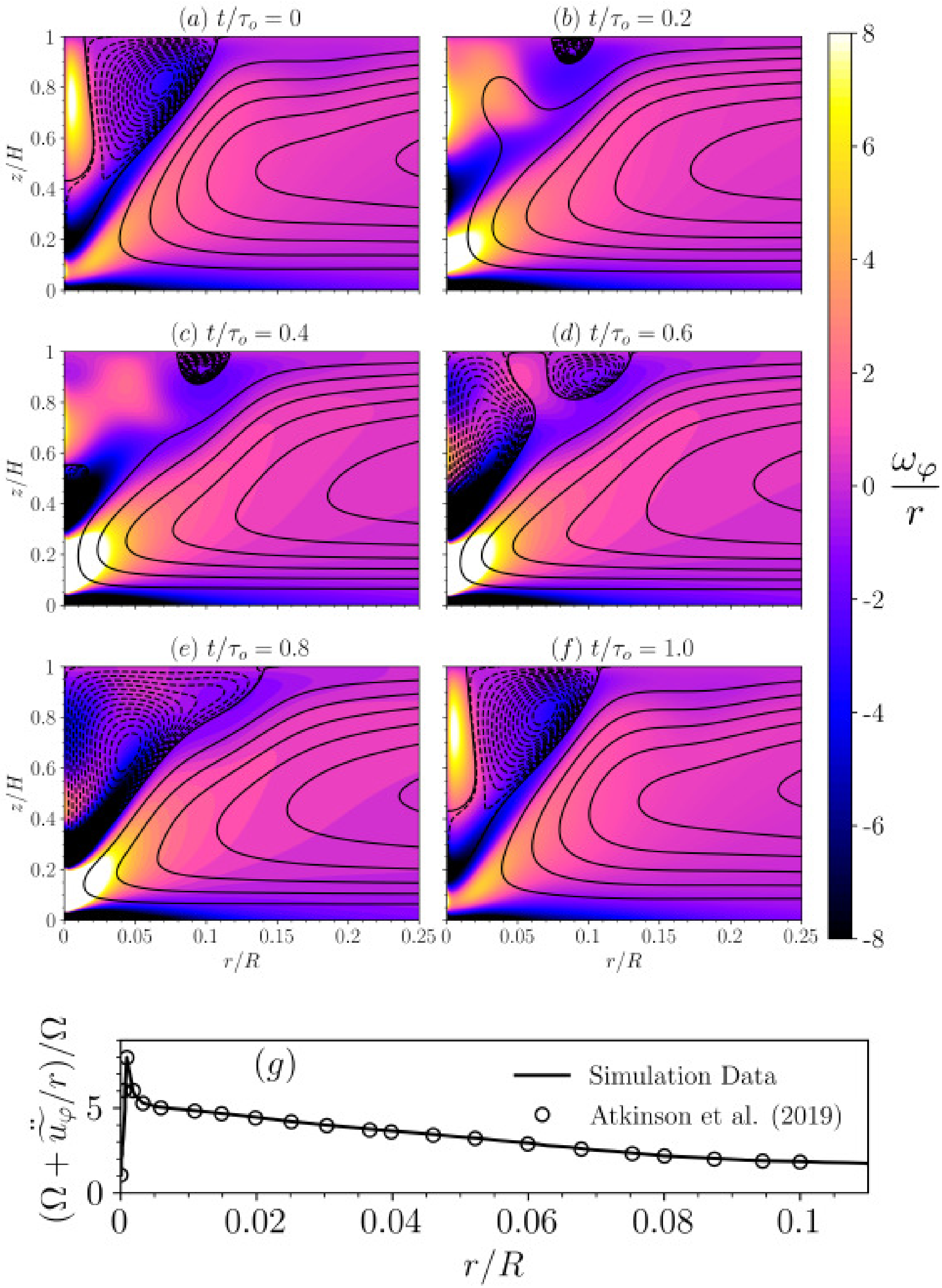

Fig. 4.3 ω_ϕ/r contour along with streamlines for an oscillatory eye over one oscillation period τ_o for case 16 in Table 4.1 with $Re = 480$, $Pr = E = \Gamma = 0.1$.

4.2 Results

4.2.1 Flow Fields

The 3D simulations are run for several tens of rotation time ($\tau = t\Omega$), and their durations are determined by monitoring the temporal evolution of three components of volume-averaged kinetic energy per unit mass, $\langle K_i \rangle_v$, in the computational domain. The simulations are stopped when $\langle K_i \rangle_v$ does not change over a period of about 40τ to 50τ. The time-averaged statistics required for the analysis discussed below are constructed using the data collected over the final 50τ period.

Figure 4.4 shows the time evolution of $K_i^* \equiv \langle K_i \rangle_\mathrm{v} / (\Omega R)^2$ for Case 12 with both insulated and isothermal sidewalls conditions. If one uses V^2 for normalisation as $K_i^+ =$

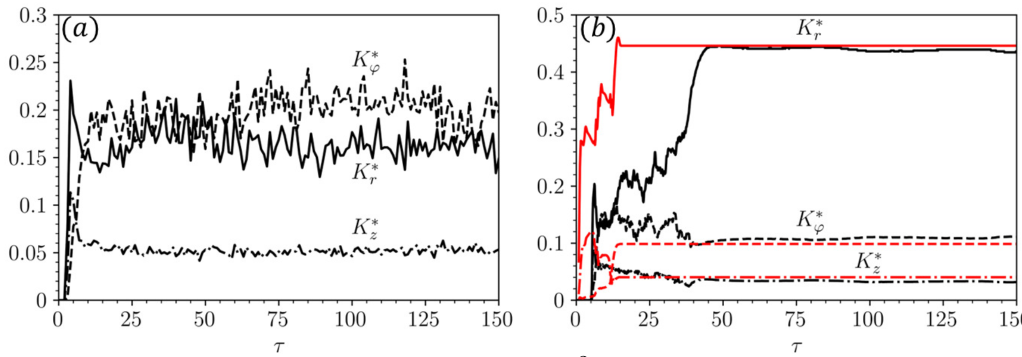

Fig. 4.4 Time evolution of $K_i^* = \langle K_i \rangle_\mathrm{v} / (\Omega R)^2$ for Case 12 with insulated (left) and isothermal (right) sidewalls. The red lines are for the axisymmetric counterpart.

$\langle K_i \rangle_\mathrm{v} / V^2$ then $K_i^* = K_i^+ Ro^2 \Gamma^2$. This figure shows that K_i^* evolves similarly for both boundary conditions until $\tau = 15$ starting from the initial quiescence. Subsequently, the energies start to level off for the insulated condition and the horizontal energies, K_r^* and K_φ^*, are dominant compared to the vertical component. The ratio of K_r^*/K_φ^* is about 1 and K_r^*/K_z^* is about 3. On the other hand from $\tau \approx 15$ onwards, K_φ^* and K_z^* decrease while K_r^* increases for the isothermal condition. The axial and azimuthal components level off at about $\tau = 40$ but the radial component increases rapidly before levelling off at about 45τ as shown in Fig. 4.4. The radial kinetic energy is about 4.4 and 11 times larger than the azimuthal and axial components respectively. Hence, the sidewall thermal boundary condition influences the kinetic energy (rather than the flow field) evolution strongly and the physical reasons for this are explained later in this chapter. However, these thermal boundary conditions do not play a role in axisymmetric simulations as reported in earlier studies Oruba et al. (2017, 2018), which is also verified here using the axisymmetric counterparts listed in Table 4.1. However,

K_i^* evolves rapidly to its steady state value in the axisymmetric counterpart as shown in Fig. 4.4b. Since the 3D simulations also lead to tropical cyclone-like vortex which is nearly axisymmetric, the differences in the steady state values of normalised kinetic energy components are negligible between the 3D and axisymmetric counterparts. These axisymmetric results and the reasons for the rapid spin up are discussed in the next subsection.

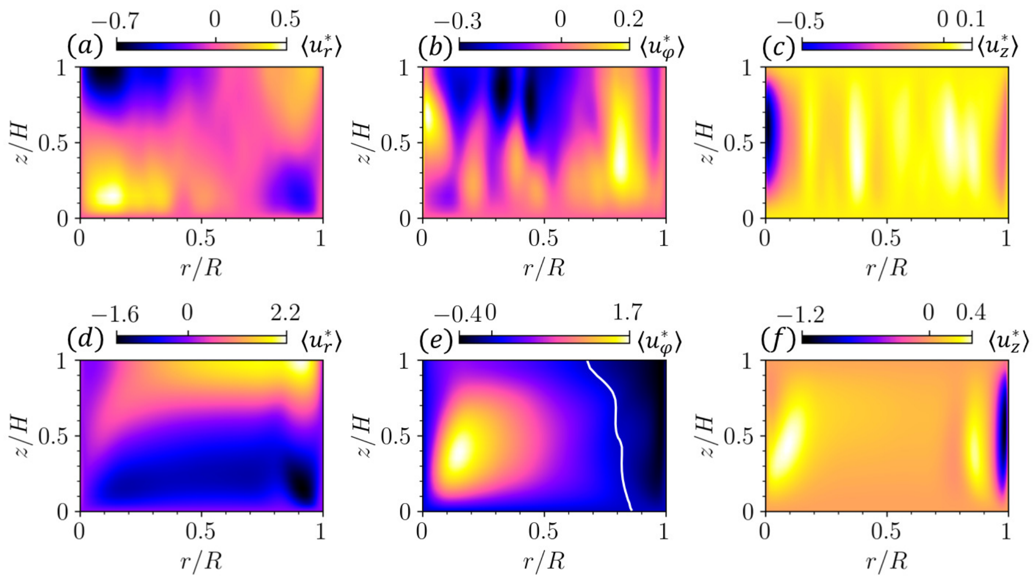

Fig. 4.5 Contours of azimuthally averaged radial (in a and d), tangential (b, e) and axial velocities (d,f) for insulated (top row) and isothermal (bottom row) sidewalls at $\tau = 100$ form Case 12.

Figure 4.5 shows typical spatial variations of azimuthally averaged velocity components in Case 12 with insulated and isothermal sidewalls. The azimuthally averaged quantity Q is obtained using $\langle Q \rangle = \int_0^{2\pi} Q d\varphi / 2\pi$. The averaged velocities are normalised using the rotational velocity, ΩR, and the results are shown for $\tau = 100$. Figures 4.5a and 4.5d shows that the maximum $\langle u_r^* \rangle$ is nearly 4 times smaller for the insulated sidewall compared to its isothermal counterpart. The spatial variation of this radial flow is drastically different, and there is radially inward flow extending to the centre near the bottom boundary in the isothermal case. In addition, there is a radial outflow near the top boundary, and these flow patterns are absent when the sidewall is insulated. The radial flow pattern is shown in Fig. 4.5d is typical when there is poloidal circulation, implying a tropical cyclone-like vortex, in the domain.

The maximum value of $\langle u_\varphi^* \rangle$ is nearly 8 times larger for the isothermal case compared to that for the insulated sidewall, although the minimum values remain more or less the same as observed in Fig. 4.5*b* and 4.1*e*. Also, higher azimuthal velocity is concentrated towards the inner region of the domain along with negative $\langle u^*_\varphi \rangle$ at a larger radius as seen in Fig. 4.5*e*. The white iso-line is for $\langle u^*_\varphi \rangle = 0$, and this azimuthal flow is organised similarly to for a tropical cyclone-like vortex. However, the flow is quite random when the sidewall is insulated, as seen in Fig. 4.5*b*. The spatial variation of $\langle u^*_z \rangle$ shown in Fig. 4.5*f* complements the radial flow pattern shown in Fig. 4.5*d* demonstrating the presence of a domain-filled poloidal (r–z plane) circulation when the sidewall is isothermal. Clearly, the flow has an organised structure resembling a tropical cyclone-like vortex shown in Fig. 4.1, but it is quite unorganised for the insulated boundary condition. This strong influence of the sidewall thermal boundary condition is not observed for the axisymmetric counterparts since a tropical cyclone-like vortex is always seen as listed in Table 4.1.

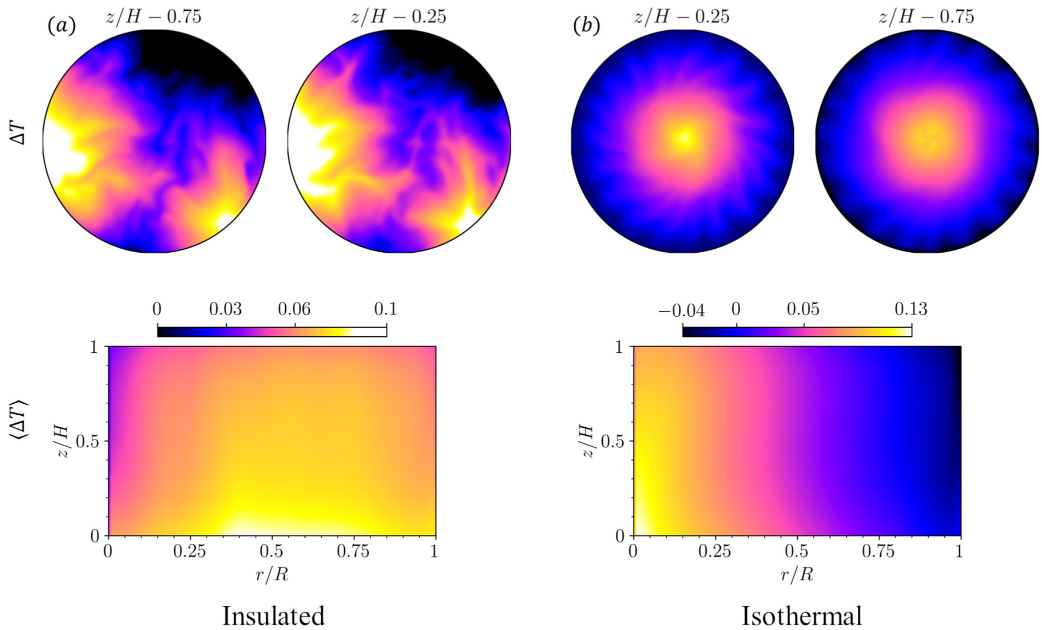

Fig. 4.6 Instantaneous $\Delta T = T - T_{\text{ref}}$ distribution at two different heights and azimuthally averaged variation, $\langle \Delta T \rangle$, in the poloidal plane for (a) insulated and (b) isothermal sidewall conditions shown for $\tau = 100$.

The organised 3D flow in the case of the isothermal sidewall can be confirmed further by studying the spatial variation of azimuthally averaged $\Delta T = T - T_{\text{ref}} = \theta - \beta z$. The spatial variation of instantaneous ΔT, is shown in the poloidal plane in Fig. 4.6 *a* and 4.6*b* for the insulated and isothermal sidewall conditions respectively. For the insulated condition, hot fluid is concentrated in some parts with cold fluids in other parts of the sidewall, as seen in Fig. 4.6*a*. Also, the distribution in the poloidal plane shows that the hot fluid is present in the region $0.4 \leq r/R \leq 0.8$ leading to the formation of counter-rotating large-scale vertical rolls as suggested by Fig. 4.5*c* (also see Fig. 4.22 discussed later). The contours of ΔT are symmetric for the isothermal sidewall with hot fluid in the central region at all heights, as shown in Fig. 4.6*b* which is seen clearly in $\langle \Delta T \rangle$ variation shown in the poloidal plane. This ensures a single poloidal flow in the whole domain, as observed from the velocity contours shown in Figs. 4.5*d* to 4.5*f*.

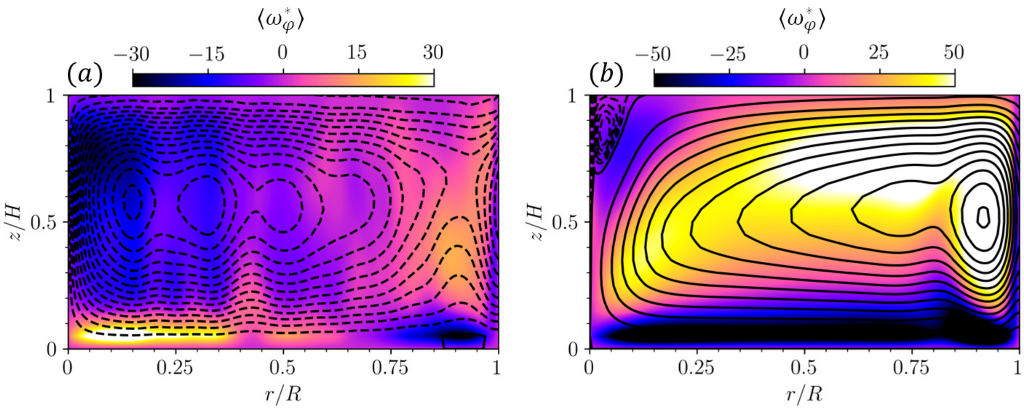

Fig. 4.7 Spatial variation of $\langle \omega_\varphi^* \rangle = \langle \omega_\varphi \rangle / \Omega$ along with poloidal flow streamlines for (*a*) insulated and (*b*) isothermal sidewalls of Case 12 at $\tau = 100$.

The poloidal flow (u_r, u_z) is embodied in the azimuthal vorticity, $\omega_\varphi = \partial u_r/\partial z - \partial u_z/\partial r$. Figure 4.7 shows the azimuthally averaged ω_φ is also normalised using Ω for Case 12 with insulated and isothermal sidewalls. The results are shown for $\tau = 100$ along with the poloidal flow streamlines. The vorticity is positive near the sidewall (outside the Stewartson layer). It changes gradually to a large negative value near the streamlines, suggesting the radial velocity is weaker than u_z. There is more than one vortex in the domain, and these variations are consistent with the velocity variations shown in Figs. 4.5*a* and 4.5*c*.

For the isothermal sidewall a uniform negative vorticity is observed within the Ekman layer as observed for the axisymmetric counterpart (see Figs. 4.2 and 4.3) in past studies (Oruba et al., 2017, 2018, Atkinson et al., 2019). The region above the boundary layer has positive vorticity arising from the variations of u_r in z and u_z in r directions (see Fig. 4.5). The high positive vorticity near the sidewall (outside the Stewartson layer) arises from the strong variation of axial velocity in the radial direction. The conical region of negative vorticity is swept up as observed in axisymmetric calculations of Oruba et al. (2017) to form the eyewall. The streamlines of azimuthally averaged poloidal flow shown for the isothermal case suggest an organised flow with structures depicted in Fig. 4.1.

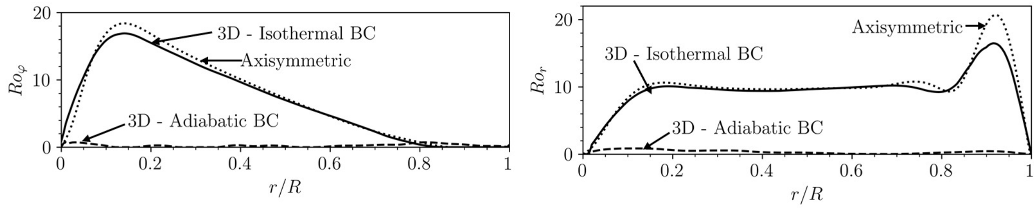

Fig. 4.8 The radial profile of Ro_φ (left) and Ro_r (right) defined in Eq. (4.4).

The strength of horizontal flow at a given radial location can be quantified through radial and tangential Rossby numbers defined as

$$Ro_r(r) = \frac{\langle \overline{u}_r \rangle_{\min}}{\Omega H}; Ro_\varphi(r) = \frac{\langle \overline{u}_\varphi \rangle_{\max}}{\Omega H} \tag{4.4}$$

respectively. The symbol $\langle \overline{Q} \rangle$ denotes the time and azimuthally averaged value of Q. The minimum value of this averaged radial velocity at a given radial location is $\langle \overline{u}_r \rangle_{\min}$ and $\langle \overline{u}_\varphi \rangle_{\max}$ is the maximum value of $\langle \overline{u}_\varphi \rangle$ at a specific r. Figure 4.8 shows the radial variations of Ro_φ and Ro_φ for Case 12 with the isothermal and insulated sidewalls, and the corresponding axisymmetric case. The value of Ro_φ increases and reaches a maximum value of about 12 (see Table 4.1) at $r/R \approx 0.15$ and then decreases gradually towards 0 to satisfy the no-slip condition at the isothermal sidewall. For the insulated case, Ro_φ is very small irrespective of the radial location. A typical variation of Ro_φ with its value of order 10 near the centreline was suggested to be required for the formation of tropical cyclone-like vortex (or eyewall) by Oruba et al. (2017) using their axisymmetric calculations, and such a variation is seen in 3D simulations only for isothermal sidewall. The maximum value of this Rossby number, $Ro_\varphi^{\max}$, for the various flow conditions investigated here is listed in Table 4.1 for both axisymmetric and 3D-isothermal cases. One sees that the axisymmetric cases have larger values (about 3% in Case 12 to 186 % in Case 19) compared to their 3D-isothermal counterparts. This behaviour reflects the observation of Moeng et al. (2004) who has noted that a flow evolving in an axisymmetric rotating system is overly efficient in generating buoyancy fluxed, leading to rapid spin-up and larger u_φ values (or intensity) while studying the planetary boundary layers. The radial variations of Ro_r shown in Fig. 4.8 suggests a weaker radial flow in the insulated case, an observation consistent with Fig. 4.7 compared to the isothermal counterpart. Ro_r value is uniform for most of the domain, and it reached a maximum at $r/R \approx 0.9$ for both axisymmetric and 3D-isothermal cases. The convective flow is initiated by buoyancy in this three 3D-isothermal, 3D-insulated and axisymmetric scenarios, but the flow is shaped by the spatial variations induced by the Coriolis force and its relative strength compared to buoyancy. A larger value of Ro_r implies stronger radial flow (higher magnitude of u_r) which yields a larger $2\Omega u_r$, influencing u_φ spatial variation (see Eqs. (4.6) and (4.9) discussed later). This yields the variation of Ro_φ, a value of order 10 near the centreline and of order 1 near the sidewall, required to form tropical cyclone-like vortex. To further probe the influences of sidewall thermal boundary conditions on shaping the flow into 3D tropical cyclone-like vortex or convective rolls, the azimuthal mode decomposition is performed to understand the evolution of azimuthal modes between the two sidewall boundary condition. Also, momentum budgets are analysed for these two sidewall boundary condition.

Azimuthal Mode Decomposition - Insulated Sidewall

Figure 4.6(b) shows that there is an organised flow in the case of the isothermal sidewall with hot fluid concentrated towards the centre and the cold fluid near the circumference of the domain, which ensures the poloidal flow setup in the domain required for the formation of a tropical cyclone-like vortex. On the other hand, in the case of the insulated sidewall, the hot and cold fluids are concentrated alternatively along the periphery of the cylindrical domain preventing the formation of poloidal flow, as seen in Fig. 4.6(a). In order to further see whether the pattern seen in ΔT for insulated sidewall remains the same at different time instant once the flow is fully evolved, the time evolution of spatial contour of ΔT is shown in Fig. 4.9 for two different axial planes $z/H = 0.25$ and 0.75 from Case 12 in Table 4.1. The spatial pattern of ΔT seen at $\tau = 100$ remains the same for three other different times as seen at $\tau = 115$, 130, & 145, except the ΔT pattern of alternating hot and cold fluid along the circumference is seen to move in a clockwise/retrograde direction (opposite to the direction of the background rotation, Ω) in time. It is visible if we can track the location of the maximum value of the ΔT contour in time, denoted by a small circle in Fig. 4.9. The instantaneous ΔT contour and its variation in time are depth independent, as seen from the $z/H = 0.25$ and 0.75 contours shown in Fig. 4.9. Azimuthal mode decomposition is performed on ΔT next to understand the distribution of ΔT among different azimuthal modes m with insulated sidewall. This will give insight into the spatial pattern observed in Fig. 4.9 which inhibits the formation of poloidal flow in the domain.

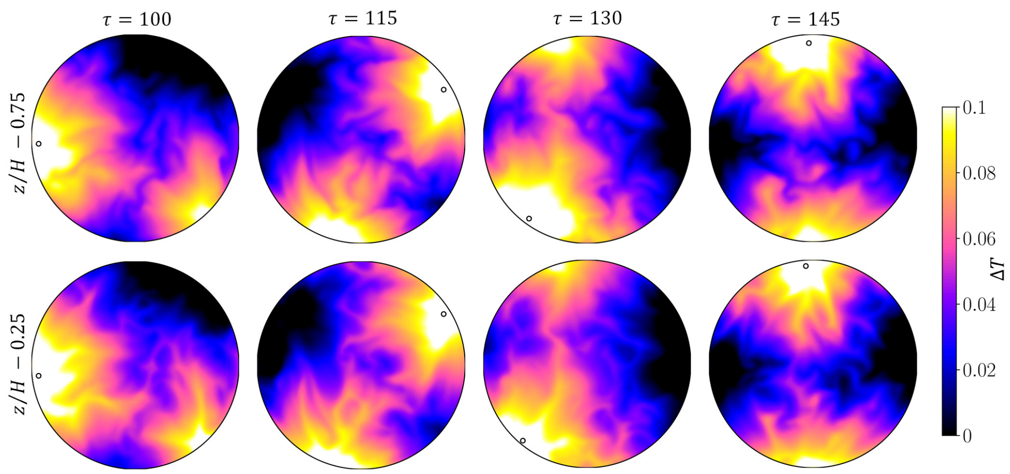

Fig. 4.9 The evolution of ΔT at $\tau = 100$, 115, 130 and 145 at two different heights $z/H = 0.25$ (bottom row) and 0.75 (top row) for Case 12 in Table 4.1.

Azimuthal mode decomposition performed through Fast Fourier transform in φ direction (with m modes) using ΔT at two different axial planes $z/H = 0.25$ and 0.75 as a function of time. This gives insight into the distribution of ΔT among axisymmetric ($m = 0$) and asymmetric modes ($m > 0$) and also the dominant asymmetric mode present in the flow in the case of the insulated sidewall. The spatial average of square of Fourier coefficients of azimuthal modes, $\overline{\overline{|\Delta\hat{T}_m|}}^2$, at two different heights $z/H = 0.25$ and 0.75 for first 8 azimuthal modes of ΔT is shown in Fig. 4.10. The time evolution of azimuthal mode distribution remains more or less the same with height. The flow starts to evolve till $\tau \approx 10$. At $\tau > 10$, higher asymmetric and axisymmetric modes start to develop. The axisymmetric mode $m = 0$ remains the dominant mode until $\tau \approx 35$. After that, the asymmetric mode, $m = 2$, begins to become dominant for $\tau > 40$ both the axisymmetric mode and $m = 2$ asymmetric modes contribute to ΔT with $m = 2$ being the dominant mode. The distribution of ΔT into the dominant asymmetric mode $m = 2$ prevents the symmetric organisation of flow into a large-scale tropical cyclonic vortex with $m = 0$. The observation of $m = 2$ to be the dominant mode for ΔT from the azimuthal mode decomposition shown in Fig. 4.10 complements the observation seen in the spatial contour of instantaneous ΔT depicted in Fig. 4.9 where two regions of alternating hot and cold fluid is observed.

Spatial distribution of the structures for the dominant asymmetric mode as observed in Fig. 4.10 can be educed by taking inverse FFT with Fourier coefficients for mode number of interest, $\Delta\hat{T}(m)$. The data spanning the entire radius is used for FFT in φ direction so that spatial extent of these structures can be seen at the two axial locations

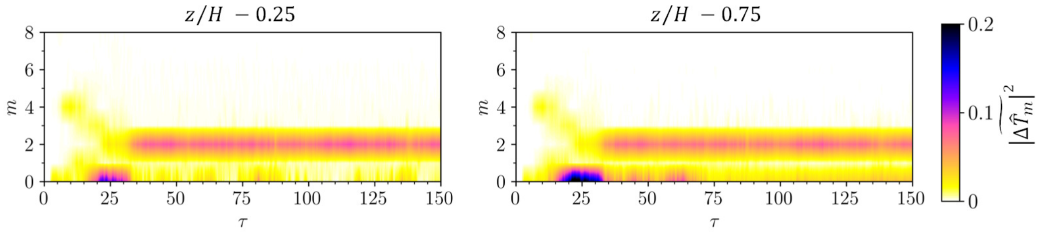

Fig. 4.10 The time evolution of spatial-averaged square of Fourier coefficient of azimuthal modes m = 1 to 8 computed for ΔT denoted by $\overline{\overline{|\Delta\hat{T}_m|}}^2$, at two different heights z/H = 0.25 and 0.75 for Case 12 in Table 4.1.

$z/H = 0.25$ and 0.75. Figure 4.11 shows these structures obtained for $\tau = 100, 115, 130$ and 145. It is observed here that the dominant asymmetric mode moves in a retrograde direction with the maximum magnitude (marked by small circle) is concentrated near the periphery of the domain. Also, the spatial structures shown here are observed to be depth independent. Thus, the spatial $\Delta T_{m=2}$ pattern of the dominant asymmetric mode complement the instantaneous ΔT contour shown in Fig. 4.9. It is also seen in Fig. 4.11 at $\tau = 130$ that there is an emergence of spiral structure with two arms near the core of the domain. In order to further understand about the spiral pattern seen in Fig. 4.11 the continuous time evolution of $\Delta T_{m=2}$ at $z/H = 0.75$ between $\tau = 88$ and 128 is shown as movie (see the video attached titled "*Ch4-movie*[1]"). The two-arm spiral in the core can be clearly seen in the movie, which rotates very fast in the retrograde direction compared to the flow near the circumference of the cylinder. The sense of rotation of the spiral is such that resulting wave propagated out from the spiral core.

Figure 4.12 shows the contour plot for logarithm of frequency-wavenumber spectrum computed from ΔT, i.e., $\log \chi$, where $\chi = |\Delta\hat{T}(m, f)|^2/|\Delta\hat{T}(m, f)|^2_{\max}$ for two radial locations $r/R = 0.2$ & 0.4 at two heights $z/H = 0.25$ & 0.75. The spectral content is dominant for the lower azimuthal modes $0 \le m \le 4$ at both $z/H = 0.25$ & 0.75. The frequency distribution among the dominant lower azimuthal modes is seen to be decreasing as one moves radially outwards from $r/R = 0.2$ to 0.8 The higher values of $\log \chi$ is seen upto $f/\Omega = 2.5$ at r/R = 0.2, whereas it reduces $f/\Omega = 2$ & 1 at $r/R = 0.4$ and 0.8 respectively. The retrograde motion of the $m = 2$ asymmetric mode of ΔT is quantitatively measured by computing the peak frequency f^+ at different

[1]The movie *Ch4-movie* shows the time evolution of $\Delta T_{m=2}$ at $z/H = 0.75$ between $\tau = 88$ and 128 for case 12 in Table 4.1 with insulated sidewall. The movie is available at https://www.dropbox.com/s/tytgk5ghe79zz27/Ch4-movie.mp4?dl=0.

radial locations from frequency-wavenumber spectrum of ΔT at $m = 2$ (as shown with dashed lines in Fig. 4.12). The radial variation of the peak frequency f^+ is shown in Fig. 4.13. The frequency calculated was found to be depth invariant complementing the observation seen in the spatial contour in Fig. 4.11 for $\Delta T_{m=2}$. As seen from the movie, the two-arm spiral in the inner core of the domain rotates at a frequency larger than the background rotation. The rotational frequency of the spirals is observed to be greater than the background rotation in the inner core region till $r/R < 0.4$. This is also inline with the observation in Fig. 4.12. The ratio of maximum to the minimum frequency of rotation of the spirals was found to be 120. Thus, there is a large variation in the frequency of rotation within the domain for the dominant mode $m = 2$. The frequency decreases exponentially as one moves towards a larger radius from the centre. Thus, the distinct hot and cold fluid pattern concentrated near the sidewall takes longer to complete one cycle, as observed in Fig. 4.9 and 4.11. The $m = 2$ asymmetric mode is the dominant mode when the flow is fully evolved for all the 3D cases in Table 4.1 with insulated sidewall.

The presence of spiral inner core with single and multi-armed spirals was also previously observed in very low aspect ratio non-rotating Rayleigh-Benard experiments ($\Gamma = 0.008$-0.05) (Bodenschatz et al., 1991, Assenheimer & Steinberg, 1994, Plapp & Bodenschatz, 1996, Plapp et al., 1998). It was observed in those studies that spiral cores rotates in the retrograde direction with a frequency considerably higher than the frequency of the overall spiral rotation (Plapp & Bodenschatz, 1996). The present results for the $m = 2$ asymmetric mode described in this section for a rotating Rayleigh-Benard study are consistent with the observation from the previous experimental studies in a Rayleigh-Benard setup. Therefore to summarise, the emergence of the dominant non-axisymmetric retrograde mode $m = 2$ and a spiral core inhibits the formation of an axisymmetric structure. These features are absent in the case with isothermal sidewall, where strong poloidal flow is observed helping the emergence of large-scale vortex. Since the previous calculations with insulated sidewall (Oruba et al., 2017, 2018, Atkinson et al., 2019) are axisymmetric, the asymmetric modes are excluded inherently. Thus, these $m = 2$ spiral inner core regions are not observed as seen in the present 3D study. Thus, the sidewall thermal boundary condition does not seem to influence the formation of tropical cyclone-like vortex in the previous axisymmetric studies (Oruba et al., 2017, 2018, Atkinson et al., 2019). The momentum budget analysis is carried out next to shed further insights and to understand the force balance for the tropical cyclone-like vortex especially near the sidewall.

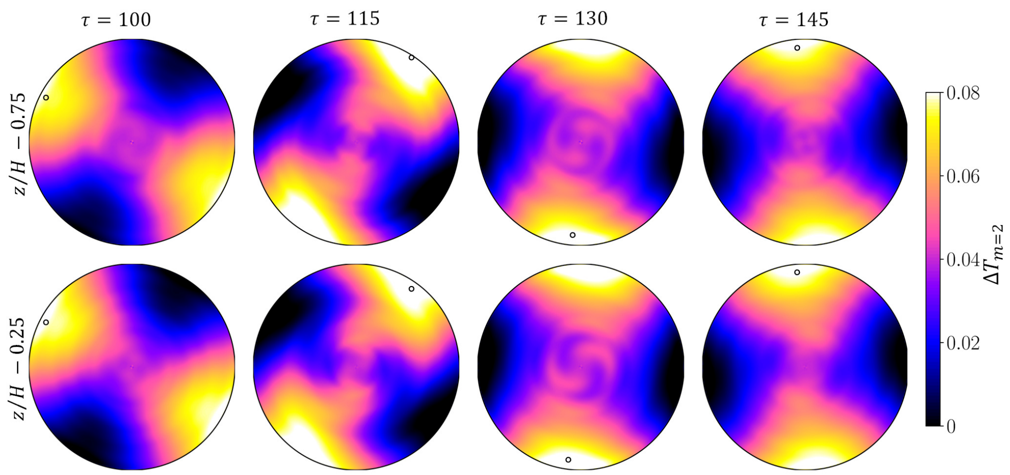

Fig. 4.11 The evolution of ΔT for the dominant mode $m = 2$ denoted by $\Delta T_{m=2}$, at τ = 100, 115, 130 and 145 at two different heights z/H = 0.25 (bottom row) and 0.75 (top row) for Case 12 in Table 4.1.

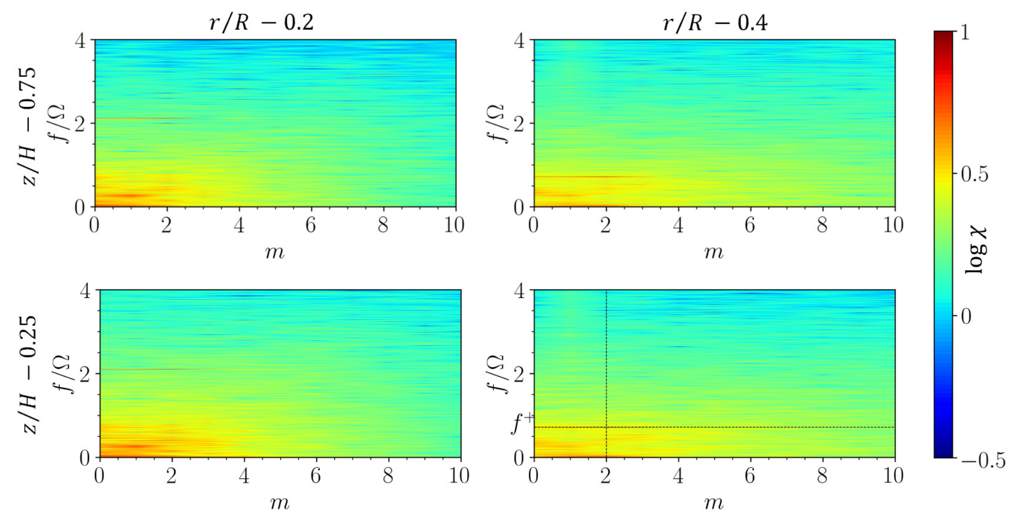

Fig. 4.12 Contour plot of frequency-wavenumber spectrum for case 12 in Table 4.1 where $\chi = |\Delta\hat{T}(m,f)|^2/|\Delta\hat{T}(m,f)|^2_{\max}$

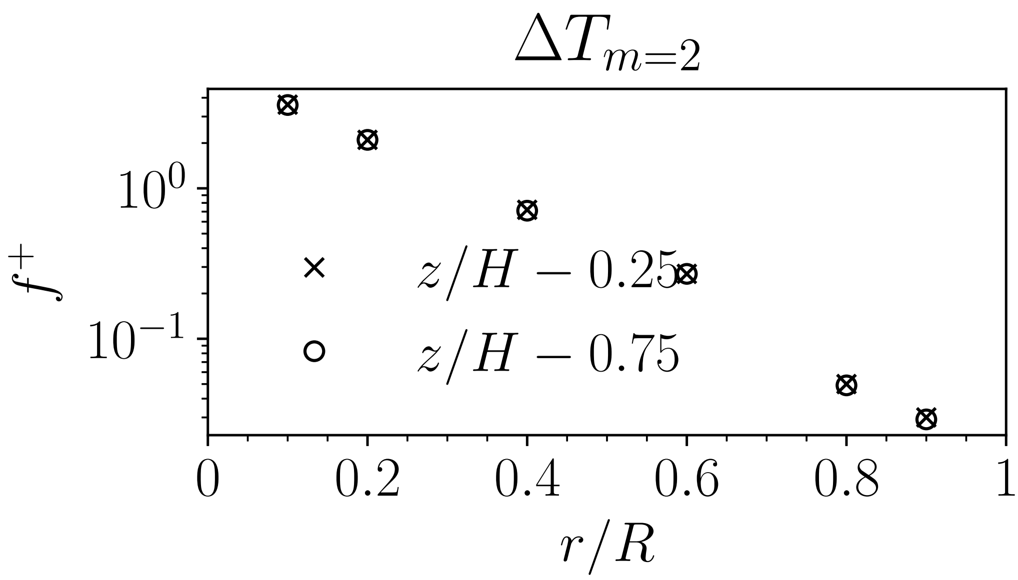

Fig. 4.13 The radial variation of peak frequency f^+ for the dominant asymmetric mode $m = 2$ normalised with background rotation Ω measured from frequency-wavenumber spectrum as shown in Fig. 4.12 at $z/H = 0.25$ ($\times$) and 0.75 ($\circ$) for case 12 in Table 4.1.

4.2.2 Momentum Budget

For the budget analysis, the instantaneous momentum equation, Eq. (4.1) is written in cylindrical coordinate system as,

$$\frac{\partial u_r}{\partial t} + u_r\frac{\partial u_r}{\partial r} + \frac{u_\varphi}{r}\frac{\partial u_r}{\partial \varphi} + u_z\frac{\partial u_r}{\partial z} - \frac{u_\varphi^2}{r} = -\frac{1}{\rho_o}\frac{\partial P}{\partial r} + 2\Omega u_\varphi + \underbrace{\nu\left[\nabla^2 u_r - \frac{u_r}{r^2} - \frac{2}{r^2}\frac{\partial u_\varphi}{\partial \varphi}\right]}_{D_r} \tag{4.5}$$

$$\frac{\partial u_\varphi}{\partial t} + u_r\frac{\partial u_\varphi}{\partial r} + \frac{u_\varphi}{r}\frac{\partial u_\varphi}{\partial \varphi} + u_z\frac{\partial u_\varphi}{\partial z} + u_r\frac{u_\varphi}{r} = -\frac{1}{\rho_o r}\frac{\partial P}{\partial \varphi} - 2\Omega u_r + \underbrace{\nu\left[\nabla^2 u_\varphi - \frac{u_\varphi}{r^2} + \frac{2}{r^2}\frac{\partial u_r}{\partial \varphi}\right]}_{D_\varphi} \tag{4.6}$$

$$\frac{\partial u_z}{\partial t} + u_r\frac{\partial u_z}{\partial r} + \frac{u_\varphi}{r}\frac{\partial u_z}{\partial \varphi} + u_z\frac{\partial u_z}{\partial z} = -\frac{1}{\rho_o}\frac{\partial P}{\partial z} + \alpha g\theta + \underbrace{\nu\left[\nabla^2 u_z\right]}_{D_z} \tag{4.7}$$

where $\nabla^2 = \frac{\partial^2}{\partial r^2} + \frac{1}{r}\frac{\partial}{\partial r} + \frac{1}{r^2}\frac{\partial^2}{\partial \varphi^2} + \frac{\partial^2}{\partial z^2}$ is the Laplacian operator in the cylindrical system. Any dependent variable Q can be expressed as the sum of its azimuthal average $\langle Q\rangle$

and a fluctuation (asymmetry part) Q' and $\langle Q'\rangle = 0$ by definition. The equations for azimuthally averaged velocities are

$$\underbrace{\frac{\partial\langle u_r\rangle}{\partial t}}_{T_r} + \underbrace{\langle u_r\rangle\frac{\partial\langle u_r\rangle}{\partial r} + \langle u_z\rangle\frac{\partial\langle u_r\rangle}{\partial z} - \frac{\langle u_\varphi\rangle^2}{r}}_{A_{s,r}} + \underbrace{\left\langle \frac{\partial(u'_r u'_r)}{\partial r} + \frac{\partial(u'_r u'_z)}{\partial z} + \frac{u'^2_r - u'^2_\varphi}{r}\right\rangle}_{A_{a,r}}$$
$$= -\underbrace{\frac{\partial\langle P/\rho_o\rangle}{\partial r}}_{P_r} + \underbrace{2\Omega\langle u_\varphi\rangle}_{C_r} + \langle D_r\rangle \quad (4.8)$$

$$\underbrace{\frac{\partial\langle u_\varphi\rangle}{\partial t}}_{T_\varphi} + \underbrace{\langle u_r\rangle\frac{\partial\langle u_\varphi\rangle}{\partial r} + \langle u_z\rangle\frac{\partial\langle u_\varphi\rangle}{\partial z} + \frac{\langle u_r\rangle\langle u_\varphi\rangle}{r}}_{A_{s,\varphi}} + \underbrace{\left\langle \frac{\partial(u'_r u'_\varphi)}{\partial r} + \frac{\partial(u'_\varphi u'_z)}{\partial z} + \frac{2u'_r u'_\varphi}{r}\right\rangle}_{A_{a,\varphi}}$$
$$= -\underbrace{2\Omega\langle u_r\rangle}_{C_\varphi} + \langle D_\varphi\rangle \quad (4.9)$$

$$\underbrace{\frac{\partial\langle u_z\rangle}{\partial t}}_{T_z} + \underbrace{\langle u_r\rangle\frac{\partial\langle u_z\rangle}{\partial r} + \langle u_z\rangle\frac{\partial\langle u_z\rangle}{\partial z}}_{A_{s,z}} + \underbrace{\left\langle \frac{\partial(u'_r u'_z)}{\partial r} + \frac{\partial(u'_z u'_z)}{\partial z} + \frac{u'_r u'_z}{r}\right\rangle}_{A_{a,z}}$$
$$= -\underbrace{\frac{\partial\langle P/\rho_o\rangle}{\partial z}}_{P_z} + \underbrace{\alpha g\langle\theta\rangle}_{B_z} + \langle D_z\rangle \quad (4.10)$$

In the above equations, the transient term of $\langle u_i\rangle$ is denoted using T_i, the azimuthal mean advection is $A_{s,i}$, the advection by the asymmetry motion is $A_{a,i}$, the contributions of pressure gradient, Coriolis force, buoyancy and the viscous diffusion are P_i, C_i, B_z, and D_i respectively.

Figures 4.14 and 4.17 show a balance diagram for the three azimuthally averaged momentum equations, Eqs. (4.8) to (4.10) respectively. These radial variations are shown for $\tau = 100$ in two axial planes located at $z/H = 0.25$ and 0.75 for Case 12 in Table 4.1. The values are normalised using $\Omega^2 R$. The relative behaviour and dominance of these quantities are similar for the two heights except for some difference in the azimuthal momentum balance because of the change in the radial flow directions (inward at $z/H = 0.25$ and outward at 0.75) in the isothermal case. Also, there are some differences in the magnitudes of these terms at the two heights shown in the figures.

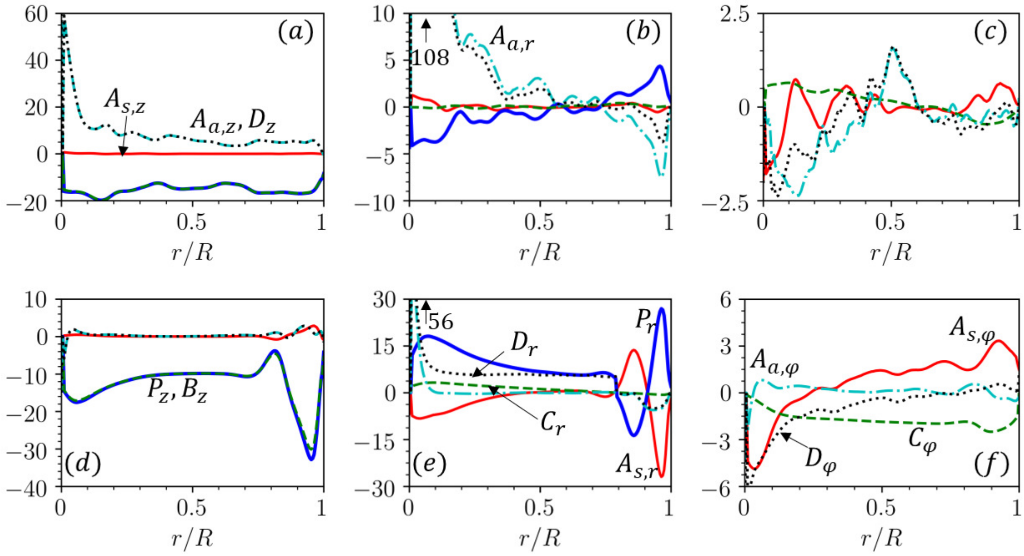

Fig. 4.14 Radial distribution of various terms in Eqs. (4.8) to (4.10) in $z/H = 0.25$ plane at $\tau = 100$ from Case 12 for 3D simulations with insulated (top row) and isothermal (bottom row) sidewall BC. The axial component is shown in the first column. Radial and azimuthal momentum terms are shown in the second and third columns respectively.

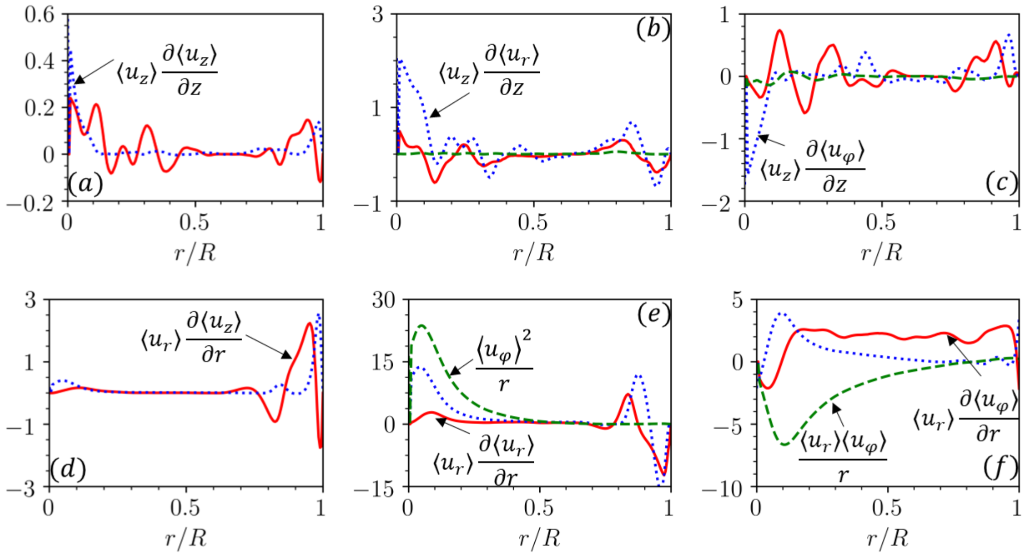

Fig. 4.15 Radial distribution of different terms in symmetric advection term $A_{s,i}$ in Eqs. (4.8) to (4.10) for Case 12 in Table 4.1 3D insulated (top row) and isothermal (bottom row) sidewall BC at $z/H = 0.25$ and $\tau = 100$.

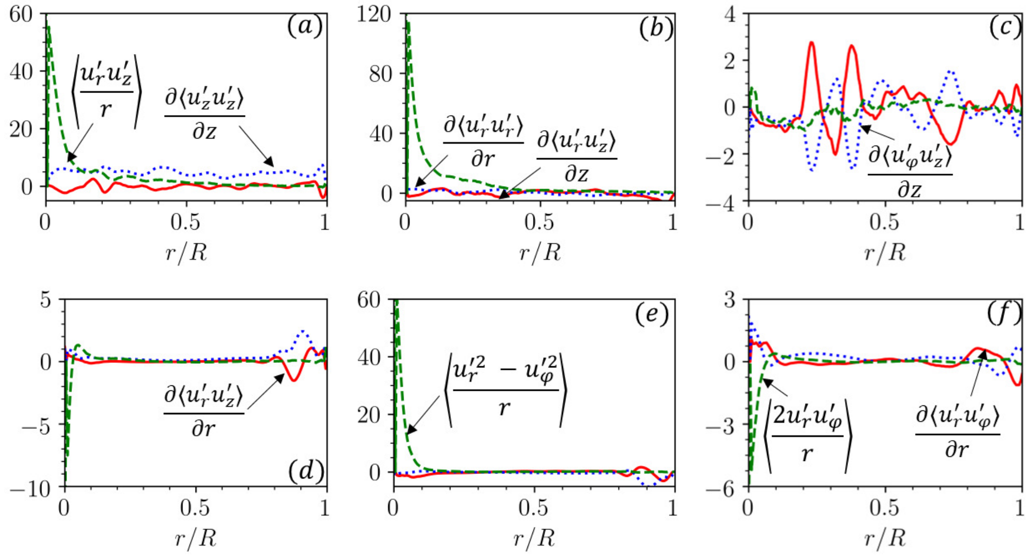

Fig. 4.16 Radial distribution of different terms in asymmetric advection term $A_{a,i}$ in Eqs. (4.8) to (4.10) for Case 12 in Table 4.1 3D insulated (top row) and isothermal (bottom row) sidewall BC at $z/H = 0.25$ and $\tau = 100$.

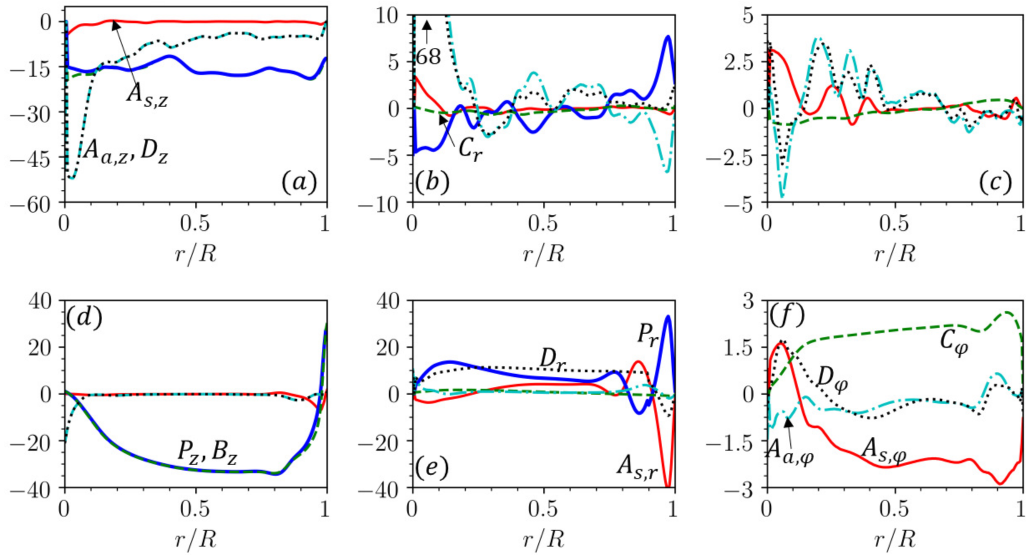

Fig. 4.17 Radial distribution of various terms in Eqs. (4.8) to (4.10) in $z/H = 0.75$ plane at $\tau = 100$ from Case 12 for 3D simulations with insulated (top row) and isothermal (bottom row) sidewall BC. The axial component is shown in the first column. Radial and azimuthal momentum terms are shown in the second and third columns respectively.

The radial variations of axial momentum budget for the insulated and isothermal conditions are shown in Figs. 4.14(a) and 4.14(d) respectively. The pressure gradient, P_z and the buoyancy, B_z are of the same magnitude and these two curves are on top of each other. The contribution of $A_{s,z}$ is negligible, indeed it is of the order of 0.05, as seen in Fig. 4.14(a). The asymmetric advection term, $A_{a,z}$, present in the insulated case has the same magnitude as the viscous diffusion. This term can also be written as $A_{a,z} = \partial\langle u'_r\, u'_z\rangle/\partial r + \partial\langle u'_z\, u'_z\rangle/\partial z + \langle u'_r\, u'_z\rangle/r$ by rearranging it after using the continuity equation. The large contribution of $A_{a,z}$ near the centreline for both insulated and isothermal conditions comes from $\langle u'_r\, u'_z\rangle/r$ due to $1/r$ (see Figs. 4.16(a) & 4.16(d)). The small increase in $A_{s,z}$ near the isothermal sidewall in Fig. 4.14(d) is because of stronger downward flow near the sidewall due to poloidal circulation leading to non- negligible mean advective fluxed of axial momentum in the radial and axial directions, see $A_{s,z}$ term in Eq. (4.10). A similar behaviour is observed for a larger height (see Fig. 4.17(a) and 4.17(d)). However, the magnitude of these advective and diffusive terms is smaller compared to P_z and B_z contributions. Thus, the predominant balance for the axial momentum is through the hydrostatics for either sidewall thermal boundary conditions.

The radial momentum budgets are shown in Figs. 4.14(b) and 4.14(e) for the insulated and isothermal boundary conditions respectively. The predominant balance is among the asymmetric advection, pressure gradient and viscous diffusion with negligible contributions from the Coriolis and symmetric advection for the insulated sidewall. The asymmetric advection and viscous diffusion are of similar magnitude near the centreline for both conditions. Analysing various components of $A_{a,r}$ (see Figs. 4.16(b) & 4.16(e)) shows that the relative large contribution of $A_{a,r}$ near the centreline is from $\langle u'^2_\varphi + u'^2_r\rangle/r$ because of $1/r$. All other terms in the radial momentum equations, Eq. (4.8), are negligible for the insulated condition as seen in Fig. 4.14(b), implying that the radial flow is weaker compared to the axial flow. This is consistent with the insight from Fig. 4.7. On the other hand, the pressure gradient and $A_{s,r}$ have a larger contribution compared to other terms in Eq. (4.8). It is observed that the dominant contribution comes from the centrifugal term, $\langle u_z\rangle\partial\langle u_r\rangle/\partial z$ contribution is about half of the centrifugal term, and the radial advection term is negligible (1/20 of the centrifugal term) in this region. However, the predominant contribution comes from these two advective fluxes, and the centrifugal term is negligible for $r/R \geq 0.8$ and this $A_{s,r}$ contribution is balance predominantly by P_r as seen in Fig. 4.14(e). It is important to note that the magnitude of P_r in the isothermal case is an order of magnitude larger compared to that of the insulated counterpart. At a larger height, these relative behaviours do not change much except for some change caused by the switch in the radial flow direction for isothermal conditions, as shown in Fig. 4.17(e). The results are shown in Fig. 4.17(b) are similar to those in Fig. 4.14(b).

Figures 4.14(c) and 4.14(f) shows the azimuthal momentum budgets for the insulated and isothermal sidewalls respectively. All the terms contribute equally for the insulated condition, and this variation does not suggest an organised azimuthal flow as seen in Fig. 4.5(b). The u_φ is organised as seen in Fig. 4.5(f) and hence the asymmetric advection, $A_{a,\varphi}$ is negligible as seen for the radial and axial components. All other terms contribute equally. However, the relative increase in $A_{a,\varphi}$ near the centreline comes from $\langle u'_\varphi u'_r \rangle / r$ (see Figs. 4.16c & 4.16(f)) similar to that seen for other two components. A larger contribution to $A_{s,\varphi}$ comes from $\langle u_r \rangle \langle u_\varphi \rangle / r$ (see Figs. 4.16(c) & 4.16(f)) for $r/R \leq 0.4$ where $\langle u_r \rangle$ is negative as seen in Figs . 4.5(d). Hence, $A_{s,\varphi}$ is negative in this region and it is positive for $r/R \geq 0.5$ as seen in Fig. 4.14(f) because of the radial flux of azimuthal momentum while remaining two terms in $A_{s,\varphi}$ are small. The Coriolis term $C_\varphi = 2\Omega \langle u_r \rangle$ acts as a source and its substantial contribution comes from large negative $\langle u_r \rangle$ resulting from the enhanced radial pressure gradient in the isothermal case. Also, the magnitude of the azimuthal momentum terms is smaller than the axial and radial momentum terms. Hence, the flow is shaped mainly by the axial and radial momentum balance, governing the poloidal flow to form tropical cyclone-like vortex. The sidewall thermal boundary conditions heavily influence this interplay in 3D flows. This comes mainly through the link of a pressure gradient to a thermal gradient near the sidewall.

From the hydrostatic balance observed in Figs. 4.14(d) and 4.17(d) for the axial momentum equation, Eq. (4.10), one gets $\partial \langle P \rangle \sim \rho_o \alpha g \langle \theta \rangle \partial z$ suggesting that one can write $\partial \langle P \rangle / \partial r \sim \rho_o \alpha g z_1 \partial \langle \theta \rangle / \partial r$ at a given height z_1. This is verified to hold for $r/R > 0.9$ by analysing the simulation results (see Fig. 4.18). Also, one must be cautious in interpreting this equation in the light of the radial momentum balance depicted in Figs. 4.3(d) and 4.17(d) showing $P_r \sim A_{s,r}$ near the sidewall. This implies that the symmetric advection near the sidewall is driven by the thermal boundary condition ($P_r \sim \partial\theta/\partial r$) as one can guess intuitively. The $\partial\theta/\partial r = 0.$ case does not yield sufficiently large P_r to drive symmetric radial advection and hence the poloidal flow does not ensue. Figure 4.19 shows the radial variation of momentum balance in the axisymmetric counterparts of Case 12 with the insulated and isothermal sidewalls. The asymmetric component, $A_{a,i}$, is zero since they are absent in the axisymmetric flow equations. These terms' relative behaviour and variation are similar for both conditions except for some small differences near the sidewall, which do not affect

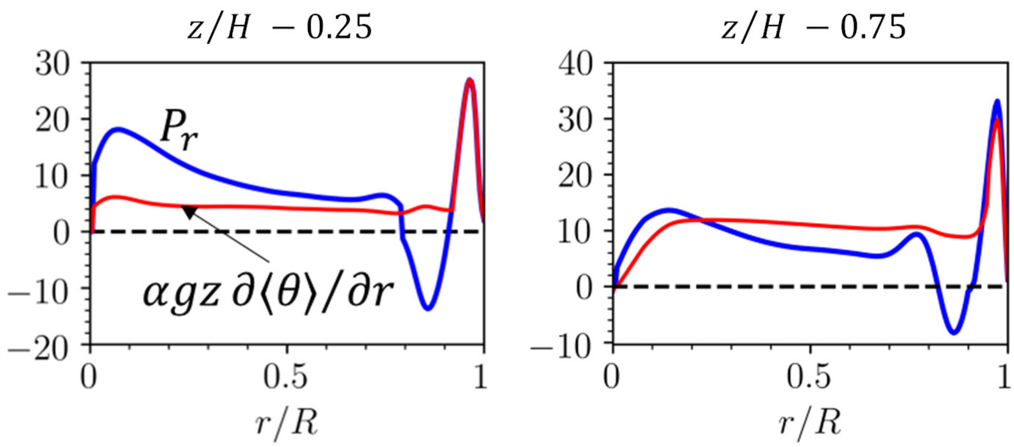

Fig. 4.18 Radial distribution of P_r and $\alpha gz\partial\langle\theta\rangle/\partial r$ in $z/H = 0.25$ and $z/H = 0.75$ plane at $\tau = 100$ from Case 12 for 3D simulation with isothermal sidewall BC.

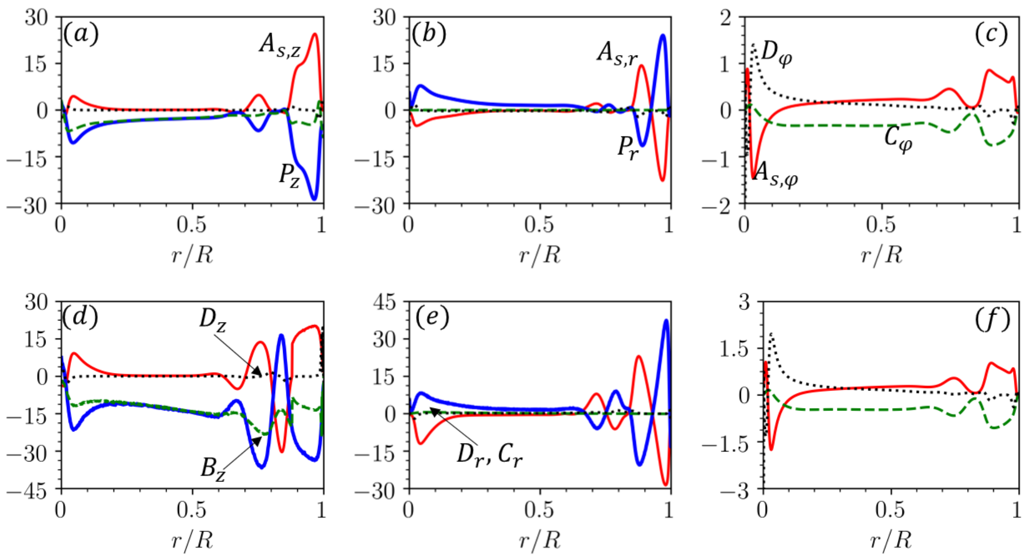

Fig. 4.19 Radial distribution of various terms in Eqs. (4.8) to (4.10) in $z/H = 0.25$ plane at $\tau = 150$ from Case 12 for axisymmetric simulation with insulated (top row) and isothermal (bottom row) sidewall BC. The axial component is shown in the first column. Radial and azimuthal momentum terms are shown in the second and third columns respectively.

the bulk behaviour. For the axial momentum, P_z and B_z are of similar magnitude for $r/R \leq 0.7$ and D_z is very small. The contribution of B_z is reduced for $r/R > 0.8$

(near-wall region) and $A_{s,z}$ also contributes significantly to balance P_z as seen in Fig. 4.19(a) and 4.19(d). This behaviour is contrastingly different from the 3D counterparts shown in Fig. 4.14 and hence once cannot relate $\partial P/\partial r$ to $\partial \theta/\partial r$ near the sidewall in the axisymmetric cases as we did for the 3D simulations. Also, the radial and azimuthal momentum balances are shown in Fig. 4.19 for the axisymmetric cases is similar to that shown for 3D- isothermal simulations in Figs. 4.14(e) and 4.14(f). Hence, the reduced degree of freedom in 2D-axisymmetric cases leads to stronger axial and radial advection in the near-wall region, leading to stronger poloidal flow. This is also reflected in the ratio of azimuthal to poloidal kinetic energy listed in Table 4.3 for a few cases. The percentage difference between the axisymmetric and 3D-isothermal counterparts suggests that the poloidal flow is stronger in the axisymmetric case. This yields a stronger eye, suggested by Ro_φ results in Fig. 4.8 and this is consistent with the observation of Moeng et al. (2004) as noted earlier. The percentage difference for Case 27 is not listed in Table 4.3 since no tropical cyclone-like vortex is seen for 3D-isothermal simulation, but it emerges in the axisymmetric calculation as noted in Table 4.1.

Table 4.3 Typical values for ratio of azimuthal kinetic energy, K_φ^*, to poloidal kinetic energy, $K_P^* = K_r^* + K_z^*$.

Case	K_φ^*/K_P		
	Axisymmetric	3D-iso	% difference
6	0.23	0.26	-11.5
12	0.23	0.25	-8
18	0.21	0.24	-12
27	0.32	0.72	-

To summarise the discussion in this section, the radial pressure gradient near the sidewall strongly influences the thermal boundary condition in 3D simulations. This pressure gradient drives a waker radial inflow for the insulated condition resulting in convective rolls in the domain, which are typical for this setup. A stronger radial thermal gradient near the sidewall under isothermal conditions leads to a stronger radial pressure gradient which drives the stronger poloidal flow. It is to be noted that in the 3D simulations, either the free-slip or no-slip velocity boundary condition for the sidewall does not change the flow evolution in the cases with both insulated and isothermal sidewall boundary conditions. It is only the sidewall thermal boundary condition that dictates the flow evolution for the parameter range explored in this work.

4.2.3 Flow Behaviour near Sidewall

The effect of sidewall thermal boundary condition on the flow is felt through radial pressure gradient in the near-wall region. This pressure gradient drives the radial flow shaping the poloidal circulation, and hence it is instructive to understand the near-wall flow structures when the sidewall is isothermal or insulated. This analysis is performed through Fast Fourier Transform (FFT) in φ direction (with m modes) using u'^*_φ and u'^*_z collected in the regions $0.9 \leq r/R \leq 1.0$ at various instants. The power spectra constructed thus are shown in Figs. 4.20 and 4.21 for u'^*_φ and u'^*_z respectively. The results are shown for both isothermal and insulated conditions. The spectral distribution is similar for both conditions at $\tau = 15$, with the 4th or 5th mode having the peak value. The peak value moves towards the higher mode as the flow evolves in time and settles at $m = 18$ when the steady-state is reached for the isothermal condition. The volume-averaged kinetic energies also reach a steady-state value by about $\tau = 50$ as shown in Fig. 4.4. The spectrum is quite broad for the insulated condition. The u'^*_z spectrum depicted in Fig. 4.21 also shows similar behaviour. However, this spectrum is broader for the insulated condition, suggesting that the structures as large as the computational domain and much smaller size ($m = 20$) have larger energies.

The spatial distribution of these structures can be deduced by taking FFT with Fourier coefficient for mode numbers of interest, $\hat{u}'^*_\varphi(m)$, and using appropriate threshold values. The data spanning the whole domain is used for FFT in φ direction so that the spatial extent of these structures can be seen. Figure 4.22(a) shows these structures obtained at $\tau = 100$ using $\hat{u}'^*_\varphi(m = 18)$ and using threshold values of $u'^*_\varphi = 0.1$ and -0.1 for the isothermal condition. These structures are seen only near the sidewall and correspond to a retrograde wave. The structures deduced as above using $\hat{u}'^*_z(m = 15)$ are shown in Fig. 4.22(b) for the insulated condition. Since u'^*_φ is weak compared to the axial component as suggested by the momentum balance in Figs. 4.14 and 4.17, u'^*_z is used to emphasis the presence of vertical rolls for the insulated condition. These structures extend well into the domain interior and feel the background rotation at a larger radius. These modal structures are also compared to the corresponding two iso-surfaces of u'^*_φ and u'^*_z shown in Figs. 4.22(c) and 4.22(d) extracted directly from the simulation data (includes all the modes). It is clear that the well-organised structures forming a retrograde wave are coming from the dominant mode, $m = 18$, for the isothermal condition. The vertical rolls for $m = 15$ shown in Fig. 4.22(b) are part of chaotic convection for the insulated condition. Therefore, the flow is unable to organise to yield a strong poloidal circulation.

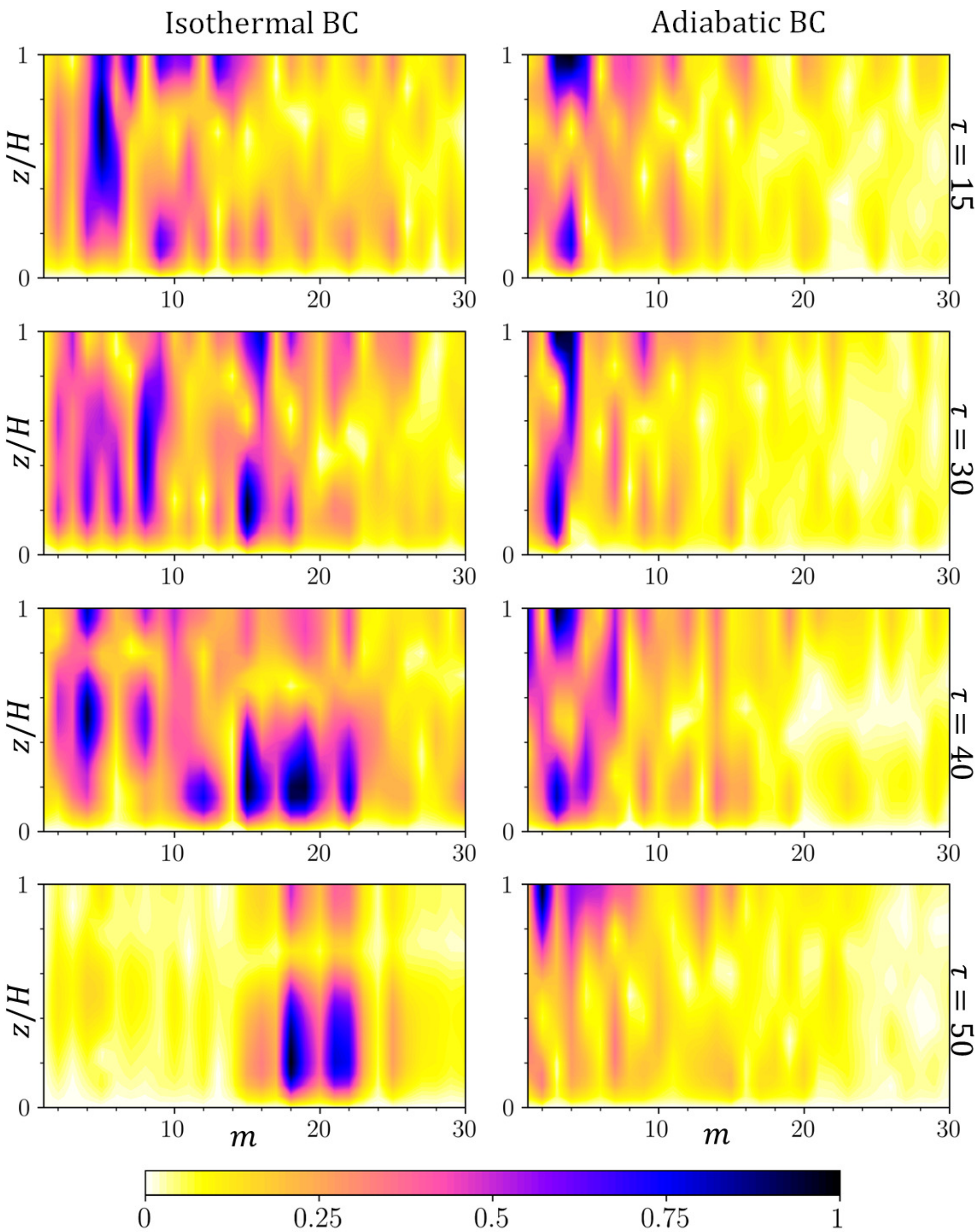

Fig. 4.20 Azimuthal power spectrum of u'^{*}_{φ} in the region $0.9 \leq r/R \leq 1.0$ at 4 different times from Case 12 with isothermal and insulated sidewalls. The values are normalised using the respective maximum and these values are 0.9 (isothermal) & 0.3 (insulated) at $\tau = 15$; 0.8 & 0.25 at $\tau = 30$; 0.65 & 0.22 at $\tau = 40$; and 0.6 & 0.23 at $\tau = 50$.

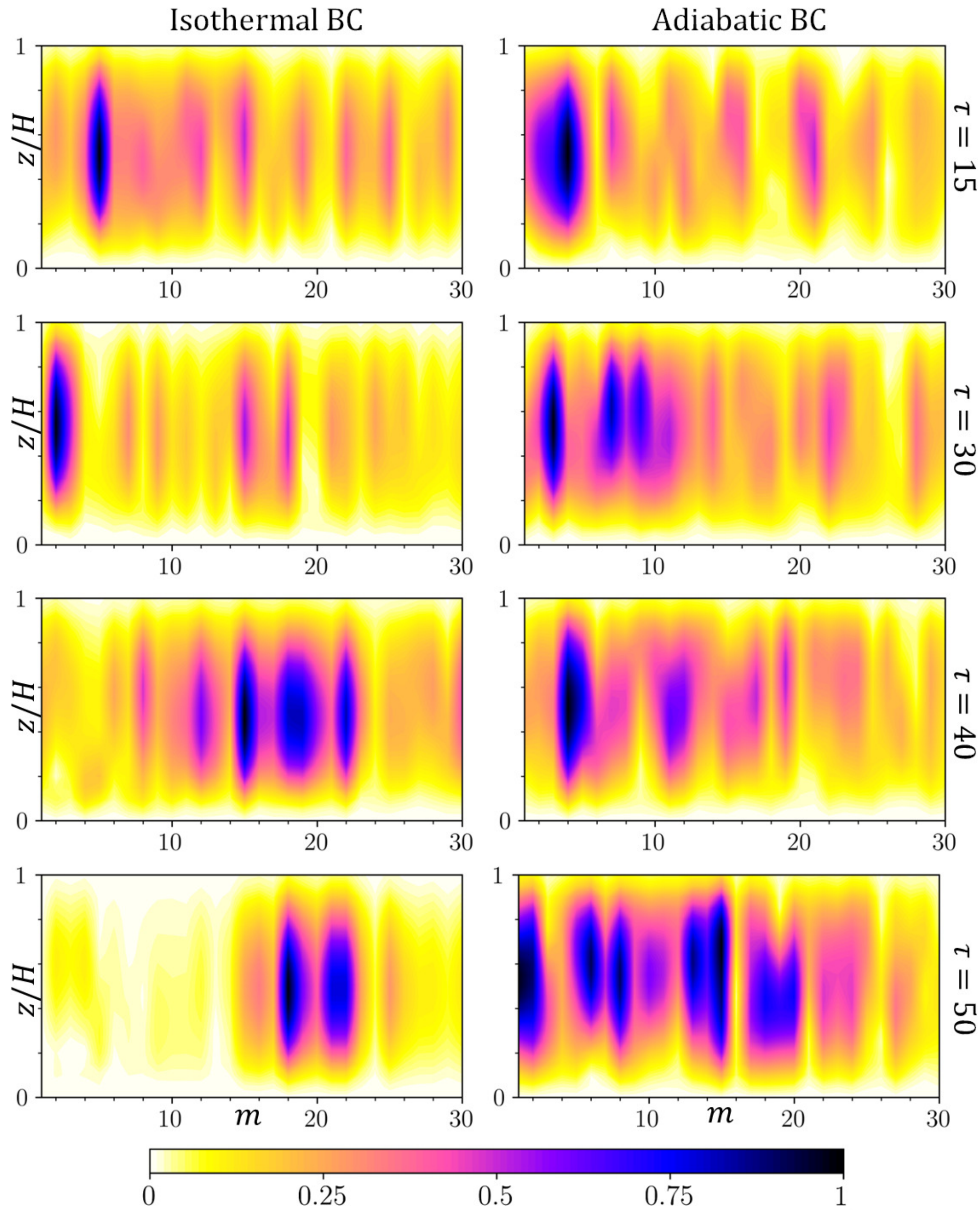

Fig. 4.21 Azimuthal power spectrum of $u_z'^*$ in the region $0.9 \leq r/R \leq 1.0$ at 4 different times from Case 12 with isothermal and insulated sidewalls. The values are normalised using the respective maximum and these values are 0.8 (isothermal) & 0.7 (insulated) at $\tau = 15$; 0.6 & 0.65 at $\tau = 30$; 0.4 & 0.6 at $\tau = 40$; and 0.3 & 0.5 at $\tau = 50$.

4.3 Summary

In this chapter, the three-dimensional effects and effects of sidewall thermal boundary condition on the formation of the tropical cyclone-like vortex are studied in detail. The following conclusions can be drawn from the analysis presented:

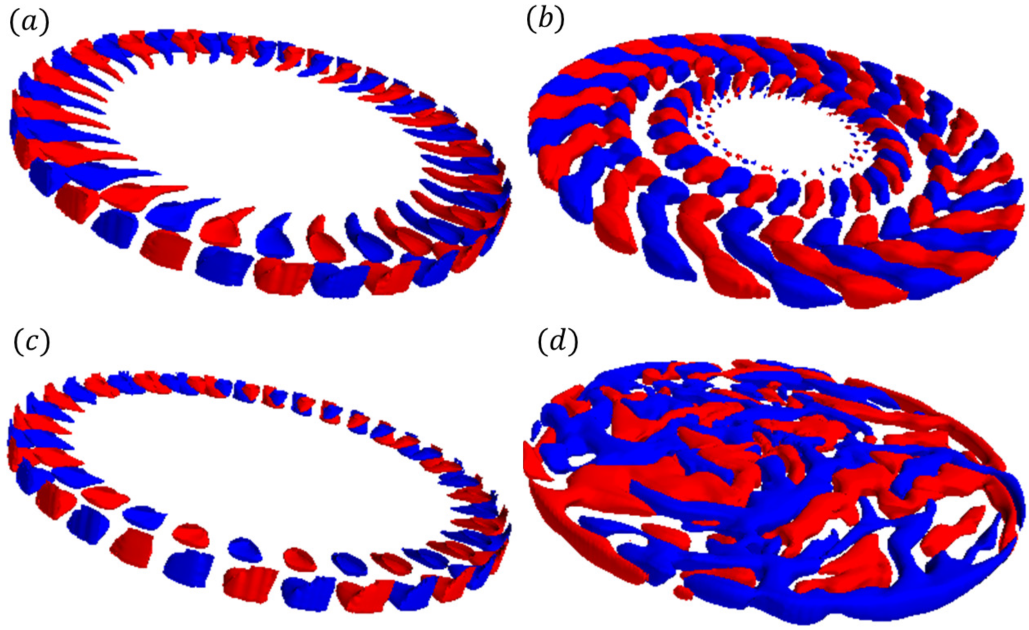

Fig. 4.22 Spatial structures for $(a)u'^*_\varphi = 0.1$ (red) and -0.1 (blue) deduced using $\hat{u}'^*_\varphi(m = 18)$ for the isothermal condition and $(b)u'^*_z = 0.1$ (red) and -0.1 (blue) deduced using $\hat{u}'^*_z(m = 15)$ dominant near sidewall for insulated condition. The corresponding iso-surfaces obtained directly from the simulation data (without involving FFT) are shown in (c) and (d). The results are shown for Case 12 at $\tau = 100$.

- *OpenFOAM* code used in this work is able to capture the steady and unsteady behaviour of tropical cyclone-like vortex in 2D-axisymmetric calculations well compared to the past studies (Oruba et al., 2017, 2018, Atkinson et al., 2019).

- Tropical cyclone-like vortex formed in 3D simulation were found to be less intense than the axisymmetric counterpart, consistent with the observation of Moeng et al. (2004). This is attributed to the stronger poloidal flow in 2D- axisymmetric calculation due to a lesser degree of freedom of the fluid. This is also the reason for tropical cyclone-like vortex formation at higher *Re* in 2D-axisymmetric cases in Table 4.1.

- The sidewall thermal boundary condition strongly influences the formation of poloidal flow and tropical cyclone-like vortex in the 3D simulations.

- 3D simulation with insulated sidewall show unorganised, chaotic convection with convective rolls filling the domain. The presence of asymmetric retrograde mode of $m = 2$ with a spiral core in ΔT variations inhibits the formation of organised flow in the domain. The corresponding simulations with isothermal sidewall show organised convection with tropical cyclone-like vortex forming in the bulk of the domain and well-organised retrograde wave in the periphery. This organised flow is observed only when $Ro \approx C/\Gamma$ is satisfied by the global flow parameters. The analysis of 27 cases in Table 4.1 suggests that $\sqrt{2} \leq C \leq 2\sqrt{2}$ for the conditions explored here.

- The isothermal sidewall boundary condition leads to a stronger radial thermal gradient near the sidewall, which directly relates to a stronger radial pressure gradient (due to hydrostatic balance), which further leads to stronger poloidal flow in the domain aiding the formation of tropical cyclone-like vortex.

The model used for analysis in this chapter is simple without additional complexities such as turbulence, stratification, latent heat from moist convection, and air-sea interaction, which are essential in an actual tropical cyclone. As stated in Chapters 1 and 2 of this thesis, turbulence will be included by considering the large eddy simulation (LES) paradigm. This task is taken up in the next chapter.

Chapter 5

Timescale for the Cyclogenesis

Rotating flows driven by natural convection between two differentially heated plates are very rich in physics and have high relevance to geophysical (Marshall & Schott, 1999) and astrophysical flows (Schumacher & Sreenivasan, 2020) and also to semiconductor industries (Dold & Benz, 1999). A wide range of flow topologies arise from instabilities, and past studies provided valuable insights; see the reviews in (Bodenschatz et al., 2000, Ahlers et al., 2009). For example, bulk convection starts to emerge between two infinitely long isothermal plates separated by a vertical distance, H, with a temperature difference of ΔT, rotating at a rate of Ω when the Rayleigh number exceeds a critical value, $Ra_c = 8.7\widehat{E}^{-4/3}$ when the Ekman number, $\widehat{E}$, becomes small (Chandrasekhar, 1961). The Rayleigh and Ekman numbers are defined, respectively, as $Ra = \alpha g \Delta T H^3 / (\nu\kappa)$ and $\widehat{E} = \nu / (2\Omega H^2)$, where α is the thermal expansivity of the fluid with a constant kinematic viscosity ν and thermal diffusivity κ and g is the gravitational acceleration. This bulk convection emerges through many bifurcations arising from flow instabilities sensitive to ΔT, thermal and hydrodynamic boundary conditions, and the Prandtl number $Pr = \nu/\kappa$. The flow patterns and structures evolving through these bifurcations were investigated in several past direct numerical simulation (DNS) (Horn & Schmid, 2017, de Wit et al., 2020, Zhang et al., 2020, Favier & Knobloch, 2020) and experimental (Zhong et al., 1991, Ecke et al., 1992, Ning & Ecke, 1993, Zhong et al., 1993, Liu & Ecke, 1997) studies. DNS studies have also shown that depth invariant long-lived cyclonic large scale vortices (LSV) form when Ra are several times larger than Ra_c for a given Ekman number imposing strong enough rotational constraints on the convective flow structures (Guervilly et al., 2014, Favier et al., 2014, Couston et al., 2020, Guzmán et al., 2020). These LSVs have been observed for Boussinesq (Guervilly et al., 2014, Favier et al., 2014) and two-layer stratified fluids (Couston et al., 2020) regardless of the hydrodynamic boundary conditions (Guzmán et al., 2020). However, it is unclear if these LSVs have eye and eyewall structures typical of tropical cyclones or hurricanes.

The upsweep of the bottom boundary layer by strong poloidal flow was shown to form eye and eyewall in axisymmetric rotating convection of a Boussinesq fluid (Oruba et al., 2017, 2018), which was also suggested in Smith (2005). This was observed only when (i) the convective Reynolds number $Re = \sqrt{Ra/Pr} = VH/\nu$, where V is the buoyancy velocity scale, is sufficiently large; (ii) the Ekman number, $E = \nu/\left(\Omega H^2\right)$ is sufficiently small, and (iii) the Rossby number, $Ro = ReE$, is between a lower and an upper bound (Oruba et al., 2018). The eye was also observed to trap inertial waves leading to its oscillation when the thermal forcing on the bottom surface was increased (Atkinson et al., 2019). These observations were made in axisymmetric simulations of rotating laminar convection of a Boussinesq fluid with the following boundary conditions. The no-slip bottom and outer radial boundaries had constant uniform heat flux and insulating conditions. The stress-free top boundary had a constant uniform heat flux condition. Despite this recent advance in our understanding, the statement of Emanuel (1991), "no laboratory analogue for tropical cyclone has been discovered," made 30 years ago still holds. This is because an answer to the question "when does a strong poloidal flow emerge in rotating convection to form tropical Cyclone-like vortex?" is unclear. In the last chapter, it was seen from 3D laminar simulations that by choosing an appropriate sidewall thermal boundary condition, organised flow with a tropical cyclone-like vortex is seen when $Ro \approx C/\Gamma$ is satisfied by the global flow parameters. It is still unclear when the initially quiescent flow starts to organise itself into a large-scale tropical cyclone-like vortex. It is necessary to know the timescale of this cyclogenesis process. It can help DNS practitioners and experimentalists with the expected runtime of the experiments and the time period at which cyclogenesis is expected. This can help them to concentrate on the particular time period of the experiments to extract relevant data so that the hydrodynamic intricacies in the tropical cyclone-like vortex formation and dynamics can be unravelled. Since the formation of a tropical cyclone-like vortex from a quiescent initial condition is a long process and it takes several 100s of the rotation time, it is important to know the estimated time taken for several processes involved in cyclogenesis. In this chapter, an attempt is made to come up with a timescale for cyclogenesis by running a simulation spanning several orders of magnitude of flow parameters and analysing the simulation data. Thus, the objectives of this chapter are:

1. To simulate a tropical cyclone-like vortex from a turbulent rotating Rayleigh-Benard convection setup using LES paradigm for a wide range of flow parameters.

2. To quantitatively compare the structure of the resulting tropical cyclone-like vortex with an actual tropical cyclone.

3. To propose a timescale for the cyclogenesis and see its implications to actual cyclogenesis.

The remainder of the chapter is structured as follows. First, the numerical procedure employed is discussed in section 5.1, detailing the equation solved, the boundary conditions used, the computational domain, the mesh information, the turbulence modelling framework and the flow parameter values used for the simulations. In the section 5.2.1, the instantaneous flow fields are shown for the 3D turbulent simulations. The time-averaged structures of the tropical cyclone-like vortex obtained for a wide range of flow parameters are compared qualitatively with a real tropical cyclone. A timescale for cyclogenesis is proposed by analysing the simulation data, and the flow evolution during cyclogenesis is briefly described in section 5.2.2. The timescale proposed for cyclogenesis is validated using storm track data from field experiments in section 5.3. The chapter is concluded with a summary.

5.1 Numerical Procedure

A cylindrical domain shown in Fig. 5.1 with a radius R and height H, giving an aspect ratio of $\Gamma = H/R$ is considered for this work. The computational domain rotates at the rate of Ω and the system has a linear background temperature variation of $T_o(z) = T_{\text{ref}} - \beta z$ to maintain a static equilibrium, where T_{ref} is the reference temperature taken at $z = 0$. The flow in the domain is initiated by imposing a uniform vertical heat flux, proportional to β, at the bottom boundary. This flow is computed by solving an equation for temperature perturbation, $\theta = T - T_o(z)$ along with the continuity and Navier-Stokes equations using large eddy simulation (LES) paradigm.

5.1.1 Large eddy simulation framework

The equations considered in the present study for carrying out numerical simulations are the grid-filtered continuity, Navier-Stokes with the added coriolis and buoyancy term, and temperature perturbation (from the background linear profile) equations for a incompressible fluid under the Boussinesq approximation (Boussinesq, 1903):

$$\frac{\partial \overline{u}_i}{\partial x_i} = 0 \tag{5.1}$$

$$\frac{\partial \overline{u}_i}{\partial t} + \frac{\partial \overline{u}_i \overline{u}_j}{\partial x_j} = -\frac{1}{\rho_o}\frac{\partial \overline{P}}{\partial x_i} + \frac{\partial \tau_{ij}}{\partial x_j} + \nu \frac{\partial^2 \overline{u}_i}{\partial x_j \partial x_j} - 2\Omega \overline{u}_j \varepsilon_{ij3} + \alpha \overline{\theta} g_i \tag{5.2}$$

$$\frac{\partial \overline{\theta}}{\partial t} + \frac{\partial \overline{u}_j \overline{\theta}}{\partial x_j} = \kappa \frac{\partial^2 \overline{\theta}}{\partial x_j \partial x_j} + \frac{\partial h_j}{\partial x_j} + \beta \overline{u}_z \tag{5.3}$$

In the above equations, overbar on the variable indicates a grid-filtered quantity, $\overline{u_i}$ (where i = 1,2,3) are the velocity components in the direction (x_1, x_2, x_3), where x_1 and x_2 are the horizontal coordinates and x_3 is the coordinate in the upward vertical direction, $\overline{P}$ is the reduced pressure, θ is the temperature perturbation from the background linear temperature profile, g_i is the gravitational vector pointing in the vertically downward direction, Ω is the background rotation rate, α is the thermal expansion coefficient, ν is the kinematic viscosity and κ is the thermal diffusivity of the fluid.

The filtered governing equation (5.2) and (5.3) contain subgrid-scale terms, which are defined as

$$\tau_{ij} = \overline{u_i u_j} - \overline{u}_i \overline{u}_j \tag{5.4}$$

$$h_j = \overline{\theta u_j} - \overline{\theta}\overline{u}_j \tag{5.5}$$

A closure model for subgrid-scale stress relates the sub-grid scale stress with resolved scale variables which enables the above-filtered equations to be integrated. This study aims at simulating a large-scale phenomenon. Hence, a simple SGS model that dissipates energy properly is preferred (also adequate) to represent the net effect of small-scale eddies. Therefore, the dynamic Smagorinsky model (Lilly, 1992) is used in this work for modelling SGS stresses. The models is described in section 2.3.

5.1.2 Numerical set-up

LES are conducted using an opensource finite volume solver *OpenFOAM* (Weller et al., 1998). The governing equations (5.2) and (5.3) written in Cartesian coordinates along with the SGS closures discussed above are solved using a second-order central difference spatial discretisation scheme and an implicit first-order Euler time-stepping. These discretised equations are advanced in time using a variable time-stepping which kept the CFL number, defined as $\Delta t \times \max(|\mathbf{u}|/\delta_c)$, to be below 0.3, where δ_c is the computational cell size with velocity magnitude $|\mathbf{u}|$ and Δt is the time step size. The pressure and velocity fields are coupled through the PISO algorithm (Issa, 1986). Figure 5.1(b) shows the various boundary conditions employed for this work. The no-slip bottom and outer radial boundaries had uniform heat flux and isothermal conditions respectively. The stress-free top boundary had a constant uniform heat

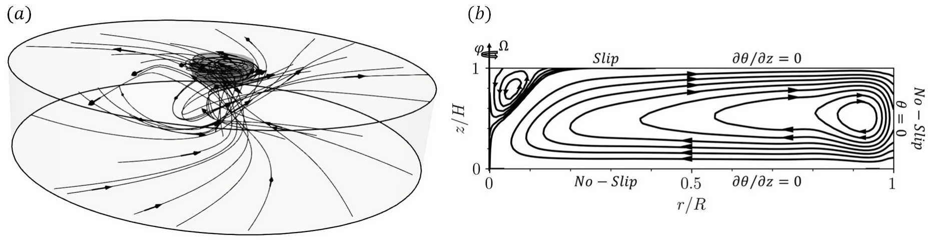

Fig. 5.1 (a) Computational domain and (b) boundary conditions.

flux condition. All the simulations are started from a quiescent initial state and the simulations are run until a stationary state (in terms of volume-averaged kinetic energy) is reached. Typical streamlines for a fully evolved tropical cyclone like vortex are shown in Fig. 5.1(a).

The LES is stopped when there isn't a significant change in the monitored volume-averaged kinetic energy per unit mass. The grid sensitivity is tested by analysing the ratio of SGS to the total kinetic energies (Pope, 2000). The mean and mode for the distribution of this ratio are observed to be about 8% or lower when 2, 4, or 8 million cells are used for the case with $Re = 1000$, and the maximum change in the eyewall, Ekman layer and size of tropical cyclone is less than 10% (these quantities are measured as described in section 4.1.2). Hence, the criterion proposed by Pope (2000), the SGS kinetic energy being less than 20% of the total kinetic energy, is used to decide the numerical resolution for other Reynolds numbers, and 11 million cells are used for the largest Re case considered for this study.

5.1.3 Simulated Cases

Past laminar axisymmetric simulations of RRBC showed that strong poloidal circulations leading to the formation of TCLV occurred only for certain combinations of Re and E (Oruba et al., 2018). This combination is observed to be more stringent for three-dimensional laminar simulations and the propensity for TCLV to form in 3D domains increases if $Ro = Re\,E \simeq C/\Gamma$ with $\sqrt{2} \leq C \leq 2\sqrt{2}$ is satisfied by the global flow parameters. The data points shown in this figure are the conditions for various simulations conducted for the study.

This condition for the formation of TCLV is independent of the Prandtl number, Pr. Nevertheless, three values of Pr, 0.025, 0.1 and 0.7, are considered for the simulations to verify this observation. It was found that irrespective of the value of Pr if $Ro = Re\,E \simeq C/\Gamma$ then tropical cyclone-like vortex is formed in the domain

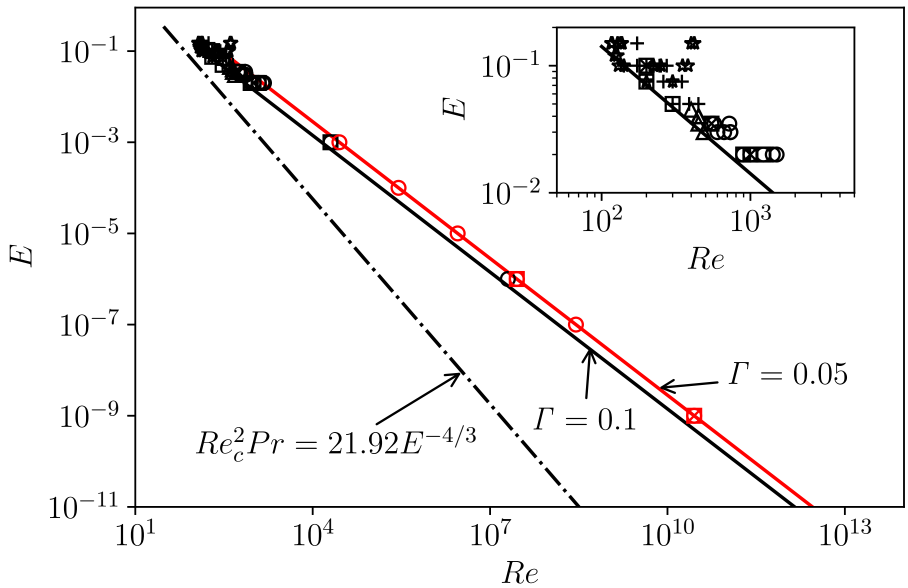

Fig. 5.2 Condition for observing a tropical cyclone-like vortex in a domain of aspect ratio Γ rotating at Ω. The dash-dotted line is the bulk convection onset condition (Chandrasekhar, 1961, Aurnou et al., 2018) for $Pr = 0.1$ and the 55 data denote conditions of simulations displaying fully evolved tropical Cyclone-like vortex structure shown in Fig. 4.1. The symbols denote $*$ - axisymmetric cases in (Oruba et al., 2017, 2018, Atkinson et al., 2019), $+$ - 3D laminar, $\triangle$ - transition, and $\circ$ - turbulent cases having $Pr = 0.1$ and cases with $Pr = 0.7$ and 0.025 are denoted using $\square$ and $\times$ respectively.

with less than 10% variation in its spatial features like, size of the vortex and width of eyewall. In total, 54 simulations covering laminar, transient, and turbulent regimes are performed and each of these cases shows a TCLV in the computational domain and are detailed in Table A.1 of Appendix A. These various simulations are marked in the Re–E space shown in Fig. 5.2. Four cases from a total of 54 simulations are listed in Table 5.1. These cases are typical examples for presenting and discussing results in the remainder of the thesis. These cases cover laminar, transition and turbulent flow regimes.

Case	Re	E	Γ	V/V_ℓ
1	224	0.1	0.1	1.0
2	1000	0.02	0.1	4.46
3	2.82×10^{7}	10^{-6}	0.05	633.92
4	2.82×10^{10}	10^{-9}	0.05	633.92

Table 5.1 Cases with $Pr = 0.1$ showing tropical cyclone-like vortex.

It is worth noting that past studies (Bodenschatz et al., 2000, Ahlers et al., 2009, Horn & Schmid, 2017, Kunnen et al., 2010, Aurnou et al., 2018) predominantly focussed on the flow stability. Also, the values of Re and E used in studies showing LSV (Guervilly et al., 2014, Favier et al., 2014, Couston et al., 2020, Guzmán et al., 2020) do not satisfy the condition $ReE \simeq C/\Gamma$. Furthermore, in those studies, $\Gamma \geq 0.25$ are atypical of tropical cyclones or hurricanes. LESs are performed to verify the above condition for the formation of tropical Cyclone-like vortex showing structures in Fig. 4.1 surviving for several tens of rotation time. This domain-filling vortex is called a fully evolved tropical Cyclone-like vortex. This is assessed by monitoring the temporal evolution of volume-averaged kinetic energy.

5.2 Results & Discussion

5.2.1 Flow Structure of Tropical Cyclone-like Vortex

Figure 5.3 shows the azimuthal-mean spatial structure of the tropical cyclone-like vortex at $\tau = 100$ for Case 2 in Table 5.1 when the tropical cyclone-like vortex is fully evolved. The velocities are non-dimensionalised with ΩH, the temperature perturbation, $\langle \theta^* \rangle$, is non-dimensionalised with βH and the azimuthal vorticity, $\langle \omega_\varphi^* \rangle$ is normalised with Ω. The hot temperature compared to background temperature $T_o(z)$ ($\theta > 0$) is concentrated towards the centre of the domain and the temperature decreases radially away from the centre to towards the sidewall. The uniform radial gradient of temperature seen from the centre to the sidewall at all heights ensures a single poloidal flow in the whole domain by enhancing the radial inflow ($\langle u_r^* \rangle < 0$) near the bottom and outflow ($\langle u_r^* \rangle > 0$) near the top. This further ensures transport of angular momentum towards the centre and a cyclonic flow near the centre of the domain ($\langle u_\varphi^* \rangle > 0$). The cyclonic flow extends throughout the height of the domain in the bulk of the domain, while anticyclonic flow ($\langle u_\varphi^* \rangle < 0$) occupies at outer radii. The Ekman layer ($\langle \omega_\varphi^* \rangle < 0$) formed at the bottom surface in the domain is seen to be swept up to form the eyewall (Oruba et al., 2017) separating the strong poloidal region ($\langle \omega_\varphi^* \rangle > 0$) from the eye formed at the core of the domain. The qualitative similarity of the symmetric tropical cyclone-like vortex structure with that of an actual tropical cyclone is discussed in detail next. The spatial features for azimuthal mean quantities shown in Fig. 5.3 are similar for other cases in Table 5.1.

The contours of $u_\varphi^* = \widetilde{\langle u_\varphi \rangle}/V_\ell$, with $\widetilde{\langle \cdot \rangle}$ denoting the azimuthal and time-averaging noted earlier, plotted in Fig. 5.4 shows the tropical Cyclone-like vortex, the eyewall

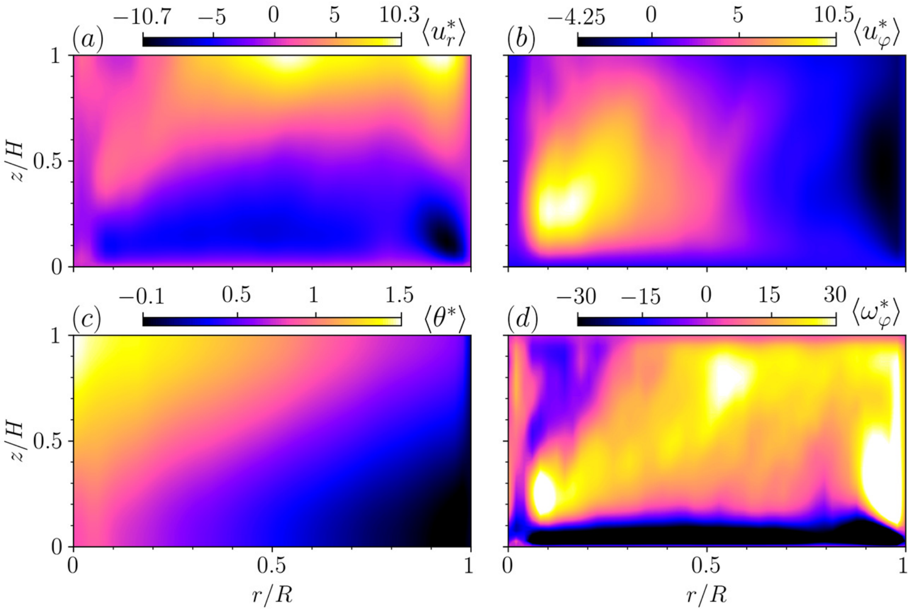

Fig. 5.3 Azimuthal averaged contours of (a) Radial velocity $\langle u_r^* \rangle$ normalised with (ΩH), (b) Azimuthal velocity $\langle u_\varphi^* \rangle$ normalised with (ΩH), (c) Temperature perturbation $\langle \theta^* \rangle$ normalised with (βH), and (d) Azimuthal vorticity $\langle \omega_\varphi^* \rangle$ normalised with background rotation Ω at $\tau = 1.2$ for case 2 in Table 5.1.

and isoline of $u_\varphi^* = 0$. V_ℓ denotes the buoyancy velocity computed for the laminar case 1 in Table 5.1. The intense swirl is in the inner quarter of the domain, and the peak u_φ^* in case 4 is nearly 14 times larger compared to the laminar case. The isoline of $u_\varphi^* = 0$ separates regions with cyclonic and anticyclonic rotations, and the size of the anticyclonic region varies with z/H and Re. Although the effects of moisture are excluded here, this variation shown in Fig. 5.4(c) for the largest Re is similar to that observed in field measurements of tropical cyclones, see Fig. 9 of (Frank, 1977). The inward shift of the eyewall with increased intensity is also seen using *in situ* observational data shown in Fig. 4 of Willoughby (Willoughby, 1990). The smaller and stronger eye at larger Re is due to stronger rotation effects arising from the constraint $Re\, E \sim C/\Gamma$ for tropical Cyclone-like vortex formation, leading to larger cyclonic vorticity. The PDF of the deviation of $\widetilde{\langle u_\varphi \rangle}$ from the gradient wind $\widetilde{V}_g$ defined by ζ around eye-eyewall region $(0 \leq r/R \leq 0.25)$ excluding the bottom Ekman layer for cases 1 (if one attempts to plot for laminar case), 2, and 1 are shown in Fig. 5.4(d). $\widetilde{V}_g$ is computed from the gradient wind balance approximation (see Eq. (2) of (Willoughby, 1990)) given by

$$\widetilde{V}_g = \frac{-2\Omega r + \sqrt{(4\Omega^2 r^2 + 4r\partial P/\partial r)}}{2} \tag{5.6}$$

The gradient wind balances the radial pressure gradient force, centrifugal, and Coriolis forces. Therefore, $\widetilde{V}_g$ solution in Eq. (5.6) is obtained by solving the gradient wind balance equation for velocity. Gradient wind balance ($\zeta \approx 0$) is seen predominantly in tropical Cyclone-like vortex since the peak of pdf is at zero for all the cases. This balance is observed in an actual tropical cyclone as well (Willoughby, 1990). ($\zeta \approx 0$) is seen around the eye-eyewall region, near $\widetilde{\langle u_\varphi \rangle}_{max}$. The spread in the pdf increases as Re increases because the tropical Cyclone-like vortex core region becomes narrower, and the flow deviates from gradient wind balance. The super-gradient flow ($\zeta > 0$) is seen in the eye-eyewall region above the location of $\widetilde{\langle u_\varphi \rangle}_{max}$. The sub-gradient flow ($\zeta < 0$) is seen at region away from the radius of maximum tangential velocity, r_{max}. Since, r_{max} becomes smaller at higher Re, the region of ($\zeta < 0$) increases thus larger spread with higher value of ζ is observed in the pdf.

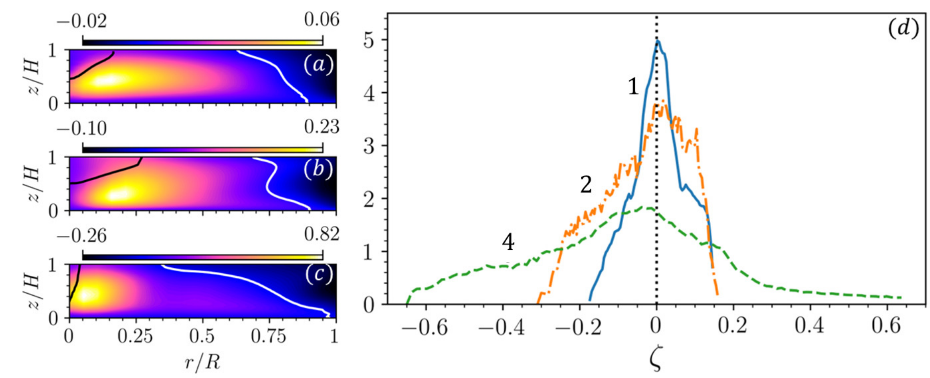

Fig. 5.4 Contours of $u^*_\varphi = \widetilde{\langle u_\varphi \rangle}/V_\ell$ for cases 1, 2 and 4 in Table 5.1 are shown in $(a)-(c)$. The black line is the outer surface of the eyewall and the white line is for $u^*_\varphi = 0$. The pdf of $\zeta = \frac{\widetilde{u}_\varphi - \widetilde{V}_g}{\widetilde{V}_g}$ within $(0 \le r/R \le 0.25)$ (excluding Ekman layer) is shown in (d) for cases 1, 2, and 4.

5.2.2 Timescale for Cyclogenesis

The strong poloidal flow is necessary for the formation of tropical cyclone-like vortex (see previous chapter Chapter 4). The formation of the large-scale poloidal circulation in the domain is known as Ekman pumping. The strength of the Ekman pumping mechanism is determined by a dimensionless flow parameter called the Ekman number. The Ekman number, E is defined as a ratio of viscous to Coriolis forces, and the small

Ekman numbers used in this study to observe tropical cyclone-like vortex indicate that the Coriolis forces which cause Ekman pumping dominate the spin-up of the fluids. Ekman pumping characteristically causes fluid to spin up over a period on the order of the Ekman time τ_E which is defined as $\tau_E \sim \Omega^{-1} E_t^{-0.5}$. Thus, it would be logical to non-dimensionalise the time with τ_E to see whether the tropical cyclone-like vortex is formed approximately within τ_E. In order to see that, the time evolution of volume-averaged kinetic energy $\langle K \rangle_v$, normalised by its maximum value in time $\langle K \rangle_v^{\max}$, is plotted in Fig. 5.5 for all the cases in Table 5.1. The time is scaled with the Ekman spin-up time (Greenspan & Howard, 1963) with an additional pre-multiplier $\Gamma/\sqrt{2}$ (found empirically from analysing all the simulation data) given by,

$$\tau_1 = \left(\frac{\Gamma}{\sqrt{2}}\right) t\Omega\sqrt{E_t}, \tag{5.7}$$

Here, E_t is the turbulent Ekman number defined based on the bottom Ekman boundary layer-averaged eddy viscosity $\langle \nu_t \rangle_{BL}$ computed from LES simulations for turbulent cases and based on ν for laminar cases. The pre-multiplier $\Gamma/\sqrt{2}$ in τ_1 is obtained by analysing the 54 tropical cyclone-like vortex simulation the current work. τ_1 denotes the time taken for the spinup of cyclonic vortex and to set up the Ekman layer in the whole domain for a fluid initially at rest. The flow saturates after τ_1 for all the cases. Thus, the tropical cyclone-like vortex is observed to be formed within the Ekman spinup time. The flow dynamics and spatial organisation happening within $0 < \tau_1 < 1$ help form a tropical Cyclone-like vortex. As we can see from Fig. 5.5, which shows the strength of the eye in the tropical Cyclone-like vortex by measuring the maximum downward velocity $u^*_{z,min}$ normalised by its absolute value of minimum in time within the LSV. The eye begins to form $u^*_{z,min} < 0$ at $\tau_1 = 0.9$ & 0.75 for cases 2 & 4 respectively. The energy in the domain is also increased by about $20 - 40$ % before reaching saturation during this time interval. Thus, the cyclogenesis process starts well before the spin-up time $\tau_1 = 1$. But it is still unclear when the cyclogenesis starts in this model for any given flow parameters as the subsidence and increase in energy happen at different τ_1 for different cases. Since there isn't any clear definition available for cyclogenesis, the start of cyclogenesis is defined here as the time when the subsidence starts to happen in the LSV to form a tropical Cyclone-like vortex, and the system's energy begins to rise due to the intensification of the tropical Cyclone-like vortex.

We propose a new timescale for the start of cyclogenesis, τ_c given by,

$$\tau_c = 2\sqrt{2}\Omega^{-1} Re_t^{0.5} \tag{5.8}$$

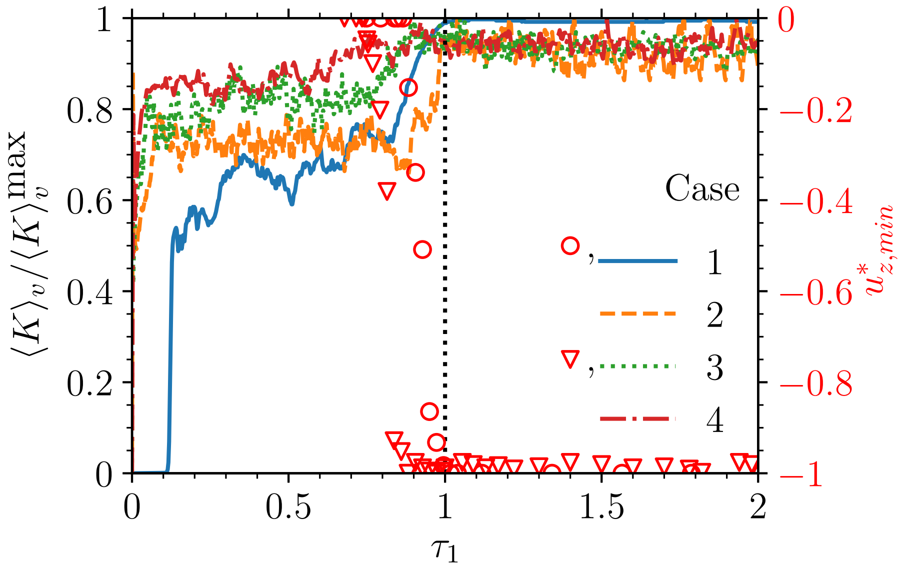

Fig. 5.5 Temporal evolution of $\langle K\rangle_v/\langle K\rangle_v^{\max}$ with τ_1. The scatter plot of $u^*_{z,\min}$ denote strength of subsidence along the centre of vortex axis.

where Re_t is the turbulent Reynolds number defined based on boundary layer- averaged eddy viscosity $\langle \nu_t\rangle_{BL}$ computed from LES simulations for turbulent cases and based on ν for laminar cases. The pre-multiplier $2\sqrt{2}$ in τ_c is obtained by analysing the 54 tropical cyclone-like vortex simulation of the current work. τ_c depends on both the convection and rotation, denoting the time at which the interaction of these two driving forces begins in the system, leading to tropical Cyclone-like vortex formation. This is time at which subsidence is seen in the large scale cyclonic vortex along with the sweeping up of bottom boundary layer resulting in the emergence of characteristic eye-eyewall to form tropical cyclone-like vortex. Figure 5.6 shows the time evolution of volume-averaged kinetic energy $\langle K\rangle_v$, normalised by its maximum value in time $\langle K\rangle_v^{\max}$ with time scaled with τ_c that is

$$\tau_2 = t\tau_c^{-1} \tag{5.9}$$

The cyclogenesis begins at around $\tau_2 = 1$ and the tropical Cyclone-like vortex eye strength increases till flow saturates at time $\tau_1 = 1$. Therefore, the cyclogenesis happens in the timespan $t = \tau_1 - \tau_2$ which is referred in this chapter & thesis as timescale of cyclogenesis.

In order to briefly describe what is meant by the timescale of cyclogenesis. The evolution of the eye within the large-scale cyclonic vortex into a tropical cyclone-like

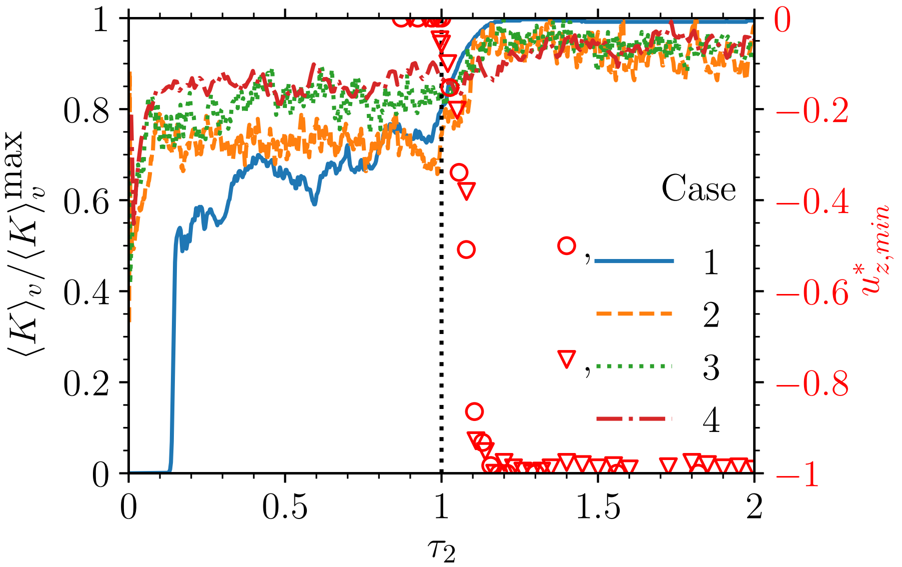

Fig. 5.6 Temporal evolution of $\langle K\rangle_v/\langle K\rangle_v^{\max}$ with τ_2. The scatter plot of $u^*_{z,\min}$ denote strength of subsidence along the centre of vortex axis.

vortex in a radial plane at $\varphi = 0°$ is shown in Fig. 5.7 for case 4 in Table 5.1. The region of the large magnitude of cyclonic vorticity ($\omega_z > 0$) is the core of the large-scale cyclonic vortex. At $\tau_2 = 0.8$, the cyclonic vortex is formed in the domain, but it is slightly off-centred. At $\tau_2 = 0.9$, the cyclonic vortex is approaching the centre of the domain and is still off-centred. During this time instant, it can be seen that the core of the vortex doesn't have any subsidence. This can be seen from the line contour of vertical velocity plotted in the same Fig. 5.7. The core of the cyclonic vortex has a net upward flow ($u_z > 0$). But it can be seen at $\tau_2 = 1.0$ that there is subsidence within the core of the cyclonic vortex (dashed contour lines denoting $u_z < 0$) spanning 50% of the domain. The subsidence seem to be increasing its strength at $\tau_2 > 1$ as seen from both Fig. 5.6 and Fig. 5.7 at $\tau = 1.1$ as the subsidence within the core seems to extend close to 60% of the domain from the top. It can also be seen that number of vertical rolls ($u_z > 0$) which are initially present in the bulk of domain reduces in time and during the start of cyclogenesis there are vertical rolls concentrated near the sidewall and finally only poloidal circulation is seen in the entire radial plane. Thus, the time $t = \tau_c \;/\; \tau_2 = 1$ denotes the time at which the eye begins to appear in the cyclonic vortex, and it starts evolving into a tropical cyclone-like vortex with all its intricate flow features (see Fig. 4.1). It is completely evolved at the Ekman spinup time $t \sim \tau_E/\; \tau_1 = 1$. Thus, the time interval $t = \tau_1 - \tau_2$ is referred to here as time scale of cyclogenesis.

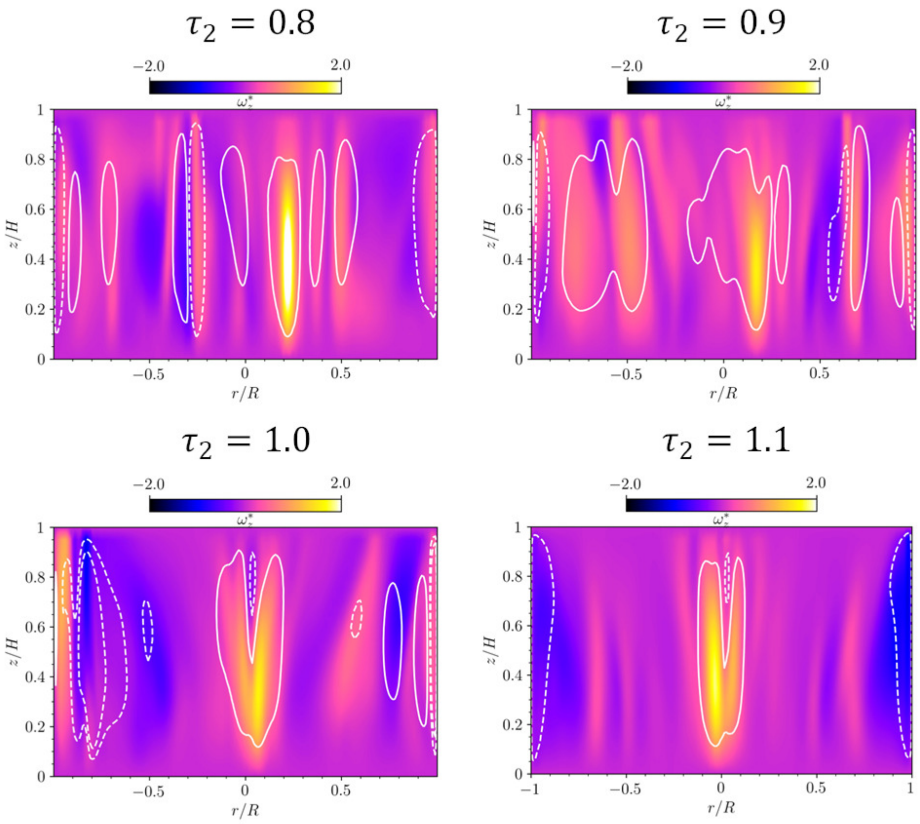

Fig. 5.7 The vertical cross-section of the azimuthal vorticity, ω_z^* normalised with Ω (colour) and the vertical velocity, $u_z^* = 0.1$ (solid line) and $u_z^* = -0.1$ (dashed line) normalised with ΩR at $\varphi = 0$ before and during cyclogenesis phase for case 2 in Table 5.1.

Thus, the global flow parameters dictate the formation of tropical Cyclone-like vortex in the domain, whereas the local flow dynamics and turbulence decide the spatial organization and start of cyclogenesis. The local flow dynamics leading to the formation of large scale tropical cyclone-like vortex in the domain are discussed in the subsequent chapters.

5.3 Implications to Actual Cyclogenesis

Research on tropical cyclogenesis has focused primarily on two aspects of the problem: the nature of the large-scale environments in which tropical cyclones form, and the hydrodynamic and thermodynamic routes taken by particular observed and/or numerically simulated cyclones as discussed in Chapter 1. Even several field campaigns have been conducted in the past to understand the cyclogenesis process such as

Tropical Experiments in Mexico (Bister & Emanuel, 1997, TEXMEX), Pre-Depression Investigation of Cloud Systems in the Tropics experiments (Montgomery et al., 2012, PREDICT) and NASA's Genesis and Rapid Intensification Processes field experiment (Braun et al., 2013, GRIP) and NOAA's Hurricane Intensity Forecasting Experiment (Rogers et al., 2013). Much has been learned, and many theories have been proposed, but a clear understanding of the cyclogenesis process remains elusive.

Empirical genesis indices have also been proposed in the recent past linking large-scale environment variables to the tropical cyclone formation. Emanuel & Nolan (2004) used the statistical fitting procedure of seasonal and spatial variation of climate data during cyclogenesis to come up with Genesis Potential index (GPI), which is a non-dimensional number defined based on relative humidity (RH), potential intensity (PI), absolute vorticity (ω_{abs}), and vertical wind shear (V_{shear}) between the heights 850 and 200 hPa. This GP index was formulated from several environmental variables that are known to be associated with tropical cyclone formation (Gray, 1968, 1979).

$$GPI = |10^5\omega_{\text{abs}}|^{3/2}\left(\frac{RH}{50}\right)^3\left(\frac{PI}{70}\right)^3(1+0.1V_{\text{shear}})^{-2} \tag{5.10}$$

This index has been used to investigate hurricane formation in global warming conditions (Nolan et al., 2006) and to access cyclogenesis in global climate models (Camargo et al., 2007a,b, Murakami & Wang, 2010). Emanuel (2010) suggested that the genesis index should not depend directly on relative humidity but rather on the mid-level saturation deficit. The revised index replacing the GPI proposed by Emanuel & Nolan (2004) comprises of absolute vorticity, potential intensity, shear, and a measure of the moist entropy deficit of the middle troposphere (χ).

$$GPI = |\omega_{\text{abs}}|^3\chi^{-4/3}\max[(PI-35),0]^2(25+V_{\text{shear}})^{-4} \tag{5.11}$$

The primary focus of this work is on understanding cyclogenesis in a simple Rotating Rayleigh-Benard Convection (RRBC) setup without any additional complexities arising from the stratification or thermodynamic effects. In this section, the simple hydrodynamic cyclogenesis condition obtained this chapter (without considering the effects of moisture as in previous works) is tested for an actual tropical cyclone. The purpose of this exploration is to test the extent of validity of the results (considering only the hydrodynamic effects in the model) presented in this thesis to the actual cyclone arising in tropical region. We hope that this emphasises the relevance and importance of the results based on hydrodynamics presented in this thesis to a real scenario and motivates further research in this direction.

5.3.1 Cyclogenesis Conditions

In this section, we will revisit the cyclogenesis conditions formulated from RRBC simulation of tropical cyclone-like vortex. It was shown in previous chapter 4 empirically that when

$$Ro\Gamma = \frac{V}{V_{rot}} \approx \mathcal{O}(1) \tag{5.12}$$

there will be strong poloidal flow in the domain leading to the formation of tropical Cyclone-like vortex, where Ro is the convective Rossby number, V is the buoyancy velocity, $V_{rot} = \Omega R$ is the rotational velocity, and $\Gamma = H/R$ is the aspect ratio.

It is also shown in this chapter from analysing the simulation data that two timescales namely,

$$\tau_E \approx \frac{\sqrt{2}}{\Gamma\Omega\sqrt{E_t}}; \tau_c \approx \frac{2\sqrt{2}\sqrt{Re_t}}{\Omega}$$

govern the dynamics of tropical Cyclone-like vortex in RRBC framework. The spin up timescale of the fluid is τ_E (multiplied with the pre-multiplier found from analysing the computational results) (Greenspan & Howard, 1963), τ_c is the timescale for the start of cyclogenesis spinup in a cyclonic vortex, Re_t and E_t are the turbulent Reynolds and Ekman number respectively defined based on the bottom Ekman boundary layer-averaged turbulent viscosity and Ω is the background rotation rate. The cyclogenesis should occur before the spin up time of the fluid which gives an additional constraint for tropical Cyclone-like vortex formation, that is,

$$\tau_c < \tau_E \Rightarrow 2\sqrt{\Gamma}\sqrt{Ro\Gamma} < 1 \tag{5.13}$$

Equations (5.12) and (5.13) when satisfied simultaneously gives the hydrodynamic condition for the formation of tropical Cyclone-like vortex in a simple RRBC setup. It will be interesting to see whether this conditions can be leveraged to predict the genesis of an actual tropical cyclone using the field data as explained next.

5.3.2 Data and Methods

Data

The Joint Typhoon Warning Center (JTWC) provides tactical tropical cyclone (TC) forecasts for U.S. Department of Defence installations operating in the North western Pacific, Indian, and South Pacific Oceans. These forecasts include position, intensity (maximum wind/tangential velocity), and the radii of maximum wind, 34, 50, and 64 kt (1 kt = 0.514 ms^{-1}) winds through 5 days. The data from JTWC (available at JTWC storm track database) will be used in the current work to test the cyclogenesis condition proposed above.

JTWC's historical best tracks provide quality controlled 6-hourly position, intensity, and the radii information for each TC tracked by JTWC. These data are in the Automated Tropical Cyclone Forecast system (ATCF) format. Due to issues such as latency of real-time data and operational security considerations, "working" best track data may contain biases, whereas the "final" best tracks have been reanalysed by JTWC following the season using all available data and current operational practices. Both working and final best tracks use units of knots and nautical miles (1 nmi $\approx$ 1.85 km) for intensity and distance, respectively, and the final best track data are used for the analysis discussed below.

Method

From the storm track data following quantities are obtained to see whether Eq. (5.12) and (5.13) holds good.

- Aspect ratio - Γ
  The aspect ratio defined as ratio of height (H) to that of radius (R) of the tropical cyclone system. Height H is the height of the tropopause from the sea surface which is approximately 10 km. Here it is assumed that the tropical cyclone system extends up to tropopause throughout its evolution. The radius R is taken to be the radius of outermost closed isobar (ROCI) to estimate the size of the tropical cyclone as proposed by Merrill (1983). The ROCI changes as the tropical cyclone evolves.

- Buoyancy velocity - V
  The buoyancy velocity V is defined as, $V = \sqrt{\alpha g(T_{sea} - T_{trop.})H}$ where $\alpha = 3.3 \times 10^{-3}$ K^{-1} is the volumetric thermal expansion coefficient of air, $g = 9.81$ m/s^2 is the acceleration due to gravity. In order to calculate V, the temperature at the sea surface, T_{sea}, and near tropopause, $T_{trop.}$ is required as it is defined based on the temperature difference between top and bottom surface of tropical cyclone. Since the top surface is assumed to be tropopause the temperature of air at tropopause ($T_{trop.} = -51°C$) can be used as temperature at the top surface (Lydolph, 1985). The sea surface temperature should be at least $26.5°C$ spanning through at minimum a 50-metre depth and is one of the precursors

needed to maintain a tropical cyclone (Webster et al., 2005). In order to obtain the maximum buoyancy velocity, the maximum sea surface temperature will be obtained from the minimum sea-level pressure data, P_{sea}, available in JTWC tropical cyclone track database as shown below (WMO, 2018),

$$T_{sea} = T_{atm} \left(\frac{P_{atm}}{P_{sea}} \right)^{-\gamma R/g}$$

Here $T_{atm} = 15°C$ and $P_{atm} = 1.01$ bar are the atmospheric temperature and pressure data. $R = 287$ J/kg/K is the specific gas constant and $\gamma = -6.5 \times 10^{-3}$ K/m is the temperature lapse rate in troposphere defined as the rate of decrease of temperature with height (Lydolph, 1985).

The buoyancy velocity formulation is used here to compute the convective velocity from storm track data. It is because convective velocity depends more on thermal buoyancy in moist convection when the raindrop terminal velocity is large (Parodi & Emanuel, 2009). Since tropical cyclone accompanies heavy rainfall with large raindrop terminal velocity (Anthes, 2016), the buoyancy scaling is used here to compute the convective updraft velocity.

- Rotational velocity - V_{rot}
  The maximum wind speed/potential intensity recorded by JTWC track data is used here as the maximum rotational velocity in the current study. This usually occurs near the eyewall at the centre of the tropical cyclone during the cyclogenesis phase.

5.3.3 Analysis

Figure 5.8 shows the time evolution of terms in Eqs. (5.12) and (5.13) obtained using JTWC data over the life of an actual cyclone. The maximum values of $Ro\Gamma$ in Eq. (5.12) for the cyclones denoted by $(Ro\Gamma)_m$ obtained from maximum buoyancy velocity estimated as above and the observed maximum wind speeds are plotted in Fig. 5.8 along with τ_c/τ_E. It is to be noted that the hydrodynamic condition proposed in this work holds good for other tropical cyclones as well that are not shown in Fig. 5.8. Around 50 tropical cyclone track data from 2002 to 2022 have been analysed from JTWC database to verify the cyclogenesis condition. For the sake of brevity the three latest tropical cyclone are shown in this chapter covering two different oceans (Pacific and Indian Ocean), two hemisphere (North and South Hemisphere) and 3 categories

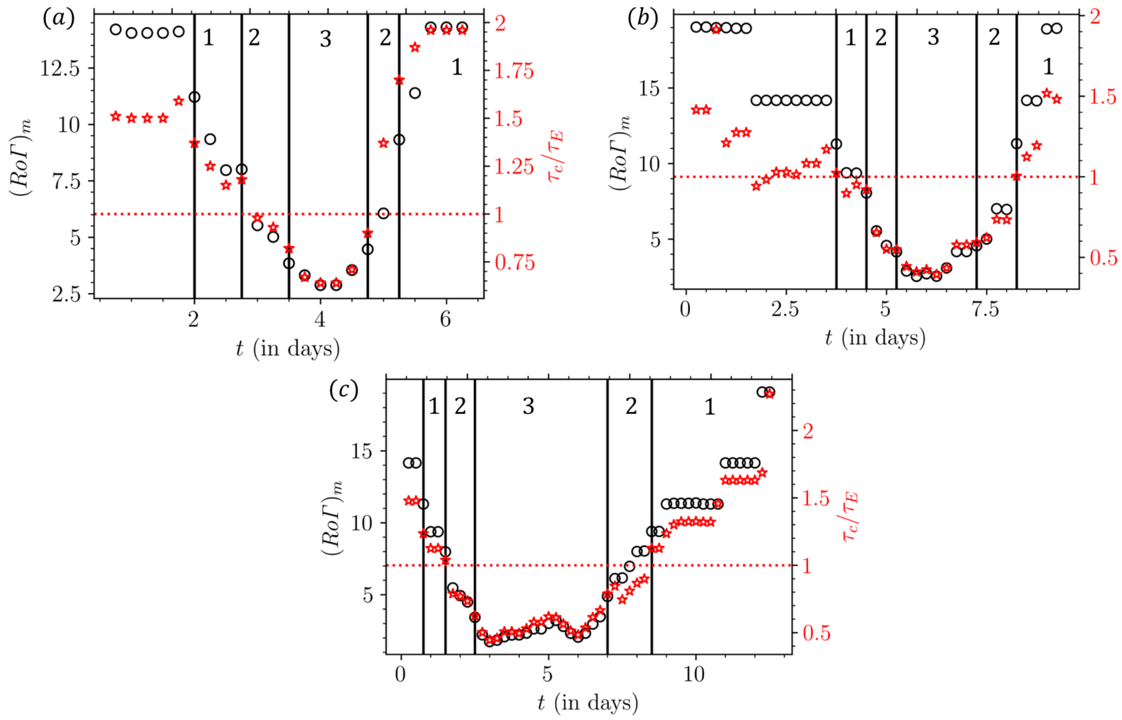

Fig. 5.8 The evolution of the quantities $(Ro\Gamma)_m$ (denoted by $\circ$) and τ_c/τ_E (denoted by $\star$) obtained from Eqs. (5.12) and (5.13) respectively for three different tropical cyclone system. The data is obtained from the JTWC storm track database available at https://www.metoc.navy.mil/jtwc/jtwc.html?best-tracks.
(a): Data from Category 2 tropical cyclone Hikaa that struck eastern Oman (Indian Ocean) in September 2019. The maximum wind speed is 46.4 m/s.
(b): Data from Category 3 tropical cyclone Vongfong that struck Philippines (Pacific Ocean) in May 2020. The maximum wind speed is 51.5 m/s.
(c): Data from Category 5 tropical cyclone Veronica that struck Western Australia (Pacific Ocean) in March 2019. The maximum wind speed is 67 m/s.
1 - Tropical Depression; 2 - Tropical Storm ; 3 - Tropical Cyclone.

of tropical cyclone (Category 2, 3 and 5 as defined in Saffir-Simpson hurricane wind scale) to show the robustness of the obtained condition.

It is seen from Fig. 5.8(a)-5.8(c) that the cyclogenesis condition holds good in the real tropical cyclone context. The cyclogenesis is said to have commenced when the tropical depression (denoted by the vertical line marked as 1) changes to a tropical storm (indicated by 2). As specified in the section 1.1, the difference between a tropical storm and a tropical cyclone (denoted by 3) is the change in the intensity of the wind. Thus for cyclogenesis, it is important to understand when the depression changes to a tropical storm. The conditions specified in Eqs. (5.12) and (5.13) seem to capture this change well. It can be seen that for all the different tropical cyclone data shown in Fig. 5.8, both the condition holds good simultaneously only in stage 2 & 3, which confirms that the conditions obtained from hydrodynamic analysis in a simple RRBC setup holds good for an actual tropical cyclones evolving in nature without any approximations.

5.4 Summary

The global flow parameters dictating the formation of tropical Cyclone-like vortex in the domain through the condition $ReE = Ro \simeq C/\Gamma$ is tested for several orders of magnitude by carrying out turbulent RRBC simulation with the LES framework. When the condition is met, the tropical Cyclone-like vortex is formed in the domain for all values of flow parameters. The spatial structure of the simulated tropical Cyclone-like vortex is qualitatively similar to that of the actual tropical cyclone. The eyewall formed was found to be shifting closer to the vortex core as the Re of the flow this compliments the observation made by Willoughby (1990) for a real tropical cyclone. Also, the gradient wind balance seen around the core by Willoughby (1990) for an actual tropical cyclone was found to be obeying for the simulated tropical cyclone-like vortex across the simulated range of flow parameters. In addition, it was found that this balance is violated with super-gradient flow observed near eye-eyewall region and sub-gradient flow outside vortex core.

By analysing the simulation data it was found that two time scales control the dynamics of the formation of like vortex in the RRBC framework. The fully evolved tropical cyclone-like vortex was found to be formed in the domain at Ekman spinup time $t \sim \tau_E$. In addition, the timescale for the start of cyclogenesis, τ_c, was found through the data analysis. The τ_c was found to be directly proportional to $\sqrt{Re}$. The τ_c is defined as the time at which eye/subsidence begins to form in the cyclonic-vortex.

The cyclogenesis happens for a timespan of about $\tau_E - \tau_c$ and hence, τ_c should be less than τ_E to see the birth of tropical cyclone-like vortex from a persisting depression in the domain.

The condition namely, (i) $ReE = Ro \simeq C/\Gamma$ and (ii) $\tau_c < \tau_E$ obtained from the RRBC simulations of tropical cyclone vortex is tested using actual tropical cyclone track data to see whether the conditions obtained in this chapter hold good in reality. The results agree well. Thus, the analysis in this chapter suggests that cyclogenesis is driven by hydrodynamics, at least in the simple model considered here and the thermodynamics process help to intensify the tropical cyclone-like vortex further. The cyclogenesis condition proposed in this work relates the major environmental parameters to cyclone formation. It reduces them to a single parameter that can provide a valuable way of assessing cyclone changes from large-scale analyses or model simulations. The motivation for establishing a simple parametric relationship is that it can be applied to climate model output to forecast cyclones and assess potential cyclone changes associated with varying and changing future climates. In the next couple of chapters, the energetics of fully evolved tropical cyclone-like vortex, asymmetric structures of the tropical cyclone-like vortex are compared qualitatively with real tropical cyclones, the local flow dynamics leading to the formation of LSV at the start of cyclogenesis and the subsequent energy transfer mechanism happening during the cyclogenesis will be discussed.

Chapter 6

Asymmetries & Energetics in Tropical Cyclone-like Vortex

The presence of azimuthal asymmetries during the evolution of tropical cyclone has been observed in radar measurements (Marks et al., 1992), satellite remote sensing (Chen et al., 2006), and three dimensional high-resolution simulations (Anthes, 1972). Although these asymmetries are seen over the entire life cycle of these cyclones they become notable during the intensification or weakening, involving significant changes in the structure and intensity, of the cyclone. Hence, the growth and decay of the asymmetries were investigated in detail in past studies (Montgomery & Davis, 2004, Montgomery et al., 2006). These studies found that the presence of asymmetries helps in strengthening the vortex, and their absence lead to the weakening of the vortex. Despite these studies, the mechanism through which these asymmetries influence the cyclone intensity is unclear since the asymmetries can arise from both external and internal processes. External asymmetries arise when the cyclonic vortex responds to changes in the external flow field like wind shear or landfall and these asymmetries lead to reorganisation of the convection and flow fields (Jones, 1995, Frank & Ritchie, 2001). On the other hand, the internal vortex dynamics can produce asymmetries such as vortical hot towers (Montgomery & Davis, 2004, Gopalakrishnan et al., 2011) and rainbands (Willoughby et al., 1984, Didlake & Houze, 2013). These asymmetries are commonly attributed to barotropic, baroclinic, and convective instabilities (Willoughby et al., 1984, Schubert et al., 1999, Kossin et al., 2000, Kossin & Schubert, 2001) and, they contribute to a major portion of upward mass transport in the vortex near the eyewall (Braun, 2002). Also, the gradient associated with the asymmetric distributions of quantities like vorticity, energy and momentum results in wave asymmetries and asymmetric fluxes, which helps in the redistribution of these quantities (Willoughby, 1977, Montgomery & Kallenbach, 1997, Hendricks et al., 2010, Moon & Nolan, 2010).

The asymmetries could increase the magnitude of azimuthal velocity in the cyclone through vortex axisymmetrisation which produces a state of circular flow in the vortex, i.e., cyclone (Melander et al., 1987, Montgomery & Kallenbach, 1997). A series of studies have studied this axisymmetrisation process and the role of asymmetries in strengthening the azimuthal velocity during tropical cyclogenesis in a barotropic asymmetric balance model (Möller & Montgomery, 1999), a three-dimensional quasigeostrophic model (Montgomery & Enagonio, 1998), a 3D asymmetric balance model (Möller & Montgomery, 2000), and a shallow-water model (Enagonio & Montgomery, 2001).

By using NASA's Doppler radar data, Heymsfield et al. (2001) tried to characterise the asymmetric structure of intense convection in hurricane Bonnie(1998) and suggested that the asymmetries might have played an important role in the storm intensification. On the other hand, past numerical studies suggest that the external asymmetries could reduce the cyclone intensity. Peng et al. (1999) and Frank & Ritchie (1999, 2001) investigated the intensity change due to large-scale environmental influences such as the wind direction, boundary layer friction, vertical wind shear, planetary vorticity gradient (beta gyre or effect) using mesoscale modelling code and showed that cyclone was weakened when one of these influences was present. However, the weakening was hypothesised to occur because of asymmetries of the eyewall region leading to an increase in centre pressure since the wind shear ventilated the eye. The beta gyre produced asymmetric circulation by distorting the vortex and this asymmetry could either co-act or oppose the asymmetry induced by the wind direction. The westerly wind was suggested to be more favourable for the cyclone intensification compared to easterly wind of the same speed (Peng et al., 1999). These studies suggested that the asymmetries had the maximum amplitudes around the radius of maximum wind and hence the weakening might be associated with the asymmetric circulation. This is consistent with the notion that intense cyclones tend to be relatively symmetric whereas less severe storms have their convection organised in asymmetric spiral bands (Willoughby et al., 1984), also known as internal asymmetries. Thus, it is important to understand the role of these asymmetries in tropical cyclone evolution. Hence, the aim of this chapter is to shed light on the role of the internal asymmetries in the formation of tropical cyclone-like vortex in a rotating Rayleigh-Benard convection (RRBC) of a Boussinesq fluid in a three-dimensional domain. The axisymmetric version of this simple model has been used in the past to study the formation of eye and eyewall (Oruba et al., 2017, 2018, Atkinson et al., 2019) and also for three-dimensional laminar flows (see chapter 4). This study relies on the hydrodynamic perspective without additional complexities arising from stratification, latent heat release from moist convection, air-sea thermodynamic disequilibrium, wind-induced surface heat exchange effects, boundary layer thermodynamics and beta gyres present in actual cyclones. Hence, the specific objectives for this chapter are:

1. To analyse the numerical data of tropical cyclone-like vortex studied from chapter 4 & 5 to extract the characteristics of internal asymmetries, specifically spiral bands, and to compare them with field observations.

2. To conduct energy budget analysis to study the contributions of axisymmetric and asymmetric processes to the cyclogenesis from an energetic viewpoint. Since there are no external processes such as wind, shear and beta effects are not considered here, there are only internal asymmetries, which is the focus, of this chapter.

The remainder of this chapter is organised as follows. The energy budget equations for symmetric and asymmetric fields are discussed in subsection 6.1 highlighting the important energy exchange terms and these equations for a RRBC model are derived in Appendix B. Results are presented and discussed in section 6.2 and the results are summarised in the final section of this chapter.

6.1 Energy Budget Equations

The kinetic energy $K = 1/2\left(u_r^2 + u_\varphi^2 + u_z^2\right)$ and potential energy $A = 1/2\,(\alpha g \theta / N)^2$ per unit mass can be split into two components namely the symmetric/azimuthal mean denoted by $\langle(\cdots)\rangle$ and asymmetric part denoted by $(\cdots)'$. The four energy equations in cylindrical coordinates can derived from Eqs. (5.2) and (5.3), namely an azimuthal mean kinetic energy $\langle K\rangle = 1/2\,(\langle u_r\rangle^2 + \langle u_\varphi\rangle^2 + \langle u_z\rangle^2)$ equation [Eq. (6.1)], an asymmetric kinetic energy $K' = 1/2\left({u'_r}^2 + {u'_\varphi}^2 + {u'_z}^2\right)$ equation [Eq. (6.2)], an azimuthal mean potential energy $\langle A\rangle = 1/2\,(\alpha g \langle\theta\rangle / N)^2$ equation [Eq. (6.3)], and an asymmetric potential energy $A' = 1/2\,(\alpha g \theta' / N)^2$ equation [Eq. (6.4)], N is the buoyancy frequency defined as $\sqrt{\alpha g \beta}$.

$$\underbrace{\frac{\partial \langle K \rangle}{\partial t}}_{T_{\langle K \rangle}} + \frac{1}{r}\frac{\partial}{\partial r}\left[r\left(\langle u_r\rangle\langle K\rangle + \langle u_r\rangle\langle u_r' u_r'\rangle + \langle u_\varphi\rangle\langle u_r' u_\varphi'\rangle + \langle u_z\rangle\langle u_r' u_z'\rangle\right)\right]$$
$$+ \frac{\partial}{\partial z}\left(\langle u_z\rangle\langle K\rangle + \langle u_r\rangle\langle u_r' u_z'\rangle + \langle u_\varphi\rangle\langle u_\varphi' u_r'\rangle + \langle u_z\rangle\langle u_r' u_z'\rangle\right)$$
$$- C_K = \underbrace{-\langle u_r\rangle\frac{\partial \langle P/\rho_o\rangle}{\partial r} - \langle u_z\rangle\frac{\partial \langle P/\rho_o\rangle}{\partial z}}_{P_{\langle K \rangle}} - C_M + D_{\langle K \rangle} \quad (6.1)$$

$$\underbrace{\frac{\partial \langle K' \rangle}{\partial t}}_{T_{K'}} + \underbrace{\frac{\partial}{\partial r}\left(\langle u_r\rangle\langle K'\rangle + \langle u_r' K'\rangle\right) + \frac{\partial}{\partial z}\left(\langle u_z\rangle\langle K'\rangle + \langle u_z' K'\rangle\right)}_{A_{K'}}$$
$$+ C_K = \underbrace{-\left\langle u_r'\frac{\partial P'}{\rho_o \partial r}\right\rangle - \left\langle u_z'\frac{\partial P'}{\rho_o \partial z}\right\rangle}_{P_{K'}} - C_P + D_{K'} \quad (6.2)$$

$$\underbrace{\frac{\partial \langle A \rangle}{\partial t}}_{T_{\langle A \rangle}} + \underbrace{\frac{1}{r}\frac{\partial}{\partial r}\left\{r\left[\langle A\rangle\langle u_r\rangle + \left(\frac{\alpha g}{\beta}\right)\langle\theta\rangle\langle u_r'\theta'\rangle\right]\right\} + \frac{\partial}{\partial z}\left\{r\left[\langle A\rangle\langle u_z\rangle + \left(\frac{\alpha g}{\beta}\right)\langle\theta\rangle\langle u_z'\theta'\rangle\right]\right\}}_{A_{\langle A \rangle}}$$
$$- C_A = C_M + D_{\langle A \rangle} \quad (6.3)$$

$$\underbrace{\frac{\partial \langle A' \rangle}{\partial t}}_{T_{A'}} + \underbrace{\frac{1}{r}\frac{\partial}{\partial r}\left(r\langle A u_r\rangle\right) + \frac{\partial}{\partial z}\left(\langle A' u_z\rangle\right)}_{A_{A'}} + C_A = C_P + D_{A'} \quad (6.4)$$

The energy exchange terms C_K, C_A, C_M, C_P are explained in detail in the next section.

6.1.1 Energy Exchange Terms

These exchanges of energy between azimuthally symmetric flows and asymmetries and between the potential and kinetic energies are commonly quantified in the manner originally suggested by Lorenz (1967) in which the flow is partitioned between symmetric (azimuthally averaged) components and departures therefrom ("asymmetries"), with four main energy reservoirs ($\langle A\rangle$, A',$\langle K\rangle$, K',) representing respectively the asymmetric and symmetric potential energy and the corresponding kinetic energies. From considerations of the energy conservation equations (see Eq. (6.1) $--$ (6.4)), expressions can be defined to represent the rates of exchange between the four energy reservoirs (James, 1995). The common terms present in Eqs. (6.1) - (6.4) denotes the energy exchange between the four different energies decomposed in the previous section. In this section, the significance of these energy exchange terms is highlighted.

$C_K - \langle K \rangle \longleftrightarrow K'$

The common terms on the Eq. (6.2) and Eq. (6.2) represent an energy exchange between $\langle K \rangle$ and K'. The term will be positive when energy exchange takes place from K' to $\langle K \rangle$, the energy exchange term can be written as

$$C_K = \Bigg[r \langle u'_r u'_\varphi \rangle \frac{\partial}{\partial r} \left(\frac{\langle u_\varphi \rangle}{r} \right) + \langle u'_r u'_z \rangle \frac{\partial \langle u_r \rangle}{\partial z} + \langle u'_\varphi u'_z \rangle \frac{\partial \langle u_\varphi \rangle}{\partial z} + \langle u'_r u'_r \rangle \frac{\partial \langle u_r \rangle}{\partial r} + \frac{\langle u_r \rangle}{r} \langle u'_\varphi u'_\varphi \rangle + \langle u'_r u'_z \rangle \frac{\partial \langle u_z \rangle}{\partial r} + \langle u'_z u'_z \rangle \frac{\partial \langle u_z \rangle}{\partial z} \Bigg]$$

The exchange invokes the covariance between the azimuthally averaged flows and the asymmetric convergence of momentum (cf. Eq. 6.1). In the kinetic energy budget formulation, this transaction between the mean and asymmetries feature as a production term (for e.g., see chapter 5 of Stull (2012)).

$C_A - \langle A \rangle \longleftrightarrow A'$

This term represents an energy exchange between $\langle A \rangle$ and A', and a positive value is defined as an energy exchange from $\langle A \rangle$ to A'. This is the common term with opposite signs in the azimuthally averaged $\langle A \rangle$ equation [Eq. (6.3)] and the A' equation [Eq. (6.4)].

$$C_A = \left[\left(\frac{\alpha g}{\beta} \right) \langle u'_r \theta' \rangle \frac{\partial \langle \theta \rangle}{\partial r} - \left(\frac{\alpha g}{\beta} \right) \langle u'_z \theta' \rangle \frac{\partial \langle \theta \rangle}{\partial z} \right]$$

The term consists of a radial (or axial) asymmetric heat flux with respect to the radial (or vertical) gradient of azimuthal mean temperature field. The exchange term is described by the covariance of asymmetric fluxes with respect to the gradient of azimuthal mean temperature fields. It is to be noted here that the sign of this term is determined by the product of a velocity asymmetry (u'_r or u'_z) with a thermal asymmetry (θ') and the gradient of mean temperature.

$C_M - \langle K \rangle \longleftrightarrow \langle A \rangle$ & $C_P - K' \longleftrightarrow A'$

An energy exchange term C_M between $\langle K \rangle$ and $\langle A \rangle$ and an energy exchange term C_P between K' and A' are the common terms with opposite signs in Eq. (6.1) and Eq. (6.3), and Eq. (6.2) and Eq. (6.4), respectively.

$$C_M = \alpha g \langle u_z \rangle \langle \theta \rangle, \quad C_P = \alpha g \langle u_z' \theta' \rangle$$

The sign of both terms are defined as being positive when potential energy is converted to kinetic energy. Both the terms are computed as a covariance between verical velocity u_z and temperature perturbation θ. When warm air rises or cold air sinks, the common term becomes positive, which means the potential energy is exchanged to kinetic energy, and vice versa. Therefore, both terms represent the process of the energy conversion between potential energy and kinetic energy.

6.2 Results & Discussion

6.2.1 Symmetric Structure and Evolution

Figure 6.1 shows the time evolution of $\langle u_\varphi^* \rangle_{\text{max}} = \langle u_\varphi / \Omega H \rangle_{\text{max}}$ with angle brackets denotes the azimuthal averaging. This quantity is directly related to the intensity of the cyclone vortex and its spatial location denotes the approximate eyewall position which is denoted using $r_m^* = R_m/R$. The axisymmetricity, $\gamma_{u_\varphi}(r, z, t)$, of the tangential velocity is defined as (Miyamoto & Takemi, 2013)

$$\gamma_{u_\varphi} = \frac{\langle u_\varphi \rangle^2}{\langle u_\varphi \rangle^2 + \mathcal{A}} \tag{6.5}$$

where $\mathcal{A} = \int_0^{2\pi} {u_\varphi'}^2 d\varphi / 2\pi$. Hence, $\gamma_{u_\varphi} = 1$ implies that the tangential velocity is axisymmetric when $\mathcal{A} = 0$ and the level of asymmetry increases as $\gamma_{u_\varphi} \to 0$. The temporal variation of volume-averaged axisymmetricity, $\overline{\gamma_{u_\varphi}}$, is also shown in Fig. 6.1. The time is non-dimensionalised using cyclogenesis timescale $\tau_c = 2\sqrt{2}\sqrt{Re_t}/\Omega$, where $Re_t = VH/\overline{\nu_t}$ is the Reynolds number based on volume averaged eddy viscosity which is also time averaged. The factors $2\sqrt{2}$ are found empirically based on the 54 simulations conduced for this study as discussed in the chapter 5. The cyclogenesis timescale, τ_c, denotes the time at which the subsidence, eye and eyewall features begin to appear in the large-scale vortex which evolves into a stationary cyclonic vortex over the spin-up timescale, τ_E. During the cyclogenesis phase, the intensity or $\langle u_\varphi^* \rangle_{max}$ increases for

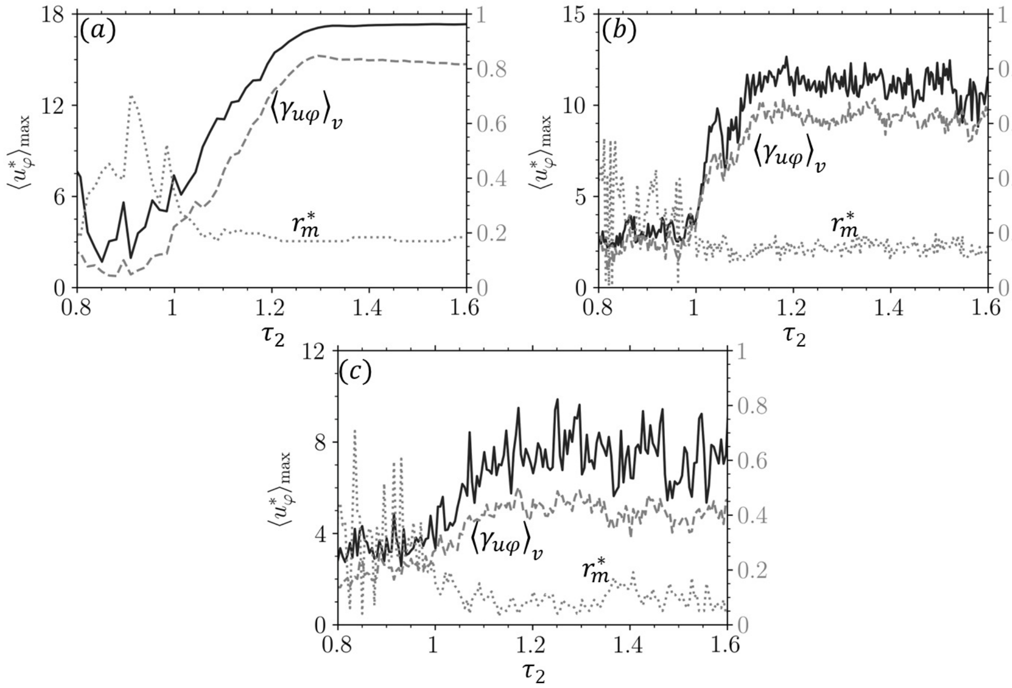

Fig. 6.1 Time evolution of maximum value of azimuthally averaged azimuthal velocity, $\langle u_\varphi^* \rangle_{max}$, the radial location of $\langle u_\varphi^* \rangle_{max}$, r_m^* and degree of axisymmetricity, $\overline{\gamma_{u_\varphi}}$ defined in Eq. (6.5) for (a) Case 1, (b) Case 2 and (c) Case 4 in Table 5.1.

all cases. During the cyclogenesis phase a single large poloidal flow is formed as shown in Fig. 5.1(b), and this tends to increase the angular momentum in the domain thereby increasing the intensity of the vortex. The $\langle u_\varphi^* \rangle_{max}$ increases nearly by 165% for the Case 1 in Table 5.1 and the increase is about 144% and 88% for Cases 2 and 4 respectively. This is because turbulent diffusion processes and advection of asymmetries in the domain begin to dominate at higher Re resulting in reducing the magnitude of angular momentum in the domain.

The radial location of maximum tangential velocity, r_m^*, decreases during the cyclogenesis phase and reaches a stationary value in all cases. This is because the maximum angular momentum in the system increases and r_m^* decreases to conserve angular momentum. The stationary value of r_m^* decreases as Re increases because the Ekman number has to decreases to maintain $Re\,E = C/\Gamma$ so that a strong poloidal flow can ensue, allowing the eye and eyewall to form. The reduction in E makes the rotational effects experienced by the fluid to be stronger, resulting in a stronger and tighter eye in flows with larger Re values which is observed in figure 6.1.

The degree of axisymmetricity, $\overline{\gamma_{u_\varphi}}$, of the vortex increases during the cyclogenesis as shown in figure 6.1 for all the cases. This is because, organised asymmetric features like spiral bands and wall modes begin to appear in regions outside the vortex core (eye and eyewall region). The spatial variation of these asymmetries are discussed in the next section. The value of $\overline{\gamma_{u_\varphi}}$ increases by about 4 times during the cyclogenesis phase for the Case I and this increase decreases considerably as Re increases. This is because (i) the region occupied by the axisymmetric vortex core is reduced as Re increases and (ii) the turbulent processes are dominant at larger Re hindering the organisation of asymmetries into axisymmetric structures. Thus, to summarise this figure, the axisymmetric vortex core forms with increasing tangential velocity during the cyclogenesis the level of axisymmetricity decreases at higer Re. The spatial structure of asymmetries are discussed next.

6.2.2 Spiral Bands

The spatial variations of depth-averaged fluctuations in kinetic energy over the azimuthal mean value are shown in figure 6.2 at four different times during the cyclogenesis for Case 2 in Table 5.1. The depth-averaging excludes the bottom boundary layer and the values are normalised using $\Omega^2 H^2$. As $\tau_2 \geq 1$, tropical cyclone-like vortex becomes more axisymmetric (see Fig. 6.1b), and the asymmetries begin to evolve into a more organised structure, namely spiral bands in the bulk of the domain and wall modes near the sidewall. Many relatively narrow bands of alternating positive and negative $\ddot{E}^*$ in the azimuthal direction are identified between $r/R = 0.2$ and $r/R = 0.8$ and are referred to here as spiral bands. Similarly, alternating positive and negative $\ddot{E}^*$ in the azimuthal direction are seen near the sidewall ($r/R \geq 0.8$) and are referred to here as wall modes (similar to that discussed in chapter 4). The number of spiral bands increases from 3 to 4 during flow evolution. Similarly, the wall modes near the sidewall also increase from 12 to 18. The dry tropical cyclone-like vortex exhibit the prominent spiral bands and wall modes not only in the kinematic fields shown in Fig. 6.2 but also in the thermodynamic fields (not shown here) throughout the height of the domain. The spiral bands in the asymmetric structure are similar to those in actual tropical cyclones, where spiral/rain bands are predominantly seen outside the inner-core region. The characteristics of the spiral bands, namely the spiral angle and the phase speed, will be discussed in the context of the actual tropical cyclone later in this section. It is to be noted that the same behaviour in the asymmetric evolution is seen during the cyclogenesis for other cases exhibiting tropical cyclone-like vortex.

An azimuthal Fourier decomposition of the fluctuations in kinetic energy, $\mathcal{E}'$ is performed to obtain insight into the dominant components of the TC flow at the height of $z/H = 0.75$ during the cyclogenesis phase and is shown in Fig. 6.3. This particular

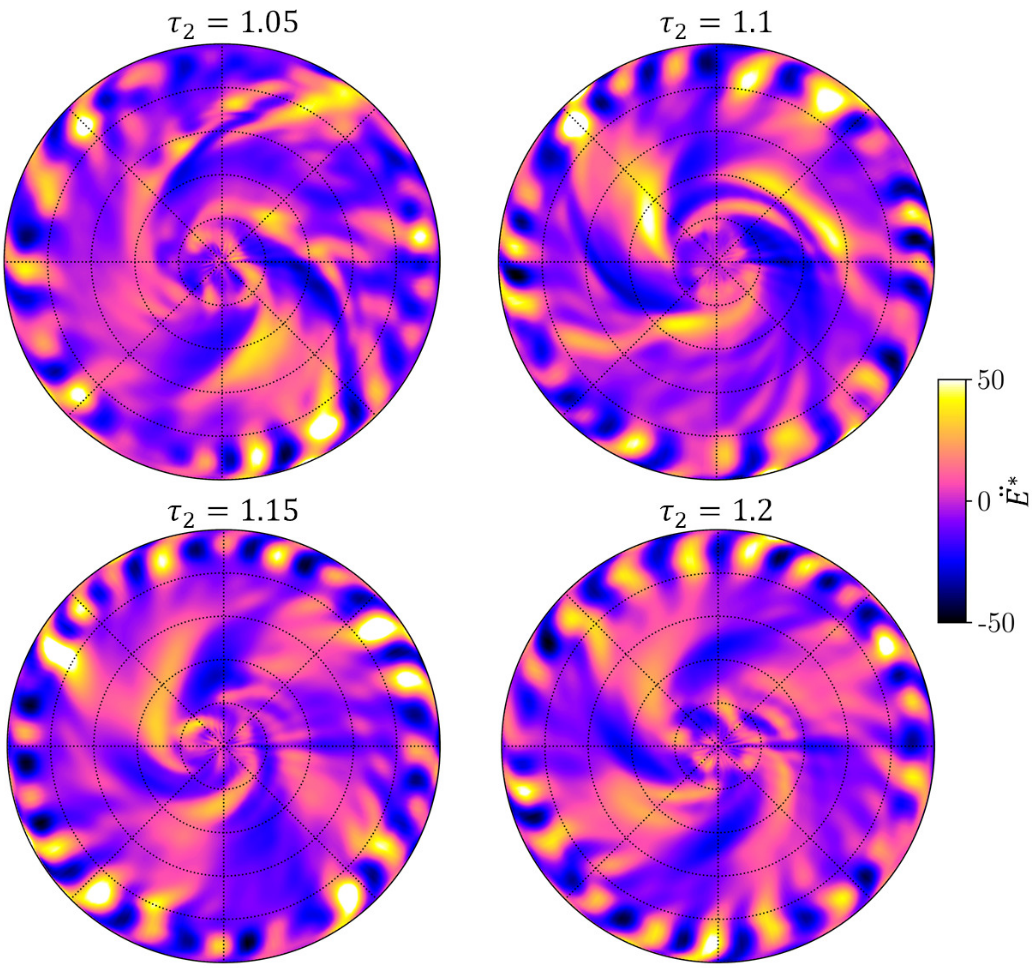

Fig. 6.2 Four snapshots, at $\tau_2 = 1.05$, 1.1, 1.15, and 1.2, of depth-averaged $\ddot{E}^* = K - \langle K \rangle$ for Case 2 in Table 5.1. The averaging is done between $z/H = 0.2$ and 1 and the results are normalised using $\Omega^2 H^2$. Dotted concentric circles are drawn for every $r/R = 0.2$ from the centre and dotted radial lines are drawn for every $\varphi = 45°$.

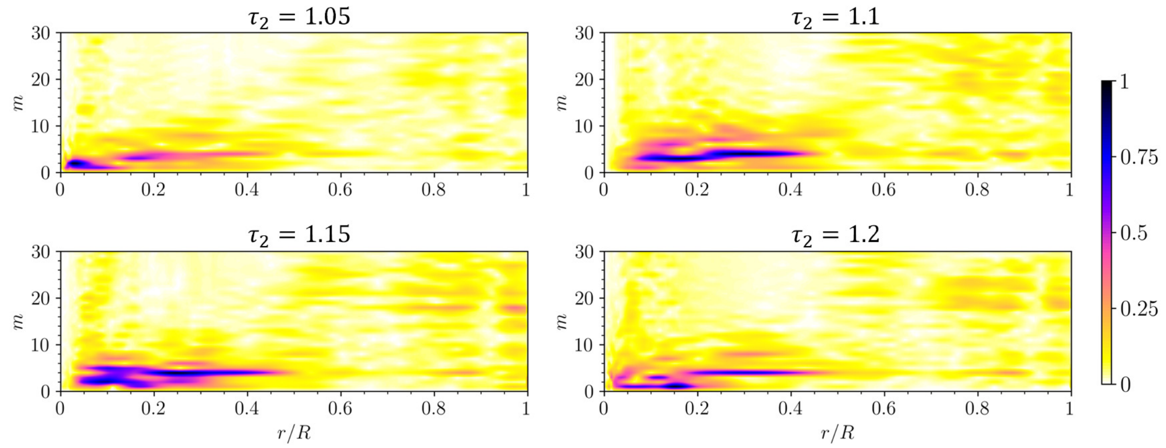

Fig. 6.3 Azimuthal power spectrum of $\mathcal{E}'^*$ in the axial plane $z/H = 0.75$ calculated at radius for azimuthal wavenumbers $m = 1$ to $m = 30$ at four different time instant (same as in Fig. 6.2) for Case 2 in Table 5.1. The values are normalised using the respective maximum and these values are 5805.1 at $\tau_2 = 1.05$; 3780.3 at $\tau_2 = 1.1$; 3443.2 at $\tau_2 = 1.15$; and 3440.1 at $\tau_2 = 1.2$.

height is chosen as the main feature of the tropical cyclone-like vortex; namely, the eye and eyewall are well defined (see Fig. 5.3d). During the start of cyclogenesis $\tau_2 = 1.05$, the dominant mode with highest power is found near the centre at wavenumber $m = 1$. At this time, the asymmetries begin to form an organised pattern (see Fig. 6.2). As the time evolves $\tau_2 \geq 1.05$, the low wave number asymmetries dominate the power spectrum. The wavenumber $m = 4$ is found to be the dominant model in the bulk of the domain $0.2 \leq r/R \leq 0.6$ denotes the spiral band-like asymmetries see in Fig. 6.2. Similarly, the wavenumber $m = 18$ is found to be the dominant mode (see for $\tau_2 \geq 1.15$) near the sidewall, $r/R \geq 0.8$ denotes the wall modes observed in Fig. 6.2. The same behaviour for azimuthal power spectrum is observed during cyclogenesis phase for other cases in Table 5.1. The near wall behaviour of evolution of asymmetries for case 1 is discussed in section 4.2.3.

The vertical structure of the spiral bands is examined for fully evolved tropical cyclone-like vortex by taking azimuth-height structures for $m = 4$, which is the dominant mode in the region outside the tropical cyclone-like vortex core $r/R \geq 0.2$. Figure 6.4 shows the vertical structure of the $m = 4$ component of temperature perturbation, $\theta'^*_{m=4}$, radial velocity, $u'^*_{rm=4}$, axial velocity, $u'^*_{zm=4}$, and azimuthal velocity, $u'^*_{\varphi m=4}$ at a radius of $r/R = 0.4$ and $\tau_2 = 1.2$. The asymmetry are titled against the vertical axis for $\theta'^*_{m=4}$, $u'^*_{rm=4}$ and $u'^*_{\varphi m=4}$ in Fig. 6.4, this is because of strong vertical shear of their azimuthal mean quantities namely $\langle\theta^*\rangle$, $\langle u^*_r\rangle$ and $\langle u^*_\varphi\rangle$ at $r/R = 0.4$ (see Fig.

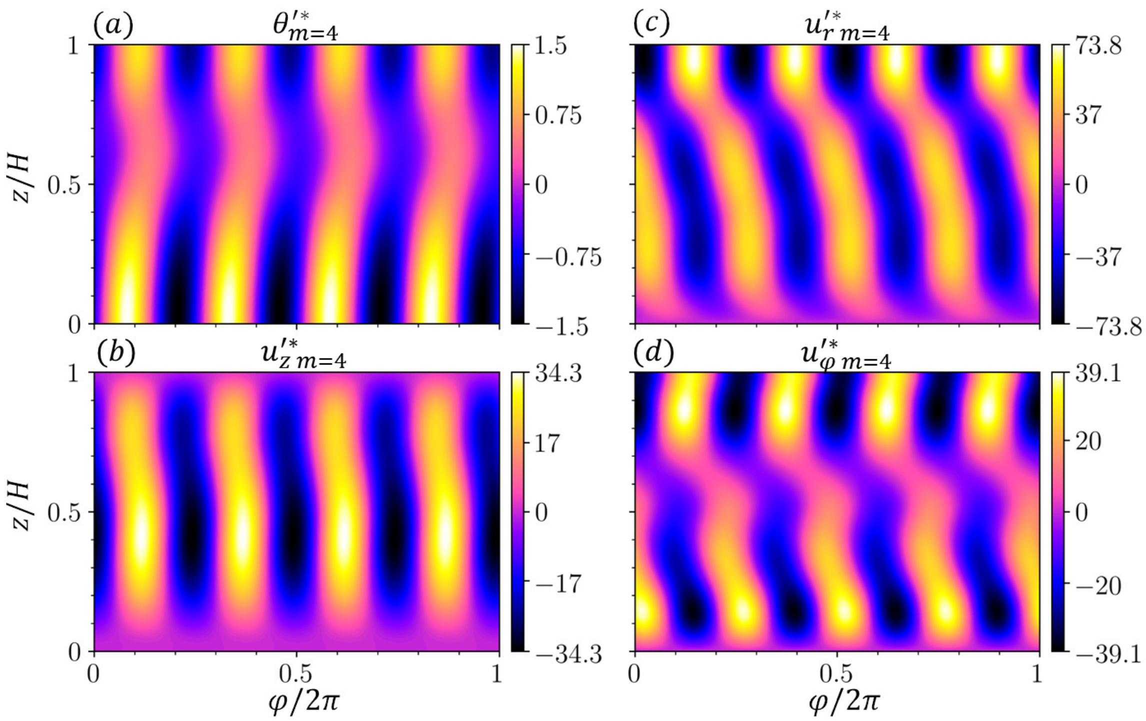

Fig. 6.4 The height-azimuth contours of asymmetries for the dominant azimuthal mode ($m = 4$) of (a) Temperature perturbation $\theta'^*_{m=4}$ normalised with (βH), (b) Radial velocity $u'^*_{rm=4}$ normalised with (ΩH), (c) Axial velocity $u'^*_{zm=4}$ normalised with (ΩH), (d) Azimuthal velocity $u'^*_{\varphi m=4}$ normalised with (ΩH), at $r/R = 0.4$ and $\tau_2 = 1.2$ for Case 2 in Table 5.1.

5.3). This leads to titling of the asymmetry at a height z where the maximum value of azimuthal mean quantities are observed. It is for the same reason that the asymmetry of $u'^*_{zm=4}$ is almost vertically oriented because the flow is poloidal in $r-z$ plane (see Fig. 5.1(b) & Fig. 5.3(d)) and hence $\langle u^*_z \rangle$ value will be uniform and negligible in the bulk of the domain. The $\theta'^*_{m=4}$ and $u'^*_{zm=4}$ are positively correlated throughout the height of the domain indicating the exchange of asymmetric potential energy to asymmetric kinetic energy in the bulk of the domain (see term C_P in Eqs. (6.2) and (6.4)).

Figure 6.5(a) shows the angle of the spiral bands as a function of the radius measured at $z/H = 0.75$ when the tropical cyclone-like vortex is fully evolved. The radius r is normalised with tropical cyclone-like vortex radius r_{tc} where r_{tc} is the radius of last closed isobar. The spiral angle ψ at a particular radius r is defined as the angle formed by the streamline (computed from time-averaged velocities) and the tangent drawn at intersection point of streamline and the concentric circle drawn at r from the centre. The spiral angle, ψ decreases as one goes away from the tropical cyclone-like vortex

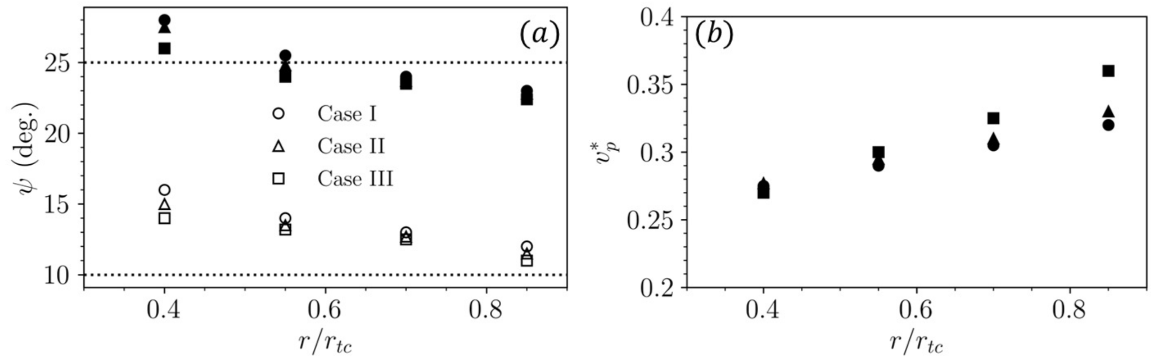

Fig. 6.5 The radial variation of the (a) maximum (open symbols) and minimum (filled symbols) spiral angle ψ (deg.) and (b) azimuthal phase speed v_p^* (filled symbols) normalised with time and azimuthal averaged azimuthal velocity $\langle \tilde{u_\varphi} \rangle$ for Case 1, 2 and 4 in Table 5.1 in a fully evolved state.

centre for all the Cases in Table 5.1. The value measured for fully evolved tropical cyclone-like vortex seems to be within the range of $10° - 30°$, which is approximately within the range observed for spiral/rain bands in an actual tropical cyclone ($10° - 25°$) from field measurements (Anthes, 2016).

Figure 6.5(b) shows the azimuthal phase speed v_p^* as a function of the radius measured at $z/H = 0.75$. v_p at a particular radius is measured by taking spatial and temporal FFT of kinetic energy fluctuations $\mathcal{E}'$ (similar to Fig. 4.12). It is then normalised with time and azimuthal-averaged azimuthal velocity, $\langle \widetilde{u_\varphi / r} \rangle$, at the same radius. The phase speed v_p^* increases by about 14%, 16% and 24% for case 1, 2 and 4 respectively as one move from $r/R = 0.3$ to $r/R = 0.6$. This is because the value of $\langle \tilde{u}_\varphi / r \rangle$ decreases radially at larger radius for a typical tropical cyclone-like vortex (see Ch, 4 & 5). The azimuthal phase speeds were observed to be slower than the mean flow velocity, $\langle \tilde{u_\varphi} \rangle$, for all the radius and for all the cases plotted in Fig. 6.5(b). This is consistent with the previous works on the theory of spiral bands (Willoughby et al., 1984, Montgomery & Kallenbach, 1997). The trend in the spiral angle ψ and the azimuthal phase speed v_p^* remains the same at $0.75 \leq z/H \leq 0.95$ and the deviation in the magnitude is less than 10%. Thus, the asymmetric features of tropical cyclone-like vortex, namely spiral bands, obtained from dry convection simulation in a RRBC setup compare well qualitatively with that of the actual tropical cyclone. The energy exchange between asymmetries and large-scale symmetric tropical cyclone-like vortex structure from an energetic viewpoint is discussed in the next section.

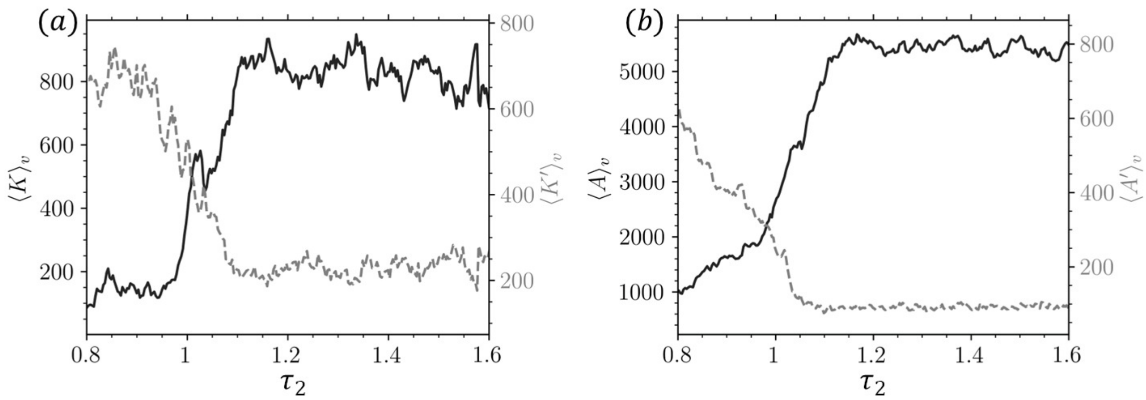

Fig. 6.6 Time evolution of volume-averaged energy components. (a) Symmetric $\langle K\rangle_v$ and asymmetric $\langle K'\rangle_v$ kinetic energy per unit mass normalised with $(\Omega R)^2$, (a) Symmetric $\langle A\rangle_v$ and asymmetric $\langle A'\rangle_v$ potential energy per unit mass normalised with $(\Omega R)^2$, for case 2 in Table 5.1.

6.2.3 Energy Exchange within Tropical Cyclone-like Vortex

The role of different energy exchange terms in Eqs. (6.1)−−(6.4) which are detailed in section 6.1.1 will be studied in this section to understand the evolution of tropical cyclone-like vortex during cyclogenesis.

Figure 6.6 shows the time evolution of volume-averaged symmetric and asymmetric components of kinetic and potential energies per unit mass during the cyclogenesis phase for case 2 in Table 5.1. The energies are normalised with $(\Omega R)^2$. It should be noted that the scales of the vertical axes for the variables in the Fig. 6.6(a) and Fig. 6.6(b) are different. The symmetric part of the kinetic energy starts increasing after $\tau_2 = 0.95$ and achieves a steady value at around $\tau_2 = 1.2$. In contrast, the asymmetric kinetic energy starts reducing well before the cyclogenesis phase and attain a steady value around $\tau_2 = 1.2$. Similarly, the symmetric potential energy starts to increase around $\tau_2 \approx 1$ and the asymmetric potential energy also decreases similar to its kinetic energy counterpart. This is consistent with the observation made in Fig. 6.1(b) that during the cyclogenesis phase of a tropical cyclone-like vortex, the vortex becomes more axisymmetric and intense. Hence, axisymmetric energies are of higher magnitude and they start to increase during the cyclogenesis phase. The evolution of the energies shown in Fig. 6.6 is similar for other cases in Table 5.1.

The evolution of volume-averaged energy exchange terms is shown in Fig. 6.7 to understand better the energy exchanges happening between the symmetric and asymmetric components of kinetic and potential energies (shown in Fig. 6.6). The

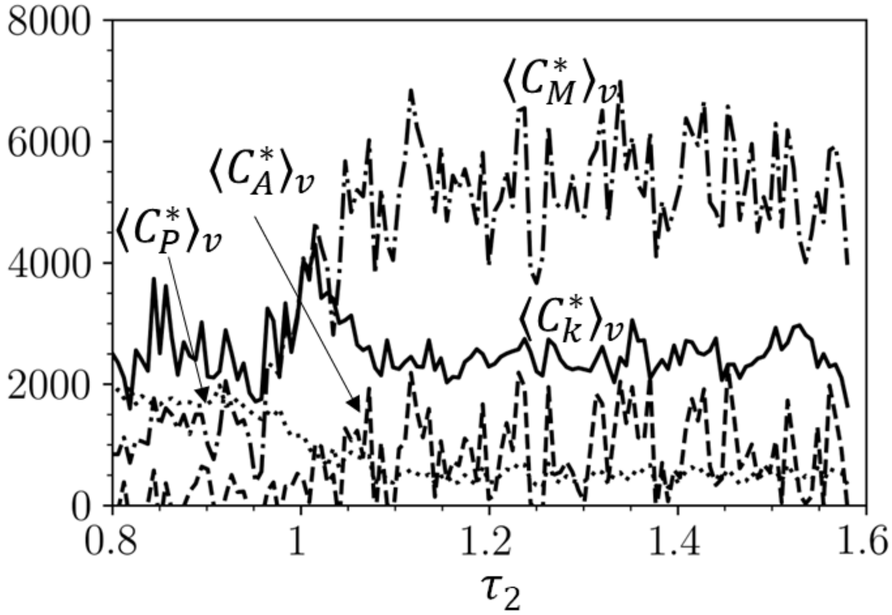

Fig. 6.7 Time evolution of the volume-averaged energy exchange terms in Eqs. (6.1)−−(6.4) for case 2 in Table 5.1. The values are normalised with $(\Omega^3 R^2)$.

values of energy exchange terms are normalised with $(\Omega^3 R^2)$. $\langle C_K^* \rangle_v$ term represented by solid line increases initially during cyclogenesis but then starts reducing by about 50% till it reaches a steady value. The volume-averaged term is positive throughout the cyclogenesis phase and beyond, indicating the energy exchange from asymmetric to symmetric kinetic energy. This is in line with the trend seen in Fig. 6.6(a). $\langle C_A^* \rangle_v$ term denotes the energy exchange from asymmetric to symmetric potential energy increases from about 0 to a positive value during cyclogenesis. This behaviour complements the evolution of potential energies seen in Fig. 6.6(b). The exchange of azimuthal mean potential to kinetic energy is the dominant energy exchange term, as seen in the evolution of $\langle C_M^* \rangle_v$. This is obvious because that is the inherent nature of convection which initiates and aids the formation of tropical cyclone-like vortex. Since the flow becomes more axisymmetric during cyclogenesis and the asymmetries energies are lower than their axisymmetric counterpart. Therefore, $\langle C_P^* \rangle_v$ denotes the energy exchange between asymmetric potential and kinetic energy reduces during cyclogenesis. The spatial variation of these terms and a summary of the overall energy exchange for a fully evolved tropical cyclone-like vortex will be discussed next.

Figure 6.8 shows the spatial variation of energy exchange terms in Eqs. (6.1)−−(6.4) for a fully evolved tropical cyclone-like vortex for case 2 in Table 5.1 at $\tau_2 = 1.2$. The individual terms are normalised by $(\Omega^3 R^2)$. The exchange of kinetic energy between azimuthal mean and asymmetries denoted by the term C_K^* is shown in Fig. 6.8(a). It is positive in the poloidal flow region (see Fig. 5.3(d)) denotes the exchange of energy towards an azimuthal mean kinetic energy, and this occupies the bulk of the domain, and hence we get to see a positive value for this term in Fig. 6.7. There is also a significant negative value of this term in the domain, and they are concentrated near the boundary layers, namely the bottom Ekman layer, eyewall (sweeping up of bottom Ekman layer (Oruba et al., 2017)) and sidewall Stewartson layer. This is because in this region, the turbulence is predominant, and the nature of turbulence is to exchange energy to smaller scales (in this case, the asymmetries) (Pope, 2000). This can be the plausible reason for the decrease in the value of $\langle C_K^* \rangle_v$ in Fig. 6.7 during cyclogenesis. This is because the boundary layer is set up throughout the bottom and sidewall and is also swept up to form an eye-eyewall during cyclogenesis leading to formation of tropical cyclone-like vortex in the domain.

The exchange of energy from asymmetric to symmetric potential energy is denoted by the term C_A^*. It can be seen from Fig. 6.8(b) that it remains positive in the bulk of the domain and this is because the thermal asymmetries and vertical velocity asymmetries are positively correlated in bulk (for example, see Fig. 6.4(a) & 6.4(b)) also the radial gradient of azimuthal mean temperature gradient is uniform in the bulk. The C_A^* term is negative near the region of maximum azimuthal velocities (see Fig. 5.3) this is because the radial gradient of $\langle \theta^* \rangle$ changes the sign. This is because the $\langle \theta^* \rangle$ is maximum near the eyewall region (where convection is predominant), and there is a quiet eye region formed near the centre, which causes the sudden change in the radial gradient sign and this is seen in the sign of C_A^*. The second sub-term in C_A^* is negligible and is an order of magnitude small in value (not shown here).

Figure 6.8(c) shows the contour of C_M^*, which represents the energy exchange between azimuthal mean potential and kinetic energy. It can be seen that it is positive in the bulk of the domain because $\langle u_z^* \rangle$ and $\langle \theta^* \rangle$ are positive in the bulk of the domain. The higher value is concentrated near the centre in the eyewall region, where the convection dominates. The value of C_M^* is negative near the centre of the domain at $z/H \geq 0.8$ this is because of the downward flow seen in the eye region therefore $\langle u_z^* \rangle$ is negative. Similarly, $\langle u_z^* \rangle$ is negative near the sidewall region to complete the poloidal flow seen in tropical cyclone-like vortex, whereas $\langle \theta^* \rangle$ is positive near the top of the domain $z/H \geq 0.5$ and negative in the bottom half. Since $\langle \theta^* \rangle$ and $\langle u_z^* \rangle$ are negatively correlated for $z/H \geq 0.5$ the C_M^* value is negative in this region.

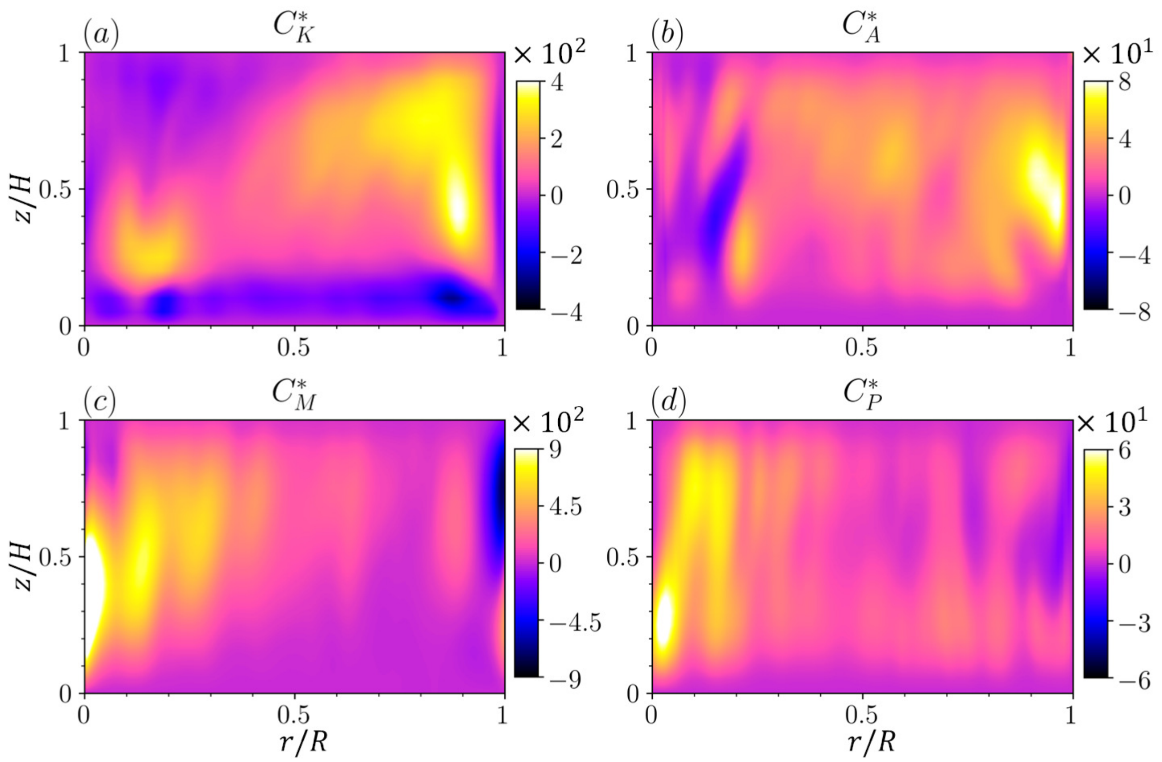

Fig. 6.8 The colour contours showing the spatial variation of energy exchange terms in Eqs. (6.1)-(6.4) for Case 2 in Table 5.1 at $\tau_2 = 1.2$. The individual terms are normalised by $(\Omega^3 R^2)$.

The contour of C_P^* is shown in Fig. 6.8(c) indicating the energy exchange between asymmetric potential and kinetic energy. It is positive in the domain because the temperature asymmetries and vertical velocity asymmetries are positively correlated. Similar to Fig. 6.8(c) there is a negative correlation between the thermal and vertical velocity asymmetries near the top half of the sidewall. Thus the C_P^* value is negative in the region. Also, the maximum value is concentrated near the centre as convection is predominant near the core. The spatial variation of all the terms shown in Fig. 6.9 is similar for all other cases with tropical cyclone-like vortex. The overall energy cycle for a fully evolved tropical cyclone-like vortex can be constructed from these exchange terms described in Fig. 6.8 and is shown next.

Figure 6.9 shows the overall energy flow diagram with the value of different energy change terms and the flow direction with an arrow for all the cases in Table 5.1. The time-averaged (for 100 rotation time after the tropical cyclone-like vortex is fully evolved) and volume averaged value of energy exchange terms are reported. The values are normalised with a maximum value of the energy exchange term to have a maximum

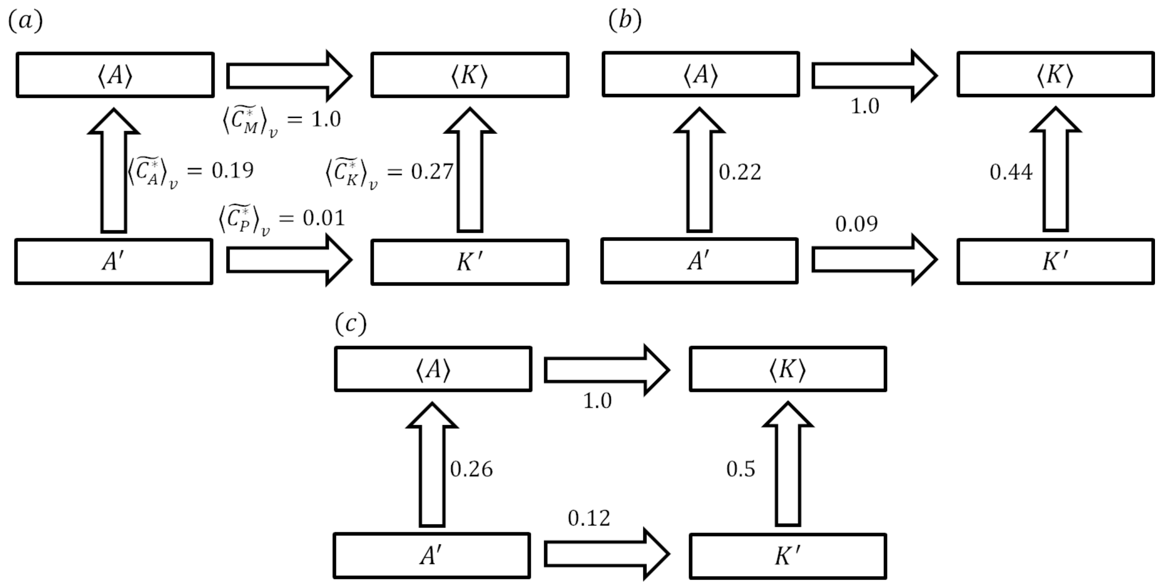

Fig. 6.9 The energy flow diagram in a fully evolved tropical cyclone-like vortex for (*a*) Case 1, (*b*) Case 2 and (*c*) Case 4 in Table 5.1. The energy exchange values are normalised to have 1.0 as a maximum value. The maximum value used for normalisation are (*a*) $\langle \tilde{C_M^*} \rangle_v = 8832.1$, (*b*) $\langle \tilde{C_M^*} \rangle_v = 5124.4$ and (*c*) $\langle \tilde{C_M^*} \rangle_v = 4661.6$.

value to be 1. It can be seen that for all the cases, the predominant energy exchange is between azimuthal mean potential and kinetic energy. Following this, the energy conversion from asymmetric to symmetric kinetic energy is dominant. This is because of the poloidal flow set up in the domain, which helps in tilting the asymmetries and contributes to this energy exchange. It is important to note here that this exchange from asymmetric kinetic energy to symmetric energy is seen only in tropical cyclone-like vortex cases where poloidal flow is set up in the domain and not for the cases that do not show tropical cyclone-like vortex (not shown here). The energy conversion between asymmetric and symmetric potential energy and the energy exchange between asymmetric potential and kinetic energy are less compared to other energy exchanges. This trend in the terms is observed for all the cases which show tropical cyclone-like vortex, as seen in Fig. 6.9. However, their relative magnitude increases compared to the maximum value for increasing Re. This is because turbulent processes dominate at higher Re, and hence the maximum value of the energy exchange term used for normalising, is reduced compared to the value of other terms.

6.3 Summary

The simulation data of tropical cyclone-like vortex in a dry rotating Rayleigh-Benard convection setup is analysed in this work. The data is decomposed into azimuthal mean and asymmetries, and the asymmetries are studied in detail. The salient findings based on this study presented in the work are as follows:

- During cyclogenesis, the asymmetries organise themselves into a spiral band as seen in the actual tropical cyclone, even in the simple dry rotating convection setup without considering moisture effects in the simulation.
- The spiral angle of the spiral bands formed in the tropical cyclone-like vortex lie in the range of that of an actual tropical cyclone reported in the literature.
- The phase speed of the bands is slower than the mean flow velocity, again in line with the theory of spiral bands (see Anthes (2016)).
- The evolution of different energy exchange terms and their spatial variation for a fully evolved tropical cyclone-like vortex is understood in detail.

Though the asymmetries have been studied in this work during cyclogenesis, it is still a simple model without any additional complexities such as stratification, moisture and beta effect, to name a few. It is important to incorporate these factors into this simple model to better understand their roles in the evolution of asymmetries and its effect on cyclogenesis. This will help to further understand the role of different environmental factors on cyclone formation and also help in developing better forecasting models. The implications of the observed energy exchange among different components of the energies in the tropical cyclone-like vortex formation are studied in the next chapter.

Chapter 7

Formation of Tropical Cyclone-like Vortex

The tropical cyclone-like vortex is simulated successfully in this study using a 3D RRBC setup for both laminar and turbulent flow conditions. The dry convection simulations are able to capture spiral bands analogous to rain bands as seen in actual tropical cyclones. The resulting spatial structure of the large-scale vortex is also found to agree qualitatively with that of real tropical cyclones. The conditions for cyclogenesis in the simple setup is obtained by analysing the computational results to come up with two distinct timescales for cyclogenesis. It was found that the hydrodynamic conditions for the cyclogenesis obtained from the present work agree well with the field data for actual tropical cyclones. The energy transfer from asymmetries (spiral bands) to axisymmetric structure is also studied in detail in the previous chapter. However, one of the objectives for this work, namely understanding the cyclogenesis process leading to the formation of the large-scale vortex and the mechanisms sustaining that structure in the domain is still unclear. This chapter attempts to find some insight into plausible reason(s) for the formation of the vortex in the simple model used for the present work.

The mechanism of tropical cyclogenesis remains a challenging scientific problem. The formation of a tropical cyclone involves several steps (as discussed in chapter 1) and might be loosely split into three stages: (i) the initial formation of weak cyclonic regions where convection prefers to occur, (ii) the formation of large-scale cyclonic circulation (aka tropical depression) and (iii) the spontaneous spinup of a large-scale cyclonic circulation and its intensification into a vortex with a self-sustaining eye-eyewall features (Montgomery et al., 2006). The last stage is referred to as cyclogenesis, wherein the large-scale cyclonic circulation becomes intense and acquires the unique eye-eyewall features absent in the tropical depression.

The formation of eye-eyewall in the axisymmetric cyclonic vortex has been studied extensively in the past by (Oruba et al., 2017, 2018). It was shown that the sweeping up of the bottom Ekman layer helped the formation of the eyewall and, in turn, the formation of the eye in the cyclonic vortex. The past studies were carried out in the axisymmetric RRBC model. The important asymmetric effects were neglected in those studies. Therefore, the study is revisited for the 3D counterpart to better understand the cyclogenesis process in the simple RRBC model. As we can see from Fig. 7.1 at $\tau_2 = 0.5$ that initially large pool of cyclones ($\omega_z > 0$) and anti-cyclones ($\omega_z < 0$) fills the domain in an highly disorganised manner. The flow evolves into an organised tropical cyclone-like vortex, as seen in the second frame of Fig. 7.1 shown for $\tau_2 = 1.5$. The detailed flow evolution from a quiescent initial condition for case 4 in Table 5.1 is attached as a video titled "*Ch7-movie*[1]" with this document.

The horizontal kinetic energy, is defined as $K_h = 1/2 \times (u_r^2 + u_\varphi^2)$. Its spectrum computed for the plane $z/H = 0.75$ is shown in the bottom row of Fig. 7.1 suggests that the dominant energy move towards the large scales as the tropical cyclone-like vortex is formed in the domain at $\tau_2 = 1.5$ as shown in past studies for a large scale vortex (Guervilly et al., 2014, Couston et al., 2020, Guzmán et al., 2020). However, it is unclear if the large scale vortex in the previous work have eye and eyewall structures typical of tropical cyclones. This chapter sheds some light on how the flow organises into a large-scale tropical cyclone-like vortex as seen in Fig. 7.1, with distinct features of eye-eyewall and spiral bands from a quiescent initial state. It is hoped that this will shed some insight into the cyclogenesis, at least for the simple 3D RRBC setup used for this study.

The remainder of this chapter is organised as follows. The overview of the barotropic and baroclinic instabilities occurring in synoptic-scale (of the order of thousands of kilometres) meteorology are discussed in subsection 7.1. The results are presented and discussed in section 7.2, and the chapter is concluded with a summary.

7.1 Overview of Barotropic & Baroclinic instability

Much of the infomation provided in this section regarding the barotropic & baroclinic instability can be found in the textbooks by Holton (2004) and Vallis (2017). In

[1]The movie *Ch7-movie* shows the evolution of axial vorticity, ω_z^*, normalised with Ω from a quiescent initial state for case 4 in Table 5.1. The movie is available at https://www.dropbox.com/s/4xrauy9yijblj5c/Ch7-movie.mp4?dl=0.

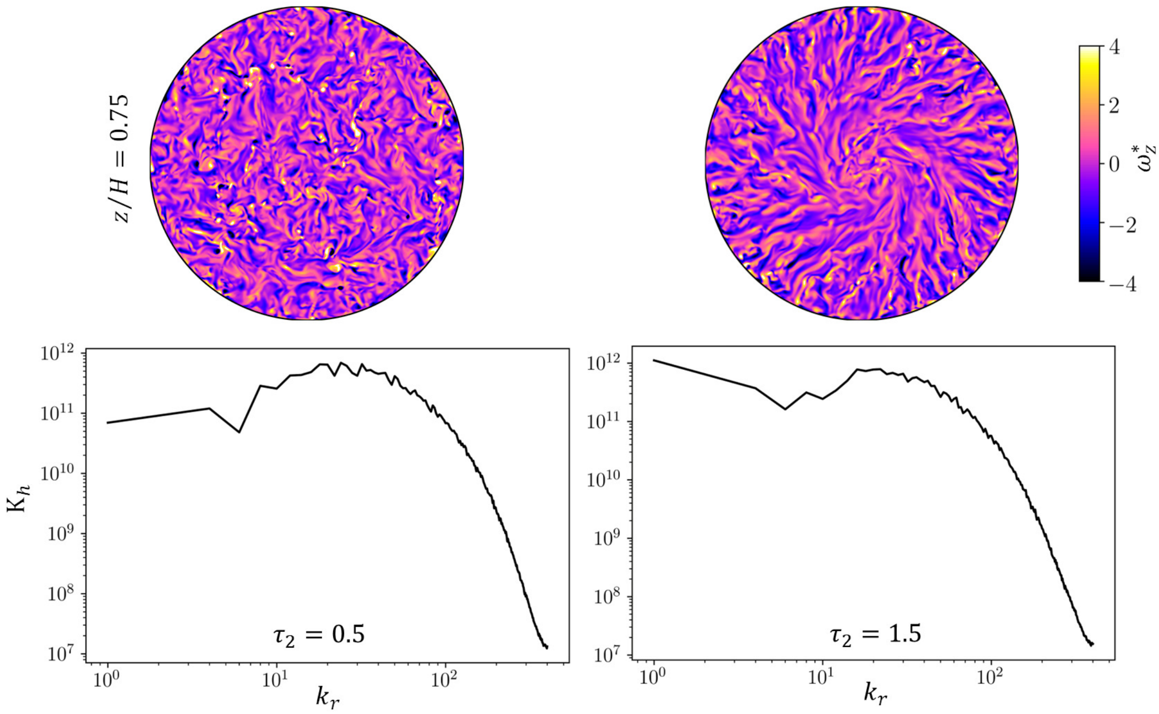

Fig. 7.1 The instantaneous axial vorticity contour ω_z^* normalised with background rotation along with the horizontal kinetic energy K_h spectrum at $z/H = 0.75$ and $\tau_2 = 0.5$ (left) and $\tau_2 = 1.5$ (right) for case 4 in Table 5.1 showing evolution of large scale vortex.

geophysical fluid dynamics, the barotropic and baroclinic instabilities are well-known mechanisms responsible for forming dominant energy-containing eddies in both atmospheric and oceanic flows. In general barotropic instabilities occur in flows wherein background rotation plays an important role, whereas baroclinic instabilities, in addition, require statistically stable stratification. They are typically distinguished energetically by the respective dominance of exchanges of either kinetic (for barotropic) or potential (for baroclinic) energy with the mean flow. Barotropic instability is associated with dominant energy exchange of kinetic energy between the background azimuthally symmetric flow and asymmetries, whereas dominant energy exchange of potential energy between background flow and asymmetries is seen for baroclinic instability. Both of these instabilities have been observed in the experiments of rotating convection system (Hide, 1969, Hide & Mason, 1975).

These exchanges of energy between azimuthally symmetric flows and asymmetries and between potential and kinetic energies are commonly quantified in the manner originally suggested by Lorenz (1967) in which the flow is partitioned between azimuthally symmetric components and departures therefrom ("asymmetries"), with four main energy reservoirs ($\langle A \rangle$, A',$\langle K \rangle$, K') representing respectively the symmetric and asymmetric potential energy and the corresponding kinetic energies. From considerations of the energy conservation equations, expressions can be defined to represent the rates of conversion between the four energy reservoirs denoted by C_K, C_A, C_M and C_P (e.g. see Lorenz (1967), James (1995), and section 6.1.1 of chapter 6). C_K is the rate of energy exchange between azimuthal mean and asymmetric kinetic energy. The rate of energy exchange between azimuthal mean and asymmetric potential energy is denoted by C_A. The rate of energy exchange between azimuthal mean potential and kinetic energy is C_M and C_P denotes the rate of energy exchange between asymmetric potential and kinetic energy. The mathematical expression for these energy exchange terms are given in section 6.1.1. Barotropic instability is associated with dominant magnitude of C_K compared to C_A. Similarly dominant value of C_A compared to C_K is associated with baroclinic instability provided criteria for baroclinic/barotropic instability is satisfied in the flow. The necessary criteria for occurrence of baroclinic/barotropic instability are discussed later in this section.

The Baroclinic effect is incorporated in an incompressible Boussinesq fluid manifest through the buoyancy term and this effect is an important mechanism of vorticity generation, and could be regarded as the essence of the buoyancy effect which converts potential energy to kinetic energy (Vallis, 2017). Such effect is due to the non alignment of pressure gradient and density gradient, and it appears in the vorticity equation as the curl of the pressure term $\nabla \times (\nabla p/\rho)$, namely the baroclinic torque. Due to the complexity caused by the coupling of pressure and density in the pressure term , it is widely preferred to substitute in the denominator $\nabla p/\rho$ by the constant reference density $\rho = \rho_o$. Apparently, such simplification completely eliminates the curl of the pressure term in the vorticity equation and requires a buoyancy term to compensate the loss of the baroclinic torque. Therefore the curl of the buoyancy term should be equal to, or approaching, in order to recover the true evolution of vorticity (Vallis, 2017).

In addition to energy considerations discussed until now, the spatial distribution of absolute vorticity (ω_{abs}) also plays a key role in determining whether an instability develops and the character of the instability when it occurs (Holton, 2004, Vallis, 2017). The absolute vorticity is the sum of axial vorticity and background rotation given by $\omega_{\text{abs}} = \omega_z + \Omega$. The subsequent non-linear evolution of the instability then depends also on both energetic and vorticity constraints, posing significant challenges to our understanding of how such instabilities evolved, interact, and equilibrate.

Analysis of linearised equations of momentum, energy and continuity has been traditionally used to study the occurrence of barotropic or baroclinic instabilities; see Chapters 9 & 10 of Vallis (2017) for detailed derivation. This type of analysis led to a well-known condition for the presence growing infinitesimal azimuthal perturbations on a mean tangential flow and this condition is called as Charney–Stern–Pedlosky (CSP) (Charney & Stern, 1962, Pedlosky, 1964) A brief discussion of deducing this condition is presented below for a flow with gradient wind and hydrostatic balances for clarity.

One starts with asymmetric radial and tangential momentum equations and , energy equation given by (B.14), (B.15) and (B.17) in Appendix B and the equation for mass conservation. In these equations, the non-linear terms and the terms involving mean radial and axial velocities, $\langle u_r \rangle$ and $\langle u_z \rangle$ respectively, are neglected to obtain simplified evolution equations for asymmetries involving only $\langle u_\varphi \rangle$. This tangential velocity is taken to be in the gradient wind balance with $\langle P \rangle$ and the equation for this is given by

$$2\Omega\langle u_\varphi\rangle + \frac{\langle u_\varphi\rangle^2}{r} = \frac{1}{\rho_o}\frac{\partial\langle P\rangle}{\partial r}.$$

One can obtain an expression for $\langle u_\varphi \rangle$ using the positive root of the above equation, which would be useful later on to get an equation for P'. Neglecting $\langle u_r \rangle$, $\langle u_z \rangle$ and the non-linear terms in Eqs.

eqrefem1 to (B.17) as noted above, one gets

$$\frac{D_v u'_r}{D_t} - \langle \mathcal{E} \rangle u'_\varphi = -\frac{1}{\rho_o}\frac{\partial P'}{\partial r} \tag{7.1}$$

$$\frac{D_v u'_\varphi}{D_t} + u'_z \frac{\partial \langle u_\varphi \rangle}{\partial z} + \langle \omega_{\text{abs}} \rangle u'_r = -\frac{1}{\rho_o}\frac{\partial P'}{r\partial \varphi} \tag{7.2}$$

$$\frac{D_v\left(\partial P'/\partial z\right)}{Dt} + \langle \mathcal{E} \rangle \frac{\partial \langle u_\varphi \rangle}{\partial z} u'_r + u'_z N^2 = 0 \tag{7.3}$$

$$\frac{1}{r}\frac{\partial\left(r u'_r\right)}{\partial r} + \frac{1}{r}\frac{\partial u'_\varphi}{\partial \varphi} + \frac{\partial u'_z}{\partial z} = 0 \tag{7.4}$$

as discussed in Shapiro & Montgomery (1993). Here, $D_v/Dt = \partial/\partial t + \langle u_\varphi \rangle \partial/r\partial\varphi$ is the advective change following a fluid parcel in the symmetric vortex with no radial and axial velocities, the symbol $\mathcal{E}$ is $\mathcal{E} = 2\Omega + 2\langle u_\varphi \rangle / r$ and $N = \sqrt{\alpha\beta g}$ is the buoyancy frequency. To derive Eq. (7.3), the hydrostatic balance, i.e, $\partial P'/(\rho_o \partial z) = \alpha g \theta'$ is assumed to get θ' in terms of P' and thermal wind relation $\partial\langle\theta\rangle/\partial r = \langle \mathcal{E} \rangle \partial \langle u_\varphi \rangle / \partial z$ is used to replace $\partial\langle u_\varphi \rangle/\partial z$ in terms of P' appropriately. An evolution equation for P' can then be obtained by replacing u'_r, u'_φ, and u'_z using appropriate expressions obtained by operating D_v/Dt on Eqs. (7.1) and (7.2) along with Eq. (7.3). The detailed derivation of this can be found in (Shapiro & Montgomery, 1993, Montgomery & Shapiro, 1995)). The final evolution equation for P' is (see Eq. (3.10) of Shapiro & Montgomery (1993))

$$\begin{aligned}\frac{D_v}{Dt}\Bigg[\frac{N^2}{\langle q \rangle \langle \mathcal{E} \rangle}\frac{1}{r^2}\frac{\partial^2 P'}{\rho_o \partial \varphi^2} + \frac{1}{r}\frac{\partial}{\partial r}\left(\frac{rN^2}{\langle q \rangle \langle \mathcal{E} \rangle}\frac{\partial^2 P'}{\rho_o \partial r}\right) + \frac{\partial}{\partial z}\left(\frac{\langle \omega_{\text{abs}} \rangle}{\langle q \rangle}\frac{\partial P'}{\rho_o \partial z}\right) \\ - \frac{1}{r}\frac{\partial}{\partial r}\left(\frac{r}{\langle q \rangle}\frac{\partial \langle u_\varphi \rangle}{\partial z}\frac{\partial P'}{\rho_o \partial z}\right) - \frac{1}{r}\frac{\partial}{\partial z}\left(\frac{r}{\langle q \rangle}\frac{\partial \langle u_\varphi \rangle}{\partial z}\frac{\partial P'}{\rho_o \partial r}\right) \\ + \left[\frac{\partial}{\partial r}\left(\frac{N^2}{\langle q \rangle}\right) - \frac{\partial}{\partial z}\left(\frac{\langle \mathcal{E} \rangle}{\langle q \rangle}\frac{\partial \langle u_\varphi \rangle}{\partial z}\right)\frac{1}{r}\frac{\partial P'}{\partial \varphi}\right] = 0\end{aligned} \tag{7.5}$$

with

$$\langle q \rangle = \frac{1}{\langle \mathcal{E} \rangle}\left[N^2 \langle \omega_{\text{abs}} \langle \mathcal{E} \rangle - \langle \mathcal{E}^2 \rangle \left(\frac{\partial \langle u_\varphi \rangle}{\partial z}\right)^2\right].$$

A modal solution of the form

$$P' = \Phi(r, z)\exp[i(m\varphi - \omega t)],$$

where m is an integer restricted to $m \geq 1$, is sought for stability analysis. Then, Eq. (7.5) becomes (see Montgomery & Shapiro (1995))

$$\sigma \left[-\frac{N^2 m^2}{\langle q \rangle \langle \mathcal{E} \rangle r^2} \Phi + \frac{1}{r} \frac{\partial}{\partial r} \left(\frac{r N^2}{\langle q \rangle \langle \mathcal{E} \rangle} \frac{\partial \Phi}{\partial r} \right) + \frac{\partial}{\partial z} \left(\frac{\langle \omega_{\text{abs}} \rangle}{\langle q \rangle} \frac{\partial \Phi}{\partial z} \right) \right.$$
$$- \frac{1}{r} \frac{\partial}{\partial r} \left(\frac{r}{\langle q \rangle} \frac{\partial \langle u_\varphi \rangle}{\partial z} \frac{\partial \Phi}{\partial z} \right) - \frac{1}{r} \frac{\partial}{\partial z} \left(\frac{r}{\langle q \rangle} \frac{\partial \langle u_\varphi \rangle}{\partial z} \frac{\partial \Phi}{\partial r} \right)$$
$$+ \frac{N^2}{\langle q \rangle} \frac{m}{r} \Phi \left(\frac{\partial \langle \omega_{\text{abs}} \rangle}{\partial r} \right) \tag{7.6}$$

where $\sigma = \omega - m \langle u_\varphi \rangle / r$ is the Doppler-shifted frequency. The existence of unstable mode is assumed by taking the imaginary part of the frequency, $\omega_i \neq 0$. On multiplying Eq. (7.6) by Φ^*, the complex conjugate of the P' amplitude, Φ, and integrating over the cross section of the vortex $0 \leq z < \infty$, $0 \leq r < \infty$ yields,

$$- \int_0^\infty \int_0^\infty \frac{r}{\langle q \rangle} \left[\frac{N^2 m^2}{\langle \mathcal{E} \rangle r^2} |\Phi|^2 + \frac{N^2}{\langle \mathcal{E} \rangle} \left| \frac{\partial \Phi}{\partial r} \right|^2 \right.$$
$$+ \frac{\langle q \rangle}{N^2} \left| \frac{\partial \Phi}{\partial z} \right|^2 drdz + \int_0^\infty \int_0^\infty \frac{N^2}{\langle q \rangle^2} \frac{\partial \langle \omega_{\text{abs}} \rangle}{\partial r} \frac{m}{\sigma} |\Phi|^2 drdz$$
$$+ \int_0^\infty \frac{m}{\sigma} \frac{\langle \mathcal{E} \rangle}{\langle q \partial u_\varphi \rangle} \frac{\partial u_\varphi}{\partial z} |\Phi|^2 \Big|_{z=0}^{z=H} dr = 0. \tag{7.7}$$

Equating the imaginary part (the last two terms) of Eq. (7.7) to zero gives a condition

$$\omega_i \int_0^\infty \int_0^\infty \frac{N^2}{\langle q \rangle^2} \frac{|\Phi|^2}{|\sigma|^2} \left(\frac{\partial \langle \omega_{\text{abs}} \rangle}{\partial r} \right) drdz + \int_0^\infty \frac{\langle \mathcal{E} \rangle \frac{\partial \langle u_\varphi \rangle}{\partial z}}{\langle q \rangle} \frac{|\Phi|^2}{|\sigma|^2} \Big|_{z=0}^{z=H} dr \quad = \quad 0 \tag{7.8}$$

If there exists an instability within the vortex then $\omega_i \neq 0$ and the integral in the L.H.S of Eq. (7.8) must be zero to satisfy Eq. (7.8). This gives the Charney–Stern–Pedlosky necessary condition for baroclinic/barotropic instability which require one or more of the following condition to be satisfied: (Charney & Stern, 1962, Pedlosky, 1964)

1. $\partial \langle \omega_{\text{abs}} \rangle / \partial r$ changes sign along some surface in the domain.
2. $\partial \langle \omega_{\text{abs}} \rangle / \partial r$ take the opposite sign to $\partial \langle u_\varphi \rangle / \partial z$ at the upper boundary at $z = H$.
3. $\partial \langle \omega_{\text{abs}} \rangle / \partial r$ take the same sign to $\partial \langle u_\varphi \rangle / \partial z$ at the lower boundary at $z = 0$. or

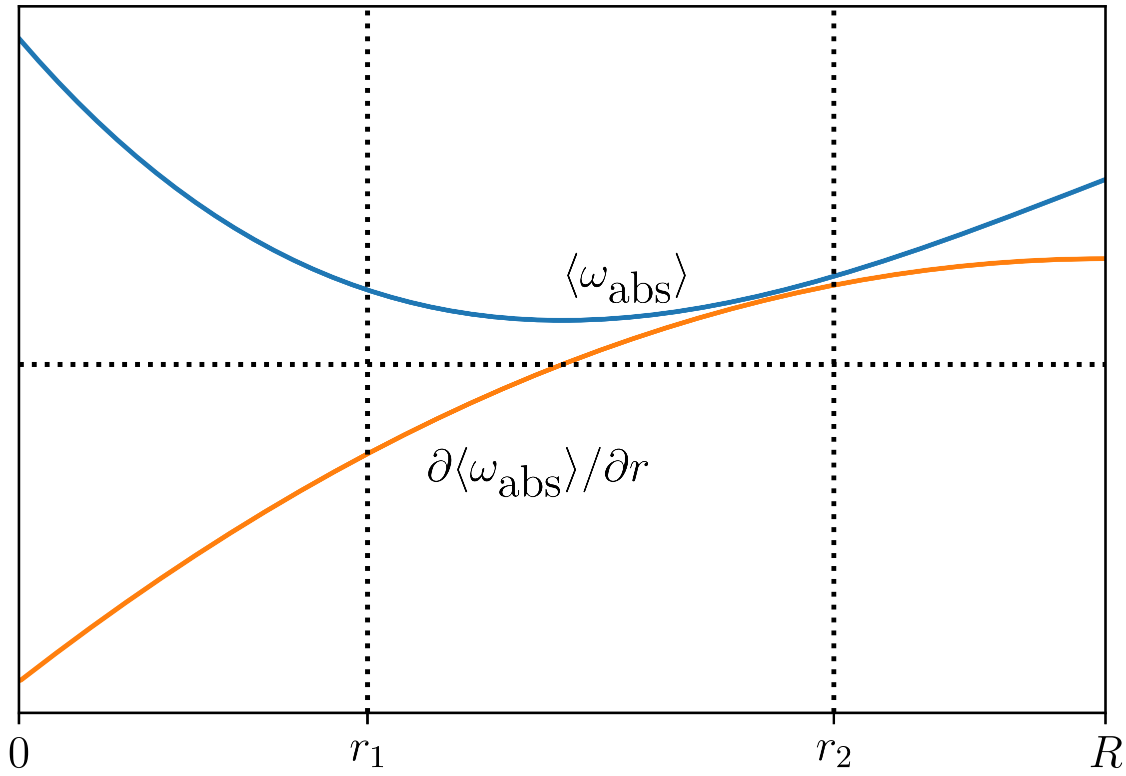

Fig. 7.2 Schematic showing the radial variation of absolute vorticity, $\langle\omega_{\mathrm{abs}}\rangle$, and radial gradient of absolute vorticity,$\partial\langle\omega_{\mathrm{abs}}\rangle/\partial r$, in a flow to illustrate Charney–Stern–Pedlosky necessary condition for baroclinic/barotropic instability.

4. $\partial\langle\omega_{\mathrm{abs}}\rangle/\partial r = 0$ in the interior and $\partial\langle u_\varphi\rangle/\partial z$ takes the same sign at both $z = 0$ and $z = H$.

If any one of the above conditions is satisfied, it gives the necessary condition for the presence of an instability (baroclinic or barotropic to determined based on energy exchange which will be discussed later in section 7.3) within the domain. It is also to be noted that the condition given in Eq. (7.8) can be satisfied anywhere in the domain implying that the wave is excited locally. Hence, the Eq. (7.8) doesn't need to be satisfied over the whole domain for the instability to exist. Figure 7.2 shows an illustration of how this condition can be satisfied in the flow. It can be seen that the integral of radial absolute vorticity over the range 0-R will be negative. However, $\partial\langle\omega_{\mathrm{abs}}\rangle/\partial r$ changes its sign in the region between r_1 and r_2 as illustrated in Fig. 7.2 and hence P' wave is excited in that region, which is only a part of the whole domain.

In the next section, the computational results for cases with and without tropical cyclone-like vortex are analysed to study the above condition illustrated in Fig. 7.2. This helps to understand plausible reason for the formation and sustenance of a large-scale tropical cyclone-like vortex in the domain.

7.2 Results & Discussion

7.2.1 Signature of Barotropic/Baroclinic Instability

In this section, the simulation showing a tropical cyclone-like vortex is analysed to check whether the CSP necessary criteria for the presence of barotropic/baroclinic instability in the flow is satisfied.

As seen in section 7.1, the spatial variation of absolute vorticity plays a key role in identifying the presence of instability. Since the background rotation is constant in the present case due to f-plane approximations, only the spatial variation of axial vorticity is analysed. Figure 7.3 shows the time- and azimuthal-averaged axial vorticity contour for case 2 in Table 5.1. The high-magnitude cyclonic vorticity is concentrated near the core of the domain. It can be seen that the magnitude of axial vorticity decreases radially as one moves from the core towards the sidewall. This behaviour is the same across heights. In order to see the variation of axial vorticity near the eye-eyewall and sidewall region, the radial gradient of time and azimuthal average axial vorticity $\partial\langle\tilde{\omega}_z^*\rangle/\partial r$ is plotted in Fig. 7.3. There is a change in sign in the $\partial\langle\tilde{\omega}_z^*\rangle/\partial r$ plot near the inner region of the eyewall at $r/R \approx 0.5$. Similarly there is a change in sign of $\partial\langle\tilde{\omega}_z^*\rangle/\partial r$ near the sidewall at $r/R \approx 0.975$. Thus, condition number 1 of the Charney-Stern-Pedlosky criteria for barotropic-baroclinic instability is satisfied for the tropical cyclone-like vortex. Therefore, the Eq. 7.8 will be satisfied near the eyewall region around $r/R \approx 0.05$ and near the sidewall at around $r/R \approx 0.975$ which will enable wave propagation in this region. Since slip boundary condition is assumed at the the upper boundary of the domain (see Fig. 5.1) therefore $\partial\langle u_\varphi\rangle/\partial z = 0$ at $z = H$. Thus, condition number 2 cannot be satisfied. Similarly, $\partial\langle\omega_z^*\rangle/\partial z \neq 0$ in the interior, which prevents satisfying the condition number 4. Also, condition number 3 is not satisfied because there is a uniform reduction in the value of $\langle\tilde{\omega}_z^*\rangle$ from the centre of the domain to the sidewall at $z/H = 0$ thus $\partial\langle\tilde{\omega}_z^*\rangle/\partial r < 0$ whereas $\partial\langle\tilde{u}_\varphi\rangle/\partial z > 0$ at $z/H = 0$. Therefore, the flow exhibits baroclinic/barotropic instability by satisfying condition 1 of the Charney-Stern-Pedlosky criteria. The time evolution of the the radial

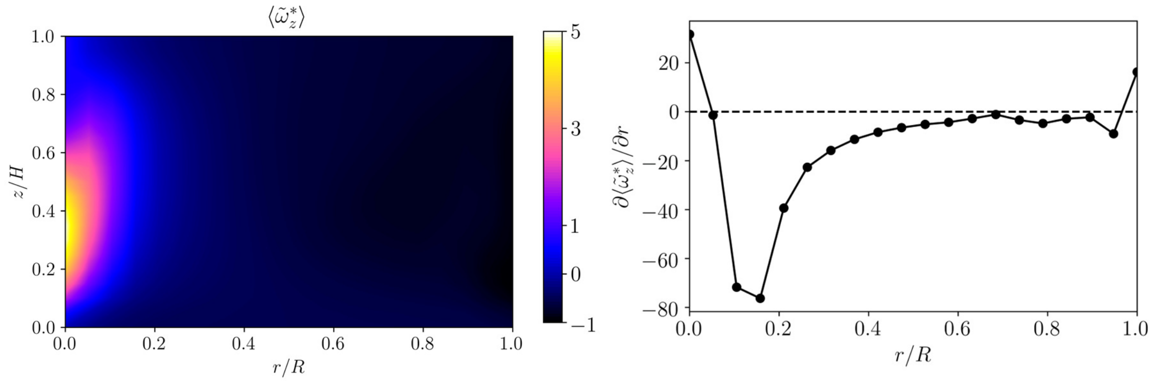

Fig. 7.3 The time- and azimuthal-average axial vorticity contour $\langle\tilde{\omega}_z^*\rangle$ for case 2 in Table 5.1 (left). The radial variation of radial gradient of $\langle\tilde{\omega}_z^*\rangle$ at $z/H = 0.75$ for case 2 in Table 5.1 (right). The axial vorticity is normalised with background rotation Ω.

gradient of axial vorticity is plotted next to get insight into what time the instability sets up in the flow.

The radial variation of $\partial\langle\omega_z^*\rangle/\partial r$ is shown in Fig. 7.4 for three different times $\tau_2 = 0.9$, 1.0, and 1.3 to understand when the $\partial\langle\omega_z^*\rangle/\partial r$ starts changing the sign in the domain for cases 2 and 4 in Table 5.1. These times are chosen to see the radial variation of the the radial gradient of axial vorticity before, during and after cyclogenesis. It can be seen that before the start of cyclogenesis, at $\tau_2 = 0.9$, there isn't a change in the sign of $\partial\langle\omega_z^*\rangle/\partial r$ within the domain. Whereas at $\tau_2 = 1.0$, and 1.3, it can be seen that there is a change in the sign of $\partial\langle\omega_z^*\rangle/\partial r$ near the centre and sidewall of the domain. It is because, as we have seen in chapter 5 that, from $\tau_2 = 1$, the eye-eyewall features begin to appear in the large-scale cyclonic vortices during the cyclogenesis time $\tau_2 = 1$, poloidal flow is set up in the domain and sweeping up of the bottom boundary layer to form an eye-eyewall is also seen near the core of the domain. In the region closer to the sidewall, a well organise structures start appearing (as wall modes are seen in chapter 4 & chapter 6). The well-defined eyewall and wall mode structure are seen around the region where $\partial\langle\omega_z^*\rangle/\partial r$ changes sign. It is still unclear as to whether the emergence of eyewall and wall modes causes the sign change in the radial plot of $\partial\langle\omega_z^*\rangle/\partial r$ or vice-versa. Therefore to summarise the CSP is a necessary criterion for baroclinic/barotropic instability, is satisfied in the flow at the start of cyclogenesis $\tau_2 = 1$. Then at the same instant, the combined evolution of eye-eyewall and wall modes is observed at these locations. The interaction between the eyewall and the wall modes near the sidewall is understood by revisiting the earlier analysis.

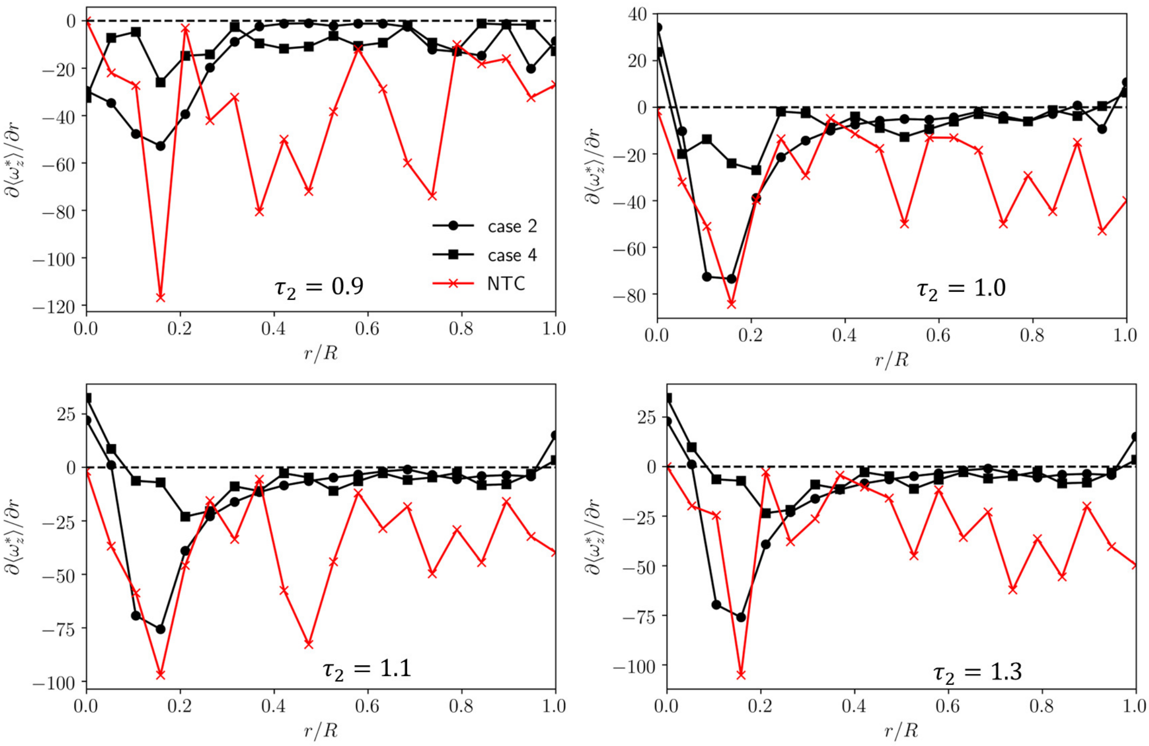

Fig. 7.4 The radial variation of radial gradient of axial vorticity, $\partial\langle\omega_z^*\rangle/\partial r$ at $z/H = 0.75$ for case 2 in Table 5.1 at three different times $\tau_2 = 0.9$, 1.0, 1.1, and 1.3 for case 2 and 4 in Table 5.1 and for case 70 in Table A.1 which does not form tropical cyclone-like vortex denoted by NTC in the figure legend. The axial vorticity is normalised with background rotation Ω.

The radial variation of $\partial\langle\omega_z^*\rangle/\partial r$ at different instants during the cyclogenesis is shown in Fig. 7.4 and the time- and volume-average $\partial\langle\tilde{\omega}_z^*\rangle/\partial r$ in Fig. 7.3 clearly shows that the radial gradient of axial vorticity changes sign near the eyewall and sidewall. As discussed in section 7.1, around the region where $\partial\langle\omega_z\rangle/\partial r$ changes sign the Eq. 7.8 is satisfied, leading to the excitation of a wave. We can see from Fig. 6.3 that azimuthal mode $m = 2$ (at $r/R = 0.05$ near eyewall) and $m = 18$ (at $r/R = 0.95$ near the sidewall) are the dominant mode in these regions during and after the cyclogenesis phase. Also, $m = 18$ wall mode near the sidewall rotates in the retrograde sense (see chapter 4) as the background azimuthal velocity near the sidewall is opposite (negative) to that of the background rotation (refer to Fig. 5.4(b)). Similarly, $m = 2$ mode dominant in the eye-eyewall region rotates in the prograde sense as the background azimuthal velocity is positive (refer to Fig. 5.4(b)). Also, the magnitude of the azimuthal velocity in the region close to eye-eyewall ($r/R \approx 0.05$) is very low compared to the magnitude of azimuthal velocity near the sidewall ($r/R \approx 0.975$). Thus, the wave with $m = 18$ mode near the sidewall rotates faster compared to the wave with $m = 2$ mode near the eyewall. Also, the phase speed of the two counter-rotating (prograde-retrograde) waves can be computed from the frequency-wavenumber plot. The phase speed for the prograde wave near the eyewall and the phase speed for the retrograde wave near the sidewall was found to be 0.1. Thus, the phase speed of these two waves is the same. Therefore, the two waves excited near the eyewall and sidewall due to a change in sign of $\partial\langle\omega_z\rangle/\partial r$ as seen in Fig. 7.4 phase-lock with each other, thereby helping sustain the large-scale cyclonic vortex in the domain.

In order to verify whether the observation seen so far are unique to only for simulation showing tropical cyclone-like vortex in the domain, computational results which do not show tropical cyclone-like vortex are analysed. To carry out the analysis, case 70 of Table. A.1 in Appendix. A is used. In order to ensure that the flow is fully evolved, the volume-averaged kinetic energy is monitored in the flow with time. The time evolution of volume-averaged kinetic energy for the case 70 is shown in Fig. 7.5 (top row). The kinetic energy is normalised by $(\Omega R)^2$. The volume-averaged kinetic energy becomes fully evolved and doesn't change much after $\tau > 70$. Figure 7.5 (bottom four frames) shows the spatial contours of axial vorticity, ω_z, and temperature perturbation, θ are shown at two time instants after the flow is fully evolved, namely, $\tau = 180$ and 200. The axial vorticity is normalised with background rotation Ω, and temperature perturbation is normalised with βH. It can be seen that though hot temperatures are concentrated near the centre of the domain, as seen for tropical cyclone-like vortex, the structure is not axisymmetric. The hot fluid concentrates near the centre because of the net transport of angular momentum towards the centre of the domain due to the presence of enhanced inflow with isothermal sidewall boundary condition (see chapter 4) but that does not help in the organisation of the flow into the symmetric vortex. The axial vorticity contour also exhibits a disorganised structure with the presence of many small-scale cyclonic vortices ($\omega_z^* > 0$) in the domain. Fig. 7.6 shows the axial velocity contour in a radial plane at $\varphi = 0°$ and azimuthal-averaged azimuthal vorticity $\langle\omega_\varphi^*\rangle$. We can see that the domain is filled with convective rolls, as seen with alternating positive and negative values of u_z^*. Also, there isn't sweeping up of bottom boundary layer ($\langle\omega_\varphi^*\rangle < 0$) which is typical in a tropical cyclone-like vortex (see chapter 4). Therefore, we have seen that for the simulation of flow outside the range of $Ro \approx C/\Gamma$, where $\sqrt{2} \le C \le 2\sqrt{2}$ does not organise into a large-scale tropical cyclone-like vortex with eye-eyewall and spiral band features. Also, the radial variation of $\partial\langle\omega_z\rangle/\partial r$ at $z/H = 0.75$ is plotted for four different time instant in Fig. 7.4. The

$\partial\langle\omega_z\rangle/\partial r$ plot does not change the sign in the radial direction for all the time instant. A similar observation is seen at all other heights in the domain for this case. Thus, we observed that the CSP condition for instability is not satisfied for a flow without a tropical cyclone-like vortex in the domain.

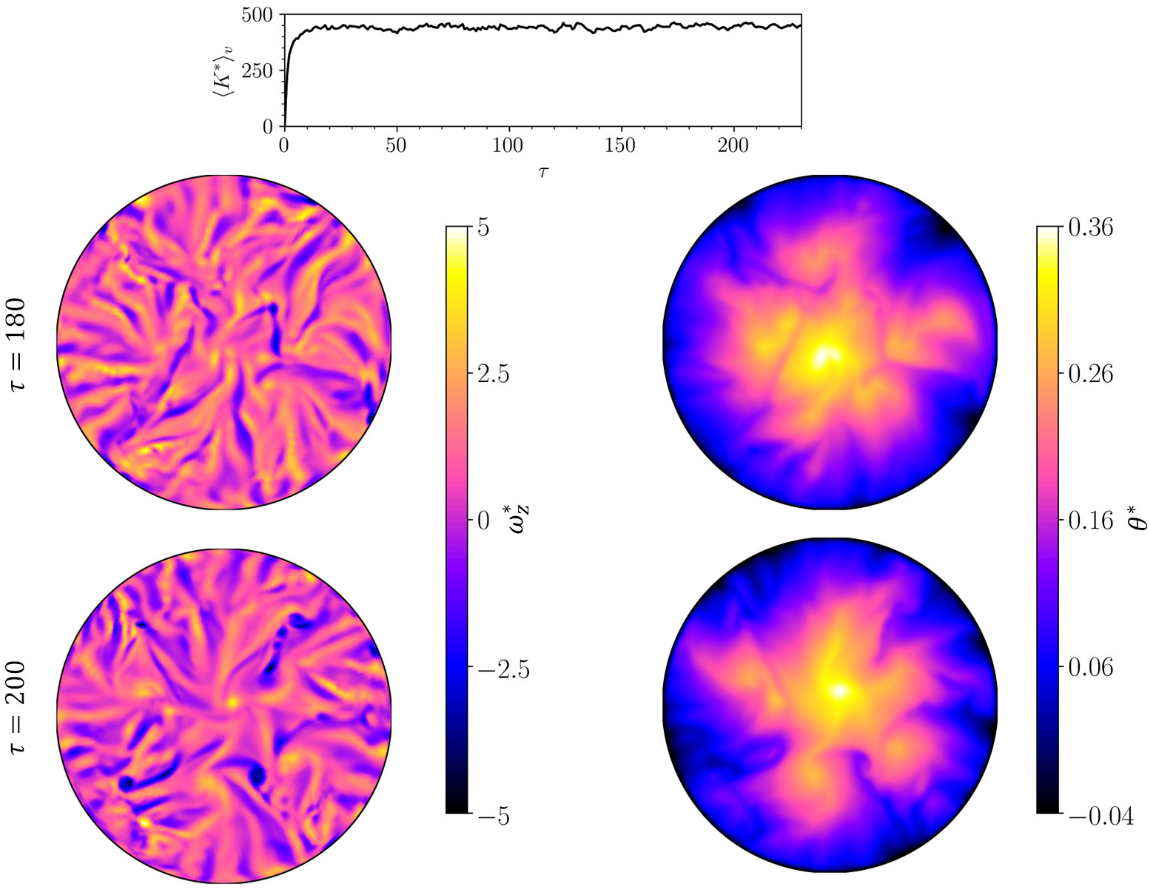

Fig. 7.5 The time evolution of volume averaged kinetic energy $\langle K^*\rangle_v$ normalised with $(\Omega R)^2$ for $Re = 4 \times 10^{10}$, $E = 10^{-9}$, $Pr = 0.1$, $\Gamma = 0.05$ (case 70 of Table. A.1) which does not form tropical cyclone-like vortex (top). The contour of axial vorticity ω_z^* normalised with rotation rate Ω and temperature perturbation θ^* normalised with βH at $z/H = 0.75$ and for $\tau = t\Omega = 180$ & 200 (bottom four frames).

To summarise this section, we have seen that condition number 1 of the Charney-Stern-Pedlosky criteria for the barotropic/baroclinic instability is satisfied in the domain. The radial gradient of axial vorticity changes signs at the onset of cyclogenesis near the eye-eyewall region and the sidewall boundary. The change in sign at these locations excites $m = 2$ prograde wave (near eyewall) and $m = 18$ retrograde wave (near sidewall). These are typical for baroclinic/barotropic instability Holton (2004), Vallis (2017),

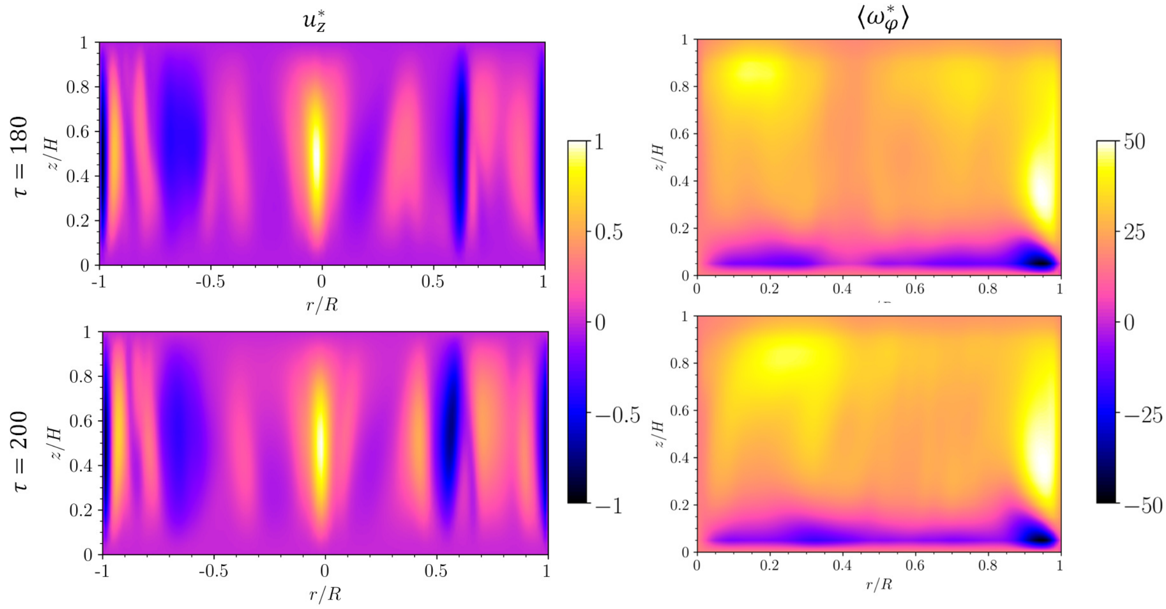

Fig. 7.6 The contour of axial velocity u_z^* normalised with (ΩR) shown in the radial plane at $\varphi = 0°$ and azimuthal-averaged tangential vorticity $\langle \omega_\varphi^* \rangle$ normalised with Ω for $\tau = t\Omega = 180$ & 200.

and they phase-lock with each other since they have the same phase speed and help maintain the large-scale vortex in the domain. The energy flow diagram is compared between simulations showing tropical cyclone-like vortex and otherwise to verify the dominant energy exchange term in the simulation showing tropical cyclone-like vortex. This helps identify the presence of either barotropic or baroclinic instability in the tropical cyclone-like vortex. In the case of the flow which does not show a tropical cyclone-like vortex in the domain the $\partial\langle\omega_z\rangle/\partial r$ does not change sign in the domain.

7.2.2 Energy Exchange Revisited

In the previous section, it became clear that the tropical cyclone-like vortex satisfy the CSP criteria near the eyewall and sidewall, and the resulting wave excited around the region phase-lock with each other to help sustain large-scale vortex in the domain. In this section, we look into the energy exchange diagram to understand whether the instability is barotropic or baroclinic.

The energy flow diagram is constructed once the volume-averaged energy in the domain is saturated for several tens of rotation time.The energy flow diagram in Fig. 7.7(a) (same as 6.9(c)) for a tropical cyclone-like vortex obtained for case 4 in Table

5.1 suggests that the dominant energy exchange is between azimuthal mean potential and kinetic energy. This is because the buoyancy drives the flow in the model and the inherent nature of the buoyant convection is to convert the potential energy into kinetic energy. The second most dominant energy exchange, which helps sustain the tropical cyclone-like vortex, is due to the exchange between azimuthal mean and asymmetric kinetic energy. This suggests that barotropic instability helps form and sustain the large-scale tropical cyclone-like vortex in the domain. However, to further verify the same, the energy flow diagram is constructed from a simulation which does not yield a tropical cyclone-like vortex, as discussed in the previous section. Figure 7.7 shows the energy flow diagram for case 70 of Table. A.1. It can be seen that the magnitude of $\langle \tilde{C}_k^* \rangle_v$ denoting the time and volume-averaged energy the exchange between the azimuthal mean kinetic energy and asymmetric kinetic energy is negligible compared to other energy exchange terms. Therefore, comparing the energy flow diagram for the case with and without a tropical cyclone-like vortex gives evidence that barotropic instability dominates in the fully evolved large-scale cyclonic vortex in the domain further to satisfy the necessary CSP criteria for the instability.

The view presented here regarding the genesis of the tropical cyclone-like vortex in the simple RRBC model differs from that expressed by Fujiwhara (1921), Montgomery et al. (2006). In those studies, genesis is attributed to merging small-scale vortices to form a large-scale cyclonic vortex. In the present work, we have seen vortex merging happen in the domain, but the resulting vortices formed from vortex merging eventually dissipate in the flow over time. The large-scale cyclonic vortex is suddenly formed from a single small-scale cyclonic vortex (see the movie titled "*Ch7-movie*" referred to earlier in this chapter with the link). And this sudden formation of a large-scale cyclonic vortex from a small-scale cyclonic vortex is attributed here to the barotropic instability, which enables the excitation and interaction of two waves far apart in the domain leading to the formation of a large-scale structure. Though the phase-locking of waves is seen in the flow with barotropic and baroclinic instability in the past for rotating convective flows (Hide, 1969, Vallis, 2017), this study shows that the barotropic instability combined with the phase-locking of waves results in the formation of tropical cyclone-like vortex in the simple RRBC model.

7.3 Summary

In this chapter, the probable reason for the formation and maintenance of a tropical cyclonic-like vortex in a RRBC setup is studied. The conclusions derived are as follows:

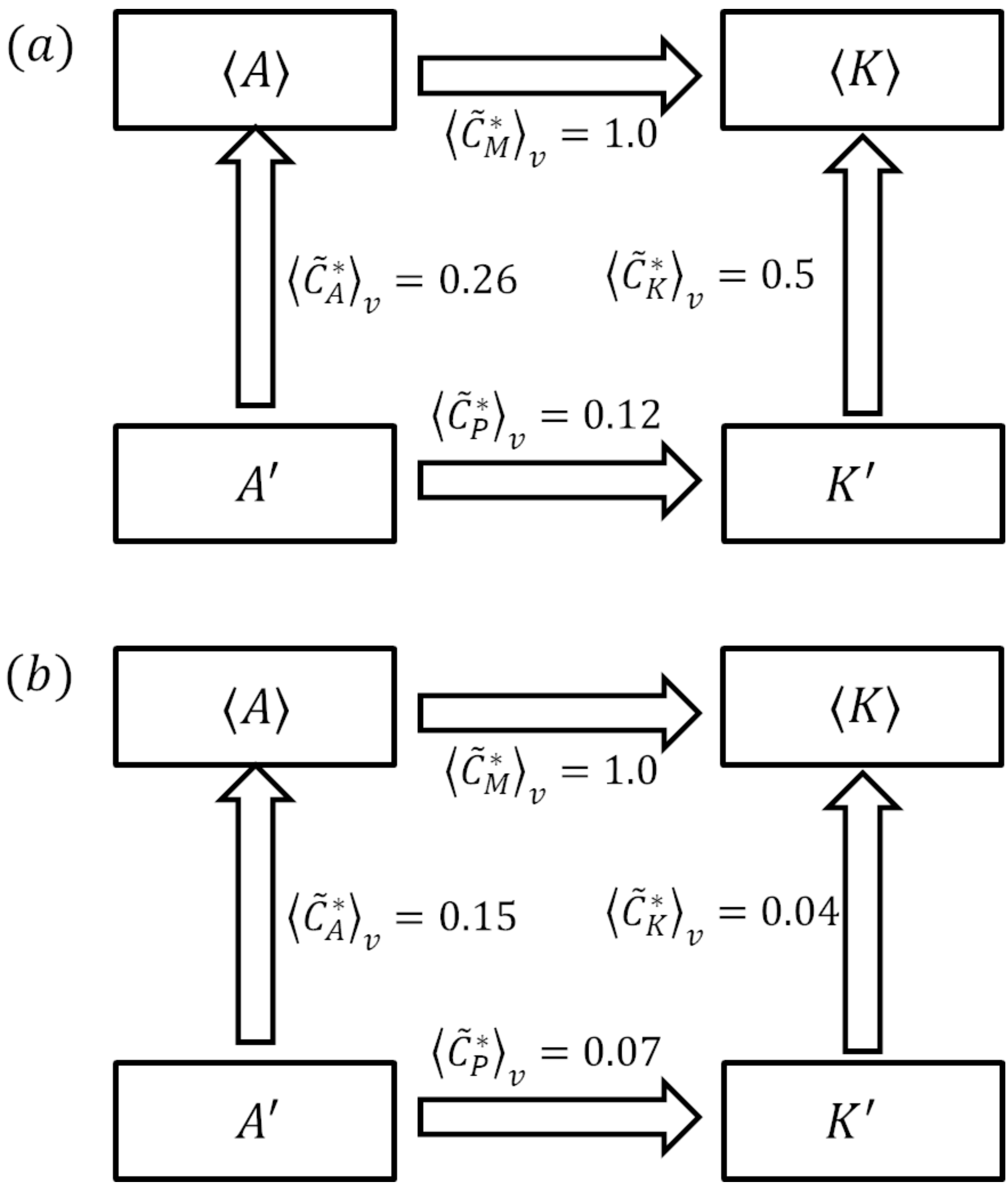

Fig. 7.7 (a) Energy flow diagram for tropical cyclone-like vortex obtained for case 4 in Table 5.1. (b) Energy flow diagram for case 70 in Table. A.1 which does not form tropical cyclone-like vortex. The energy exchange values are normalised to have 1.0 as a maximum value. The maximum value used for normalisation is (a) $\langle \tilde{C_M^*} \rangle_v = 4661.6$ and (b) $\langle \tilde{C_M^*} \rangle_v = 4102.1$

1. The radial gradient of axial vorticity changes sign in the domain at two different locations near the eyewall and sidewall, thereby satisfying the condition 1 of the Charney-Stern-Pedlosky criteria for baroclinic/barotropic instability.

2. The radial gradient of axial vorticity begins to change signs at $\tau_2 \approx 1$, i.e., during the start of the cyclogenesis when the eye-eyewall and spiral bands features begin to appear on the large-scale cyclonic vortex.

3. $m = 2$ prograde (near eyewall) and $m = 18$ retrograde (near sidewall) mode is dominant around the the region where the radial gradient of axial vorticity changes sign. These two mode phase lock with each other, resulting in the sustenance of the large-scale tropical cyclone-like vortex in the domain for the remainder of the simulation time.

4. The comparison of energy flow diagram between simulation with and without tropical cyclone-like vortex in the domain confirms the barotropic instability in the flow with the rate of energy exchange from asymmetric to azimuthally averaged kinetic energy has a dominant magnitude compared to the energy exchange rate from asymmetric to azimuthally averaged potential energy.

5. Thus, the combined evolution of eyewall and wall modes with the simultaneous excitation of the waves at these locations, due to the onset of barotropic instability, lead to the formation of the desired tropical cyclone-like vortex in the domain.

Chapter 8

Conclusions and Future Work

In this work, an attempt is made to study the hydrodynamics of cyclogenesis using a simple rotating Rayleigh Benard convection setup. To this aim a 3D laminar and turbulent tropical cyclone-like vortex was simulated in a rotating Rayleigh-Benard convection setup with a Boussinesq fluid in a shallow cylindrical domain. A large Eddy Simulation (LES) framework has been used to model the turbulence. The effects and accuracy of the numerical model on the simulated tropical cyclone-like vortex are studied. The similarity of the resulting structure of the tropical cyclone-like vortex with an actual tropical cyclone is highlighted. Subsequently, the results obtained from the simulation are analysed to get physical insights into the hydrodynamics of cyclogenesis. This chapter summarises the results presented in the thesis and suggests directions for future work.

8.1 Effects and Accuracy of Numerical Model

In Chapter 4, the axisymmetric and 3D tropical cyclone-like vortex are compared to better understand the effect of the vortex evolution along the third dimension, the azimuthal direction. It was found that due to diffusive effects the 3D tropical cyclone-like vortex is found to be less intense compared to its axisymmetric counterpart. Also, the effect of sidewall thermal boundary condition on the formation of 3D tropical cyclone-like vortex was studied by changing the sidewall boundary condition from insulated to isothermal. It was found that with the insulated boundary conditions the retrograde asymmetric mode $m = 2$ with spiral inner core are more dominant compared to axisymmetric mode $m = 0$ thereby preventing the formation of symmetric large scale tropical cyclone-like vortex in the domain. On the other hand, axisymmetric tropical cyclone-like vortex were obtained with isothermal sidewall. Thus, the thermal boundary condition along the sidewall strongly influence the formation of large-scale tropical cyclone-like vortex in the domain. However, the upsweep of the bottom boundary forming the eye-eyewall observed by Oruba et al. (2017) in their laminar axisymmetric calculations is also observed in the current 3D simulations.

In Chapter 5, turbulent tropical cyclone-like vortex are simulated using a Large Eddy Simulation (LES) paradigm. The capabilities of LES in resolving large scale turbulence and modelling small scale turbulence is leveraged to conduct simulation of tropical cyclone-like vortex spanning 10 orders of magnitude. The tropical cyclone-like vortex obtained from both laminar and turbulent simulations are compared qualitatively with real tropical cyclones data (Frank, 1977, Willoughby, 1990, Anthes, 2016). It was found that the structure obtained compares well. Also, the gradient wind balance as observed in an actual tropical cyclone are also seen for the tropical cyclone-like vortex around its core obtained from the simple model (Willoughby, 1990). The gradient wind balance is the balance of the pressure, Coriolis and centrifugal forces (Willoughby, 1990). In chapter 6, the asymmetries in the azimuthal direction for the tropical cyclone-like vortex are analysed. The spatial features of asymmetries present in the dry convection simulations conducted here take the form of spiral bands resembling the rain bands seen in the actual tropical cyclones. The angle and the phase speed for the spatial bands are measured from the simulation and are compared with that of actual tropical cyclones (Anthes, 2016). It was found that results agree well.

8.2 Insights of Cyclogenesis

The simulation data are analysed in chapter 5 and a timescale for start of cyclogenesis is proposed. It is the time at which the subsidence inside the large-scale cyclonic vortex begins thereby giving it the unique spatial feature such as eye, eyewall and spiral bands, although the eyewall is formed earlier through upsweep of the bottom boundary layer. This timescale is found to be proportional to $\sqrt{Re_t}$ where $Re_t = VH/\langle\nu_t\rangle_{\rm BL}$ is the turbulent Reynolds number. It is found that two timescales control the spinup of the tropical cyclone-like vortex in the model, namely a timescale for the start of cyclogenesis and the spin-up timescale, which is proportional to $1/\sqrt{E_t}$ where $E_t = \langle\nu_t\rangle_{\rm BL}/\Omega H^2$ (Greenspan & Howard, 1963). By the later timescale, the vortex with all its features including eye, eyewall and spiral bands are clearly visible. The timescale for the start of cyclogenesis is smaller thanthe spin-up timescale for the formation of the large scale vortex. To see the implication of the results to actual cyclogenesis, the tropical cyclone track data obtained from United States Military's Joint Typhoon

Warning Centre (JTWC) database are analysed using these two timescales. It is found that hydrodynamic conditions for cyclogenesis obtained from the present work agree well for the real tropical cyclone. The energy transfer from asymmetries to the symmetric vortex is studied in detail in chapter 6 to understand the importance of the energy transfer process in sustaining the tropical cyclone-like vortex in the domain. In chapter 7, the plausible reason for the formation of large-scale tropical cyclone like vortex from quiescent state is studied. When simulations are performed for the flow parameter outside the range $\sqrt{2} \leq Ro\Gamma \leq 2\sqrt{2}$ tropical cyclone-like vortex is not observed and the exchange of energy from asymmetric to azimuthal kinetic energy is not dominant as seen for the tropical cyclone-like vortex (see chapter 6). The dominant energy exchange between azimuthal mean and asymmetric kinetic energy denotes the presence of barotropic instability in the flow (Holton, 2004). The presence of barotropic instability in the tropical cyclonic vortex is further confirmed by plotting the radial variation of radial gradient of axial vorticity (Holton, 2004). It is seen that radial gradient of axial vorticity changes sign in the radial direction near the eyewall and sidewall denoting the excitation of counter-rotating wave in these regions. These wave phase-lock with each other thereby helping the sustenance of large scale tropical cyclone-like vortex in the domain. Thus, the combined evolution of eyewall and wall modes with the simultaneous excitation of the waves at these locations due to the onset of barotropic instability leads to the formation of the desired tropical cyclone-like vortex in the domain.

8.3 Future Work

The work and analysis presented in this thesis have provided useful insights into the hydrodynamics of cyclogenesis. Nevertheless, there are still various aspects where additional simulations and analysis would be of interest. The specific future works recommended are as follows:

- Regarding the sidewall thermal boundary condition effects, it would be of interest to study the cause for the asymmetric modes to be dominant with insulated sidewall leading to chaotic convection inhibiting the formation of tropical cyclone-like vortex in the domain.

- The cyclogenesis timescale proposed in this work is checked only for tropical cyclone track data available in the JTWC database. The conditions need to be checked for tropical cyclone track data from other databases like MET office, NASA etc.

- The simulations can be made more realistic by replacing f-plane with β plane approximations to study the influences of Rossby wave phenomenon that are ubiquitous in atmospheric flows.

- Finding a suitable algorithm to automatically track the small scale cyclones and anticylones separately as the computations evolve would be of great intrest and very useful. This can enable us to better understand whether vortex merging plays a role in the formation of the large-scale tropical cyclone-like vortex. Also, the individual trajectory of the cyclonic and anti-cyclonic vortices obtained by tracking them will be useful to study the role of Ekman pumping in the flow evolution.

- The role of kinetic and potential energy transfer between different wavenumbers needs to be studied in detail to understand the inverse cascade of energy required to form a large tropical cyclone-like vortex from a small scale cyclonic vortex.

- The results from this work suggests that the hydrodynamical effects play an important role in the formation and maintenance of tropical cyclone-like vortex. However, additional effects which are present in reality such as stratification, moisture, external wind shear effects and variation of rotation rate must be considered. Incorporating these effects gradually would be helpful to assess their individual influences on the cyclogenesis.

References

Ahlers, G., Grossmann, S., & Lohse, D. (2009). Heat transfer and large scale dynamics in turbulent Rayleigh-Bénard convection. *Rev. Mod. Phys.*, 81(2):503.

Anthes, R. (2016). *Tropical cyclones: their evolution, structure and effects*, volume 19. Springer.

Anthes, R. A. (1972). Development of asymmetries in a three-dimensional numerical model of the tropical cyclone. *Mon. Weather Rev.*, 100(6):461–476.

Assenheimer, M. & Steinberg, V. (1994). Transition between spiral and target states in Rayleigh–Bénard convection. *Nature*, 367(6461):345–347.

Atkinson, J. W., Davidson, P. A., & Perry, J. E. G. (2019). Dynamics of a trapped vortex in rotating convection. *Phys. Rev. Fluids*, 4(7):1–15.

Aurnou, J. M., Bertin, V., Grannan, A. M., Horn, S., & Vogt, T. (2018). Rotating thermal convection in liquid gallium:multi-modal flow, absent steady columns. *J. Fluid Mech.*, 846:846.

Bergeron, T. (1954). The problem of tropical hurricanes. *Q. J. R. Meteorol. Soc.*, 80(344):131–164.

Bister, M. & Emanuel, K. A. (1997). The genesis of Hurricane Guillermo: TEXMEX analyses and a modeling study. *Mon. Weather Rev.*, 125(10):2662–2682.

Blackadar, A. K. (1962). The vertical distribution of wind and turbulent exchange in a neutral atmosphere. *J. Geophys. Res.*, 67(8):3095–3102.

Bodenschatz, E., de Bruyn, J. R., Ahlers, G., & Cannell, D. S. (1991). Transitions between patterns in thermal convection. *Phys. Rev. Lett.*, 67(22):3078.

Bodenschatz, E., Pesch, W., & Ahlers, G. (2000). Recent developments in Rayleigh-Benard convection. *Ann. Rev. Fluid Mech.*, 32(1):709–778.

Bosart, L. F. & Bartlo, J. A. (1991). Tropical storm formation in a baroclinic environment. *Mon. Weather Rev.*, 119(8):1979–2013.

Boussinesq, J. (1903). *Thōrie analytique de la chaleur*, volume 2. Gauthier-Villars.

Braun, S. A. (2002). A cloud-resolving simulation of Hurricane Bob (1991): Storm structure and eyewall buoyancy. *Mon. Weather Rev.*, 130(6):1573–1592.

Braun, S. A., Scott, A., Kakar, R., Zipser, E., & others (2013). NASA's Genesis and Rapid Intensification Processes (GRIP) field experiment. *Bull. Amer. Meteor.*, 94(3):345–363.

Bryan, G. H. & Rotunno, R. (2009). The maximum intensity of tropical cyclones in axisymmetric numerical model simulations. *Mon. Weather Rev.*, 137(6):1770.

Buell, J. C. & Catton, I. (1983). The effect of wall conduction on the stability of a fluid in a right circular cylinder heated from below. *Trans. ASME J. Heat Transfer*, 105:255.

Caldwell, D. R., Atta, C. W. V., & Helland, K. N. (1972). A laboratory study of the turbulent Ekman layer. *Geophys. Astrophys. Fluid Dyn.*, 3:125–160.

Camargo, S. J., Emanuel, K. A., & Sobel, A. H. (2007a). Use of a genesis potential index to diagnose ENSO effects on tropical cyclone genesis. *J. Climate*, 20(19):4819–4834.

Camargo, S. J., Sobel, A. H., Barnston, A. G., & Emanuel, K. A. (2007b). Tropical cyclone genesis potential index in climate models. *Tellus A*, 59(4):428–443.

Chandrasekhar, S. (1961). *Hydrodynamic and hydromagnetic stability*. The Clarendon Press, Oxford, UK.

Charney, J. G. & Stern, M. E. (1962). On the stability of internal baroclinic jets in a rotating atmosphere. *J. Atmos. Sci.*, 19(2):159–172.

Chen, S. S., Knaff, J. A., & Marks, F. D. (2006). Effects of vertical wind shear and storm motion on tropical cyclone rainfall asymmetries deduced from TRMM. *Mon. Weather Rev.*, 134(11):3190–3208.

Chereskin, T. K. & Roemmich, D. (1991). A comparison of measured and wind-derived Ekman transport at 11 N in the Atlantic Ocean. *J. Phys. Oceanogr.*, 21(6):869–878.

Coleman, G. N. (1999). Similarity statistics from a direct numerical simulation of the neutrally stratified planetary boundary layer. *J. Atmos. Sci.*, 56(6):891–900.

Coleman, G. N., Ferziger, J. H., & Spalart, P. R. (1990). A numerical study of the turbulent Ekman layer. *J. Fluid Mech.*, 213:313–348.

Couston, L.-A., Lecoanet, D., Favier, B., & Bars, M. L. (2020). Shape and size of large-scale vortices: a generic fluid pattern in geophysical fluid dynamics. *Phys. Rev. Res.*, 2:023143–1–15.

Cross, M. C. & Hohenberg, P. C. (1993). Pattern formation outside of equilibrium. *Rev. Mod. Phys.*, 65(3):851.

Davidson, N. E. (1995a). Vorticity budget for AMEX. Part I: diagnostics. *Mon. Weather Rev.*, 123(6):1620–1635.

Davidson, N. E. (1995b). Vorticity budget for AMEX. Part II: Simulations of monsoon onset, midtropospheric lows, and tropical cyclone behavior. *Mon. Weather Rev.*, 123(6):1636–1659.

Davidson, P. A. (2013). *Turbulence in rotating, stratified and electrically conducting fluids*. Cambridge University Press.

de Wit, X. M., Guzmán, A. J. A., Madonia, M., Cheng, J. S., Clercx, H. J. H., & Kunnen, R. P. J. (2020). Turbulent rotating convection confined in a slender cylinder: the sidewall circulation. *Phys. Rev. Fluids*, 5(2):023502.

Dengler, K. & Reeder, M. J. (1997). The effects of convection and baroclinicity on the motion of tropical-cyclone-like vortices. *Q. J. R. Meteorol. Soc.*, 123(539):699–725.

Didlake, A. C. & Houze, R. A. (2013). Convective-scale variations in the inner-core rainbands of a tropical cyclone. *J. Atmos. Sci.*, 70(2):504–523.

Dold, P. & Benz, K. W. (1999). Rotating magnetic fields: fluid flow and crystal growth applications. *Prog. Crystal Growth and Charact.*, 38:7–38.

Ecke, R. E., Zhong, F., & Knobloch, E. (1992). Hopf bifurcation with broken reflection symmetry in rotating Rayleigh-Bénard convection. *Euro. Phys. Lett.*, 19(3):177.

Ekman, V. W. (1905). On the influence of the earth's rotation on ocean-currents.

Emanuel, K. (2010). Tropical cyclone activity downscaled from NOAA-CIRES reanalysis, 1908–1958. *J. Adv. Model. Earth Syst.*, 2(1).

Emanuel, K. A. (1989). The finite-amplitude nature of tropical cyclogenesis. *J. Atmos. Sci.*, 46(22):3431–3456.

Emanuel, K. A. (1991). The theory of hurricanes. *Annu. Rev. Fluid Mech.*, 23(1):179–196.

Emanuel, K. A. (1994). The physics of tropical cyclogenesis over the eastern Pacific. *Tropical cyclone disasters*, 136:142.

Emanuel, K. A. (1995). The behavior of a simple hurricane model using a convective scheme based on subcloud-layer entropy equilibrium. *J. Atmos. Sci.*, 52(22):3960–3968.

Emanuel, K. A. (2018). 100 Years of Progress in Tropical Cyclone Research. *Meteorol. Monogr.*, 59(1979):15.1–15.68.

Emanuel, K. A. & Nolan, D. S. (2004). Tropical cyclone activity and the global climate system. In *26th conference on hurricanes and tropical meteorolgy*.

Enagonio, J. & Montgomery, M. T. (2001). Tropical cyclogenesis via convectively forced vortex Rossby waves in a shallow water primitive equation model. *J. Atmos. Sci.*, 58(7):685–706.

Expedition 56 Crew NASA (2018). Hurricane Hector just south of the Hawaiian island chain. [online] https://www.nasa.gov/image-feature/hurricane-hector-just-south-of-the-hawaiian-island-chain accessed on June 3, 2022.

Favier, B. & Knobloch, E. (2020). Robust wall modes in rapidly rotating Rayleigh-B\'enard convection. *J. Fluid. Mech.*, 895.

Favier, B., Silvers, L. J., & Proctor, M. R. E. (2014). Inverse cascade and symmetry breaking in rapidly rotating Boussinesq convection. *Phys. Fluids*, 26:096605.

Frank, W. M. (1977). The structure and energetics of the tropical cyclone I. Storm structure. *Mon. Weath. Rev.*, 105:1119–1135.

Frank, W. M. & Ritchie, E. A. (1999). Effects of environmental flow upon tropical cyclone structure. *Mon. Weather Rev.*, 127(9):2044–2061.

Frank, W. M. & Ritchie, E. A. (2001). Effects of vertical wind shear on the intensity and structure of numerically simulated hurricanes. *Mon. Weather Rev.*, 129(9):2249–2269.

Fujiwhara, S. (1921). The natural tendency towards symmetry of motion and its application as a principle in meteorology. *Q. J. R. Meteorol. Soc.*, 47(200):287–292.

Germano, M., Piomelli, U., Moin, P., & Cabot, W. H. (1991). A dynamic subgrid-scale eddy viscosity model. *Phys. Fluids*, 3(7):1760–1765.

Geurts, B. J. (2003). *Elements of direct and large eddy simulation*. RT Edwards, Inc.

Gnanadesikan, A. & Weller, R. A. (1995). Structure and instability of the Ekman spiral in the presence of surface gravity waves. *J. Phys. Oceanogr.*, 25(12):3148–3171.

Gopalakrishnan, S. G., Marks, F. D., Zhang, X., Bao, J. W., Yeh, K. S., & Atlas, R. (2011). The experimental HWRF system: A study on the influence of horizontal resolution on the structure and intensity changes in tropical cyclones using an idealized framework. *Mon. Weather Rev.*, 139(6):1762–1784.

Gray, W. M. (1968). Global view of the origin of tropical disturbances and storms. *Mon. Weather Rev.*, 96(10):669–700.

Gray, W. M. (1979). Hurricanes: Their formation, structure and likely role in the tropical circulation. *Meteorology over the tropical oceans*, 155:218.

Greenspan, H. P. & Howard, L. N. (1963). On a time-dependent motion of a rotating fluid. *J. Fluid Mech.*, 17(3):385.

Guervilly, C., Hughes, D. W., & Jones, C. A. (2014). Large-scale vortices in rapidly rotating Rayleigh-Bénard convection. *J. Fluid Mech.*, 758:407–435.

Guzmán, A. J. A., Madonia, M., Cheng, J. S., R. Ostilla-Mónico, Clercx, H. J. H., & Kunnen, R. P. J. (2020). Competition between Ekman plumes and vortex condensates in rapidly rotating thermal convection. *Phys. Rev. Lett.*, 125:214501.

Hébert, F., Hufschmid, R., Scheel, J., & Ahlers, G. (2010). Onset of Rayleigh-Bénard convection in cylindrical containers. *Phys. Rev. E*, 81(4):046318.

Hendricks, E. A., Schubert, W. H., Fulton, S. R., & McNoldy, B. D. (2010). Spontaneous-adjustment emission of inertia-gravity waves by unsteady vortical motion in the hurricane core. *Q. J. R. Meteorol. Soc.*, 136(647):537–548.

Heymsfield, G. M., Halverson, J. B., Simpson, J., Tian, L., & Bui, T. P. (2001). ER-2 Doppler radar investigations of the eyewall of Hurricane Bonnie during the Convection and Moisture Experiment-3. *J. Appl. Meteorol. Climatol.*, 40(8):1310–1330.

Hide, R. (1969). Some laboratory experiments on free thermal convection in a rotating fluid subject to a horizontal temperature gradient and their relation to the theory of the global atmospheric circulation. *The global circulation of the atmosphere*.

Hide, R. & Mason, P. J. (1975). Sloping convection in a rotating fluid. *Adv. Phys.*, 24(1):47–100.

Holland, G. J. (1993). *Global guide to tropical cyclone forecasting*. Secretariat of the World Meteorological Organization.

Holton, J. R. (2004). *An introduction to dynamic meteorology*. International Geophysics Series. Elsevier Academic Press„ Burlington, MA, 4 edition.

Horn, S. & Schmid, P. J. (2017). Prograde, retrograde, and oscillatory modes in rotating Rayleigh-Bénard convection. *J. Fluid. Mech.*, 831:182.

Horn, S. & Shishkina, O. (2015). Toroidal and poloidal energy in rotating Rayleigh–Bénard convection. *J. Fluid. Mech.*, 762:232.

Hu, Y., Ecke, R., & Ahlers, G. (1993). Convection near threshold for Prandtl numbers near 1. *Phys. Rev. E*, 48(6):4399.

Ibanez, T., Keppel, G., Menkes, C., Gillespie, T. W., Lengaigne, M., Mangeas, M., Rivas-Torres, G., & Birnbaum, P. (2019). Globally consistent impact of tropical cyclones on the structure of tropical and subtropical forests. *J. Ecol.*, 107(1):279–292.

Issa, R. I. (1986). Solution of the implicitly discretised fluid flow equations by operator-splitting. *J. Comput. Phys.*, 62(1):40–65.

James, I. N. (1995). *Introduction to circulating atmospheres*. Cambridge University Press.

Jasak, H., Jemcov, A., Tukovic, Z., et al. (2007). OpenFOAM: A C++ library for complex physics simulations. In *International workshop on coupled methods in numerical dynamics*, volume 1000, page 1. IUC Dubrovnik Croatia.

Jones, S. C. (1995). The evolution of vortices in vertical shear. I: Initially barotropic vortices. *Q. J. R. Meteorol. Soc.*, 121(524):821–851.

King, E. M. & Aurnou, J. M. (2013). Turbulent convection in liquid metal with and without rotation. *Proc. Natl. Acad. Sci. U.S.A.*, 110(17):6688–6693.

Knutson, T. R., Camargo, S. J., Chan, J. C. L., Emanuel, K. A., Ho, C. H., Kossin, J. P., Mohapatra, M., Satoh, M., Sugi, M., Walsh, K., et al. (2019). Tropical cyclones and climate change assessment: Part I: Detection and attribution. *Bull. Am. Meteorol. Soc.*, 100(10):1987–2007.

Knutson, T. R., Camargo, S. J., Chan, J. C. L., Emanuel, K. A., Ho, C. H., Kossin, J. P., Mohapatra, M., Satoh, M., Sugi, M., Walsh, K., et al. (2020). Tropical cyclones and climate change assessment: Part II: Projected response to anthropogenic warming. *Bull. Am. Meteorol. Soc.*, 101(3):E303–E322.

Knutson, T. R., McBride, J. L., Chan, J. C. L., Emanuel, K. A., Holland, G., Landsea, C., Held, I., Kossin, J. P., Srivastava, A. K., & Sugi, M. (2010). Tropical cyclones and climate change. *Nat. Geosci.*, 3(3):157.

Kolmogorov, A. N. (1941). The local structure of turbulence in incompressible viscous fluid for very large Reynolds numbers. *Cr Acad. Sci. URSS*, 30:301–305.

Kossin, J. P. & Schubert, W. H. (2001). Mesovortices, Polygonal Flow Patterns, and Rapid Pressure Falls in Hurricane-Like Vortices. *J. Atmos. Sci.*, 58(15):2196–2209.

Kossin, J. P., Schubert, W. H., & Montgomery, M. T. (2000). Unstable interactions between a hurricane's primary eyewall and a secondary ring of enhanced vorticity. *J. Atmos. Sci.*, 57(24):3893–3917.

Kunnen, R. P. J., Geurts, B. J., & Clercx, H. J. H. (2010). Experimental and numerical investigation of turbulent convection in a rotating cylinder. *J. Fluid Mech.*, 626:445.

Leibovich, S. & Lele, S. K. (1985). The influence of the horizontal component of Earth's angular velocity on the instability of the Ekman layer. *J. Fluid Mech.*, 150:41–87.

Lilly, D. K. (1992). A proposed modification of the Germano subgrid-scale closure method. *Phys. Fluids*, 4(3):633–635.

Liu, Y. & Ecke, R. E. (1997). Eckhaus-Benjamin-Feir instability in rotating convection. *Phys. Rev. Lett.*, 78(23):4391.

Lorenz, E. (1967). The nature and theory of the general circulation of the atmosphere. *WMO*, 161.

Lydolph, P. E. (1985). *The climate of the earth.* Government Institutes.

Marks, F. D., Houze, R. A., & Gamache, J. F. (1992). Dual-aircraft investigation of the inner core of Hurricane Norbert. Part I: Kinematic structure. *J. Atmos. Sci.*, 49(11):919–942.

Marshall, J. & Schott, F. (1999). Open-ocean convection: Observations, theory, and models. *Rev. Geophys.*, 37(1):1.

Melander, M. V., McWilliams, J. C., & Zabusky, N. J. (1987). Axisymmetrization and vorticity-gradient intensification of an isolated two-dimensional vortex through filamentation. *J. Fluid Mech.*, 178:137–159.

Merrill, R. T. (1983). A comparison of large and small tropical cyclones. *Mon. Wea. Rev.*, 112:1408–1418.

Miyamoto, Y. & Takemi, T. (2013). A transition mechanism for the spontaneous axisymmetric intensification of tropical cyclones. *J. Atmos. Sci.*, 70(1):112–129.

Moeng, C. H., McWilliams, J. C., Rotunno, R., Sullivan, P. P., & Weil, J. (2004). Investigating 2D modeling of atmospheric convection in the PBL. *J. Atmos. Sci.*, 61(8):889.

Möller, J. D. & Montgomery, M. T. (1999). Vortex Rossby waves and hurricane intensification in a barotropic model. *J. Atmos. Sci.*, 56(11):1674–1687.

Möller, J. D. & Montgomery, M. T. (2000). Tropical cyclone evolution via potential vorticity anomalies in a three-dimensional balance model. *J. Atmos. Sci.*, 57(20):3366–3387.

Montgomery, E. A. H. M. T. & Davis, C. A. (2004). The role of "vortical" hot towers in the formation of Tropical Cyclone Diana (1984). *J. Atmos. Sci.*, 61(11):1209–1232.

Montgomery, M. T., Davis, C., Dunkerton, T., Wang, Z., & others (2012). The Pre-Depression Investigation of Cloud-Systems in the Tropics (PREDICT) experiment: Scientific basis, new analysis tools, and some first results. *Bull. Amer. Meteor.*, 93(2):153–172.

Montgomery, M. T. & Enagonio, J. (1998). Tropical cyclogenesis via convectively forced vortex Rossby waves in a three-dimensional quasigeostrophic model. *J. Atmos. Sci.*, 55(20):3176–3207.

Montgomery, M. T. & Farrell, B. F. (1993). Tropical cyclone formation. *J. Atmos. Sci.*, 50(2):285–310.

Montgomery, M. T. & Kallenbach, R. J. (1997). A theory for vortex Rossby-waves and its application to spiral bands and intensity changes in hurricanes. *Q. J. R. Meteorol. Soc.*, 123(538):435–465.

Montgomery, M. T., Nicholls, M. E., Cram, T. A., & Saunders, A. B. (2006). A vortical hot tower route to tropical cyclogenesis. *J. Atmos. Sci.*, 63(1):355–386.

Montgomery, M. T. & Shapiro, L. J. (1995). Generalized Charney-Stern and Fjortoft theorems for rapidly rotating vortices. *J. Atmos. Sci.*, 52(10):1829–1833.

Montgomery, M. T. & Smith, R. K. (2017). Recent developments in the fluid dynamics of tropical cyclones. *Annu. Rev. Fluid Mech.*, 49:541–574.

Moon, Y. & Nolan, D. S. (2010). Do gravity waves transport angular momentum away from tropical cyclones? *J. Atmos. Sci.*, 67(1):117–135.

Murakami, H. & Wang, B. (2010). Future change of North Atlantic tropical cyclone tracks: Projection by a 20-km-mesh global atmospheric model. *J. Climate*, 23(10):2699–2721.

NASA, M. R. R. T. (2006). Pacific Typhoon. [online] https://earthobservatory.nasa.gov/images/6816/pacific-typhoons accessed on June 3, 2022.

National Weather Service (2019). Cross section of a typical hurricane. [online] https://www.weather.gov/jetstream/tc_structure accessed on June 3, 2022.

Neria, Y. & Shultz, J. M. (2012). Mental health effects of Hurricane Sandy: characteristics, potential aftermath, and response. *JAMA*, 308(24):2571–2572.

Nguyen, M. C., Reeder, M. J., Davidson, N. E., Smith, R. K., & Montgomery, M. T. (2011). Inner-core vacillation cycles during the intensification of Hurricane Katrina. *Q. J. R. Meteorol. Soc.*, 137(657):829–844.

Ning, L. & Ecke, R. E. (1993). Rotating Rayleigh-Bénard convection: Aspect-ratio dependence of the initial bifurcations. *Phys. Rev. E*, 47(5):3326.

Nolan, D. S., Rappin, E. D., & Emanuel, K. A. (2006). Could hurricanes form from random convection in a warmer world ? In *Proc. of 27th Conference on Hurricanes and Tropical Meteorology*.

North, G. R., Pyle, J. A., & Zhang, F. (2014). *Encyclopedia of atmospheric sciences*, volume 1. Elsevier.

Oruba, L., Davidson, P. A., & Dormy, E. (2017). Eye formation in rotating convection. *J. Fluid Mech.*, 812:890–904.

Oruba, L., Davidson, P. A., & Dormy, E. (2018). Formation of eyes in large-scale cyclonic vortices. *Phys. Rev. Fluids*, 3(1):1–18.

Palmen, E. (1948). On the formation and structure of tropical hurricanes. *Geophysica*, 3(1):26–38.

Parodi, A. & Emanuel, K. A. (2009). A theory for buoyancy and velocity scales in deep moist convection. *J. Atmos. Sci.*, 66(11):3449–3463.

Pedlosky, J. (1964). The stability of currents in the atmosphere and the ocean: Part I. *J. Atmos. Sci.*, 21(2):201–219.

Peng, M. S., Jeng, B. F., & Williams, R. T. (1999). A numerical study on tropical cyclone intensification. Part I: Beta effect and mean flow effect. *J. Atmos. Sci.*, 56(10):1404–1423.

Persing, J., Montgomery, M. T., McWilliams, J. C., & Smith, R. K. (2013). Asymmetric and axisymmetric dynamics of tropical cyclones. *Atmos. Chem. Phys.*, 13(24):12299.

Plapp, B. B. & Bodenschatz, E. (1996). Core dynamics of multi-armed spirals in Rayleigh-Bénard convection. *Phys. Scr.*, 1996(T67):111.

Plapp, B. B., Egolf, D. A., Bodenschatz, E., & Pesch, W. (1998). Dynamics and selection of giant spirals in Rayleigh-Bénard convection. *Phys. Rev. Lett.*, 81(24):5334.

Pope, S. B. (2000). *Turbulent flows*. Cambridge University Press, Cambridge, UK.

Prandtl, L. (1932). Meteorologische anwendung der strömungslehre. *Beitr. Phys. Atmos*, 19:188–202.

Price, J. F. & Sundermeyer, M. A. (1999). Stratified Ekman layers. *J. Geophys. Res. Oceans*, 104(C9):20467–20494.

Price, J. F., Weller, R. A., & Schudlich, R. R. (1987). Wind-driven ocean currents and Ekman transport. *Science*, 238(4833):1534–1538.

Puigjaner, D., Herrero, J., Giralt, F., & Simo, C. (2004). Stability analysis of the flow in a cubical cavity heated from below. *Phys. Fluids*, 16(10):3639–3655.

Puigjaner, D., Herrero, J., Simo, C., & Giralt, F. (2008). Bifurcation analysis of steady Rayleigh–Bénard convection in a cubical cavity with conducting sidewalls. *J. Fluid. Mech.*, 598:393–427.

Ramage, C. S. (1959). Hurricane development. *J. Atmos. Sci.*, 16(3):227–237.

Riehl, H. (1948). On the formation of typhoons. *J. Atmos. Sci.*, 5(6):247–265.

Riehl, H. (1950). A model of hurricane formation. *J. Appl. Phys.*, 21(9):917–925.

Ritchie, E. A. & Holland, G. J. (1993). On the interaction of tropical-cyclone-scale vortices. II: Discrete vortex patches. *Q. J. R. Meteorol. Soc.*, 119(514):1363–1379.

Rogers, R., Aberson, S., Aksoy, A., Annane, B., & others (2013). NOAA'S hurricane intensity forecasting experiment: A progress report. *Bull. Amer. Meteor.*, 94(6):859–882.

Rossby, C. G. & Montgomery, R. B. (1935). *The layer of frictional influence in wind and ocean currents.* Massachusetts Institute of Technology and Woods Hole Oceanographic Institution.

Rotunno, R. & Emanuel, K. A. (1987). An air–sea interaction theory for tropical cyclones. Part II: Evolutionary study using a nonhydrostatic axisymmetric numerical model. *J. Atmos. Sci.*, 44(3):542–561.

Roy, C. & Kovordányi, R. (2012). Tropical cyclone track forecasting techniques — A review. *Atmos. Res.*, 104:40–69.

Sadler, J. C. (1976). A role of the tropical upper tropospheric trough in early season typhoon development. *Mon. Weather Rev.*, 104(10):1266–1278.

Schubert, W. H., Montgomery, M. T., Taft, R. K., Guinn, T. A., Fulton, S. R., Kossin, J. P., & Edwards, J. P. (1999). Polygonal Eyewalls, Asymmetric Eye Contraction, and Potential Vorticity Mixing in Hurricanes. *J. Atmos. Sci.*, 56(9):1197–1223.

Schumacher, J. & Sreenivasan, K. R. (2020). Colloquium: Unusual dynamics of convection in the sun. *Rev. Mod. Phys.*, 92(4):041001.

Sebastian, A., Mico, M., Natalija, N., Marcos, P. R., Evgenia, P., & Petia, T. (2017). The Effects of Weather Shocks on Economic Activity: How can Low-Income Countries Cope? Technical report, IMF.

Shapiro, L. J. (1977). Tropical storm formation from easterly waves: A criterion for development. *J. Atmos. Sci.*, 34(7):1007–1022.

Shapiro, L. J. & Montgomery, M. T. (1993). A three-dimensional balance theory for rapidly rotating vortices. *J. Atmos. Sci.*, 50(19):3322–3335.

Simpson, J., Ritchie, E., Holland, G. J., Halverson, J., & Stewart, S. (1997). Mesoscale interactions in tropical cyclone genesis. *Mon. Weather Rev.*, 125(10):2643–2661.

Simpson, R. H. & Riehl, H. (1958). Mid-tropospheric ventilation as a constraint on hurricane development and maintenance. In *Proc. Tech. Conf. on Hurricanes*.

Smagorinsky, J. (1963). General circulation experiments with the primitive equations: I. The basic experiment. *Mon. Weather Rev.*, 91(3):99–164.

Smith, R. K. (2005). "Why must hurricanes have eyes?"–revisited. *Weather*, 60(11):326.

Sobel, A. H. & Bretherton, C. S. (1999). Development of synoptic-scale disturbances over the summertime tropical northwest Pacific. *J. Atmos. Sci.*, 56(17):3106–3127.

Stevens, R. J. A. M., Lohse, D., & Verzicco, R. (2014). Sidewall effects in Rayleigh–Bénard convection. *J. Fluid. Mech.*, 741:1.

Stull, R. B. (2012). *An introduction to boundary layer meteorology*, volume 13. Springer Science & Business Media.

Tennekes, H. & Lumley, J. L. (1972). *A first course in turbulence*. MIT press.

Vallis, G. K. (2017). *Atmospheric and oceanic fluid dynamics*. Cambridge University Press.

Verzicco, R. (2002). Sidewall finite-conductivity effects in confined turbulent thermal convection. *J. Fluid. Mech.*, 473:201–210.

Wan, Z. H., Wei, P., Verzicco, R., Lohse, D., Ahlers, G., & Stevens, R. J. A. M. (2019). Effect of sidewall on heat transfer and flow structure in Rayleigh–Bénard convection. *J. Fluid. Mech.*, 881:218–243.

Webster, P. J., Holland, G. J., Curry, J. A., & Chang, H.-R. (2005). Changes in Tropical Cyclone Number, Duration, and Intensity in a Warming Environment. *Science*, 309(5742):1844–1846.

Weller, H. G., Tabor, G., Jasak, H., & Fureby, C. (1998). A tensorial approach to computational continuum mechanics using object-oriented techniques. *Comput. phys.*, 12(6):620–631.

Willoughby, H. E. (1977). Inertia-buoyancy waves in hurricanes. *J. Atmos. Sci.*, 34(7):1028–1039.

Willoughby, H. E. (1990). Gradient balance in tropical cyclone. *J. Atmos. Sci.*, 47:265–274.

Willoughby, H. E., Marks, F. D., & Feinberg, R. J. (1984). Stationary and moving convective bands in hurricanes. *J. Atmos. Sci.*, 41(22):3189–3211.

WMO (2018). *Guide to Instruments and Methods of Observation*. World Meteorological Organization Geneva.

Wyngaard, J. C. (2010). *Turbulence in the Atmosphere*. Cambridge University Press.

Zhang, X., Gils, D. P. M. V., Horn, S., Wedi, M., Zwirner, L., Ahlers, G., Ecke, R. E., Weiss, S., Bodenschatz, E., & Shishkina, O. (2020). Boundary zonal flow in rotating turbulent Rayleigh-B énard convection. *Phys. Rev. Lett.*, 124(8):084505.

Zhong, F., Ecke, R. E., & Steinberg, V. (1991). Asymmetric modes and the transition to vortex structures in rotating Rayleigh-Bénard convection. *Phys. Rev. Lett.*, 67(18):2473.

Zhong, F., Ecke, R. E., & Steinberg, V. (1993). Rotating Rayleigh–Bénard convection: asymmetric modes and vortex states. *J. Fluid. Mech.*, 249:135.

Zhong, J. Q., Stevens, R. J. A. M., Clercx, H. J. H., Verzicco, R., Lohse, D., & Ahlers, G. (2009). Prandtl-, Rayleigh-, and Rossby-number dependence of heat transport in turbulent rotating Rayleigh-Bénard convection. *Phys. Rev. Lett.*, 102(4):044502.

Appendix A

Flow Parameter Values

Table A.1 Summary of the parameter values simulated in this work with isothermal sidewall.

S.No	H (m)	R (m)	ν (m^2/s)	Ω (s^{-1})	β (K/m)	V (m/s)	E	Re	Ro	Pr	Γ	TCLV?[1]
1	10^3	10^4	10^{-6}	$6.67 \cdot 10^{-12}$	$3 \cdot 10^{-17}$	$1.34 \cdot 10^{-7}$	$1.5 \cdot 10^{-1}$	$1.34 \cdot 10^2$	20.12	0.1	0.1	✓
2	10^3	10^4	10^{-6}	$6.67 \cdot 10^{-12}$	$3 \cdot 10^{-17}$	$1.73 \cdot 10^{-7}$	$1.5 \cdot 10^{-1}$	$1.73 \cdot 10^2$	25.98	0.1	0.1	✓
3	10^3	10^4	10^{-6}	$6.67 \cdot 10^{-12}$	$3 \cdot 10^{-17}$	$2 \cdot 10^{-7}$	$1.5 \cdot 10^{-1}$	$2 \cdot 10^2$	30	0.1	0.1	✘
4	10^3	10^4	10^{-6}	$6.67 \cdot 10^{-12}$	$3 \cdot 10^{-17}$	$2.82 \cdot 10^{-7}$	$1.5 \cdot 10^{-1}$	$2.82 \cdot 10^2$	42.43	0.1	0.1	✘
5	10^3	10^4	10^{-6}	$6.67 \cdot 10^{-12}$	$3 \cdot 10^{-17}$	$3.46 \cdot 10^{-7}$	$1.5 \cdot 10^{-1}$	$3.46 \cdot 10^2$	51.96	0.1	0.1	✘
6	10^3	10^4	10^{-6}	$6.67 \cdot 10^{-12}$	$3 \cdot 10^{-17}$	$4 \cdot 10^{-7}$	$1.5 \cdot 10^{-1}$	$4 \cdot 10^2$	60	0.1	0.1	✘
7	10^3	10^4	10^{-6}	$6.67 \cdot 10^{-12}$	$3 \cdot 10^{-17}$	$4.47 \cdot 10^{-7}$	$1.5 \cdot 10^{-1}$	$4.47 \cdot 10^2$	67.08	0.1	0.1	✘
8	10^3	10^4	10^{-6}	$6.67 \cdot 10^{-12}$	$3 \cdot 10^{-17}$	$4.89 \cdot 10^{-7}$	$1.5 \cdot 10^{-1}$	$4.89 \cdot 10^2$	73.48	0.1	0.1	✘
9	10^3	10^4	10^{-6}	$6.67 \cdot 10^{-12}$	$3 \cdot 10^{-17}$	$5.29 \cdot 10^{-7}$	$1.5 \cdot 10^{-1}$	$5.29 \cdot 10^2$	79.37	0.1	0.1	✘
10	10^3	10^4	10^{-6}	$6.67 \cdot 10^{-12}$	$3 \cdot 10^{-17}$	$5.65 \cdot 10^{-7}$	$1.5 \cdot 10^{-1}$	$5.65 \cdot 10^2$	84.85	0.1	0.1	✘

[1] Tropical Cyclone-like Vortex

11	10^3	10^4	10^{-6}	10^{-11}	$1.99 \cdot 10^{-17}$	$1.22 \cdot 10^{-7}$	10^{-1}	$1.22 \cdot 10^2$	12.25	0.1	0.1	✘
12	10^3	10^4	10^{-6}	10^{-11}	$1.99 \cdot 10^{-17}$	$1.41 \cdot 10^{-7}$	10^{-1}	$1.41 \cdot 10^2$	14.12	0.1	0.1	✓
13	10^3	10^4	10^{-6}	10^{-11}	$3 \cdot 10^{-17}$	$1.73 \cdot 10^{-7}$	10^{-1}	$1.73 \cdot 10^2$	17.32	0.1	0.1	✓
14	10^3	10^4	10^{-6}	10^{-11}	$4 \cdot 10^{-17}$	$2 \cdot 10^{-7}$	10^{-1}	$2 \cdot 10^2$	20	0.1	0.1	✓
15	10^3	10^4	10^{-6}	10^{-11}	$4 \cdot 10^{-17}$	$2 \cdot 10^{-7}$	10^{-1}	$2 \cdot 10^2$	20	0.7	0.1	✓
16	10^3	10^4	10^{-6}	10^{-11}	$4 \cdot 10^{-17}$	$2 \cdot 10^{-7}$	10^{-1}	$2 \cdot 10^2$	20	0.025	0.1	✓
17	10^3	10^4	10^{-6}	10^{-11}	$5 \cdot 10^{-17}$	$2.24 \cdot 10^{-7}$	10^{-1}	$2.24 \cdot 10^2$	22.36	0.1	0.1	✓
18	10^3	10^4	10^{-6}	10^{-11}	$6 \cdot 10^{-17}$	$2.45 \cdot 10^{-7}$	10^{-1}	$2.45 \cdot 10^2$	24.5	0.1	0.1	✓
19	10^3	10^4	10^{-6}	10^{-11}	$6.25 \cdot 10^{-17}$	$2.5 \cdot 10^{-7}$	10^{-1}	$2.5 \cdot 10^2$	25	0.1	0.1	✓
20	10^3	10^4	10^{-6}	10^{-11}	$7.5 \cdot 10^{-17}$	$2.74 \cdot 10^{-7}$	10^{-1}	$2.74 \cdot 10^2$	27.39	0.1	0.1	✓
21	10^3	10^4	10^{-6}	10^{-11}	$7.5 \cdot 10^{-17}$	$3 \cdot 10^{-7}$	10^{-1}	$3 \cdot 10^2$	30	0.1	0.1	✘
22	10^3	10^4	10^{-6}	10^{-11}	$7.5 \cdot 10^{-17}$	$4.8 \cdot 10^{-7}$	10^{-1}	$4.8 \cdot 10^2$	48	0.1	0.1	✘
23	10^3	10^4	10^{-6}	10^{-11}	$7.5 \cdot 10^{-17}$	$5.47 \cdot 10^{-7}$	10^{-1}	$5.47 \cdot 10^2$	54.77	0.1	0.1	✘
24	10^3	10^4	10^{-6}	$1.33 \cdot 10^{-11}$	$4 \cdot 10^{-17}$	$2 \cdot 10^{-7}$	$7.5 \cdot 10^{-2}$	$2 \cdot 10^2$	15	0.1	0.1	✓
25	10^3	10^4	10^{-6}	$1.33 \cdot 10^{-11}$	$4 \cdot 10^{-17}$	$2 \cdot 10^{-7}$	$7.5 \cdot 10^{-2}$	$2 \cdot 10^2$	15	0.7	0.1	✓
26	10^3	10^4	10^{-6}	$1.33 \cdot 10^{-11}$	$9 \cdot 10^{-17}$	$3 \cdot 10^{-7}$	$7.5 \cdot 10^{-2}$	$3 \cdot 10^2$	22.5	0.1	0.1	✓
27	10^3	10^4	10^{-6}	$1.33 \cdot 10^{-11}$	$1.2 \cdot 10^{-16}$	$3.46 \cdot 10^{-7}$	$7.5 \cdot 10^{-2}$	$3.46 \cdot 10^2$	25.98	0.1	0.1	✓
28	10^3	10^4	10^{-6}	$1.33 \cdot 10^{-11}$	$1.2 \cdot 10^{-16}$	$4.24 \cdot 10^{-7}$	$7.5 \cdot 10^{-2}$	$4.24 \cdot 10^2$	31.82	0.1	0.1	✘
29	10^3	10^4	10^{-6}	$2 \cdot 10^{-11}$	$9 \cdot 10^{-17}$	$3 \cdot 10^{-7}$	$5 \cdot 10^{-2}$	$3 \cdot 10^2$	15	0.1	0.1	✓
30	10^3	10^4	10^{-6}	$2 \cdot 10^{-11}$	$9 \cdot 10^{-17}$	$3 \cdot 10^{-7}$	$5 \cdot 10^{-2}$	$3 \cdot 10^2$	15	0.7	0.1	✓
31	10^3	10^4	10^{-6}	$2 \cdot 10^{-11}$	$1.5 \cdot 10^{-16}$	$3.87 \cdot 10^{-7}$	$5 \cdot 10^{-2}$	$3.87 \cdot 10^2$	19.36	0.1	0.1	✓
32	10^3	10^4	10^{-6}	$2 \cdot 10^{-11}$	$2 \cdot 10^{-16}$	$4.47 \cdot 10^{-7}$	$5 \cdot 10^{-2}$	$4.47 \cdot 10^2$	22.36	0.1	0.1	✓
33	10^3	10^4	10^{-6}	$2.22 \cdot 10^{-11}$	$1.6 \cdot 10^{-16}$	$4 \cdot 10^{-7}$	$4.5 \cdot 10^{-2}$	$4 \cdot 10^2$	18	0.1	0.1	✓
34	10^3	10^4	10^{-6}	$2.5 \cdot 10^{-11}$	$2 \cdot 10^{-16}$	$4.47 \cdot 10^{-7}$	$4 \cdot 10^{-2}$	$4.47 \cdot 10^2$	17.89	0.1	0.1	✓
35	10^3	10^4	10^{-6}	$2.5 \cdot 10^{-11}$	$2.03 \cdot 10^{-16}$	$4.5 \cdot 10^{-7}$	$4 \cdot 10^{-2}$	$4.5 \cdot 10^2$	18	0.1	0.1	✓
36	10^3	10^4	10^{-6}	$2.86 \cdot 10^{-11}$	$2 \cdot 10^{-16}$	$4.47 \cdot 10^{-7}$	$3.5 \cdot 10^{-2}$	$4.47 \cdot 10^2$	15.65	0.1	0.1	✓

37	10^3	10^4	10^{-6}	$2.86 \cdot 10^{-11}$	$3 \cdot 10^{-16}$	$5.48 \cdot 10^{-7}$	$3.5 \cdot 10^{-2}$	$5.48 \cdot 10^2$	19.17	0.1	0.1	✓
38	10^3	10^4	10^{-6}	$2.86 \cdot 10^{-11}$	$3 \cdot 10^{-16}$	$5.48 \cdot 10^{-7}$	$3.5 \cdot 10^{-2}$	$5.48 \cdot 10^2$	19.17	0.7	0.1	✓
39	10^3	10^4	10^{-6}	$2.86 \cdot 10^{-11}$	$3 \cdot 10^{-16}$	$5.48 \cdot 10^{-7}$	$3.5 \cdot 10^{-2}$	$5.48 \cdot 10^2$	19.17	0.025	0.1	✓
40	10^3	10^4	10^{-6}	$2.86 \cdot 10^{-11}$	$3.25 \cdot 10^{-16}$	$5.7 \cdot 10^{-7}$	$3.5 \cdot 10^{-2}$	$5.7 \cdot 10^2$	19.95	0.1	0.1	✓
41	10^3	10^4	10^{-6}	$2.86 \cdot 10^{-11}$	$5.2 \cdot 10^{-16}$	$7.21 \cdot 10^{-7}$	$3.5 \cdot 10^{-2}$	$7.21 \cdot 10^2$	25.24	0.1	0.1	✓
42	10^3	10^4	10^{-6}	$3.33 \cdot 10^{-11}$	$2.35 \cdot 10^{-16}$	$4.85 \cdot 10^{-7}$	$3 \cdot 10^{-2}$	$4.85 \cdot 10^2$	14.55	0.1	0.1	✓
43	10^3	10^4	10^{-6}	$3.33 \cdot 10^{-11}$	$3.6 \cdot 10^{-16}$	$6 \cdot 10^{-7}$	$3 \cdot 10^{-2}$	$6 \cdot 10^2$	18	0.1	0.1	✓
44	10^3	10^4	10^{-6}	$3.33 \cdot 10^{-11}$	$4.44 \cdot 10^{-16}$	$6.66 \cdot 10^{-7}$	$3 \cdot 10^{-2}$	$6.66 \cdot 10^2$	19.98	0.1	0.1	✓
45	10^3	10^4	10^{-6}	$3.33 \cdot 10^{-11}$	$5.37 \cdot 10^{-16}$	$7.33 \cdot 10^{-7}$	$3 \cdot 10^{-2}$	$7.33 \cdot 10^2$	21.99	0.1	0.1	✓
46	10^3	10^4	10^{-6}	$3.33 \cdot 10^{-11}$	$5.38 \cdot 10^{-16}$	$7.33 \cdot 10^{-7}$	$3 \cdot 10^{-2}$	$7.33 \cdot 10^2$	22	0.1	0.1	✓
47	10^3	10^4	10^{-6}	$5 \cdot 10^{-11}$	$7.99 \cdot 10^{-16}$	$8.94 \cdot 10^{-7}$	$2 \cdot 10^{-2}$	$8.94 \cdot 10^2$	17.88	0.1	0.1	✓
48	10^3	10^4	10^{-6}	$5 \cdot 10^{-11}$	$7.99 \cdot 10^{-16}$	$8.94 \cdot 10^{-7}$	$2 \cdot 10^{-2}$	$8.94 \cdot 10^2$	17.88	0.7	0.1	✓
49	10^3	10^4	10^{-6}	$5 \cdot 10^{-11}$	10^{-15}	10^{-6}	$2 \cdot 10^{-2}$	10^3	20	0.1	0.1	✓
50	10^3	10^4	10^{-6}	$5 \cdot 10^{-11}$	10^{-15}	10^{-6}	$2 \cdot 10^{-2}$	10^3	20	0.7	0.1	✓
51	10^3	10^4	10^{-6}	$5 \cdot 10^{-11}$	10^{-15}	10^{-6}	$2 \cdot 10^{-2}$	10^3	20	0.025	0.1	✓
52	10^3	10^4	10^{-6}	$5 \cdot 10^{-11}$	$1.5 \cdot 10^{-15}$	$1.22 \cdot 10^{-6}$	$2 \cdot 10^{-2}$	$1.22 \cdot 10^3$	24.48	0.1	0.1	✓
53	10^3	10^4	10^{-6}	$5 \cdot 10^{-11}$	$1.5 \cdot 10^{-15}$	$1.22 \cdot 10^{-6}$	$2 \cdot 10^{-2}$	$1.22 \cdot 10^3$	24.48	0.7	0.1	✓
54	10^3	10^4	10^{-6}	$5 \cdot 10^{-11}$	$1.5 \cdot 10^{-15}$	$1.22 \cdot 10^{-6}$	$2 \cdot 10^{-2}$	$1.22 \cdot 10^3$	24.48	0.025	0.1	✓
55	10^3	10^4	10^{-6}	$5 \cdot 10^{-11}$	$2 \cdot 10^{-15}$	$1.41 \cdot 10^{-6}$	$2 \cdot 10^{-2}$	$1.41 \cdot 10^3$	28.28	0.1	0.1	✓
56	10^3	10^4	10^{-6}	$5 \cdot 10^{-11}$	$2 \cdot 10^{-15}$	$1.41 \cdot 10^{-6}$	$2 \cdot 10^{-2}$	$1.41 \cdot 10^3$	28.28	0.7	0.1	✓
57	10^3	10^4	10^{-6}	$5 \cdot 10^{-11}$	$2 \cdot 10^{-15}$	$1.5 \cdot 10^{-6}$	$2 \cdot 10^{-2}$	$1.5 \cdot 10^3$	30	0.1	0.1	✘
58	10^3	10^4	10^{-6}	10^{-9}	$4 \cdot 10^{-13}$	$2 \cdot 10^{-5}$	10^{-3}	$2 \cdot 10^4$	20	0.1	0.1	✓
59	10^3	10^4	10^{-6}	10^{-9}	$4 \cdot 10^{-13}$	$2 \cdot 10^{-5}$	10^{-3}	$2 \cdot 10^4$	20	0.7	0.1	✓
60	10^3	10^4	10^{-6}	10^{-6}	$4 \cdot 10^{-7}$	$2 \cdot 10^{-2}$	10^{-6}	$2 \cdot 10^7$	20	0.1	0.1	✓
61	500	10^4	$2.5 \cdot 10^{-6}$	10^{-8}	$8.01 \cdot 10^{-11}$	$1.42 \cdot 10^{-4}$	10^{-3}	$2.83 \cdot 10^4$	28.3	0.1	0.05	✓
62	500	10^4	$2.5 \cdot 10^{-7}$	10^{-8}	$8.01 \cdot 10^{-11}$	$1.42 \cdot 10^{-4}$	10^{-4}	$2.83 \cdot 10^5$	28.3	0.1	0.05	✓

63	500	10^4	$2.5 \cdot 10^{-9}$	10^{-8}	$8.01 \cdot 10^{-11}$	$1.42 \cdot 10^{-4}$	10^{-6}	$2.83 \cdot 10^7$	28.3	0.1	0.05	✓
64	500	10^4	$2.5 \cdot 10^{-9}$	10^{-8}	$8.01 \cdot 10^{-11}$	$1.42 \cdot 10^{-4}$	10^{-6}	$2.83 \cdot 10^7$	28.3	0.7	0.05	✓
65	500	10^4	$2.5 \cdot 10^{-10}$	10^{-8}	$8.01 \cdot 10^{-11}$	$1.42 \cdot 10^{-4}$	10^{-7}	$2.83 \cdot 10^8$	28.3	0.1	0.05	✓
66	500	10^4	$2.5 \cdot 10^{-10}$	10^{-8}	$8.01 \cdot 10^{-11}$	$2 \cdot 10^{-4}$	10^{-7}	$4 \cdot 10^8$	40	0.1	0.05	✘
67	500	10^4	$2.5 \cdot 10^{-12}$	10^{-8}	$8.01 \cdot 10^{-11}$	$1.42 \cdot 10^{-4}$	10^{-9}	$2.83 \cdot 10^{10}$	28.3	0.1	0.05	✓
68	500	10^4	$2.5 \cdot 10^{-12}$	10^{-8}	$8.01 \cdot 10^{-11}$	$1.42 \cdot 10^{-4}$	10^{-9}	$2.83 \cdot 10^{10}$	28.3	0.7	0.05	✓
69	500	10^4	$2.5 \cdot 10^{-12}$	10^{-8}	$8.01 \cdot 10^{-11}$	$1.42 \cdot 10^{-4}$	10^{-9}	$2.83 \cdot 10^{10}$	28.3	0.025	0.05	✓
70	500	10^4	$2.5 \cdot 10^{-12}$	10^{-8}	$8.01 \cdot 10^{-11}$	$2 \cdot 10^{-4}$	10^{-9}	$4 \cdot 10^{10}$	40	0.025	0.05	✘

$\alpha = 10^{-4} K^{-1}$ & $g = 10\ ms^{-2}$ for all the simulations.

Appendix B

Derivation of Energy Budget Equations

This appendix contains derivation of the energy budget Eqs. (6.1)-(6.4) from the momentum and temperature perturbation equations in cylindrical coordinates given by,

$$\frac{\partial u_r}{\partial t} + u_r\frac{\partial u_r}{\partial r} + \frac{u_\varphi}{r}\frac{\partial u_r}{\partial \varphi} + u_z\frac{\partial u_r}{\partial z} - \frac{u_\varphi^2}{r} = -\frac{\partial P}{\rho_o \partial r} + 2\Omega u_\varphi + \underbrace{\nu\left[\nabla^2 u_r - \frac{u_r}{r^2} - \frac{2}{r^2}\frac{\partial u_\varphi}{\partial \varphi}\right] - \frac{\partial \tau_{r,i}}{\partial x_i}}_{D_r} \tag{B.1}$$

$$\frac{\partial u_\varphi}{\partial t} + u_r\frac{\partial u_\varphi}{\partial r} + \frac{u_\varphi}{r}\frac{\partial u_\varphi}{\partial \varphi} + u_z\frac{\partial u_\varphi}{\partial z} + u_r\frac{u_\varphi}{r} = -\frac{1}{r}\frac{\partial P}{\rho_o \partial \varphi} - 2\Omega u_r + \underbrace{\nu\left[\nabla^2 u_\varphi - \frac{u_\varphi}{r^2} - \frac{2}{r^2}\frac{\partial u_r}{\partial \varphi}\right] - \frac{\partial \tau_{\varphi,i}}{\partial x_i}}_{D_\varphi} \tag{B.2}$$

$$\frac{\partial u_z}{\partial t} + u_r\frac{\partial u_z}{\partial r} + \frac{u_\varphi}{r}\frac{\partial u_z}{\partial \varphi} + u_z\frac{\partial u_z}{\partial z} = -\frac{\partial P}{\rho_o \partial z} - \alpha g\theta + \underbrace{\nu\left[\nabla^2 u_z\right] - \frac{\partial \tau_{z,i}}{\partial x_i}}_{D_z} \tag{B.3}$$

$$\frac{\partial \theta}{\partial t} + u_r\frac{\partial \theta}{\partial r} + \frac{u_\varphi}{r}\frac{\partial \theta}{\partial \varphi} + u_z\frac{\partial \theta}{\partial z} = \beta u_z + \underbrace{\nu\left[\nabla^2 \theta\right] - \frac{\partial \tau_{\theta j}}{\partial x_j}}_{D_\theta} \tag{B.4}$$

All variables can be separated into the azimuthal mean $\langle X \rangle$ and its asymmetric term X'.

$$u_r = \langle u_r \rangle(r, z, t) + u'_r(r, \varphi, z, t) \tag{B.5}$$

$$u_\varphi = \langle u_\varphi \rangle(r, z, t) + u'_\varphi(r, \varphi, z, t) \tag{B.6}$$

$$u_z = \langle u_z \rangle(r, z, t) + u'_z(r, \varphi, z, t) \tag{B.7}$$

$$P = \langle P \rangle(r, z, t) + P'(r, \varphi, z, t) \tag{B.8}$$

$$\theta = \langle \theta \rangle(r, z, t) + \theta'(r, \varphi, z, t) \tag{B.9}$$

After substituting these relationships into Eq.(B.1) to Eq.(B.4) and taking the azimuthal average, the azimuthal mean momentum and temperature perturbation equations can be written as follows:

$$\frac{\partial \langle u_r \rangle}{\partial t} + \langle u_r \rangle \frac{\partial \langle u_r \rangle}{\partial r} + \langle u_z \rangle \frac{\partial \langle u_r \rangle}{\partial z} + \left\langle u'_r \frac{\partial u'_r}{\partial r} + \frac{u'_\varphi}{r} \frac{\partial u'_r}{\partial \varphi} + u'_z \frac{\partial u'_r}{\partial z} \right\rangle - \frac{\langle u_\varphi \rangle^2}{r} - \frac{\langle u'^2_\varphi \rangle}{r} = -\frac{\partial \langle P/\rho_o \rangle}{\partial r} + 2\Omega \langle u_\varphi \rangle + \langle D_r \rangle \tag{B.10}$$

$$\frac{\partial \langle u_\varphi \rangle}{\partial t} + \langle u_r \rangle \frac{\partial \langle u_\varphi \rangle}{\partial r} + \langle u_z \rangle \frac{\partial \langle u_\varphi \rangle}{\partial z} + \left\langle u'_r \frac{\partial u'_\varphi}{\partial r} + \frac{u'_\varphi}{r} \frac{\partial u'_\varphi}{\partial \varphi} + u'_z \frac{\partial u'_\varphi}{\partial z} \right\rangle + \frac{\langle u_r u_\varphi \rangle}{r} + \frac{\langle u'_r u'_\varphi \rangle}{r} = -2\Omega \langle u_r \rangle + \langle D_\varphi \rangle \tag{B.11}$$

$$\frac{\partial \langle u_z \rangle}{\partial t} + \langle u_r \rangle \frac{\partial \langle u_z \rangle}{\partial r} + \langle u_z \rangle \frac{\partial \langle u_z \rangle}{\partial z} + \left\langle u'_r \frac{\partial u'_z}{\partial r} + \frac{u'_\varphi}{r} \frac{\partial u'_z}{\partial \varphi} + u'_z \frac{\partial u'_z}{\partial z} \right\rangle = -\frac{\partial \langle P/\rho_o \rangle}{\partial z} - \alpha g \langle \theta \rangle + \langle D_z \rangle \tag{B.12}$$

$$\frac{\partial \langle \theta \rangle}{\partial t} + \langle u_r \rangle \frac{\partial \langle \theta \rangle}{\partial r} + \langle u_z \rangle \frac{\partial \langle \theta \rangle}{\partial z} + \left\langle u'_r \frac{\partial \theta'}{\partial r} + \frac{u'_\varphi}{r} \frac{\partial \theta'}{\partial \varphi} + u'_z \frac{\partial \theta'}{\partial z} \right\rangle = \beta \langle u_z \rangle + \langle D_\theta \rangle \tag{B.13}$$

The asymmetric momentum equations can be derived by subtracting the azimuthal mean equations [Eqs. (B.10) to (B.13)] from the total momentum equations [Eq. (B.1) to Eq. (B.4)], respectively,

$$\frac{\partial u_r'}{\partial t} + u_r'\frac{\partial\langle u_r\rangle}{\partial r} + u_z'\frac{\partial\langle u_r\rangle}{\partial z} + u_r'\frac{\partial u_r'}{\partial r} + \frac{u_\varphi'}{r}\frac{\partial u_r'}{\partial\varphi} + u_z'\frac{\partial u_r'}{\partial z} + \langle u_r\rangle\frac{\partial u_r'}{\partial r} + \frac{\langle u_\varphi\rangle}{r}\frac{\partial u_r'}{\partial\varphi} + \langle u_z\rangle\frac{\partial u_r'}{\partial z}$$
$$- \left\langle u_r'\frac{\partial u_r'}{\partial r} + \frac{u_\varphi'}{r}\frac{\partial u_r'}{\partial\varphi} + u_z'\frac{\partial u_r'}{\partial z}\right\rangle + \frac{\langle u_\varphi'^2\rangle}{r} - \frac{u_\varphi'^2}{r} - 2\frac{\langle u_\varphi\rangle u_\varphi'}{r} = -\frac{\partial P'}{\rho_o\partial r} + 2\Omega u_\varphi' + D_r' \tag{B.14}$$

$$\frac{\partial u_\varphi'}{\partial t} + u_r'\frac{\partial\langle u_\varphi\rangle}{\partial r} + u_z'\frac{\partial\langle u_\varphi\rangle}{\partial z} + u_r'\frac{\partial u_\varphi'}{\partial r} + \frac{u_\varphi'}{r}\frac{\partial u_\varphi'}{\partial\varphi} + u_z'\frac{\partial u_\varphi'}{\partial z} + \langle u_r\rangle\frac{\partial u_\varphi'}{\partial r} + \frac{\langle u_\varphi\rangle}{r}\frac{\partial u_\varphi'}{\partial\varphi} + \langle u_z\rangle\frac{\partial u_\varphi'}{\partial z}$$
$$- \left\langle u_r'\frac{\partial u_\varphi'}{\partial r} + \frac{u_\varphi'}{r}\frac{\partial u_\varphi'}{\partial\varphi} + u_z'\frac{\partial u_\varphi'}{\partial z}\right\rangle + \frac{\langle u_r\rangle u_\varphi'}{r} + \frac{\langle u_\varphi\rangle u_r'}{r} + \frac{u_r'u_\varphi'}{r} - \frac{\langle u_r'u_\varphi'\rangle}{r} = -\frac{1}{r}\frac{\partial P'}{\rho_o\partial\varphi} - 2\Omega u_r' + D_\varphi' \tag{B.15}$$

$$\frac{\partial u_z'}{\partial t} + u_r'\frac{\partial\langle u_z\rangle}{\partial r} + u_z'\frac{\partial\langle u_z\rangle}{\partial z} + u_r'\frac{\partial u_z'}{\partial r} + \frac{u_\varphi'}{r}\frac{\partial u_z'}{\partial\varphi} + u_z'\frac{\partial u_z'}{\partial z} + \langle u_r\rangle\frac{\partial u_z'}{\partial r} + \frac{\langle u_\varphi\rangle}{r}\frac{\partial u_z'}{\partial\varphi} + \langle u_z\rangle\frac{\partial u_z'}{\partial z}$$
$$- \left\langle u_r'\frac{\partial u_z'}{\partial r} + \frac{u_\varphi'}{r}\frac{\partial u_z'}{\partial\varphi} + u_z'\frac{\partial u_z'}{\partial z}\right\rangle = -\frac{\partial P'}{\rho_o\partial z} - \alpha g\theta' + D_z' \tag{B.16}$$

$$\frac{\partial\theta'}{\partial t} + u_r'\frac{\partial\langle\theta\rangle}{\partial r} + u_z'\frac{\partial\langle\theta\rangle}{\partial z} + u_r'\frac{\partial\theta'}{\partial r} + \frac{u_\varphi'}{r}\frac{\partial\theta'}{\partial\varphi} + u_z'\frac{\partial\theta'}{\partial z}$$
$$+ \langle u_r\rangle\frac{\partial\theta'}{\partial r} + \frac{\langle u_\varphi\rangle}{r}\frac{\partial\theta'}{\partial\varphi} + \langle\theta\rangle\frac{\partial u_z'}{\partial z} - \left\langle u_r'\frac{\partial\theta'}{\partial r} + \frac{u_\varphi'}{r}\frac{\partial\theta'}{\partial\varphi} + u_z'\frac{\partial\theta'}{\partial z}\right\rangle = \beta u_z' + D_\theta' \tag{B.17}$$

An azimuthal mean kinetic energy equation $\langle K\rangle$ is obtained by adding the three components of momentum equations after multiplying $\langle u_r\rangle$ by Eq. (B.10), $\langle u_\varphi\rangle$ by Eq. (B.11) and $\langle u_z\rangle$ by Eq. (B.12) and further simplified using the continuity equation $(1/r)(\partial/\partial r)(ru_r) + (1/r)(\partial u_\varphi/\partial\varphi) + (\partial u_z/\partial z) = 0$. An azimuthal mean asymmetric kinetic energy equation K' can be obtained by the same method after multiplying u_r'

by Eq. (B.14), u'_φ by Eq. (B.15) and u'_z by Eq. (B.16):

$$\begin{aligned}
&\underbrace{\frac{\partial\langle K\rangle}{\partial t}}_{T_{\langle K\rangle}} + \frac{1}{r}\frac{\partial}{\partial r}\left[r\left(\langle u_r\rangle\langle K\rangle + \langle u_r\rangle\langle u'_r u'_r\rangle + \langle u_\varphi\rangle\langle u'_r u'_\varphi\rangle + \langle u_z\rangle\langle u'_r u'_z\rangle\right)\right] \\
&\quad + \frac{\partial}{\partial z}\left(\langle u_z\rangle\langle K\rangle + \langle u_r\rangle\langle u'_r u'_z\rangle + \langle u_\varphi\rangle\langle u'_\varphi u'_r\rangle + \langle u_z\rangle\langle u'_r u'_z\rangle\right) \\
&\quad - \left[r\langle u'_r u'_\varphi\rangle\frac{\partial}{\partial r}\left(\frac{\langle u_\varphi\rangle}{r}\right) + \langle u'_r u'_z\rangle\frac{\partial\langle u_r\rangle}{\partial z}\right. \\
&\quad \left. + \langle u'_\varphi u'_z\rangle\frac{\partial\langle u_\varphi\rangle}{\partial z} + \langle u'_r u'_r\rangle\frac{\partial\langle u_r\rangle}{\partial r} + \frac{\langle u_r\rangle}{r}\langle u'_\varphi u'_\varphi\rangle + \langle u'_r u'_z\rangle\frac{\partial\langle u_z\rangle}{\partial r} + \langle u'_z u'_z\rangle\frac{\partial\langle u_z\rangle}{\partial z}\right] \\
&\quad = \underbrace{-\langle u_r\rangle\frac{\partial\langle P/\rho_o\rangle}{\partial r} - \langle u_z\rangle\frac{\partial\langle P/\rho_o\rangle}{\partial z}}_{P_{\langle K\rangle}} - \underbrace{\alpha g\langle\theta\rangle\langle u_z\rangle}_{C_M} + D_{\langle K\rangle}
\end{aligned} \tag{B.18}$$

$$\begin{aligned}
&\underbrace{\frac{\partial\langle K'\rangle}{\partial t}}_{T_{K'}} + \underbrace{\frac{\partial}{\partial r}\left(\langle u_r\rangle\langle K'\rangle + \langle u'_r K'\rangle\right) + \frac{\partial}{\partial z}\left(\langle u_z\rangle\langle K'\rangle + \langle u'_z K'\rangle\right)}_{A_{K'}} \\
&\quad + \left[r\langle u'_r u'_\varphi\rangle\frac{\partial}{\partial r}\left(\frac{\langle u_\varphi\rangle}{r}\right) + \langle u'_r u'_z\rangle\frac{\partial\langle u_r\rangle}{\partial z}\right. \\
&\quad \left. + \langle u'_\varphi u'_z\rangle\frac{\partial\langle u_\varphi\rangle}{\partial z} + \langle u'_r u'_r\rangle\frac{\partial\langle u_r\rangle}{\partial r} + \frac{\langle u_r\rangle}{r}\langle u'_\varphi u'_\varphi\rangle + \langle u'_r u'_z\rangle\frac{\partial\langle u_z\rangle}{\partial r} + \langle u'_z u'_z\rangle\frac{\partial\langle u_z\rangle}{\partial z}\right] \\
&\quad = \underbrace{-\left\langle u'_r\frac{\partial P'}{\rho_o\partial r}\right\rangle - \left\langle u'_z\frac{\partial P'}{\rho_o\partial z}\right\rangle}_{P_{K'}} - \underbrace{\alpha g\langle\theta' u'_z\rangle}_{C_P} + D_{K'}
\end{aligned} \tag{B.19}$$

By multiplying $(\alpha g/N^2)\langle\theta\rangle$, $(\alpha g/N^2)\theta'$ by Eq. (B.13) and Eq. (B.17), respectively, an azimuthal mean $\langle A\rangle$ and a perturbation A' potential energy equation can be obtained. $N = \sqrt{\alpha g\beta}$ is the buoyancy frequency.

$$\begin{aligned}
&\underbrace{\frac{\partial\langle A\rangle}{\partial t}}_{T_{\langle A\rangle}} + \underbrace{\frac{1}{r}\frac{\partial}{\partial r}\left\{r\left[\langle A\rangle\langle u_r\rangle + \left(\frac{\alpha g}{\beta}\right)\langle\theta\rangle\langle u'_r\theta'\rangle\right]\right\} + \frac{\partial}{\partial z}\left\{r\left[\langle A\rangle\langle u_z\rangle + \left(\frac{\alpha g}{\beta}\right)\langle\theta\rangle\langle u'_z\theta'\rangle\right]\right\}}_{A_{\langle A\rangle}} \\
&\quad - \underbrace{\left[\left(\frac{\alpha g}{\beta}\right)\langle u'_r\theta'\rangle\frac{\partial\langle\theta\rangle}{\partial r} - \left(\frac{\alpha g}{\beta}\right)\langle u'_z\theta'\rangle\frac{\partial\langle\theta\rangle}{\partial z}\right]}_{C_A} = \underbrace{\alpha g\langle u_z\rangle\langle\theta\rangle}_{C_M} + D_{\langle A\rangle}
\end{aligned} \tag{B.20}$$

$$\underbrace{\frac{\partial \langle A' \rangle}{\partial t}}_{T_{A'}} + \underbrace{\frac{1}{r}\frac{\partial}{\partial r}\left(r\langle A u_r \rangle\right) + \frac{\partial}{\partial z}\left(\langle A' u_z \rangle\right)}_{A_{A'}}$$
$$+ \underbrace{\left[\left(\frac{\alpha g}{\beta}\right)\langle u_r' \theta' \rangle \frac{\partial \langle \theta \rangle}{\partial r} - \left(\frac{\alpha g}{\beta}\right)\langle u_z' \theta' \rangle \frac{\partial \langle \theta \rangle}{\partial z}\right]}_{C_A} = \underbrace{\alpha g \langle u_z' \theta' \rangle}_{C_P} + D_{A'} \quad \text{(B.21)}$$